



TECHNISCHE
UNIVERSITÄT
WIEN

Tunable filters in Mid-Infrared and Raman Spectroscopy

A thesis submitted for the degree of
Doctor of Technical Sciences (Dr. techn.)
at

Vienna University of Technology
Faculty of Technical Chemistry
Institute of Chemical Technologies and Analytics

under supervision of
Univ. Prof. Dr. Bernhard Lendl

defended by
DI Christoph Gasser
Mat.Nr. 0727265

Place and Date

Christoph Gasser

Zusammenfassung

Unter den Stichworten Industrie 4.0 und Process Analytical Technology (PAT) findet sich ein großes Themengebiet mit dem Schwerpunkt von optimierter Prozesskontrolle durch Generierung prozessnaher Information. Dazu benötigt es dedizierte und kompakte Sensoren, die in den Prozess integriert werden können ohne selbigen zu beeinflussen. Infrarot Spektroskopie bietet eine zerstörungsfreie Analysenmethode mit hoher chemischer Selektivität und Empfindlichkeit. Der erste Teil dieser Dissertation befasst sich mit dem Design kompakter, spektroskopischer Sensoren auf Basis von miniaturisierbaren, durchstimmbaren Filter im mittleren Infrarotbereich (MIR), die es ermöglichen, zielgerichtete Messungen durchzuführen, ohne auf Selektivität und Empfindlichkeit zu verzichten. Hierzu wurden durchstimmbare Fabry-Perot Filter mit kleinen thermischen Lichtquellen und innovativen Lasersystemen gekoppelt, die einen hohen Grad an Integrierbarkeit aufweisen. Es wurde zunächst ein Prototyp für die on-line Bestimmung des Nebenprodukts Methylformiat in einem Formaldehyd-Prozess gebaut und anschließend an der Anlage getestet. Gleichzeitig konnte gezeigt werden, dass auch eine Mehrkomponentenanalyse mit diesen Sensoren möglich ist. Hier wurde ein Gasgemisch typisch für den C₄-Schnitt einer petrochemischen Raffinerie untersucht. Weiters wurde diese Art des Sensors mit einem inline-fähigen Probeninterface für die Messung von Flüssigkeiten erweitert, einer sogenannten abgeschwächten Totalreflexions-Einheit (ATR). Dieser Prototyp wurde zur kontinuierlichen Überwachung des Wasserstoffperoxid-Gehalts in einem modernen Gaswäscher zur Entfernung von H₂S in Biogasanlagen eingesetzt und getestet. Zusätzlich konnte dieser Sensor durch Einsatz einer neuen Art von Laser, dem Super-Kontinuums-Laser, als Lichtquelle erheblich verbessert werden, indem Lichtdurchsatz und damit das Signal zu Rauschen Verhältnis vergrößert wurde.

Der zweite Teil beschäftigte sich mit der Kombination von Laser-Doppler Anemometrie (LDA) und Raman Spektroskopie zur gleichzeitigen Messung von Strömungseigenschaften und -zusammensetzung in chemischen Prozessen. Durch den Einsatz eines einzigen Lasers zur Messung sowohl mit LDA als auch Raman wird garantiert, dass die gewonnenen Information aus ein und derselben Stelle stammt. Der Aufbau wurde an einem einfachen T-Mischer mittels Messung und computerunterstützter Simulation validiert.

Der dritte Teil dieser Dissertation beschäftigte sich mit der Fernerkundung durch Raman-Spektroskopie. Hier wurde ein bereits bestehender Prototyp, der eine Punktmessung erlaubt, mit einer elektronisch gesteuerten Strahlpositionierung ausgestattet, um rasternd chemische Bilder zu erzeugen. Zudem wurde mit Hilfe eines durchstimmbaren Filters im sichtbaren Bereich des elektromagnetischen Spektrums ein ganz neuer, auf einer direkt abbildenden Methode basierender Prototyp geplant und gebaut. Der hier verwendete durchstimmbare Filter besitzt eine große optische Apertur, der eine direkte abbildende Messung erlaubt. So wurden sogenannte Hyperspectral Images (HSI) er-

zeugt, Datenwürfel also, bei denen zwei Achsen die Ortskoordinaten darstellen und eine Achse die spektralen Informationen enthält. HSIs bestehen meist aus großen Datenmengen und sind selbst für Experten schwer interpretierbar. Darum wurde in einem nächsten Schritt mittels Bildauswertungsalgorithmen und Chemometrie ein möglichst einfaches, bereits klassifiziertes Bild erzeugt, das auch von Laien verstanden werden kann. Die primäre Anwendung war die Detektion von kleinen Mengen an Gefahren- und Sprengstoffen auf Distanzen von bis zu 15 m.

Schlagworte: Infrarotspektroskopie ■ Raman Spektroskopie ■ Prozessüberwachung ■ Industrie 4.0 ■ Optische Sensoren ■ Process Analytical Technologies (PAT) ■ Fernerkundung ■ Hyperspectral Imaging ■ Chemometrie ■ Sprengstoffe

Abstract

Process analytical technology (PAT) encompasses several fields of chemistry as well as physics with the goal of developing sensor systems, which offer high selectivity and sensitivity and at the same time can be used inside the process (in-line), are robust and cost effective. Mid-Infrared (MIR) spectroscopy is a non-destructive method relying on the specific absorbance of materials in the infrared region of light and produces a *fingerprint* of the analyte. In the first part of this thesis, small dedicated MIR sensors have been developed by employing MEMS fabricated, tunable Fabry-Perot (FP) filters in combination with small thermal light sources. This allowed for the construction of compact prototypes for gas sensing applications. Their usefulness in PAT applications was tested for the direct monitoring of methyl formate as a byproduct of the formaldehyde production process. Furthermore, it was shown that multi-component analysis of different gas species is possible and feasible with the use of chemometrics on an example of C₄ hydrocarbons, a fraction prominent in the steam cracking process of naphtha. Simultaneously, an attenuated total reflection (ATR) interface was designed as a sample interface in order to integrate the sensors into liquid phase analysis. Here, a prototype was built with the intention to monitor the hydrogen peroxide concentration in the absorber stream of an oxidative gas scrubbing process, used for the removal of hydrogen sulfide in biogas production plants. Additionally, this sensor was improved by adding a novel laser type, the supercontinuum laser, as the radiation source. Thereby, light throughput could be significantly increased and the limit of detection lowered. In summary, a general purpose sensor system using FP filter in the MIR region was established, which can be used in PAT applications in both gas and liquid phase sensing.

The second part of the thesis concerns itself with the combination of Laser-Doppler Velocimetry (LDV) and Raman spectroscopy for the simultaneous determination of fluid characteristics and chemical composition in process streams. The proposed setup was tested with a simple T-mixer and the results of the measurements were validated through computational fluid dynamic simulation.

The third part is centered around the stand-off detection of chemicals using Raman spectroscopy, a technique known as stand-off Raman spectroscopy. An already established prototype was first enhanced using a electronically controlled mirror to accurately position the laser beam at a target distance. Using this instrument and mapping the laser beam over the sample surface, chemical images of the target could be acquired. Additionally, a liquid crystal tunable filter (LCTF) with a large input aperture allowed the design and testing of direct imaging system, as oppose to a more classical pointwise mapping systems using spectrographs. The result of such an imager is a 3D-databcube, where two axis are populated with local coordinates and the third is a spectral axis. This is usually called a Hyperspectral Image (HSI) cube, accordingly the technique de-

veloped was named stand-off Hyperspectral Raman Imaging (HSRI). The datacubes created commonly contain a large amount of datapoints, making them hard to interpret even for Raman experts. Therefore, using image processing algorithms and chemometrics, a classifier was developed, whose output is an easy interpretable false-color image. The primary application of the stand-off HSRI was the remote detection of hazardous and explosive materials on different surfaces at distances up to 15 m.

Keywords: Infrared spectroscopy ■ Raman spectroscopy ■ Process monitoring ■ Industry 4.0 ■ Optical sensors ■ Process Analytical Technologies (PAT) ■ stand-off ■ Hyperspectral Imaging ■ Chemometrics ■ Explosives

Acknowledgments

After these last years I want take the opportunity to express my gratitude to all the people who have accompanied me during the itinerary to my PhD thesis.

First and foremost I want to thank my supervisor, Bernhard Lendl, for giving me the opportunity to do research in his group on a variety of different topics. You have always been supportive, open for discussion and very generous with opportunities to attend and present at international conferences. I greatly appreciate your suggestions on how to tell a good story in presentations and publications. I admire your drive and efficiency in procuring a productive working environment for all of us worker bees.

Some of the great projects during this thesis were not possible without the involvement of Michael Harasek and his research group. Thanks go to Christian Jordan, Paul Ecker and Bahram Haddadi, which are great engineers and people full of ideas, whom I enjoyed working with.

Thanks go out to all current and former members of the workgroup who have made the office and lab a special place to be: A. Hobro, A. Genner, A. Schwaighofer, A. Balbekova, B. Zachhuber, B. Baumgartner, C. Kristament, C. Reidl-Leuthner, C. Wagner, E. Chrysostom, E. Gonzalez Garcia, F. Mayr, G. Ramer, H. Moser, J. Hayden, J. Ofner, J. Kuligowski, K. Wieland, M. Gonzalez Cabrera, M. Brandstetter, M. Goeschl, N. Caballero, P. Waclawek, Q. Alcaraz, R. Plata Torres, S. Lindner, S. Freitag, S. Radel, S. Tauber, T. Sumalowitsch, T. Aichinger and V. Bauer.

I was able to meet some special people, that over the time have become dear friends: Andreas Genner was very helpful designing all the prototypes that went out to our industrial partners and in hindsight I remember those nights at the lab before deadlines fixing the last bugs in our electronics very fondly.

Cosima Koch relieved me of overbearing thoughts through drinks and thoughtful discussions, never devoid of useful life tips.

I would like to express my gratitude to Georg Ramer for all the times he helped me through programming hiccups. We decided at the beginning of the 3D printing hype, that also our group (and especially ourselves) deserved a (of course custom-built) version of these marvelous machines, although not everybody (nobody else) was a fan. Low and behold, the 3D printer has become an essential part of the works done in Bernhard's Lab and I like to think we were the initiating spark.

My deepest appreciation goes to Karin Wieland for all the support over the years, even when good ideas did not work out as intended. You were very supportive and instrumental in the last steps of this thesis.

I would also like to thank Markus Brandstetter for helpful insights into spectroscopy and dry humor.

Thanks to the party posse - I will not give names here, you know who you are - for the unforgettable evenings (mostly nights) for excessive fun and entertainment.

I would like to express my gratitude to Johannes Lohninger, who helped me in the chemometrics department and in the development of the data structure for the imaging prototype.

Special thanks go to Johannes Frank for the help and introduction into mechanical engineering and Wolfgang Tomischko for the guidance through the world of moving electrons.

Special thanks to Stefan Tauber, whom I always could and can count on. I could not be happier to start our entrepreneurial endeavors together (like we had in the past), let us see how far we can go.

The most important person to thank is of course Monika. Not only was she able to live together with me for more than 10 years, which is astonishing by itself, but she was always supportive, generous and understanding. She gave me the most important gift yet, a new life, two wondering eyes which look at the world without prejudice, ready to take in and enjoy everything and everyone, reminding me of the capacity of unconditional love we humans are able to. Here's to you, little Paul.

Zuletzt möchte ich mich bei allen Freunden und Verwandten bedanken, die mich immer mit einem Lächeln empfangen haben und so ein ideales Umfeld für produktives und kreatives Leben und Arbeiten geschaffen haben.

Besonderer Dank gebührt meinen Eltern Reinhard und Norma und meinem Bruder Valentin für ihre Unterstützung über die Jahre. Aufgrund ihres Einsatzes wurde mein Studium ermöglicht und ich bin ihnen sehr dankbar dafür.

*...when you have eliminated the impossible, whatever remains, however improbable,
must be the truth.*

Sir Arthur Conan Doyle

Sherlock Holmes: The Sign of The Four, 1890

To my family, especially Moni and Pauli

Contents

| | | |
|----------|--|-----------|
| 1 | Introduction | 1 |
| 2 | Fundamentals of vibrational spectroscopy | 5 |
| 2.1 | The electromagnetic spectrum | 5 |
| 2.2 | Ro-Vibrational transitions in molecules | 8 |
| 2.3 | Infrared spectroscopy | 11 |
| 2.3.1 | Prerequisites for observing infrared spectra | 11 |
| 2.3.2 | Recording an IR absorption spectrum | 12 |
| 2.3.3 | ATR IR spectroscopy | 14 |
| 2.4 | Raman spectroscopy | 18 |
| 2.4.1 | Prerequisites for observing Raman spectra | 18 |
| 2.4.2 | Recording a Raman spectrum | 21 |
| 2.5 | Contrasting IR and Raman Spectroscopy | 23 |
| 3 | Instrumentation in vibrational spectroscopy | 25 |
| 3.1 | MIR spectroscopic instrumentation | 25 |
| 3.1.1 | MIR light sources | 26 |
| 3.1.1.1 | Thermal sources | 26 |
| 3.1.1.2 | Laser based IR sources | 27 |
| 3.1.1.3 | Novel MIR broadband lasers | 28 |
| 3.1.2 | MIR Detectors | 29 |
| 3.1.2.1 | Thermal detectors | 29 |
| 3.1.2.2 | Photon detectors | 30 |
| 3.1.3 | FTIR spectroscopy | 32 |

| | | |
|----------|--|------------|
| 3.1.4 | MIR spectroscopy using tunable filters: Filtometers | 33 |
| 3.1.5 | Fundamentals of a Fabry-Pérot cavity | 34 |
| 3.2 | Instrumentation for Raman spectroscopy | 38 |
| 3.2.1 | Collection optics | 38 |
| 3.2.2 | Lasers | 39 |
| 3.2.3 | Wavelength discrimination | 40 |
| 3.2.4 | Birefringent interferometers/filters | 43 |
| 3.2.4.1 | Polarization of light | 43 |
| 3.2.4.2 | Lyot filters | 44 |
| 3.2.4.3 | Liquid-crystal tunable filters | 47 |
| 3.2.5 | Detectors | 47 |
| 4 | Vibrational spectroscopy as a tool in process analysis | 51 |
| 4.1 | A brief introduction into process analytical chemistry | 51 |
| 4.2 | Infrared and Raman spectroscopy in PAC/PAT | 54 |
| 4.3 | Mid-infrared process sensors | 55 |
| 4.3.1 | Filtometers using tunable filters | 55 |
| 4.3.2 | MEMS-based tunable FP-filter | 56 |
| 4.3.3 | Characterization of the tunable FPF-detectors | 58 |
| 4.3.4 | Compact gas sensing | 60 |
| 4.3.5 | Enhanced liquid-phase sensing | 64 |
| 4.4 | Raman spectroscopy and Laser Doppler Velocimetry | 67 |
| 4.4.1 | Laser Doppler Velocimetry | 67 |
| 4.4.2 | LDV-Raman Coupling | 68 |
| 4.5 | Publication I: On-line monitoring of methanol and methyl formate in the exhaust gas of an industrial formaldehyde production plant by a mid-IR gas sensor based on tunable Fabry-Pérot filter technology | 71 |
| 4.6 | Publication II: Application of tunable Fabry-Pérot filtometer to mid-infrared gas sensing | 83 |
| 4.7 | Publication III: Enhanced mid-infrared multi-bounce ATR spectroscopy for online detection of hydrogen peroxide using a supercontinuum laser | 91 |
| 4.8 | Publication IV: Simultaneous Laser Doppler Velocimetry and stand-off Raman spectroscopy as a novel tool to assess flow characteristics of process streams | 105 |
| 5 | Stand-off Hyperspectral Raman Imaging | 119 |
| 5.1 | Stand-off Raman spectroscopy | 120 |
| 5.1.1 | Stand-off Raman instrumentation | 122 |
| 5.2 | Remote chemical detection using Hyperspectral Raman Imaging | 124 |
| 5.2.1 | Hyperspectral Imaging: an overview | 125 |

| | |
|---|------------|
| 5.2.2 Stand-off Raman mapping | 126 |
| 5.2.3 Building a stand-off HSRI | 128 |
| 5.2.4 Characterization of the HSRI | 130 |
| 5.2.5 Characterization of the pulsed, air-cooled laser | 132 |
| 5.2.6 Design of a mobile, rugged and versatile stand-off HSRI | 134 |
| 5.3 Chemometrics and HSI: a perfect fit | 137 |
| 5.3.1 Random decision forest | 138 |
| 5.4 Publication V: Comparing mapping and direct hyperspectral imaging in stand-off Raman spectroscopy for remote material identification | 141 |
| 5.5 Publication VI: Stand-off hyperspectral Raman imaging and random decision forest classification: a potent duo for the fast, remote identification of explosives | 159 |
| Bibliography | 169 |
| List of Figures | 181 |
| List of Tables | 187 |
| List of Publications | 189 |
| Curriculum vitae | 193 |

Glossary

α absorption coefficient in cm^{-1} .

A absorbance of a sample.

α polarizability tensor.

B_{ν} spectral radiance per unit wavenumber in Wcm/m^2 .

c_0 speed of light in vacuum; $299\,792\,458\text{ m s}^{-1}$.

χ_i anharmonicity constant.

\tilde{n} complex refractive index composed of $n + ik_{\nu}$.

c concentration of a sample in mol l^{-1} .

d distance between mirrors.

d_l pathlength of the flow cell used for transmission measurements.

D^* specific detectivity in $\text{cm Hz}^{0.5} \text{W}^{-1}$.

E electric field strength.

ϵ molar extinction coefficient or molar absorptivity in $\text{l mol}^{-1} \text{cm}^{-1}$.

ν frequency in Hz.

ν_i fundamental frequency of the vibrational mode i in Hz.

h Planck's constant; $6.626070040 \times 10^{-34}$ J s.

I_0 intensity of the optical radiation source.

I intensity of the electromagnetic radiation as $|E|^2$.

K spring stiffness or force constant.

k_B Boltzmann's constant; 1.381×10^{-23} J K⁻¹.

k_ν absorption index.

λ wavelength.

μ reduced mass e.g. $\frac{m_1 m_2}{m_1 + m_2}$.

μ' induced dipole moment.

μ_i dipole moment along the axis i .

n refractive index.

$\Delta\phi$ Phase shift of the electromagnetic wave.

Q normal coordinate.

R reflectivity.

r reflectivity coefficient.

σ standard deviation.

T_0 temperature in K.

θ angle of incidence of the light beam.

θ_c critical incidence angle.

T transmittance.

t transmittance coefficient.

u_i vibrational quantum number of the i th mode.

$\tilde{\nu}$ wavenumber in cm⁻¹.

Acronyms

- ADC** analog digital converter.
- ASIC** Application-Specific Integrated Circuit.
- ATR** Attenuated Total Reflection.
- CARS** Coherent anti-Stokes Raman Spectroscopy.
- CCD** Charge Coupled Device.
- CFD** Computational Fluid Dynamics.
- CPP** Critical Process Parameters.
- CPU** Central Processing Unit.
- CQA** Critical Quality Attributes.
- CVD** Chemical Vapor Deposition.
- CVF** Circular Variable Filter.
- DBR** Distributed Bragg Reflector.
- DFG** Difference Frequency Generation.
- DPSS** Diode-Pumped Solid-State.
- EC-QCL** External Cavity Quantum Cascade Laser.

emCCD electron-multiplying Charge Coupled Device.

FDA Food and Drug administration.

FFT Fast Fourier Transform.

FIR Far-Infrared.

FOV Field Of View.

FP Fabry-Pérot.

FPF Fabry-Pérot Filter.

FTIR Fourier Transform Infrared.

FWHM Full Width at Half Maximum.

HSI Hyperspectral Imaging.

HSRI Hyperspectral Raman Imaging.

iCCD intensified Charge Coupled Device.

ICL Interband Cascade Laser.

IR Infrared.

LCTF Liquid Crystal Tunable Filter.

LDV Laser Doppler Velocimetry.

LIBS Laser Induced Breakdown Spectroscopy.

LOQ Limit Of Quantification.

LVF Linear Variabel Filter.

MCP Microchannel Plate.

MEMS Micro-electromechanical Systems.

MIR Mid-Infrared.

MLR Multiple Linear Regression.

MOEMS Micro-optical-electromechanical Systems.

NA Numerical Aperture.

NDIR Non-Dispersive Infrared.

- NEP** Noise Equivalent input Power.
- NIR** Near-Infrared.
- OOB** Out-Of-Bag.
- OPO** Optical Parametric Oscillators.
- PAC** Process Analytical Chemistry.
- PAT** Process Analytical Technology.
- PCR** Principal Component Regression.
- PCS** Process Control System.
- PLS** Partial Least Squares.
- PMT** Photo-Multiplier Tube.
- QbD** Quality by Design.
- QCD** Quantum Cascade Detector.
- QCL** Quantum Cascade Laser.
- QWIP** Quantum Well Infrared Photodetector.
- R&D** Research & Development.
- RDF** Random Decision Forest.
- RMSEP** Root Mean Square Error of Prediction.
- SCL** Supercontinuum laser.
- SHS** Spatial Heterodyne Spectrometer.
- SNR** Signal to Noise Ratio.
- SORS** Spatially Offset Raman Spectroscopy.
- SRS** Stimulated Raman Spectroscopy.
- TEC** Thermoelectric Cooling.
- THz** Terahertz.
- TIR** Total Internal Reflection.
- UART** Universal Asynchronous Receiver-Transmitter.

UV Ultra-Violet.

VIF Variance Inflation Factor.

VIS Visible.

WAN Wide Area Network.

CHAPTER 1

Introduction

Mid-Infrared (MIR) and Raman spectroscopy are complementary spectroscopic techniques, which can provide sensitive and selective molecular information in a non-destructive manner. From first commercial spectrometers in the late 1940s [1] to the sophisticated instruments used today, these fields seem to be in an ever-evolving state. Comparing the share of numbers of publications in the field, a steady increase for both techniques can be observed over the years, culminating in approximately 30% for MIR and 12%¹ for Raman spectroscopy as of 2017. Similarly, the fields of applications now span over a multitude of different scopes, with spectrometers entering more and more into the industrial process analysis. The key upside lays in their ability to be integrated into the process, either on- or inline, measuring important process parameters without interfering with the same. Since regulatory standards demand better controlled procedures, the term Process Analytical Technology (PAT) was coined to encompass different analytical techniques which deliver swift and accurate information about the state of a given process. Since the FDA published their guidelines on the topic in 2004 [2], several research groups as well as Research & Development (R&D) centers are developing new methods to reach the goal of a dedicated (spectroscopic) sensor, giving selective and sensitive information on the chemical constitution of the investigated medium as well as exhibiting easy integrability, small electrical as well as mechanical footprint and the

¹Ratio of number of publications obtained by searching title, abstract and keywords for "infrared spectroscopy" and "Raman spectroscopy" to just "spectroscopy" sorted by year on Scopus.

ruggedness needed when operating sensitive instruments in industrial environments in a stable and reproducible manner. Often, these efforts include the integration of standard equipment in the field, for MIR spectroscopy namely the Fourier Transform Infrared (FTIR) spectrometer. These instruments were first developed and commercialized in the late 1960s [3], where the rise of the laser as a wavelength standard in Michelson interferometers took place and got another boost in the late 1980s, where the calculation power of computers allowed for digital processing of the raw interferometric signal. Modern commercial FTIR spectrometers aim for a broad user-base, with instruments getting smaller and smarter (e.g. with internal evaluation protocols, interpreting the spectra for the user or allowing automated library based lookups). Still regarded as the gold standard in MIR spectroscopy and rightfully so, the technique comes with a significant price tag and through great effort for miniaturization [4, 5], FTIR spectrometers are now available in compact, even hand-held sizes.

Concurrently, developments on other means of wavelength discrimination were undertaken. Optical bandpass filters can be used to facilitate wavelength discrimination, often using interference filters. A Fabry-Pérot (FP) cavity is an example of such an optical bandpass, where also tunability of the center wavelength can be achieved by varying, amongst others, the distance between the cavity mirrors. Since recently, Micro-electromechanical Systems (MEMS) based tunable FP filters with integrated detectors are available commercially and allow the design of rugged miniaturized sensors in combination with pulsed MEMS thermal light sources [6]. In this thesis, such a dedicated instrument was designed based on MIR spectroscopy for online multi-component gas monitoring [7]. Analogously, the analysis of liquid samples is possible. Due to its robustness and integrability into process streams, Attenuated Total Reflection (ATR) IR spectroscopy, where total internal reflection in certain materials is used to probe the adjacent liquid, is an established and popular technique. Therefore, a dedicated spectroscopic sensor based on FP filter technology was combined with an ATR sample interface for the inline detection of hydrogen peroxide used in oxidative gas scrubbers for the cleaning of biogas.

The constant progress and innovation regarding optical components also affects the light source itself. Most common radiation sources in the MIR are thermal emitters. However, again starting in the 60s, the first lasers emitting in the MIR region were developed until in the late 90s a breakthrough was reached with the first demonstrations of the ability of Quantum Cascade Laser (QCL) based sources [8] in the MIR. QCLs deliver high power narrow-band optical output, which can be tuned over several tens (Vernier QCLs) to several hundred wavenumbers (External Cavity Quantum Cascade Laser (EC-QCL)). In the last years, such lasers have been used for gas phase [9, 10] as well as liquid phase MIR spectroscopy [11–14] and through constant improvement of stability and output power are challenging the dominance of FTIR spectrometers. Very recently,

a third type of laser has begun peaking into the MIR spectral region: the Supercontinuum laser (SCL). Usually pulses from seed lasers in the near infrared are used and are spectrally broadened by non-linear processes, e.g. in certain kinds of optical fibers. The obtained laser pulses with a broad spectral bandwidth can be described as having a super-wide continuous optical spectrum. Hence, the term SCL was coined [15]. SCLs nowadays offer broadband spectral emission up to $16\ \mu\text{m}$ [16] and high optical power output up to several watts [17] combined with high spatial coherence and repetition rates in the MHz range. Hence, the SCL can be regarded as a highly interesting radiation source for spectroscopic applications in the MIR region. The combination of such a laser system and a tunable FP filter with the scope of a spectroscopic sensor for the continuous monitoring of hydrogen peroxide in oxidative gas scrubbers will also be presented [18].

The second part of this thesis is concerned with Raman spectroscopy. The most noteworthy innovation here was the combination of Laser Doppler Velocimetry (LDV) and Raman spectroscopy for the simultaneous fluid dynamic characterization and determination of the fluid's chemical composition. By using only one laser source for both techniques, information acquisition from a defined and common point in space is possible. A proof of concept experiment and validation through fluid dynamic simulations are presented in this thesis [19].

Raman spectroscopy can also be used as a remote detection system. Stand-off Raman spectroscopy is a technique where the instrument is physically separated from the sample of interest. This is useful when dangerous materials, e.g. explosives, or hard to reach areas are to be safely investigated in a non-destructive manner. Raman spectroscopy is particularly suitable for this detection scheme, since the excitation beam can be directed anywhere if there is a clear propagation path and the backscattered photons containing the molecular information can be conveniently captured with adequate collection optics, e.g. a telescope. One of the primary application areas of such systems is the remote mineral detection on landers used for planetary exploration [20] or the detection of hazardous, often explosive substances from afar [21]. It is often useful, however, to not just detect a single point, but to gather spatially resolved images. The combination of spectroscopic techniques with lateral resolution is generally known as Hyperspectral Imaging (HSI), where the method can vary from simple Visible (VIS) applications [22] to laterally resolved mass spectrometry [23]. In Raman spectroscopy, such HSI are usually acquired by mapping the focused laser beam over the area of interest, generating an image point by point with a lateral resolution of the size of the focused beam [24]. This scheme was also implemented here. The biggest downside is the time-consuming mapping of the point when large area scans are required. Therefore, a direct stand-off Raman imager, the Hyperspectral Raman Imaging (HSRI) instrument, was designed, using another type of tunable filter, the Liquid Crystal Tunable Filter (LCTF). This

way, spectral snapshots can be acquired, which, stacked together, form the HSI cube. The main advantages of the HSRI are a bigger field of view while featuring a high local resolution and higher optical throughput. In this thesis, a pointwise imager is directly compared to the HSRI, evaluating the most important differences.

HSI datasets with many pixels tend to grow very large very fast. Hence, chemometric and image processing algorithms are often used to extract useful information, which ultimately allow correct interpretation of the measurement. In this thesis, this is shown for the application of a compact HSRI prototype for detecting explosives at 15 m distance, with immediate classification of the results and subsequent presentation as a false-color image to a potential user. For that, a Random Decision Forest (RDF) classifier was used to efficiently select the most important variables (i.e. spectral positions for snapshot), essentially reducing the required measurement time whilst maintaining high quality classification.

Fundamentals of vibrational spectroscopy

In the following sections a brief overview of the underlying phenomena regarding vibrational spectroscopy are given, which encompasses Infrared (IR) and Raman spectroscopy. It should be mentioned at this point, that also rotational, even rotational-vibrational transitions are important to both techniques, but are not discussed here. The simple reason is that these rotational-(ro-)vibrational transitions are only observed in the gas phase and that, with the spectral resolution of the monochromators used during this thesis, such transitions are not distinguishable (not even for small molecules).

2.1 The electromagnetic spectrum

Spectroscopy is a cumulative term involving a variety of techniques which use electromagnetic radiation to probe the physical and chemical properties of matter. Historically, the first region to be explored was the visible spectrum. Understandable so, since sources of electromagnetic radiation in that region were readily available since the early stages of modern sciences. The same holds true for detectors, which are already, conveniently enough, built into the human body equipped with sophisticated signal preprocessing and image processing capabilities. It was only discovered later that the spectrum of electromagnetic radiation extended further both ways, towards

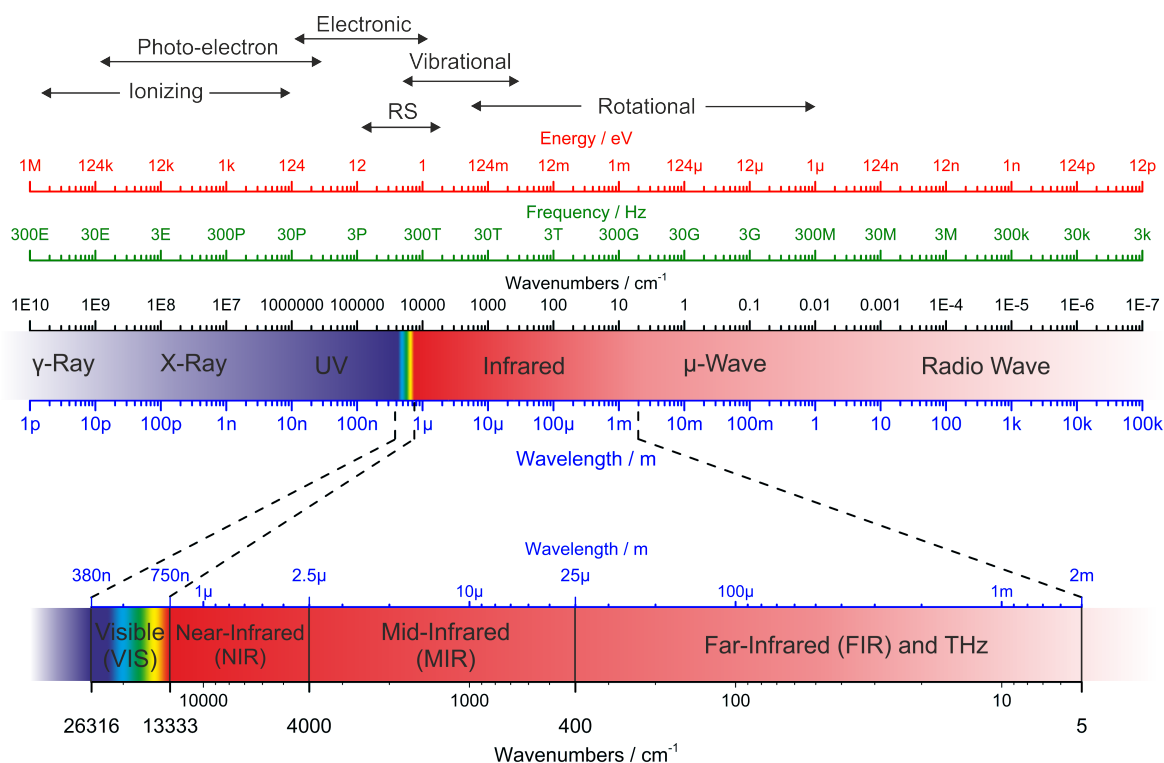


Figure 2.1: Illustration of the electromagnetic spectrum over several orders of magnitude in frequency, energy as well as wavelength. The two most important regions for this work are highlighted, namely the IR and VIS range. Additionally, the light-matter interactions are broadly depicted. RS is used as an abbreviation for Raman spectroscopy and shows the region where RS is mostly performed. Illustration adapted from [25].

higher as well as lower energetic radiation. As the name suggests, electromagnetic radiation is commonly described as a coupled system of periodically changing electric and magnetic fields, either described as waves or particles, depending on the experiment performed. Considering light as a wave, it will have certain periodicity or frequency, which is directly linked to its wavelength and energy via the Einstein-Planck relation.

$$E = h\nu = h\frac{c_0}{\lambda} = hc_0\tilde{\nu} \quad (2.1)$$

where E is the photon energy, h is the Planck constant, ν is the frequency, c_0 is the speed of light in vacuum and $\tilde{\nu}$ is the vacuum wavenumber.

In vibrational spectroscopy it is common practice to use the vacuum wavenumber ($\tilde{\nu}$, with the unit inverse centimeter, cm^{-1}) as the preferred measure of energy. As the light travels through different media with different optical properties, the wavelength will change, but the spectroscopic wavenumber in vacuum (i.e. frequency) stays constant.

$$\lambda = \frac{1}{n\tilde{\nu}} \qquad n = \frac{c_0}{c_m}, \qquad (2.2)$$

where c_m is the speed of light in the respective medium. The refractive index n is used to factor in the change of the speed of the radiation inside a given medium ($c_m = c_0/n$). As electromagnetic waves interact with matter, energy can be transferred through absorption or scattering processes, interacting with the total internal energy of the molecule or atom. The associated energy levels and the transitions between them are quantized. Due to different magnitudes in energies, the transition energies can be treated as a sum of different contributions, a concept known as Born-Oppenheimer approximation, and are usually divided into:

- **Electronic transitions**, where the excitation of an electron of the atom or molecule into an excited state is key,
- **Vibrational transitions**, where the energy of oscillations of the atoms of the molecule changes and
- **Rotational transitions**, where the energy of rotational movement of the molecule in respect to its center of mass is meant.

As Figure 2.1 suggests, different parts of the electromagnetic spectrum have different fundamental interplay with matter. In Ultra-Violet (UV)/VIS absorption spectroscopy transitions of electronic states of valence electrons are typically observed, whereas in IR spectroscopy vibrational and rotational transitions are probed. The IR part of the EM spectrum is further divided into three spectral regions:

- The **Near-Infrared (NIR)** region (0.75 to 2.5 μm) is located right next to the VIS light spectrum and includes transition energies related to higher harmonic vibrations (often referred to as *overtones*) or combination vibrations.
- The **Mid-Infrared (MIR)** region spans from 400 to 4000 cm^{-1} . Here, observed bands are attributed to fundamental vibrational modes of molecules. In this region most IR spectroscopic studies of molecular structure are located.
- The **Far-Infrared (FIR)** region spans from 25 to 350 μm , the part with the lowest energies, which mainly excites lattice vibrations, but is used intensively for pure rotational spectroscopy, denoting to the low transition energies found for molecular rotations as mentioned before.

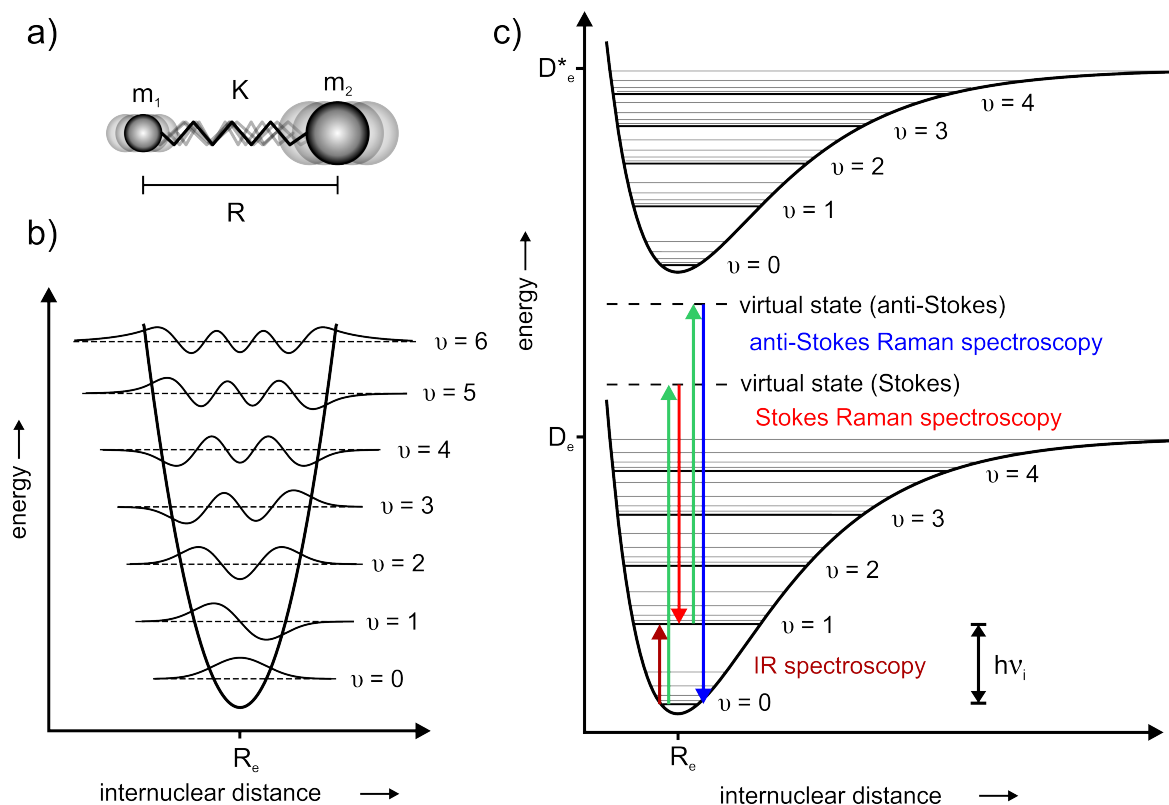


Figure 2.2: **a)** Illustration of a simple model of a harmonic oscillator, where k is the stiffness of the spring connecting the two masses m_1 and m_2 . **b)** Potential energy of a diatomic molecule as a function of the atomic displacement (R) during a vibration of a harmonic oscillator. The eigenfunctions of the vibrational energies are depicted as solid lines, the corresponding eigenvalues as dashed lines. **c)** Potential energy of a diatomic molecule as a function of the atomic displacement (R) during a vibration as a Morse potential. Ground state and first electronic excited state are depicted. Rotational energies are drawn in light grey. The term schemata for IR spectroscopy and Stokes-, as well as anti-Stokes-Raman spectroscopy are shown.

2.2 Ro-Vibrational transitions in molecules

IR and Raman spectroscopic features arise from quantized vibrational transitions between vibrational energy states within a molecule. The vibrational motion of a simple diatomic molecule can be approximated with a simple ball spring model (Figure 2.2a), where two masses m_1 and m_2 oscillate harmonically about their equilibrium positions, held together by a spring of stiffness K . The resonance frequency of this harmonic

oscillator is given by:

$$f = \frac{1}{2\pi c} \sqrt{\frac{K}{\mu}} \quad \text{with} \quad \mu = \frac{m_1 m_2}{m_1 + m_2} \quad (2.3)$$

with K denoting spring stiffness or force constant and μ denoting reduced mass. Based on this equation principal tendencies in vibrational spectroscopy can be explained. As K increases (and therefore the strength of the bonding) bands will shift to higher wavenumbers $\tilde{\nu}$. On the other hand if the reduced mass changes for different atoms involved, also the absorption band position in the spectrum will change, e.g. for heavier atoms to smaller wavenumbers $\tilde{\nu}$. This simple model can be used to approximate the band location quite accurately. C-H vibrations in saturated aliphatic molecules absorb around 2900 cm^{-1} and given that the force constant for single bonds in first row elements of the periodic table changes with the inverse square root of the reduced mass, we can estimate the location of C-C vibrations using equation 2.3 at around 1140 cm^{-1} (approximately where they actually can be found).

At this point, it is important to note that quantum mechanics is needed to describe the discrete nature of molecular transitions. For all modes of harmonic motions in the molecule, all involved atoms vibrate at a certain characteristic frequency ν_i and the energies associated with it can be described as:

$$E_{v,i} = h\nu_i \left(v_i + \frac{1}{2} \right) \quad (2.4)$$

where ν_i is the fundamental frequency of the i th mode and v_i is the vibrational quantum number of the i th mode. These energies are the eigenvalues of the time-independent Schrödinger's equation and are depicted in Figure 2.2b together with their eigenfunctions. In an idealized case all molecules reside in the vibrational ground state ($v_i=0$) and get elevated via absorption of a photon with the appropriate energy ($h\nu_i$) into the first excited state ($v_i=1$), with the selection rule of $v_i \pm 1$. Additionally, all energy levels $E_{v,i}$ are equally spaced and energies associated with the transition from the vib. ground state to the first vib. excited state (fundamental vib. modes) are in the range of the MIR region.

For a better approach to reality, however, the harmonic potential must be described using an anharmonic (Morse-type) potential function, as depicted in Figure 2.2c. It includes the boundary case of large internuclear distances R ($R \rightarrow \infty$), which is a substantial stretching of the molecule to the point of reaching an energy high enough to break the bonding. This energy is known as dissociation energy, denoted as D_e . Additionally, equation 2.4 has to be expanded with an anharmonic term:

$$E_{v,i} = h\nu_i \left(v_i + \frac{1}{2} \right) - h\nu_i \chi_i \left(v_i + \frac{1}{2} \right)^2 \quad (2.5)$$

where χ_i is the anharmonicity constant. The result of equation 2.5 can be observed in Figure 2.2c, where the energy differences of subsequent increasing vibrational quantum numbers become smaller. A Morse type potential function softens the strict selection rule stated before, to the point that higher harmonic transitions (often called *overtone*s) $|\Delta\nu_i| > 1$ are allowed. Additionally, combination bands, where different vibrational modes are excited simultaneously, appear in the MIR region, albeit weakly. However, they play a major role in the NIR region, and thereby for NIR spectroscopy.

When all possible vibrational modes are to be explored, the number of possible vi-

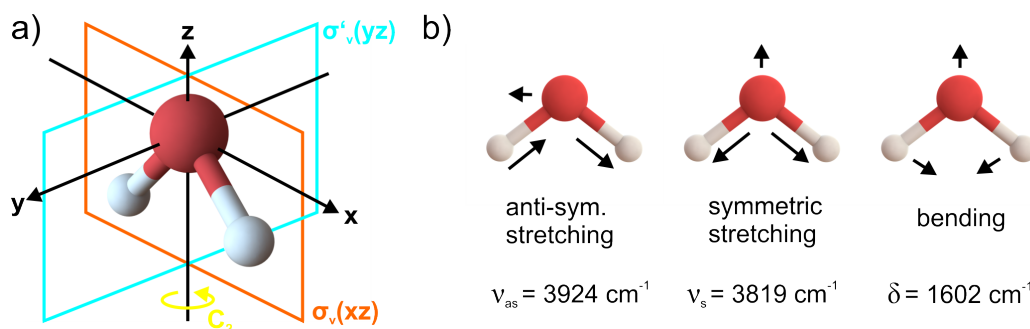


Figure 2.3: **a)** 3D model of the water molecule with all possible symmetry operations. C_2 denotes the axis of rotation and $\sigma_v(xz)$ and $\sigma'_v(yz)$ denote the mirror planes. **b)** The normal modes of the water molecule with their respective fundamental frequencies.

brations has to be determined. Generally, each of the N atoms in a molecule has 3 degrees of freedom to move in space. Translational and rotational displacement of the whole molecule will not result in any vibration. This leads to $3N-6$ possible vibrational modes for non-linear molecules. Linear molecules lose one rotational degree of freedom, meaning the number of possible vibrational modes is $3N-5$. Often, for molecules with certain elements of symmetry, vibrational modes can be degenerate, meaning they share the same vibrational frequency (and therefore have the same energy) or the associated transitions are not allowed by the different selection rules for IR and Raman spectroscopy. Hence, the number of observable fundamental vibrational modes by one technique is commonly less than the aforementioned numbers. More general, molecules can be associated with point groups in group theory, allowing for the analysis of vibrational modes using symmetry operations and character tables. For a given molecule a specific point group can be found, describing all possible symmetry operations. For the water molecule depicted in 2.3a, a two-fold rotation axis (C_2) can be identified, as well as two different mirror planes (σ'_v, σ_v), resulting in the symmetry group C_{2v} according to the Schönflies notation [26]. Referring to the C_{2v} character table, the irreducible representations to each symmetry class can be determined and by subtracting the rotational and translational degrees of freedom, the vibrational modes can be distinguished. For most vibrational modes, only a few atoms show resonance

and vibrate, whereas the rest of the molecule remains almost stationary. The involved atoms commonly form a functional group and show spectral features in distinct regions of the spectrum, helping a user with assigning bands in a measured spectrum through the use of tabulated structure references found in literature. This way, spectroscopic bands can be associated with vibrational modes of molecules, empowering vibrational spectroscopy as a powerful tool in elucidation of molecular structure.

In addition, each of the above described vibrational transitions has rotational transitions associated with it. This combination of rotational and vibrational motion is called rotational-vibrational (ro-vibrational) coupling. Usually, spectra of small molecules in gas phase show a distinct fine structure due to transitions between these quantized rotational energy levels occurring at the same time as vibrational transitions. Rotational transitions are of smaller magnitude compared to vibrational transitions. Therefore, high spectral resolution instruments are needed to resolve the rotational fine structure.

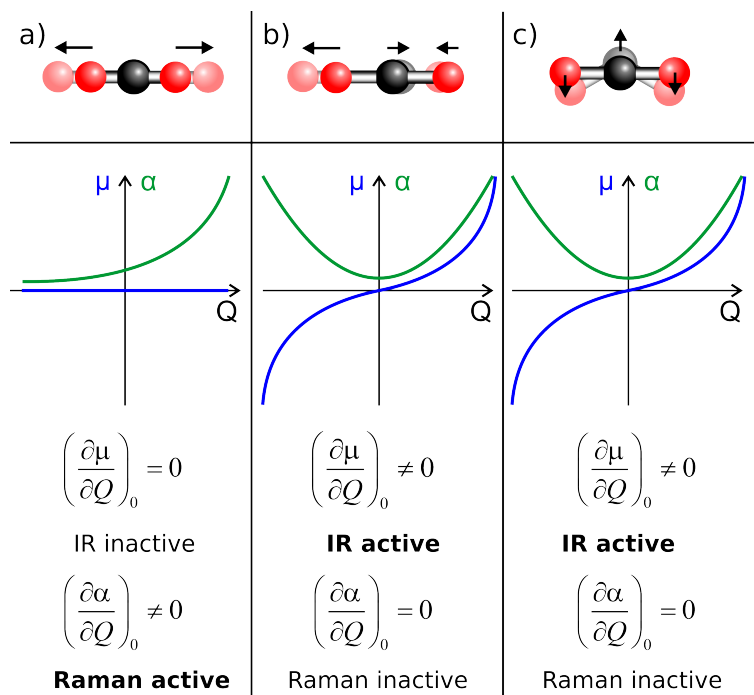
2.3 Infrared spectroscopy

2.3.1 Prerequisites for observing infrared spectra

For a molecular vibration to manifest itself in an IR spectrum, the electric dipole moment during a normal vibrational mode must change and the energy of the absorbed photon must match the energy difference of the vibrational transition. The dipole moment μ_i of a molecule is a measure of charge inequality along a given axis. Usually normal coordinates are used, denoted as Q , which are related to internal displacement coordinates and are better suited to describe the quantum-mechanical equations that govern molecular vibrations. So at least one component of the electric dipole moment during a normal vibration must change, meaning that

$$\left(\frac{\partial \mu_i}{\partial Q_k}\right)_0 \neq 0. \quad (2.6)$$

This explains why homonuclear diatomic molecules have no IR spectrum. During a vibration the symmetry of the molecule is retained and no dipole is generated. The same holds true for the heteroatomic linear molecule CO_2 for the symmetric stretching shown in figure 2.4a ($\nu_s = 1388 \text{ cm}^{-1}$). The center of symmetry is preserved during the vibration, meaning it behaves like a homonuclear linear molecule. This is different for the bending vibration in figure 2.4c ($\delta = 667 \text{ cm}^{-1}$) and the asymmetric stretching shown in figure 2.4b ($\nu_{as} = 2349 \text{ cm}^{-1}$), which both distort the distribution of charges and create a dipole, making them IR active. For all the vibrational modes in a molecule

**Figure 2.4:**

The three normal vibrational modes of CO_2 with the corresponding variation of the dipole moment μ_i and polarizability α along the normal coordinate Q . Additionally, the change of both parameters in equilibrium are given, which determines their IR or Raman activity.

corresponding to the C_{2v} point group this is true as well, meaning they are all IR active. In the example given in figure 2.3b all the vibrational modes and their respective band positions are listed for the water molecule. In this case all vibrational modes are IR active.

2.3.2 Recording an IR absorption spectrum

IR absorption spectroscopy commonly relies on the measurement of the infrared radiation transmitted through an analyte of interest in a sample in contrast to a reference beam, which passed through the sample without the analyte of interest. It therefore requires the measurement of two spectra, one background spectrum of intensity I_0 and one sample spectrum of intensity I . The transmittance T is then defined as the ratio of I and I_0 as in

$$T(\tilde{\nu}) = \frac{I}{I_0} = e^{-a(\tilde{\nu})d_l} \quad (2.7)$$

where a is the absorption coefficient in cm^{-1} and d_l the thickness of the sample i.e. the pathlength of light inside the absorbing medium. The absorbance A is defined as the decadic logarithm of the reciprocal transmission T , so that equation 2.7 simplifies to

$$A(\tilde{\nu}) = \log \frac{1}{T(\tilde{\nu})} = \log \frac{I_0}{I} = \frac{1}{\ln 10} a(\tilde{\nu})d_l = \varepsilon(\tilde{\nu})cd_l \quad (2.8)$$

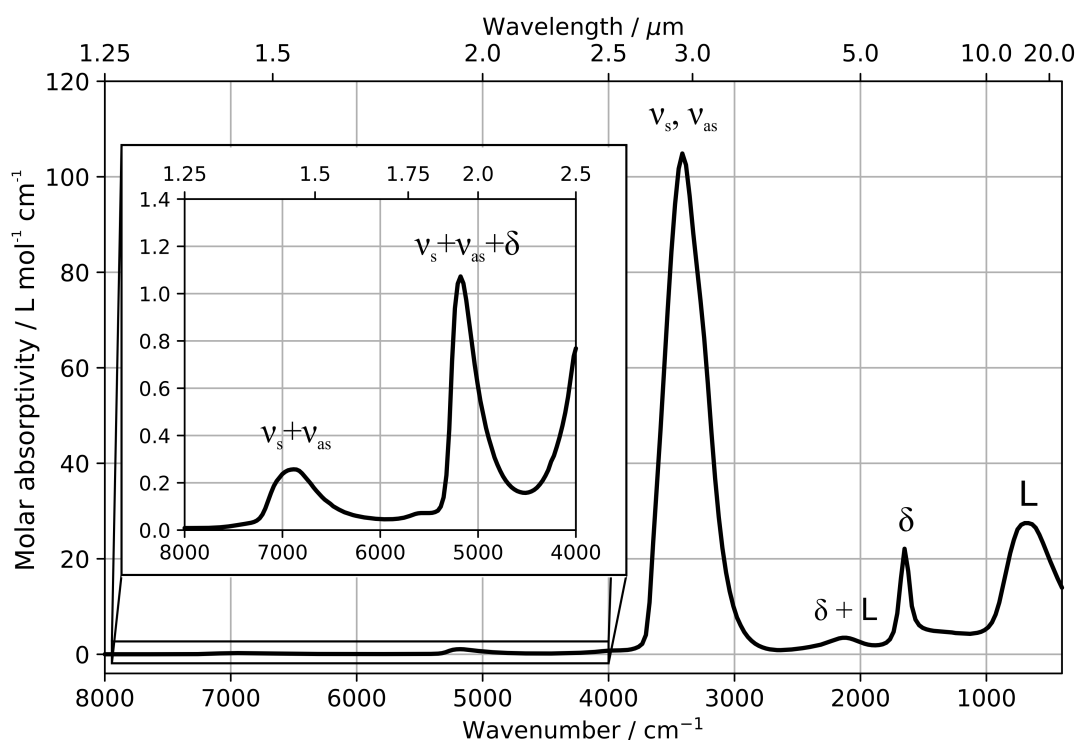


Figure 2.5: Molar absorption coefficient of water in liquid phase for the IR region. The inset shows a zoomed part of the NIR region with the associated molecular vibrations. Data taken from Bertie et al. [27]

with $\frac{1}{\ln 10} a$ combining to the molar absorptivity ϵ and c as the concentration of a specific component. This is known as the Bouguer-Beer-Lambert law or more commonly Beer's law [28]. For a mixture of N components absorbing in a given sample, the absorbance can be written as

$$A(\tilde{\nu}) = \sum_{i=1}^N \epsilon_i(\tilde{\nu}) c_i d_i \quad (2.9)$$

Equation 2.9 gives as a linear correlation between the intensity of a band with the abundance of a specific analyte in the sample, hence allowing for the determination of the concentration of a component using a calibration procedure, even in a mixture. It should be noted that the linearity of Beer's law is only valid if some restrictions are made, such as omitting reflection or scattering of light at optical components or at the sample, the absence of intermolecular interactions and postulating a perfectly linear response of the detector.

Figure 2.5 shows the molar absorptivity of liquid water over the MIR and NIR spectral range. At first glance one can detect the three normal modes at around 3920, 3820

and 1600 cm^{-1} given in figure 2.3b of the water molecule, but they seem overly broad and also additional bands can be seen. Until now, isolated molecules were considered when talking about molecular vibrations and IR absorption. In nature, this situation is rarely encountered. The closest viable scenario are gases at low pressures. Here, also isolated rotational and ro-vibrational transitions can be measured, if the spectral resolution of the spectrometer is sufficient and the lines are sufficiently spaced. In liquid phase, interaction between molecules affect the appearance of the absorbance band by perturbing and reducing the lifetime of the ro-vibrational states through energy-transfer processes. This leads to broad and smooth band contours, as depicted in figure 2.5. Additionally, a broad band (L) centering around 680 cm^{-1} is visible, which cannot be assigned to the vibrational modes discussed before. This band arises from hindered rotation of hydrogen-bonded water molecules in the liquid and is known as the libration (denoted with L) mode. Another band is found at 2130 cm^{-1} , which is assigned to the combination of libration and H-O-H bending mode. The spectral position and form of these bands are strongly dependent on the structure of the hydrogen-bonding network of water [29].

When an analyte of interest is present in gaseous phase, long gas cells are usually necessary for gas measurements mainly because of the low density of gaseous samples. Gas molecules can occupy a volume about one thousand times greater than the volume of a comparable mass of condensed phase material. Additionally, a component might only be weakly concentrated in a gaseous matrix. Long path length for gas cells are usually based on multiple reflections at mirrors [30].

Analogous to gas cells, liquid sampling is commonly performed by using a flow cell with an adequate thickness. For highly absorbing fluids (e.g. water) optical thicknesses of $< 10\ \mu\text{m}$ have to be employed [31, 32]. Such transmission cells suffer from several drawbacks, mainly their instability due to pressure change while the liquid is pumped and the affinity to clog or collect and persistently maintain air bubbles at the measurement window. It is a tedious process designing and using such thin flow cells, hence often another sampling techniques is used in IR spectroscopy, namely Attenuated Total Reflection (ATR) spectroscopy.

2.3.3 ATR IR spectroscopy

Total reflection is a special case of refraction. When light propagates from an optically denser (n_1) to an optically rarer (n_2) medium at an arbitrary angle θ , part of the light gets reflected and another part gets transmitted, depending on the optical properties of the materials. This situation is shown in figure 2.6a. If the incident beam enters the interface at an angle greater than the critical angle θ_c , all of the light will be reflected

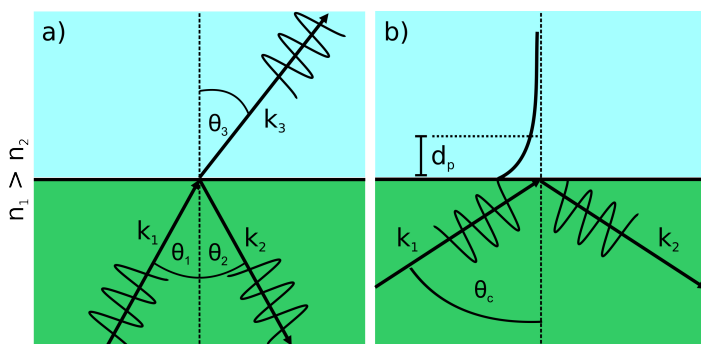


Figure 2.6:
a) Reflected and transmitted beam at a surface between two dielectric media with the refractive indices $n_1 > n_2$. **b)** When the angle θ reaches θ_c , total internal reflection occurs.

(figure 2.6b). This is called total internal reflection. Using Snell's law the critical angle can be determined.

$$n_1 \sin \theta_1 = n_2 \sin \theta_3 \quad (2.10)$$

For the transition from an optically denser medium to the optically rarer medium, there are angles θ_1 for which there are no real angles θ_3 that fulfill Snell's law. The critical angle is reached when θ_3 becomes 90° and can be calculated as:

$$\theta_c = \arcsin \frac{n_2}{n_1} \quad (2.11)$$

So far, we only considered media not showing absorption. Since the goal is to measure absorbance spectra of the optically rarer medium, a more accurate approach would be to assume a complex refractive index

$$\tilde{n}(\tilde{\nu}) = n(\tilde{\nu}) + ik_\nu(\tilde{\nu}), \quad (2.12)$$

where \tilde{n} is the complex refractive index, n the real part and k_ν the imaginary part of the complex refractive index. k_ν is also known as absorption index, since it's correlated to the absorption coefficient α with

$$k_\nu(\tilde{\nu}) = \frac{\alpha(\tilde{\nu})}{4\pi\tilde{\nu}}. \quad (2.13)$$

Therefore, the absorption index has a very similar form to the absorbance spectrum of a given compound. Figure 2.7c shows both the real refractive index and the absorption index of water for its band at 1640 cm^{-1} . The fluctuating change in the real part of the refractive index around the absorption band is what is generally referred to as anomalous dispersion (instead of normal dispersion, where the refractive index increases with increasing wavenumber). The amplitudes of the electric field of the reflected wave can be derived using the continuity conditions based on Maxwell's equations. The light has to be split up into the parallel (denoted by \parallel) and perpendicular (denoted by \perp) polarized electric field. Then by applying Snell's law the reflectance for both polarization

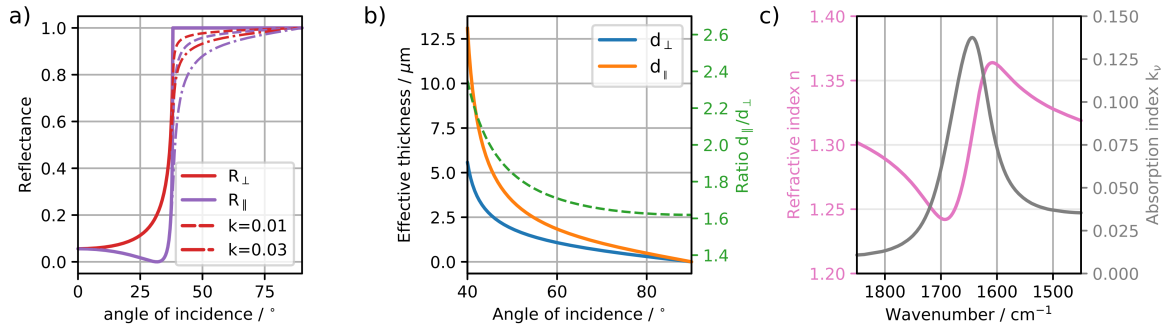


Figure 2.7: **a)** Reflectance for both parallel and perpendicular polarized light for different angles of incidence with absorbing and non-absorbing medium. n_1 was chosen to be 2.43, n_2 was 1.5 with absorption indices ranging from 0 to 0.03, calculated for a wavelength of $3.5 \mu\text{m}$. **b)** Effective thickness for both parallel and perpendicular polarized light and the ration between them. **c)** Refractive index and absorption index for the bending vibration band of liquid water. Data taken from Bertie et al. [27]

states can be calculated [33] as

$$R_{\parallel} = \left| \frac{\tilde{n}_2^2 \cos \theta_1 - n_1 \sqrt{\tilde{n}_2^2 - n_1^2 \sin^2 \theta_1}}{\tilde{n}_2^2 \cos \theta_1 + n_1 \sqrt{\tilde{n}_2^2 - n_1^2 \sin^2 \theta_1}} \right|^2 \quad (2.14)$$

$$R_{\perp} = \left| \frac{n_1 \cos \theta_1 - \sqrt{\tilde{n}_2^2 - n_1^2 \sin^2 \theta_1}}{n_1 \cos \theta_1 + \sqrt{\tilde{n}_2^2 - n_1^2 \sin^2 \theta_1}} \right|^2 \quad (2.15)$$

These equations are known as Fresnel equations. For a medium with vanishing absorption index (non-absorbing, hence the imaginary part is zero), the reflectance reaches 100 % for angles of incidence large than the critical angle θ_c . Is the probed medium absorbing, the dependence of the intensity of the reflected light is different. There is no longer a sharp critical angle, with higher absorption index the intensity drops (see figure 2.7a). The reason for this is the evanescent field, which reaches into the optically rarer medium. The intensity of the electric field drops exponentially, like illustrated in figure 2.6b. Since it stretches out through the interface boundary into the optical thinner medium, it's what enables Attenuated Total Reflection (ATR) spectroscopy. Harrick, one of the pioneers of ATR spectroscopy, recognized the potential of Total Internal Reflection (TIR) for chemical sensors and was one of the forerunners to develop this technique to its widespread use today [34, 35]. The extent of the outreaching field can also be quantified and is commonly referred to as depth of penetration d_p

$$d_p = \frac{\lambda}{2\pi \sqrt{n_1^2 \sin^2 \theta_1 - n_2^2}}. \quad (2.16)$$

Besides the depth of penetration, the effective thickness is often used in ATR spectroscopy. It is defined as the equivalent thickness of a film of the sample material that would give the same absorbance for transmission at normal incidence as that obtained with the ATR. Different relations for parallel and perpendicular polarized radiation respectively are needed to calculate the corresponding values for the effective thicknesses d_{\parallel} and d_{\perp} .

$$d_{\parallel} = \frac{\lambda n_{21} \cos \theta [2 \sin^2 \theta - n_{21}^2]}{n_1 \pi (1 - n_{21}^2) [(1 + n_{21}^2) \sin^2 \theta - n_{21}^2] \sqrt{\sin^2 \theta - n_{21}^2}} \quad (2.17)$$

$$d_{\perp} = \frac{\lambda n_{21} \cos \theta}{n_1 \pi (1 - n_{21}^2) \sqrt{\sin^2 \theta - n_{21}^2}} \quad (2.18)$$

For illustration the effective thickness for both polarization states is depicted in figure 2.7b. Although the expressions for the penetration depth and effective thickness given in equations 2.16 to 2.18 can be seen analogously to the pathlength in typical transmission measurements, there are distinct differences.

Wavelength Equations 2.17 and 2.18 reveal that the effective depth of penetration in an ATR setup depends linearly on the wavelength of the incident radiation. Hence, bands with the same absorption coefficient will appear stronger at lower wavenumbers than at higher wavenumbers. Relative intensity comparisons to transmission spectra have to be adjusted accordingly.

Angle of incidence The angle of incidence can be found also in the equations for the effective thickness in ATR measurements. A larger angle of incidence will decrease the effective thickness of the ATR measurement, this can be used to tune the sensitivity of the ATR measurement. It is however seldom done for in-line probes, as it requires a sophisticated adjustable optic and does certainly not add to an improved robustness of the setup.

Polarization of light According to equations 2.17 and 2.18, the effective thicknesses vary with the input polarization of the incident light. Figure 2.7b shows how both values change over angle of incidence. d_{\parallel} is always larger than d_{\perp} , especially for angles close to the critical angle θ_c .

Refractive index of the involved materials The refractive indices of the sample and the ATR crystal influence the ATR spectrum, the most important aspect being the relative change to each other, given in the index ratio $n_{21} = n_2/n_1$, often termed index matching. Usually, the high refractive index of the ATR element itself is almost constant over a large wavelength range, showing mostly normal dispersion. The sample however, exhibits anomalous dispersion close to absorption bands, as

shown in figure 2.7c for the O-H deformation band of water. The real part of the refractive index on the low wavenumber flank of the absorption band will increase, followed by a sudden drop and return to its original value after the absorption band. This leads to an increase in effective thickness on the low wavenumber side and analogously to a decrease in effective thickness on the high wavenumber side of the absorption band. Compared to transmission spectra, the maximum of the band in ATR spectra seems to be shifted toward lower wavenumbers. The extent of this effect depends again on the refractive index of the ATR crystal (or better: the index matching), the angle of incidence and the polarization of the incident light.

Requirements like high refractive index (to reach a desired critical angle) and optical applicability (and stability) limits the candidates of suitable (and most commonly used) materials to diamond ($n = 2.4$), ZnSe ($n = 2.4$), ZnS ($n = 2.3$), Si ($n = 3.4$) and germanium ($n = 4.0$), only to name the most important.

2.4 Raman spectroscopy

2.4.1 Prerequisites for observing Raman spectra

Whenever Raman spectroscopy or the Raman effect are mentioned, scattering of light is the central topic of conversation. It was mentioned in the previous chapter that the dipole moment may change during a normal vibration of a molecule. Classically, the theory of Raman (and Rayleigh) scattering is based on the concept of an oscillating incident electric field (e.g. electromagnetic radiation) inducing oscillating electric dipoles. The induced electric dipole moment, assuming linear and spontaneous Raman scattering, can be then written as

$$\mu' = \alpha E \quad (2.19)$$

α is known as the polarizability tensor and is a measure of the flexibility of the electron cloud surrounding the molecule during a normal vibration. The polarizability is a tensor of rank 2 and has therefore elements (α_{ij}) having two indices. This tensor is often represented as an ellipsoid with three different half-axes, conventionally chosen to coincide with the symmetry axes of the molecule. Now let's consider the variation of the α tensor during a normal vibration around the equilibrium position, this can be expressed in a Taylor series, as follows

$$\alpha = (\alpha)_0 + \left(\frac{\partial \alpha}{\partial Q_k} \right)_0 Q_k + \dots \quad (2.20)$$

2.4. Raman spectroscopy

with Q_k being the normal coordinate of a vibration of wavenumber $\tilde{\nu}_k$. We can simplify this series at the first linear term, which is often referred to as electric harmonic approximation. On the same note, the normal vibrations can be treated as being harmonic, which leads to

$$Q_k(t) = Q_{k,0} \cos 2\pi c \tilde{\nu}_k t. \quad (2.21)$$

Analogous to this concept the induced dipole moment μ' is modulated by an oscillating electric field (the incident electromagnetic radiation with wavenumber $\tilde{\nu}_0$)

$$E(t) = E_0 \cos 2\pi c \tilde{\nu}_0 t. \quad (2.22)$$

Combining equations 2.20, 2.21 and 2.22 into equation 2.19 gives us

$$\mu'(t) = \alpha_0 E_0 \cos 2\pi c \tilde{\nu}_0 t + \left(\frac{\partial \alpha}{\partial Q_k} \right)_0 \cdot Q_{k,0} E_0 \cos 2\pi c \tilde{\nu}_0 t \cdot \cos 2\pi c \tilde{\nu}_k t. \quad (2.23)$$

using the trigonometric identity $2 \cos \alpha \cos \beta = \cos(\alpha - \beta) + \cos(\alpha + \beta)$, this can be rewritten as

$$\begin{aligned} \mu'(t) = & \alpha_{,0} E_0 \cos 2\pi c \underbrace{\tilde{\nu}_0}_{\text{Rayleigh}} t \\ & + \frac{1}{2} \left(\frac{\partial \alpha}{\partial Q_k} \right)_0 Q_{k,0} E_0 \cdot \left[\cos 2\pi c \underbrace{(\tilde{\nu}_0 - \tilde{\nu}_k)}_{\text{Stokes}} t + \cos 2\pi c \underbrace{(\tilde{\nu}_0 + \tilde{\nu}_k)}_{\text{Anti-Stokes}} t \right]. \end{aligned} \quad (2.24)$$

The induced dipole moment has three arguments in the cosine. The first equals the frequency of the incident radiation. There is no change in frequency, hence no energy between the molecule and the radiation was exchanged. This scattered radiation is called Rayleigh scattered light. The second term involves a change in wavenumber of the light, namely $\tilde{\nu}_0 - \tilde{\nu}_k$, which means it is shifted towards higher wavelengths, commonly referred to as a red-shift, known in Raman spectroscopy as Stokes Raman scattering. The last term yields an increase in wavenumber by $\tilde{\nu}_0 + \tilde{\nu}_k$ and therefore a transition to smaller wavelengths or blue-shifted light, which is known as Anti-Stokes Raman scattering. This can also be described as beat frequencies of the oscillating electric field of the incident radiation $\tilde{\nu}_0$ modulated by the molecular vibration $\tilde{\nu}_k$. Figure 2.8 shows a Raman spectrum of sulfur with both Stokes and Anti-Stokes scattering bands. Since the wavelength of the incident radiation was 532 nm, we find a very intensive peak at this wavelength due to the Rayleigh scattering. As the energy of molecular transitions for a vibrational mode is specific for a molecule, an absolute wavelength or wavenumber scale is not useful for a Raman spectrum, as it would produce bands at different spectral positions for different wavelengths of the incident radiation. Hence, most often the Raman shift is used, a quantity which is related to the excitation wavelength and gives a wavenumber scale for the energies of the molecular transitions analogous to the IR spectra. It is defined as

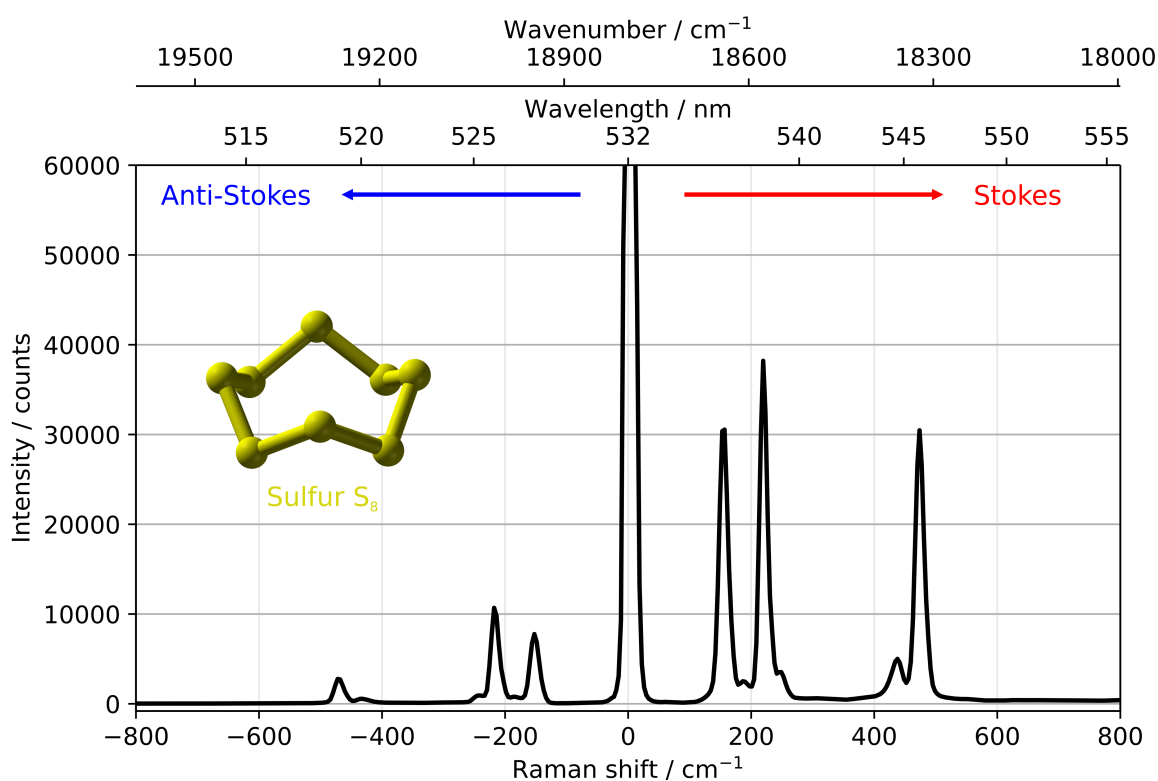


Figure 2.8: Measured Raman spectrum of sulfur with Stokes and Anti-Stokes region in wavelength, wavenumber and Raman shift. The spectrum was acquired using a confocal Raman microscope (Horiba LabRam 800) using a excitation wavelength of 532 nm.

$$\Delta\tilde{\nu} = \tilde{\nu}_0 - \tilde{\nu}_k. \quad (2.25)$$

where $\Delta\tilde{\nu}$ is the Raman shift, $\tilde{\nu}_0$ the wavenumber of the incident radiation and $\tilde{\nu}_k$ the wavenumber of the vibrational mode. Figure 2.9a shows the wavelength range which is spanned for a Raman shift of 400 to 4000 cm^{-1} for three different excitation lasers, namely the second (532 nm), third (355 nm) and fourth (266 nm) harmonic of the Nd:YAG solid state laser. The extent of the relevant part of the spectrum gets narrower when shorter excitation wavelengths are used, as depicted in figure 2.9b. It is therefore necessary to use higher resolution dispersive elements for Raman spectroscopy in the UV range than for excitation in the NIR region.

Another important takeaway is the prerequisite to Raman activity, which is

$$\left(\frac{\partial \alpha}{\partial Q_k} \right)_0 \neq 0. \quad (2.26)$$

It contrasts the requirement for IR activity discussed in section 2.3.1, this is why often Raman and IR spectroscopy are said to be complementary techniques. As example again the CO_2 can be used. The symmetric stretch vibration depicted in figure 2.4a

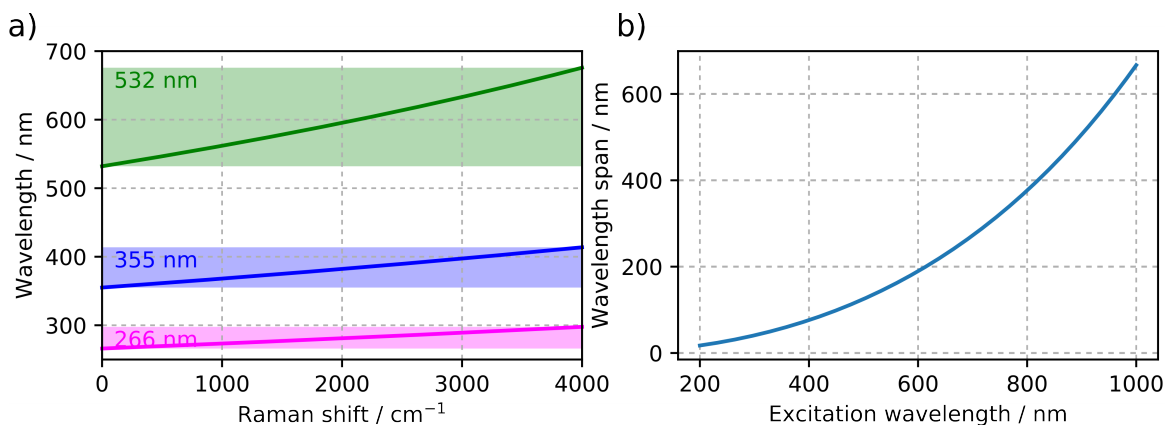


Figure 2.9: **a)** Raman shift conversion for the second, third and fourth harmonic of a Nd:YAG laser used as excitation laser. **b)** Extend of the Raman spectrum (400-4000 cm⁻¹) in wavelength over the excitation wavelength.

shows a gradient of the polarizability tensor at equilibrium position and is therefore Raman active, whereas the asymmetric stretch and the deformation induce a symmetric change in the polarizability tensor, leading to no gradient and hence to no Raman activity.

Equation 2.24 represents the main learnings from the classical approach to Raman scattering. Taking another look at figure 2.8 the difference in intensity of Stokes and Anti-Stokes bands becomes apparent. To explain this effect, a quantum mechanical approach is needed. The energy term schemata of figure 2.2c show the transitions during a Raman scattering event. It depicts it as a two-photon process. An incoming photon excites the molecule to a virtual state, whose energy is the sum of the ground state and the photon energy of the laser and by releasing a photon of energy $\tilde{\nu}_0 - \tilde{\nu}_k$ (Stokes) it relaxes into the first vibrational excited state. In the Anti-Stokes case, the molecule transfers energy to the photon by relaxing back into the ground state. Obviously the difference in intensity of Stokes and Anti-Stokes will be a function of the Boltzmann distribution law, eventually leading to

$$\frac{I_{Stokes}}{I_{Anti-Stokes}} = \frac{(\tilde{\nu}_0 - \tilde{\nu}_k)^4}{(\tilde{\nu}_0 + \tilde{\nu}_k)^4} e^{\left(\frac{hc\tilde{\nu}_k}{k_B T_0}\right)}. \quad (2.27)$$

By simultaneous measurement of Stokes and Anti-Stokes lines this can be exploited to derive the temperature of the sample.

2.4.2 Recording a Raman spectrum

In contrast to IR absorption spectroscopy, Raman relies on the detection of Stokes or Anti-Stokes scattered radiation. To discuss intensities in Raman spectroscopy it is op-

portune to start at the oscillating induced dipole, focusing on the Stokes scattering, equation 2.24 simplifies to

$$\mu'_{Stokes}(t) \propto \left(\frac{\partial \alpha}{\partial Q_k} \right)_0 \cdot Q_{k,0} E_0 \cos 2\pi c(\tilde{\nu}_0 - \tilde{\nu}_k)t. \quad (2.28)$$

The total emitted intensity of a Hertzian dipole is proportional to $|\ddot{\mu}'|^2$ and with the temporal average over the oscillating part of equation 2.28, it can be rewritten as

$$I_{Stokes} \propto \left(\frac{\partial \alpha}{\partial Q_k} \right)_0^2 \cdot E_0^2 \cdot (\tilde{\nu}_0 - \tilde{\nu}_k)^4 N_m d\Omega. \quad (2.29)$$

From this relation can be deduced that the instrumental parameter $E_0^2 = I_{Laser}$, essentially the laser irradiance and $\tilde{\nu}_0 = \tilde{\nu}_{Laser} = \frac{c_0}{\lambda}$, the excitation laser wavelength play a crucial role in the intensity of the Raman scattered light. The more power the incident laser can provide, the more Stokes scattered Raman photons are produced. Additionally, smaller excitation wavelengths lead to higher Raman intensities, this is very important since it's factored in with the fourth power. Therefore, Raman spectroscopy would be ideally done in the UV region, but due to high probability to induce fluorescence or self-absorption of the sample this is usually avoided. The keen reader might have noticed two additional terms in equation 2.29 not present in equation 2.28: the number of molecules N_m irradiated by the incident laser and the solid angle Ω . The latter takes into account, that the scattering commonly takes place over the whole solid angle Ω , whereas detection usually involves a given direction within a small element of solid angle, denoted by $d\Omega$.

To use Raman spectroscopy for quantitative determination the term N_m is crucial. The more molecules are present in the irradiated volume, the more Raman photons are generated and can hence be detected. At this point it is important to note that the scattering cross section, meaning the probability of the generation of a scattered photon, varies greatly between Rayleigh and Raman scattering. Raman scattering is significantly weaker, commonly only one in 10^{8-10} photons show a Raman shift. This leads to the necessity of Rayleigh filters, also known as laser line filters, which suppress the elastically scattered light. Without those, the overwhelmingly intense Rayleigh band at 0 cm^{-1} Raman shift would mask the Raman bands, rendering the spectrum useless. Usually, Raman spectrometers are composed of the following components: The monochromatic source of EM radiation (laser) for excitation, a collection optic for efficient gathering of scattered photons, a monochromator usually in form of a grating spectrograph and an array photon detector. Figure 2.10 presents the concept of a Raman measurement. It becomes clear, that for reproducible quantitative determination of a compound a couple of requirements have to be fulfilled. First, the laser power has to be as stable as possible, since it influences directly the amount of generated Raman photons. Secondly, the properties of the collection optic has to be constant, meaning

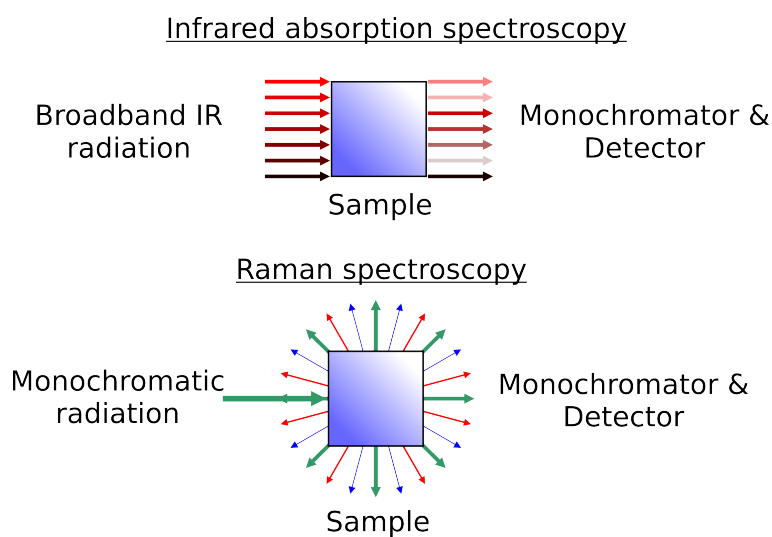


Figure 2.10:

Top: Simple illustration of a common IR absorption experiment. A broadband IR light source is shined through the sample and the transmitted radiation is spectrally analyzed and detected. **Bottom:** Simple illustration of a Raman experiment. A monochromatic light source is directed at the sample and the scattered photons (Stokes is depicted in red, Anti-Stokes in blue) are spectrally analyzed and detected.

Table 2.1: Overview over interaction cross sections (σ in $\text{cm}^2/\text{molecule}$) selected spectroscopic techniques. Adapted from [36]

| <i>Technique</i> | <i>Interaction</i> | <i>$-\log \sigma$</i> |
|------------------|--------------------|----------------------------------|
| Mid Infrared | Absorption | 25-18 |
| Near Infrared | Absorption | 28-22 |
| Raman | Scattering | 35-28 |

the light gathering power has to be the same for consecutive measurements. Third, and probably the most difficult, the light scattering properties of the sample have to be the same. However, this can also be argued as an advantage of Raman spectroscopy. The scattering nature allows non-invasive probing even through transparent materials in a simple back-scattering geometry. This is especially useful when remote or stand-off detection is sought after.

2.5 Contrasting IR and Raman Spectroscopy

The previous sections revealed that molecular vibrations are responsible for the appearance of absorption bands in the IR spectrum and for scattering of light at shifted frequencies, i.e. bands in the Raman spectrum. The main difference lies in the activity requirement for the respective technique during a normal mode of vibration. Is a change in the dipole moment involved, the molecule will absorb infrared light of the

same energy as the vibrational transition. If however, a change in polarizability during the normal mode happens, the scattered light will contain shifted photons, i.e. a Raman band. The energy will again be equal to the energy of the vibrational transition. Intensity-wise, the probability of an absorption, scattering or emission event can be described by cross sections, interpreted as effective areas and usually given in $\text{cm}^2/\text{molecule}$. The larger the cross section, the more likely it is for the specific event to happen and this depends on the molecular structure of a certain compound and on selection rules [36]. This leads to the fundamental vibrations seen in the MIR to be orders of magnitude more likely event than the first, second or third overtone seen in the NIR (see table 2.1). Aside from that, figure 2.10 illustrates the two spectroscopy variants. Infrared absorption spectroscopy uses polychromatic light in the right wavelength range of a broadband emitter, which is passed through the sample and the attenuated light is spectrally analyzed and detected. Raman spectroscopy uses monochromatic light to excite the molecule into a vibrational transition and usually the scattered photons are spectrally analyzed and detected, with the focus on the red-shifted (Stokes) photons.

Instrumentation in vibrational spectroscopy

3.1 MIR spectroscopic instrumentation

The basic optical setup for direct absorption spectroscopy is almost always composed of three different parts: a light source delivers electromagnetic radiation in the MIR range, a second element, commonly of interferometric or dispersive nature, discriminates the different incident wavelengths before a detector senses the intensity of the radiation emitted by the aforementioned source after having passed the sample. The absorption spectrum is then generated by recording an intensity spectrum of the "empty" beam, commonly referred to as background single channel or just background spectrum and recording a spectrum with a specific sample between the source and the detector, known as sample single channel or sample spectrum, where the sample may be gaseous, liquid or solid. According to Beer's law discussed in section 2.3.1, the absorption spectrum is then calculated by the decadic logarithm of the inverse transmission (equation 2.8).

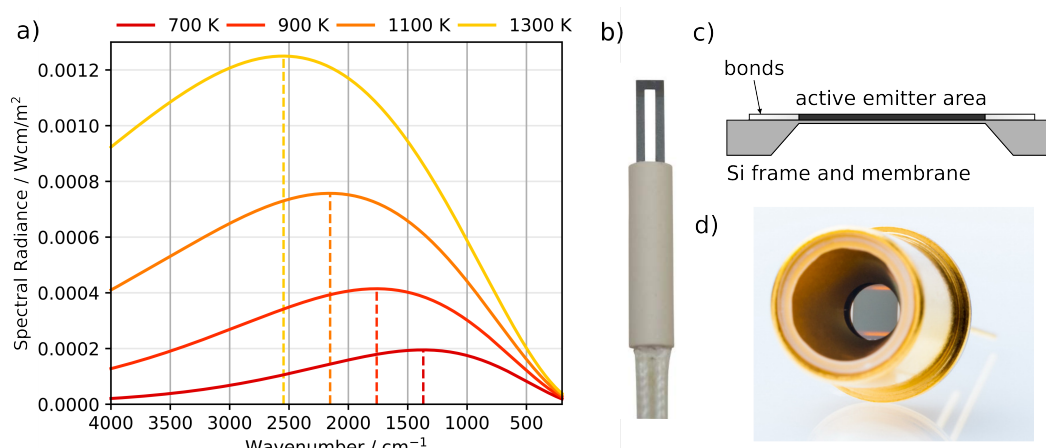


Figure 3.1: **a)** Planck's law for black-body surfaces heated to different temperatures. **b)** Image of a SiC (Globar) incandescent light source for the MIR. **c)** Illustration of the pulsed emitter membrane, suspended on a silicon frame. **d)** Packaged pulsed emitter with a parabolic reflector.

3.1.1 MIR light sources

3.1.1.1 Thermal sources

Incandescent or thermal light sources for the MIR region are usually heated surfaces, which will emit radiant power. In an ideal case, the emitted radiation follows Planck's law [37], which describes the spectral radiance per unit wavenumber $B_{\tilde{\nu}}$ of a black body at equilibrium temperature T_0 as

$$B_{\tilde{\nu}} = 2hc^2\tilde{\nu}^3 \frac{1}{e^{\frac{hc\tilde{\nu}}{k_B T_0}} - 1} \quad (3.1)$$

with k_B being the Boltzmann constant. With higher temperature the spectral radiance increases and the maximum shifts towards higher wavenumbers, known as Wien's displacement law, which is depicted in figure 3.1a

Thermal light sources for the MIR are generally heated elements with good stability and stable emission. The most common material used is sintered silicon carbide (SiC), which can be stably operated at temperatures over 1400 K in air for over several years [38] by applying electrical current. These elements are more commonly known by the trade name Globar and found in most commercial MIR spectrometers today (one example can be seen in figure 3.1b). Other materials like tungsten or sintered zirconium–thorium–cerium oxide (known as Nernst glower) can be heated to higher temperatures, but show less emissivity at lower wavenumbers and are therefore not as suitable for applications in the MIR and FIR region.

Another innovation for these kinds of light sources was the use of thin films of different alloys of metals or semiconductors, which have a very low heat capacity and therefore consume low electrical power during heating [39]. Although only lower maximum temperatures of 1000 K can be achieved on these devices, the small heat capacity enables pulsed operation by just applying switching driving voltages, satisfying the need for optical modulation. By lithographically structuring the surface of these emitters with patterns resembling photonic materials, the emissivity can be tuned both spectrally as well as intensity-wise [40, 41]. These pulsed emitters are now heavily used for Non-Dispersive Infrared (NDIR) spectroscopic applications [42]. They are usually MEMS-based, electrically modulated resistive heating elements integrated into a thin dielectric membrane, which is suspended on a MEMS silicon structure. Due to the low thermal mass of the thin heating element, they exhibit low power consumption and high emissivity. The fact that they can be electrically modulated means there is no need for other forms of modulating the radiation e.g. with a mechanical chopper. Hence, no mechanical parts are necessary for the application of these instruments. Additionally, these emitters usually have a parabolic reflector on top of the TO-39 case, which gives a already directed beam that can easily be collimated and subsequently focused on the detector. They can also be quipped with protective windows at the front, which allows the heating element to be purged in inert gases. This greatly improves the longevity of these types of radiation sources, extending their lifetime to over 10 years. The electrical ratings are considerably low with a maximal voltage of approximately 5 V and no higher current than 100 mA.

3.1.1.2 Laser based IR sources

First lasers in the MIR region were based on cryogenically cooled lead salt diode elements [43]. These diode lasers are based on transitions over the band-gap of the associated materials, whose energies are small (since they lase in the IR) and cooling is necessary [44]. Additionally, the output power is not very high. An alternative are coherent sources based on Optical Parametric Oscillators (OPO)s [45] and Difference Frequency Generation (DFG) [46], which are big and bulky instruments with high maintenance needs.

In 1994 the first working example of a different kind of laser, the Quantum Cascade Laser (QCL), capable of emission into the MIR region, was shown [47]. Using multiple quantum wells in a wide band-gap III-V material, lasing in QCLs is engineered to occur between energy levels located in quantum wells and barriers entirely within the conduction band of a semiconductor, providing transitions that are independent of the actual material band-gap. Each electron passes through the cascade structure and in doing so

emits a photon. Decoupling the emission wavelength from the material band-gap allows the tuning of emission wavelength from the MIR to the Terahertz (THz) region. Recently, the combination interband transitions with cascaded quantum well designs has led to the development of Interband Cascade Laser (ICL) devices [48], which form a so-called W-like quantum well structure using a second InAs layer and are shown to be more efficient in the region from 2700 to 3000 cm^{-1} . However, the tuning range of a given QCL is quite limited by itself, so external cavities (EC) are used in conjunction with a broad gain medium to gain tuning over a wider range. These EC-QCLs can scan over several hundred wavenumbers [49], whilst emitting high power radiation. After years of solving practical issues with EC-QCLs [50], the devices available today are well-developed and are on the verge of revolutionizing the choice of MIR radiation source due to their wide and fast tunability and stable, high power output [11, 12].

For completion, Synchrotron radiation can and is also used for MIR spectroscopy [51].

3.1.1.3 Novel MIR broadband lasers

Unlike QCL sources mentioned in section 3.1.1, recently also Supercontinuum lasers (SCLs) are becoming available for the MIR spectral region. Alfano [15] describes them as follows in his book titled "The Supercontinuum Laser Source": "*The white-light continuum called Supercontinuum is generated using ultrafast laser pulses propagating in solids, liquids, gases, and various designs of optical fibers (single mode, multimode, microstructured, etc.). The SC light source has become the ultimate white-light source, spread worldwide, and has advanced ultrafast laser spectroscopy, condensed matter, biology, physics, and chemistry.*" Widely used in the VIS regime, SCLs based on infrared transparent materials are now available commercially. They are either based on chalcogenide or fluoride glass fibers. Compared to chalcogenide fibers, fluoride fibers seem to be more suitable for lasing action due to their higher achievable doping levels, high strength, high stability, and low background loss. Though rare-earth-doped chalcogenide fiber lasers and amplifiers are also studied, their efficiencies and output powers are relatively low due to the lower available rare-earth doping level, larger background loss, and the fragility of chalcogenide glasses. For the fluoride glass materials, the most common used composition is a mixture of ZrF_4 - BaF_2 - LaF_3 - AlF_3 - NaF with a molar composition of 53 % ZrF_4 , 20 % BaF_2 , 4 % LaF_3 , 3 % AlF_3 and 20 % NaF . Termed ZBLAN glasses, they are considered as the most stable fluoride based glass usable for optical fiber applications [52]. MIR SCL sources based on these kinds of glasses are reported with up to 21.8 W average power [17], repetition rates in the MHz regime and spectacular spectral coverage from 2 to 16 μm [16] have been presented previously. The combination of large spectral bandwidth and high spatial coherence, predestine SCL sources for vari-

ous fields of application.

We obtained a prototype of a now commercially available laser system from NKT Photonics, which exhibited an output power of 75 mW at a repetition rate of 40 kHz. The average pulse length was about 3 ns with the output spectrum extending from 1.75 (5700 cm^{-1}) to $4.2 \mu\text{m}$ (2380 cm^{-1}). It was used for the improvement of an ATR based MIR sensor, designed for the detection of hydrogen peroxide in oxidative gas scrubbers (Publication III).

3.1.2 MIR Detectors

An infrared detector can be described as a transducer converting infrared radiation into some other form of measurable energy, most commonly an electrical signal. Generally, two parameters are important for characterization of an infrared detector: the spectral response, meaning the sensitivity as a function of the impinging wavelength and the achievable Signal to Noise Ratio (SNR) and the thereof dependent specific detectivity D^* . The achievable SNR is limited by the noise of the incident radiation and by the inherent noise of the detector. The detector noise is commonly expressed by the Noise Equivalent input Power (NEP), which refers to the ratio of the noise power density (noise power per unit bandwidth) at the detector output divided by the detector responsivity. The specific detectivity D^* is normalized to the detector surface area by dividing the square root of the detector size with NEP, giving values in $\text{cm Hz}^{0.5} \text{ W}^{-1}$ or Jones [53].

$$D^* = \frac{\sqrt{A\Delta f}}{NEP} = \frac{\sqrt{A\Delta f}}{P} \cdot \frac{V_S}{V_N}, \quad (3.2)$$

with Δf being the detector bandwidth, P the input power and V_S/V_N the signal-to-noise ratio.

IR detectors can be divided into the two basic groups: thermal and photon detectors. Both differ by the underlying physical effect used for the detection process.

3.1.2.1 Thermal detectors

In thermal detectors, the energy absorbed from the incident radiation increases the element temperature and causes changes in the temperature-dependent properties of the detector, which can be measured. The signal, which is produced per unit input normalized to 1 W of radiation is independent of photon energy, hence they exhibit wavelength-independent sensitivity. Thermal detectors can be based on the thermoelectric effect (thermocouples or stacked to thermopiles), materials with a high temperature coefficient resistance (bolometers) or pyroelectric materials [55]. The latter

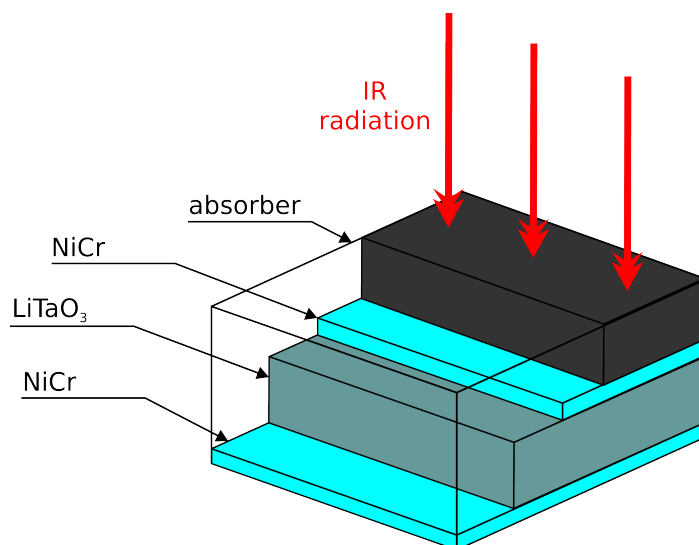
**Figure 3.2:**

Illustration of a pyroelectric detector. The sensing element LiTaO_3 is sandwiched between nm-thin NiCr electrodes. The top side is coated with a black polymer, acting as an absorbing layer. Adapted from [54]

exhibit a large internal electric polarization and temperature changes modify the crystal structure, creating a surface charge: This will be neutralized soon after due to leakage of charge to the surroundings. When incident radiation is heating the element periodically however, the change is manifested in a voltage drop in the element, which can be monitored electronically. This means the incident light has to be chopped or otherwise modulated for detection with a pyroelectric detector. The most common material for such detectors is triglycine sulfate (TGS), which suffers from a rather low Curie point of 49°C . Therefore, deuterated TGS (DTGS) and deuterated L-alanine doped TGS (DLaTGS) have been developed, both with higher Curie points of 60°C and 74°C , respectively. Lithium tantalate (LiTaO_3) shows a smaller pyroelectric coefficient compared to TGS, but has a substantially higher Curie point at 620°C , can be fabricated large in size and can be operated at ambient conditions. Detector elements based on the pyroelectric effect are a practical choice for broadband IR usage and offer advantages in terms of signal strength and time constants (see table 3.1) compared to thermistors and thermopiles. In general, thermal IR detectors use absorbing layers of dark materials, which help facilitate the maximal possible temperature change, thus increasing the sensitivity. Figure 3.2 shows the typical structure of a pyroelectric LiTaO_3 detector. The element itself has a thickness of several tens of μm and is sandwiched by nm-thick NiCr electrodes. On top a black polymer layer is deposited, acting as the absorbing layer.

3.1.2.2 Photon detectors

In photon detectors, the radiation is absorbed on a semi-conducting junction, which results in the generation of charge carriers i.e. electrons in the conduction band of the

3.1. MIR spectroscopic instrumentation

Table 3.1: Overview over a selection of light detectors for the MIR region. Typical values are given for the detectivity D^* in $\text{cm Hz}^{0.5} \text{W}^{-1}$, the time constant τ , the usable spectral range and the operating temperatures.

| | <i>physical effect</i> | <i>materials used</i> | D^* | τ | <i>range</i> | <i>op. T</i> |
|---------|-------------------------------|-----------------------|----------------|-----------------|----------------------|--------------|
| thermal | thermoelectric effect | Chromel-Alumel | $\sim 10^8$ | 50 ms | full MIR | 298 K |
| | temperature coefficient | silicon | $\sim 10^8$ | 20 ms | full MIR | 298 K |
| | pyroelectric effect | DTGS | $\sim 10^8$ | 1 ms | full MIR | 298 K |
| photon | generation of charge carriers | HgCdTe | $\sim 10^{11}$ | 1 μs | to 26 μm | 77 K |
| | | PbS | $\sim 10^{10}$ | 1 ms | to 3.5 μm | 298 K |
| | | PbSe | $\sim 10^9$ | 5 μs | to 6.5 μm | 298 K |
| | quantum well | III-V materials | $\sim 10^{10}$ | 5 ps | to 10 μm | 200 K |

device and holes in the valence band. These photodiodes can be built as photovoltaic or photoconductive devices. In photoconductive applications a reverse bias is applied across the diode and the photogenerated charge carriers increase the conductivity of the device. The increase in current flow is detected as the electrical signal. In photovoltaic mode, the photo-generated charge carriers are allowed to diffuse to the metal contacts on the diode where a photocurrent is produced and measured. These kinds of detectors find widespread use in IR spectroscopy, with the most commonly used material being the ternary II-VI alloy of CdTe and HgTe featuring a tunable bandgap spanning the whole infrared region up to 30 μm . These HgCdTe detectors, often referred to as MCT detectors, have excellent properties, including a small time constant, high quantum efficiency, reduced cooling requirements and innovative structure design by epitaxial growth technologies. They achieve their highest sensitivity combined with repeatable and stable performance at cryogenic temperatures (77 K) [56]. The lead sulfide (PbS) intrinsic photoconductor detector was one of the first infrared detectors to be used and still finds applications today although its limited use up to about 5 μm . Lead selenide (PbSe) features an extended response to about 6.5 μm , however both materials suffer from high temperature coefficients of response and therefore require active temperature control.

Lastly, the possibility of using the same structures as in QCLs also as detectors was discovered shortly after the first implementations of QCLs. The name was coined accordingly, Quantum Cascade Detector (QCD) [57]. Belonging to the class of Quantum Well Infrared Photodetector (QWIP)s, electrons are extracted via tunneling and scattering through a sub-band ladder and the resulting current is measured. These detectors

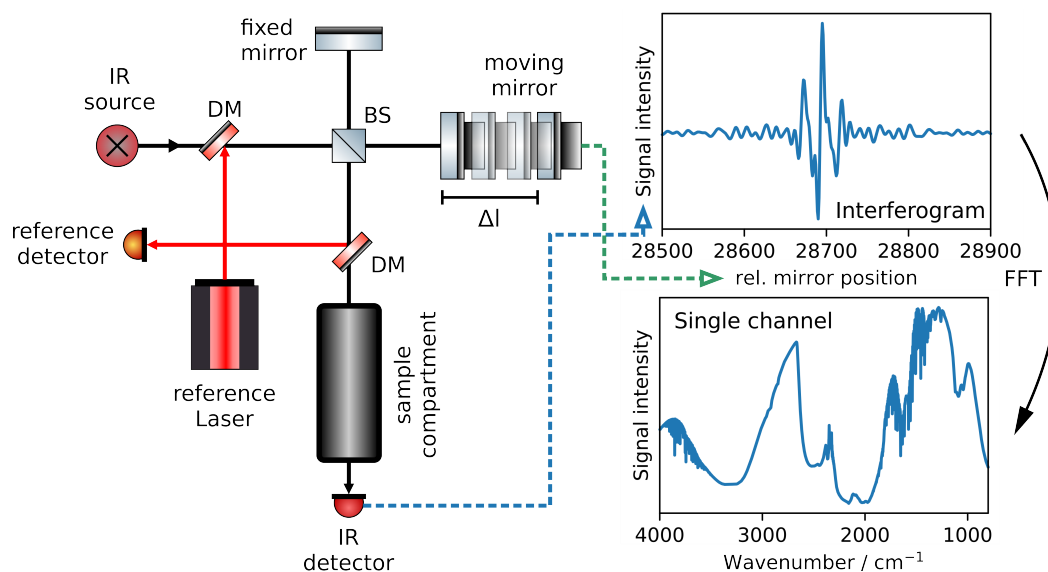


Figure 3.3: Schematic illustration of the working principle of the FTIR spectrometer with BS...beamsplitter, DM...dichroic mirror, FFT...Fast Fourier Transform. The movement of the translated mirror is indicated with Δl .

hold great promise for very fast response times and good detectivities.

3.1.3 FTIR spectroscopy

Currently, the most commonly used spectrometer in MIR spectroscopy is certainly the Fourier-Transform Infrared FTIR spectrometer. As described in the introduction in chapter 1 these instruments were first built in the 1930s. They consist of scanning Michelson interferometers, whose basic working principle is depicted in figure 3.3. The radiation from a broadband IR source is splitted into equal parts using a beamsplitter. Both arms of the interferometer use mirrors at the end, with one of the mirrors being translated. The retro-reflected beams can subsequently interact at the beamsplitter, interfering constructively or destructively depending on the wavelength and the path length difference Δl . This leads the intensity variation in the output arm of the interferometer to be the cosine transform of the input light spectrum, as

$$S(\Delta l) = \int_{-\infty}^{\infty} I(\tilde{\nu}) \cos(2\pi\tilde{\nu}\Delta l) d\tilde{\nu}. \quad (3.3)$$

It essentially transforms the high frequency of an optical wave into a more accessible intensity modulation in the radio frequency range [33]. The original intensity spectrum is then recovered by applying the inverse cosine transform, which for real input is the real part of a Fourier transform and hence the fast, optimized algorithms for Fast Fourier

3.1. MIR spectroscopic instrumentation

Transform (FFT) are eligible for calculation [58]. This interferometric approach comes with three advantages:

Multiplex or Fellgett advantage All frequencies emitted from the IR source are modulated simultaneously by the interferometer into a single interferogram signal (onto a single detector). Therefore, the SNR of a Fourier transform instrument recording N data points will be \sqrt{N} higher than that of a dispersive instrument.

Throughput or Jacquinot advantage The FTIR spectrometer accepts a circular beam shape as opposed to classical dispersive instruments employing a slit. The stringent link between throughput and resolution is removed, which allows FTIR instruments to operate at a higher SNR while providing the same spectral resolution [59].

Precision or Connes advantage With the accessibility of stable laser radiation in the early 1960s, an internal reference for the mirror position can be funneled into the interferometer, increasing the precision of the wavelength axis [60].

The superior performance of the FTIR spectrometer compared to dispersive instruments made it the standard instrument in MIR spectroscopy, still regarded as the gold standard. However, FTIR instruments are generally rather costly, require a certain size and are thus often featured as table-top devices.

3.1.4 MIR spectroscopy using tunable filters: Filtometers

Another way of discriminating wavelengths is to use bandpass filters, which feature a narrow transmission band in the spectrum. Usually, layer stacks of two dielectric materials with a different refractive index are applied alternately to a substrate made from an infrared-transparent material. Interference effects lead to a wavelength-dependent extinction or enhancement of the incident electromagnetic wave. Thus, different spectral ranges of high and low transmission are created, which can be used for various types of optical filters. These filters can be used in combination with a radiation source and detector element to build a sensing device, which can detect intensity as a function of wavelength. Since a filter is employed as the wavelength-discriminating device, these instruments are often referred to as filtometers, a term coined from filter and photometer. Since most of the following (especially tunable) filter systems are based on interference filters based on FP cavities, the theory behind them will be discussed shortly.

3.1.5 Fundamentals of a Fabry-Pérot cavity

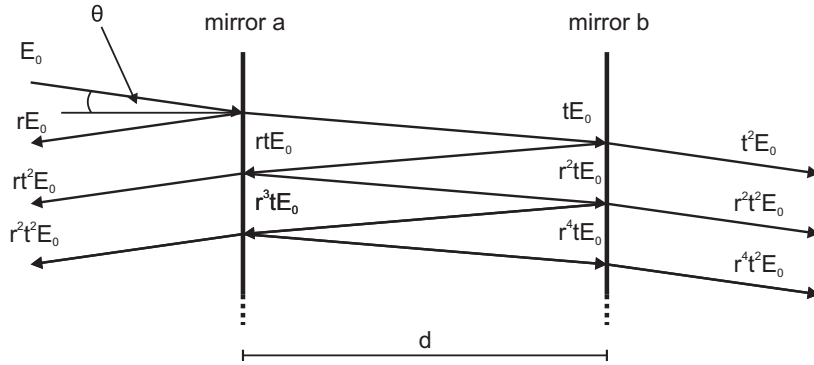


Figure 3.4: Illustration of the simplest form of a Fabry-Pérot resonator. θ indicates the angle of incidence of the beam, d the distance between the two mirrors, E the field strength and r and t are the reflectivity and transmittance coefficient respectively.

Figure 3.4 illustrates the simplest form of a FP resonator, which consists of two plane mirrors. For reason of simplicity we assume that the incoming light consists of a monochromatic and coherent plane wave. It can be expressed by:

$$E(x, t) = E_0 \cos(\omega t - kx) + \phi(x) \quad (3.4)$$

with k being the wave vector, ϕ being the phase shift and ω being the angular frequency. As figure 3.4 suggests, the transmitted electric field can be described by

$$E_t = E_0 t^2 (1 + |r|^2 e^{i\Delta\phi} + |r|^4 e^{i2\Delta\phi} + \dots) \quad (3.5)$$

where r and t embody the complex reflectivity and transmission coefficients, respectively, which are generally defined by the ratio of the reflected or transmitted amplitude with the incident amplitude of the electric field. They can be written in the following way [61]:

$$r = |r|e^{i\Delta\phi} \quad \text{and} \quad t = |t|e^{i\Delta\phi} \quad (3.6)$$

Equation 3.5 represents a geometric series and can be solved using the sum formula of the same:

$$\sum_{n=1}^{\infty} q^{n-1} = \frac{1}{1-q} \quad (3.7)$$

leading to

$$E_t = E_0 t^2 \frac{1}{1 - |r|^2 e^{i\Delta\phi}} \quad (3.8)$$

3.1. MIR spectroscopic instrumentation

The squares of t and r are often referred to as R ($|r|^2$) and T ($|t|^2$). Since generally it is more interesting knowing intensities rather than electric field strengths, the following expression is adequate:

$$\frac{I_t}{I_0} = \frac{|E_t|^2}{|E_0|^2} = \frac{T^2}{|1 - Re^{i\Delta\phi}|^2} \quad (3.9)$$

with I as intensities of the transmitted and the incident beam. The maxima of equation 3.9 can be determined from the roots of the denominator.

$$|1 - Re^{i\Delta\phi}|^2 = (1 - Re^{i\Delta\phi})(1 - Re^{-i\Delta\phi}) = 1 - \underbrace{Re^{i\Delta\phi} - Re^{-i\Delta\phi}}_{2R \cos \Delta\phi} + R^2 \underbrace{(e^{i\Delta\phi} e^{-i\Delta\phi})}_1 \quad (3.10)$$

Using Euler's identity (replacing the exponential with the cosinus) and the trigonometric formula $\cos(x) = 1 - 2 \sin^2(x/2)$ equation 3.10 can be rewritten as:

$$1 - 2R(1 - 2 \sin^2(\Delta\phi/2)) + R^2 = 1 - 2R + 4R \sin^2(\Delta\phi/2) + R^2 \quad (3.11)$$

$$\rightarrow (1 - R)^2 \left(1 + \frac{4R \sin^2(\Delta\phi/2)}{(1 - R)^2} \right) \quad (3.12)$$

Combining equation 3.12 with equation 3.9 yields the following result:

$$\frac{I_t}{I_0} = \frac{T^2}{(1 - R)^2} \left(1 + \frac{4R \sin^2(\Delta\phi/2)}{(1 - R)^2} \right)^{-1} \quad (3.13)$$

This expression exhibits the transmitted intensity as a function of T , R and the phase shift $\Delta\phi$. The function reaches its maximum when $\Delta\phi = 2m\pi$. Taking a second look at figure 3.4 and equation 3.4 it is possible to account for the phase shift in this system. When the beam travels through the first mirror, it will undergo a phase shift $\Delta\phi_s$ and the expression for the plane wave will change.

$$E(x, t) = E_0 \cos(\omega t - kx + \Delta\phi_s) \quad (3.14)$$

As it passes through the medium to the second mirror, the wave vector changes accordingly. In this case we are only considering the interferometer axis (indicated with x), so the projection of the wave vector onto this axis has to be considered ($\cos \theta d$)

$$E(x, t) = E_0 \cos(\omega t - k \cos \theta d + \Delta\phi_s) \quad (3.15)$$

With

$$k = n \frac{\omega}{c_0} = nk_0 \quad (3.16)$$

the equation changes into

$$E(x, t) = E_0 \cos(\omega t - k_0 n \cos \theta d + \Delta\phi_s) \quad (3.17)$$

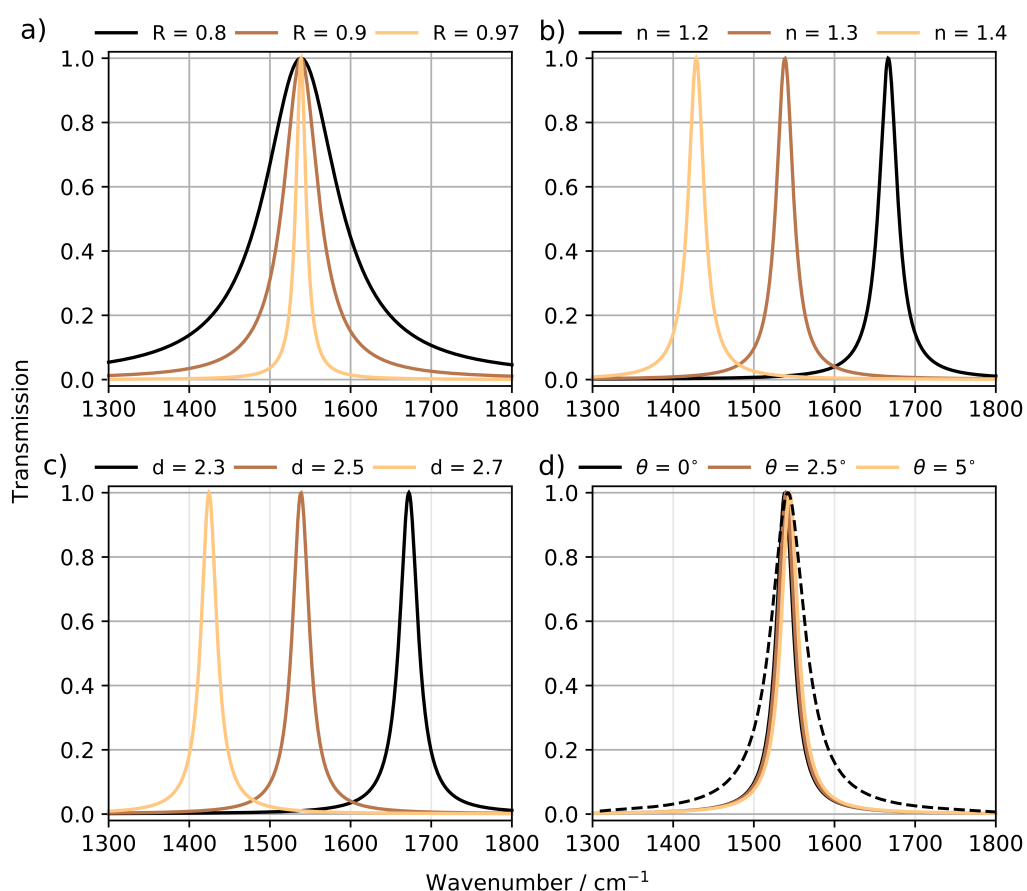


Figure 3.5: Calculated transmission of a Fabry-Pérot interferometer with starting parameters of $n = 1.3$, $d = 2.5\mu\text{m}$, $R = 0.95$ and the incident angle θ of 0° . **a)** The reflectivity R and with it, the Finesse, is altered. **b)** The effect of a change in refractive index is shown. **c)** The shift of the center position when changing the distance between the two reflective surfaces. **d)** The effect of different angles of incidence with the convolution (dotted lines, normalized) between them to show how a focused beam affects the transmission window.

When the wave finally returns, the phase shift will be incremented by another $\Delta\phi_s$ from the second mirror and of course also the term for the distance in between changes accordingly. The cumulative phase shift $\Delta\phi$ can therefore be rewritten as:

$$\Delta\phi = 2\Delta\phi_s - 2k_0nd\cos\theta = 2\Delta\phi_s - 2\frac{\omega}{c_0}nd\cos\theta = 2\Delta\phi_s - 4\pi\tilde{\nu}nd\cos\theta \quad (3.18)$$

The last term is particularly useful as it contains the wavenumber $\tilde{\nu}$ instead of the wavelength or angular frequency, which are not commonly used in IR spectroscopy. Like mentioned before, the transmission reaches its maximum at a phase shift every

3.1. MIR spectroscopic instrumentation

$2m\pi$, which now can be inserted into 3.18.

$$2m\pi = 2\Delta\phi_s - 4\pi\nu nd \cos\theta \quad (3.19)$$

So for given distances d the phase condition is fulfilled for the following wavenumbers:

$$\nu = \frac{1}{2\pi nd \cos\theta} (m\pi + \Delta\phi_s) := \Delta\tilde{\nu}_s + m\Delta\tilde{\nu}_r \quad (3.20)$$

The phase shift at the mirrors $\Delta\tilde{\nu}_s = \Delta\phi_s/2\pi nd \cos\theta$ will only result in a cumulative shift of all resonances and is therefore neglected. This leaves us with

$$\Delta\tilde{\nu}_r = \frac{m}{2nd \cos\theta}, \quad (3.21)$$

which is also known as *free spectral range*, as it gives an expression for the spectral spacing between resonance wavenumbers.

An other important figure of merit of a Fabry-Pérot interferometer is the *Finesse*. It is defined in the following way:

$$F := \pi \frac{\sqrt{R}}{1-R} \quad (3.22)$$

Inserting the two identities shown in equation 3.21 and 3.22 into equation 3.13 yields

$$\frac{I_t}{I_0} = \frac{1}{1 + (2F/\pi)^2 \sin^2(2\pi\tilde{\nu}nd\cos\theta)} \quad (3.23)$$

For ideal mirrors without absorption the term $T^2/(1-R)^2$ yields one and hence can be neglected. Equation 3.23 allows to show important parameters that define the central wavenumber (or central wavelength) of the FP resonator. The Finesse of the resonator is a function of the reflectivity R , where a higher reflectivity produces transmission bands with smaller Full Width at Half Maximum (FWHM) values (Figure 3.5a). The spectral position of the resonance wavenumber differs when the refractive index n of the medium changes (Figure 3.5b). Analogously, when the distance d between the mirrors changes, so does the transmission band's spectral position (Figure 3.5c). Additionally, the angle of incidence of the incoming beam changes the spectral position of the transmission band (Figure 3.5d). This point is especially important to consider, because in most MIR instruments, the light beam is perfectly collimated, in fact, most of the time the light rays are focused onto the detector element to achieve highest possible SNR. This leads to a broadening of the transmission band, as rays of different angles will be transmitted simultaneously through the cavity (indicated in figure 3.5d as dashed lines).

3.2 Instrumentation for Raman spectroscopy

The following section will briefly discuss the makeup of a standard Raman spectrometer. It is usually comprised of a monochromatic light source (commonly a laser), collection optics for the efficient gathering of the scattered photons, a monochromator for the spectral analysis and a sensitive detector. Another important part never missing in a Raman spectrometer is the Rayleigh or laser line filter. It helps block out the elastically scattered light, which otherwise would generate Raman signals only specific to the optical elements used in the collection optics and due to the weakness of the Raman scattering cross section compared to Rayleigh scattering would mask the Raman signal on the detector. These filters usually come in two variants, either as long-pass edge-filter, which only transmit the Stokes photons, or as notch-filters, which block only the region of the excitation laser. The important features are a high blocking at the laser line and a smooth and clean transmission in the region of the Raman spectrum.

3.2.1 Collection optics

In section 2.4, equation 2.29 postulates that the extend of the solid angle, which can be collected, influences the amount of detected backscattered photons. Ideally, it should be as big as possible. The optical parameter usually defined here is the Numerical Aperture (NA) as

$$NA = n \sin \theta \quad (3.24)$$

with n being the refractive index and θ the maximal half-angle of the cone of light that enters the optical element (marginal ray). Related, often the f-number N_f is used to describe the light gathering power of an optical component. It is defined as follows:

$$N_f = \frac{f}{D} \quad (3.25)$$

where f is the focal length and D is the diameter of the entrance pupil (effective aperture). Commonly, f-numbers are written preceded by $f/$, giving a relation between N_f and the focal length. So with the previous arguments in mind, it is favorable to have a as large as possible numerical aperture and inversely, a small N_f . It is important to keep this in mind when using Raman microscopes, a very common implementation of Raman spectroscopy, which generally feature a selection of different objectives exhibiting varying magnifications and with it varying numerical apertures.

3.2.2 Lasers

Nowadays a plethora of different lasers based on varying lasing principles are employed. The most important features for a laser to be used for Raman spectroscopy, are the following:

Linewidth The spectral linewidth of the output radiation of the laser limits the spectral resolution of the system. The linewidth of the laser should be narrower than the spectral resolution of the spectrometer. Single mode laser are usually sufficient.

Wavelength stability The spectral position of the laser line has to be constant over the measurement time. This can be facilitated by using e.g. external gratings and accurate temperature control.

Wavelength purity There should be no side modes creating additional laser lines in the excitation beam.

Beam quality For ideal focusing of the laser beam, the laser beam should exhibit a diffraction-limited TEM₀₀ mode structure.

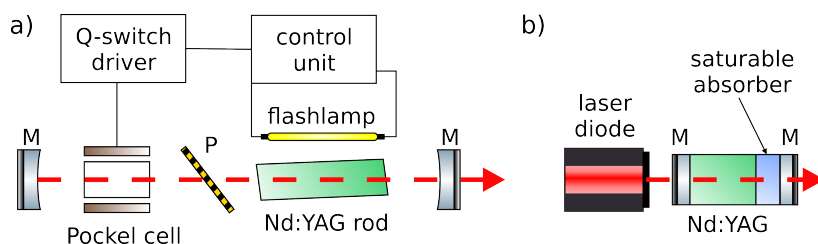
Output power stability Since the amount of backscattered photons is directly proportional to the intensity of the excitation laser, output power stability is key in enabling longer acquisition times, especially if quantification is of interest.

Recently solid state lasers are mainly used for excitation in Raman spectroscopy, because of their easy and rugged operation. As the name implies, the lasing element in these devices are solid crystals, the most commonly used are neodymium-doped yttrium aluminum garnet (Nd:YAG) and generally Nd-doped glasses. To create the population inversion needed for lasing, optical pumping by either using a flashlamp or diode laser is used. Diode-Pumped Solid-State (DPSS) lasers tend to be much more efficient and have become much more common as the cost of high-power semiconductor lasers has decreased. The fundamental laser line of the ND:YAG is located at 1064 nm and is currently one of the most used excitation wavelengths for NIR Raman spectroscopy. Second and higher order harmonic non-linear crystals can be used to double, triple or quadruple the frequency of the laser (in fact, one of the lasers used in this thesis had add-ons for 4 different wavelengths, meaning three different harmonics.)

For special applications of Raman spectroscopy, pulsed lasers are needed. Solid state lasers can be pulsed by employing a Quality-(Q-)switch. The basic principle behind Q-switching the laser is to pump the laser gain medium for a specific amount of time while preventing laser operation, only to suddenly allow for laser operation, so that the stored energy is quickly released in the form of a short, intense light pulse. To control the laser emission, we introduce optical losses in the cavity that are initially high (low Q) and then

Figure 3.6:

a) Active Q-switched laser module as used in the EK-SPLA laser. **b)** Passive Q-switched microchip laser architecture employing a saturable absorber. M are mirrors, P is a polarizer.



suddenly lowered (high Q). In the case of active Q-switching, an electrically controlled modulator is used, normally an acousto-optic or electro-optic modulator. In the case of the EK-SPLA laser used in this thesis, a Pockel cell is used to rotate the polarization of the beam passing through, creating a switchable attenuation unit in conjunction with the polarizer P (see figure 3.6a). Passive Q-switched microchip laser present a rather novel and very efficient way of producing short laser pulses. Microchip lasers are alignment-free monolithic solid-state lasers, where the laser crystal is directly contacted with the mirrors of the laser resonator as depicted in figure 3.6b. They are usually pumped by a semiconductor laser diode. Additionally, they feature a saturable absorber, an optical component with a given optical loss, which is lost at high optical intensities [62]. This way, the losses are automatically modulated with the absorber and no active switching is required. Compared with active Q-switching, passive Q-switching is simple and cost-effective and it is suitable for very high pulse repetition rates. However, the pulse energies are typically lower. Also, external triggering of the pulses is not possible. For this reason, the passive Q-switched laser used in this work as an internal photodiode, which not only allows continuous monitoring of the output power, but also acts as a reliable trigger featuring low jitter. Additionally, pulse widths in the low ps-regime are possible [63]. Table 3.2 summarizes the properties of the pulsed lasers used in this thesis. Both feature pulse widths in the low nanosecond time scale. The Explorer One however, being of the passively Q-switched variety, is significantly smaller, air-cooled and therefore more suitable for the design of a portable and rugged stand-off Raman instrument.

3.2.3 Wavelength discrimination

Nowadays the most used dispersive element used in Raman spectroscopy is the diffraction grating, with different types of grating [64]. Most commonly, transmission or reflection gratings in form of volume, ruled or holographic gratings are employed. The simplest form is the surface grating, which feature grooves on the surface of a reflecting or transmitting material. These kind of gratings are usually manufactured by mechan-

3.2. Instrumentation for Raman spectroscopy

Table 3.2: Pulsed solid state lasers used in the works presented in this thesis and their respective properties.

| | <i>NL301HT</i> | <i>Explorer One HE 532-200</i> |
|---------------------|---------------------------------|--------------------------------|
| Manufacturer | EKSPLA | Spectra Physics |
| Wavelength | 1064, 532, 355, 266 nm | 532 nm |
| Pulse duration | 4.4 ns | <15 ns |
| Pulse energy | 380 mJ | >0.2 mJ |
| Average power | 3.8 W @ 10 Hz | 2 W @ 10 kHz |
| Repetition rate | 10 Hz | 1-60 kHz |
| Cooling | water-cooled | air-cooled |
| Pulse energy noise | 1.5 % rms | <3 % rms |
| Long term stability | < ± 2 % | < ± 2 % |
| Beam shape | Top Hat, Gaussian in far fields | Gaussian |
| Beam diameter | 6 mm | 0.18 mm |
| Beam divergence | <0.6 mrad | 3.9 mrad |
| Operating voltage | 220 V _{AC} | 24 V _{DC} |
| Power consumption | <1 kW | <100 W |
| Size / mm | 154x475x128 & 330x490x585 | 240x95x94 |
| Weight | >20 kg | 3.1 kg |

ically cutting or stamping grooves into the substrate. Volume gratings use patterned refractive index or absorbance through the depth of a material as grating. Holographic gratings can be manufactured by crossing two laser beams to produce an interference pattern on a photosensitive material to create grooves. Holographic gratings tend to have more precise groove spacing and groove shape than ruled gratings. Surface holographic gratings also tend to show less unwanted scattering and feature more complex groove patterns compared to ruled gratings. Volume phase holographic gratings are a special subtype of the holographic volume grating and are more and more used as dispersive element in high-performance imaging spectrographs for Raman spectroscopy [65].

A diffraction gratings performance can be described by what extent the input light is dispersed, which is generally a function of groove density or spacing given in lines per mm. So a diffraction grating with the right resolving power has to be selected, according to the excitation wavelength and desired spectral resolution. Generally, shorter excita-

tion wavelengths need higher spectral resolution, as the Raman spectrum is dispersed over a smaller spectral range (see figure 2.9). The blazed groove shape used by modern diffraction gratings directs most of the diffracted light into a single order of diffraction. A particular blazed grating will have better efficiency at certain wavelengths, so the grating has to be selected for the spectral region used. Hence, a wide range of diffraction gratings are commercially available today. One of the most popular geometries for a dispersive monochromator for Raman spectroscopy is the Czerny–Turner spectrograph, which was also used for parts of the work presented here. Its optical layout is depicted in figure 5.5. Incident light from the entrance slit is collimated by a concave mirror, diffracted by the plane grating mounted on a grating turret for easy changing and adapting the imaged spectral range on the array detector. Subsequently, the photons are focused again through an exit port by a second concave mirror onto the array detector. Spherical mirrors can be replaced by toroidal mirrors to reduce astigmatism. Nevertheless, optical aberrations generally limit Czerny–Turner spectrographs f-numbers to $f/4$ or worse. Of course, the need of an entrance slit makes the light throughput challenging, as the trade-off between spectral resolution and transmitted intensity is always present. To somehow circumvent this problem, we used a special fiber arrangement to couple the collection optic to the spectrograph. A round-to-slit fiber features a round arrangement of 19 200 μm fibers on one side and a lined-up arrangement on the other, which can be placed collinear to the entrance slit of the spectrograph.

At this point, one has to wonder why not use FT-spectrometers, as is done in IR spectroscopy. Here, the performance of FT- and dispersive-Raman spectrometers has to be compared. As already mentioned a couple of times, shorter wavelengths are advantageous for Raman spectroscopy due to the significantly better Raman scattering cross section. This means the bulk of Raman applications right now are located in the visible region of the EM spectrum. In the late 1980s and early 1990s, Charge Coupled Device (CCD) array detectors with quantum efficiencies exceeding that of a single Photo-Multiplier Tube (PMT) were introduced [66]. Hence, a typical dispersive Raman spectrometer comprising a visible laser, grating spectrograph, and Thermoelectric Cooling (TEC) CCD array detector is almost an order of magnitude more sensitive than an FT-Raman spectrometer with an Nd:YAG laser (@ native 1064 nm) and a germanium detector. However, FT-Raman instruments are still used for one very important reason, they allow measurement deeper into the NIR region, effectively reducing the chance to induce fluorescence in the sample to zero.

Another type of FT-spectrograph is also worth mentioning here: the Spatial Heterodyne Spectrometer (SHS). Its basic setup is very similar to the Michelson interferometer presented in figure 3.3, except with the mirrors exchanged with fixed reflective gratings. The gratings are usually arranged in Littrow-configuration to the excitation wavelength.

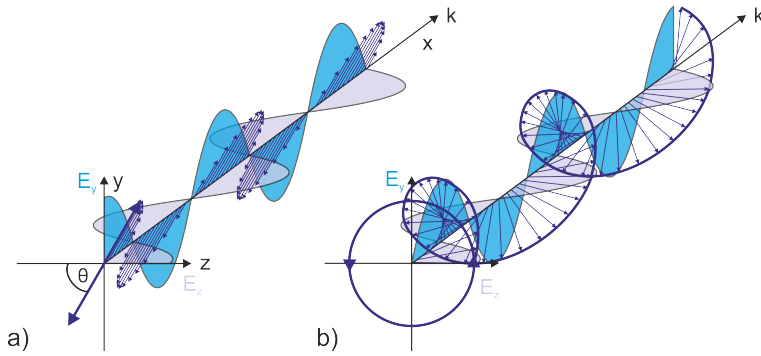


Figure 3.7:
a) Linearly polarized light at the angle θ and the respective components. **b)** Right circularly polarized light forming a helix illustrated with the respective components.

Any wavelength different from that will undergo a change in direction, resulting in a tilted wavefront after beam combination, which produces a interferometric pattern on an array detector. The major advantages of this kind of spectrometer are the absence of moving parts and the high optical throughput [67].

3.2.4 Birefringent interferometers/filters

Before the theory of birefringent interferometry will be discussed, a quick introduction about the concept of polarization in photonics will be given.

3.2.4.1 Polarization of light

The orientation of the electric field vector in respect to the plane orthogonal to the propagation direction x or \mathbf{k} is called the polarization state of light. The wave vector of a plane wave can be represented by two components, namely:

$$E_y(x, t) = E_{0,y} \cos(\omega t - kx) \quad E_z(x, t) = E_{0,z} \cos(\omega t - kx + \Delta\phi), \quad (3.26)$$

where $\Delta\phi$ is the phase shift between the two fields. For unpolarized light, the phase shift has no fixed correlation. If $\Delta\phi$ is constant, the resulting polarization state is called right or left elliptically polarized, as the wave vector describes an ellipse on the yz plane. Two special cases can be distinguished: First, $\Delta\phi = 0$, meaning both fields oscillate in phase, leads to a compression of the ellipse to a line, which oscillates at an angle $\theta = \arctan(E_{0,y}/E_{0,z})$ in the yz plane (figure 3.7a). This state is called linearly polarized. The second case occurs at a phase shift of $\Delta\phi = \pm\pi/2$, where the wave vector describes a circle in the yz plane (figure 3.7b).

When a specific polarization of light is needed, most often polarizers are used. Usually, polarizers transmit the desired polarization while reflecting the rest. Wire grid polarizers are a common example of this, consisting of many thin wires arranged parallel to

each other. Light that is polarized along these wires is reflected, while light that is polarized perpendicular to these wires is transmitted. Another technique for polarizers is to use the Brewster angle. Brewster's angle is a specific angle of incidence under which only one polarization is reflected. Yet another method is the specific absorption of one polarization of light, used in dichroic polarizers. If unpolarized light hits an ideal linear polarizer, only one of the two linear polarizations will be transmitted, reducing the initial unpolarized intensity by half.

Manipulating the polarization of a given beam is also possible. Waveplates, or wave retarders, transmit light and modify its polarization state without attenuating, deviating, or displacing the beam. They do this by retarding one component of polarization with respect to its orthogonal component by a specific amount. If the retardation, or the phase shift between polarization components is equal to π , the waveplate is commonly known as half-wave plate and can be used to rotate the polarization axis of linearly polarized light. Analogously, when the phase shift is $\pi/2$, it's called a quarter-wave plate, which can be used to convert linearly polarized light into circular polarized light and vice-versa.

3.2.4.2 Lyot filters

The basic principle of this birefringent filter is based on the interference of polarized light after passing through a birefringent crystal. For the following considerations we assume a linearly polarized wave

$$\mathbf{E} = \mathbf{A} \cos(\omega t - kx) \quad \text{with} \quad \mathbf{A} = \{0, A_y, A_z\} \quad A_y = |A| \sin \theta \quad A_z = |A| \cos \theta. \quad (3.27)$$

Figure 3.8 shows the coordinate system with a birefringent crystal of length L with the ordinary axis n_o along the z -axis and the extraordinary axis n_e along the y -axis. The electric vector \mathbf{E} enters the crystal at an angle θ to the optical axis. The crystal splits the wave into two orthogonal components, one called the ordinary beam with $k_o = n_o k$ and the other called the extraordinary beam with $k_e = n_e k$. So for the partial beams traveled through the crystal the components of the \mathbf{E} vector are as follows:

$$E_y = A_y \cos(\omega t - k_e L) \quad E_z = A_z \cos(\omega t - k_o L). \quad (3.28)$$

They show a phase difference of

$$\Delta\phi = k(\Delta n)L = \frac{2\pi}{\lambda} \Delta n L \quad \text{with} \quad \Delta n = n_o - n_e \quad (3.29)$$

After passing the crystal, the two waves interfere, superimposing to generally elliptically polarized light. For phase differences of $\Delta\phi = 2m\pi$ the resulting wave will be again linearly polarized with $\mathbf{E}(L) \parallel \mathbf{E}(0)$. When $\Delta\phi = (2m + 1)\pi$ and $\theta = 45^\circ$ the exiting wave

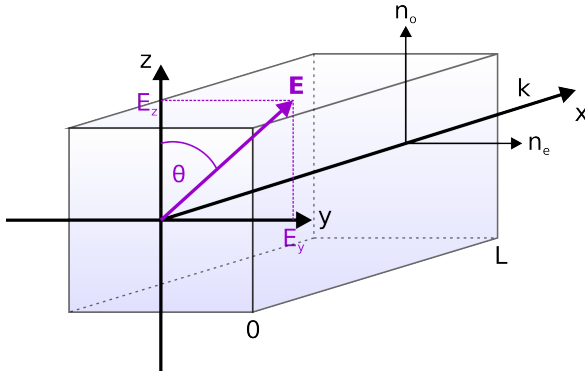

Figure 3.8:

Illustration of linearly polarized light entering the birefringent crystal of length L with the ordinary axis n_o along the z -axis and the extraordinary axis n_e along the y -axis.

is also linearly polarized, but with $\mathbf{E}(L) \perp \mathbf{E}(0)$.

The simplest form of a Lyot filter consists of a birefringent crystal sandwiched between two linear polarizers. Let these polarizers both be arranged parallel to \mathbf{E} of the incoming wave. So the second polarizer only transmits the projection of \mathbf{E}

$$\begin{aligned} \mathbf{E} &= E_y \sin \theta + E_z \cos \theta \\ &= A \left[\sin^2 \theta \cos(\omega t - k_e L) + \cos^2 \theta \cos(\omega t - k_o L) \right] \end{aligned} \quad (3.30)$$

of the amplitudes. Since detectors usually cannot follow the high frequency of the electromagnetic wave, they usually measure the time averaged intensity

$$\langle I \rangle = \frac{c \epsilon_0 E_0^2}{T} \int_0^T \cos^2(\omega t - kx) dt = \frac{1}{2} c \epsilon_0 E_0^2. \quad (3.31)$$

With this, equation 3.30 results in the transmitted intensity I_t

$$I_t = I_0 (\sin^4 \theta + \cos^4 \theta + 2 \sin^2 \theta \cos^2 \theta \cos \Delta \phi). \quad (3.32)$$

With the trigonometric relations $2 \sin \theta \cos \theta = \sin 2\theta$ and $\cos \phi = 1 - 2 \sin^2 \frac{\phi}{2}$, this can be rewritten as

$$\begin{aligned} I_t &= I_0 \left[\sin^4 \theta + \cos^4 \theta + \frac{1}{2} \sin^2(2\theta) \left(1 - 2 \sin^2 \left(\frac{\Delta \phi}{2} \right) \right) \right] \\ &= I_0 \left[\underbrace{\sin^4 \theta + \frac{1}{2} \sin^2(2\theta) + \cos^4 \theta}_{(\sin^2 \theta + \cos^2 \theta)^2 = 1} - \sin^2(2\theta) \sin^2 \left(\frac{\Delta \phi}{2} \right) \right]. \end{aligned} \quad (3.33)$$

With $\theta = 45^\circ$, this is further reduced to

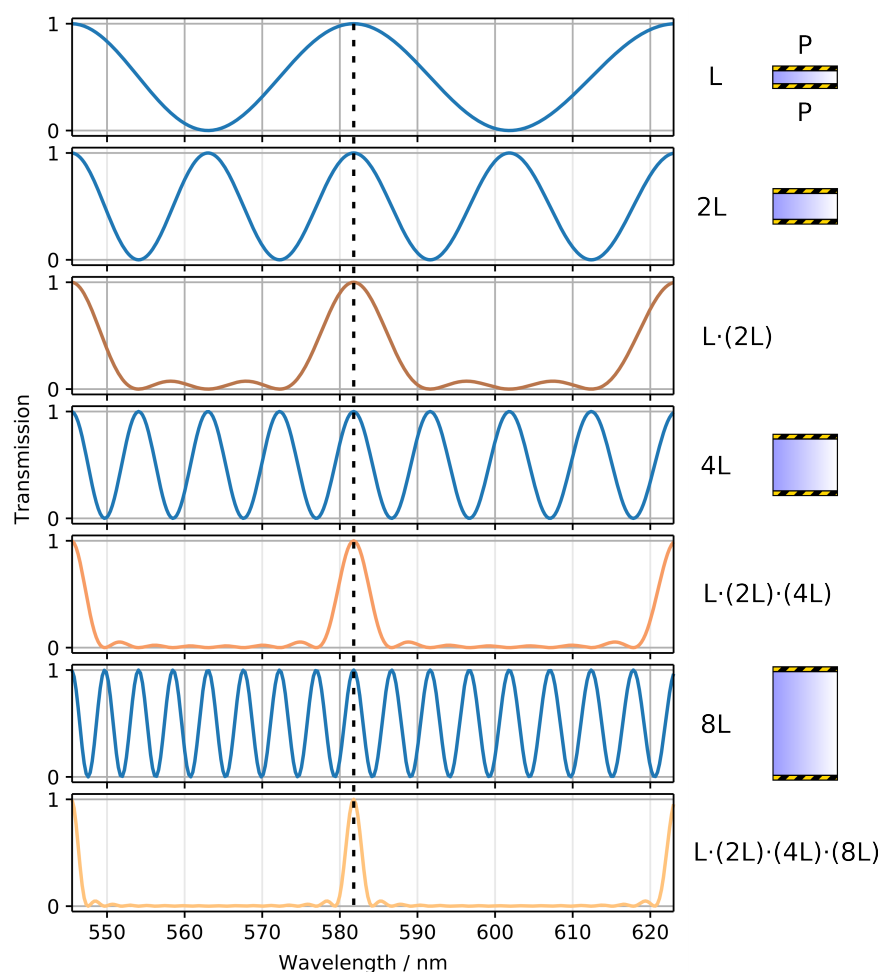
$$I_t = I_0 \left[1 - \sin^2 \left(\frac{\Delta \phi}{2} \right) \right] = I_0 \cos^2 \left(\frac{\Delta \phi}{2} \right). \quad (3.34)$$

The transmission of a single Lyot element is then given by

$$T(\lambda) = \frac{I_t}{I_0} \cos^2 \left(\frac{\pi \Delta n L}{\lambda} \right). \quad (3.35)$$

Figure 3.9:

Transmission of a stack of Lyot filters. Every Lyot element has double the extend of its predecessor and their cumulative transmission is also shown for every additional element. Calculated with $n_e = 1.51$, $n_o = 1.47$ and a crystal length L of 10 mm.



The transmission is thereby primarily a function of phase retardation, which depends on the birefringence and the length of the crystal and the wavelength. The result can be seen in the first graph in figure 3.9. Usually, filters based on the Lyot concept consist of more than one element. Stacking several Lyot elements with each element exhibiting double the length of its predecessor, a small linewidth transmission filter can be created, as figure 3.9 shows. The cumulative transmission for a stack of N elements becomes

$$T(\lambda) = \prod_{m=1}^N \frac{I_t}{I_0} \cos^2 \left(\frac{\pi \Delta n L_m}{\lambda} \right). \quad (3.36)$$

It becomes clear from the calculated transmission bands in figure 3.9 that the shortest element in the stack determines the free spectral range. The linewidth of the transmission after the stack is however mainly influenced by the longest part of the stack.

3.2.4.3 Liquid-crystal tunable filters

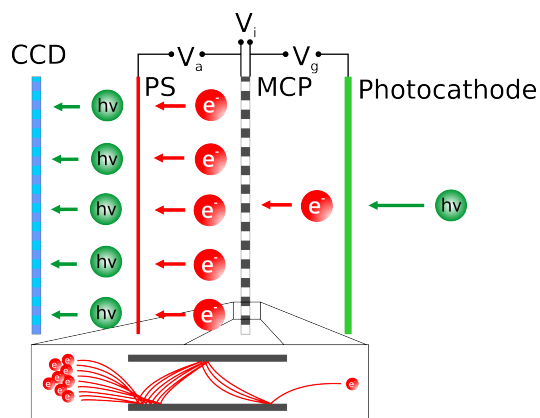
Several forms of the birefringent filter are possible with different width of field and complexity of construction. They all are based, however, on the interference of polarized radiation after passing a birefringent element. Evans and van Raalte give a good overview over the different technological advancements in this field [68, 69]. All these types of filters can be made tunable by changing the birefringence Δn . A common method is to use a material, where Δn can be changed by applying an electric field, e.g. potassium dihydrogen phosphate. Another possibility is to use liquid crystals, which describes a state of matter with properties between those of liquids and of solid crystals. Usually the molecules of a liquid crystal are susceptible to an applied electric field, which can be used to enforce a single ordered domain in a macroscopic fashion and thus tuning the birefringence. This makes liquid-crystal devices particularly interesting in addition to their high transparency over a large spectral range and their very large electro-optic coefficients, which allow broad tuning ranges. Additionally, large optical apertures are possible. In 2010 Peter Miller working at Cambridge Research & Instrumentation (CRI) was granted a patent for an "Optical filter assembly with selectable bandwidth and rejection" [70], in which he describes a liquid-crystal tunable filter (LCTF) for use in different spectral ranges with electro-optical tuning. These kinds of filter were used to facilitate the wavelength discrimination in a stand-off hyperspectral imager, which will be presented in chapter 5.

3.2.5 Detectors

Although several different kinds of light detection techniques are available today, for the synchronized pulse-gate measurement needed for stand-off Raman spectroscopy, only devices capable of fast and reliable gating can be effectively used in this area. The most common suitable light detector is the intensified Charge Coupled Device (iCCD) camera. Initially developed for military night vision purposes, these cameras provide a detector array needed for detecting the dispersed spectrum exiting the spectrograph, the fast gating for selectively detecting at the time of return of the Raman scattered photons and the necessary amplification. Figure 3.10 shows a simplified sketch of the working principle of an iCCD. The CCD chip itself consists of a two-dimensional array of elements (called pixels) on a silicon substrate. Each pixel is composed of metal-oxide semiconductor electrodes, called gates, which create potential wells storing electrons created by incident photons. The array is read out by shifting the electrons from gate to gate across the chip into a shift register consisting of an integrating capacitor and amplifier followed by an analog digital converter (ADC) for conversion into a digital and

Figure 3.10:

Illustration of the working principle of an intensified CCD camera. The photocathode creates an electron, which is accelerated towards the MCP. The MCP acts as spatially resolved secondary electron amplifier. Afterwards the electrons are accelerated toward a phosphor screen, where they are converted back to photons and detected by a cooled CCD.



computer-readable signal [71].

The gating and amplification occurs in the image intensifier tube, an evacuated tube, which comprises the photocathode, a Microchannel Plate (MCP) and a phosphor screen. The properties of these elements govern the performance of the device. The photocathode is usually coated on the inside surface of the input window, where when a photon of the image strikes, a photo-electron is emitted, which is then drawn towards the MCP by the applied electric field V_g . The MCP is a thin disc made of honeycomb-ordered glass channels, each with a resistive coating. A high potential V_i is applied across the MCP, which acts a secondary electron amplification unit (Figure 3.10, inset). The produced electrons will then be accelerated towards the phosphor screen. Gain in electron numbers in the range of 10^4 can readily be achieved. The degree of electron multiplication, and therefore gain, depends on the voltage V_i applied across the MCP. The output of the intensifier tube is coupled to the CCD by either a lens or a fiber optic coupler. Fiber coupled systems are physically compact with low optical distortion levels, high efficiency and in turn with better dynamic range. A lens has the advantage of allowing the image intensifier to be removed and having slightly better image quality. Gating in iCCD is facilitated by changing the potential V_g to either block or accelerate electrons produced by the photocathode. To achieve the desired fast gating a high voltage pulser must be used, which is able to create pulses (V_g up to 200 V) with sub-nanosecond rise and fall times. Typically, the time resolution of this kind of gating is limited by the physical extent of the intensifier unit. For example, during a 200 ps flat top gating pulse the light travels 6 cm, which is approximately the distance between the gating electronics and CCD sensor. Most commercially available iCCD cameras offer gating down to several hundreds ps. Very recently however, Cester et al. published a method to bring the time resolution down to 10 ps [72], which would open up a lot of new possibilities regarding the time-gated operation of stand-off Raman spectroscopy.

Typical gain for the MCP is reached with stable voltages range of 600 to 900 V. Acceleration to the phosphor screen is facilitated by applying voltages around 5-10 kV, depend-

Table 3.3: iCCD cameras used in the works presented in this thesis. Both devices were manufactured by Princeton Instruments.

| | <i>PI-MAX</i> | <i>PI-MAX 4</i> |
|--------------------|--------------------------------|--------------------------------|
| CCD format | 1024x256 px | 1024x1024 px |
| Pixel size | 26 μm | 13 μm |
| Gating | > 500 ps | > 500 ps |
| Intensifier | Gen II RB | Gen III Hbf |
| Phosphor | P46 ($\tau = 10 \text{ ms}$) | P46 ($\tau = 10 \text{ ms}$) |
| Quantum efficiency | 7.5 % @ 600 nm | 45 % @ 600 nm |

ing on the phosphor screen and tube type. The spectral response of an iCCD camera is primarily determined by the photocathode material. There are a number of intensifiers routinely used in the scientific applications (classified by military standards, known as generations and usually abbreviated with Gen). Gen I intensifiers are no longer in use and are therefore not treated here. Gen II intensifiers use Bi- or Multi-alkali photocathodes, also used for PMT operation. These are typically applied to quartz windows and allow reasonable response to extend into the UV region. The material composition and thickness can be altered to tune the wavelength response. Gen III intensifiers incorporate a semiconductor photocathode made from gallium arsenide (GaAs), which is only available on a glass, limiting the spectral response to the visible and NIR region. Gen III photocathodes [73] are very thin and delicate, prone to being poisoned by impurities in the image intensifier tube (impurity ions can be accelerated back from the MCP). Hence, a protection layer consisting of a thin coating of aluminum is often applied to the input of the MCP. To penetrate this barrier the photoelectrons must be accelerated by a much higher electric field, increasing the noise arising from the amplification process and posing a bigger challenge for the gating circuitry. These are known as Gen III filmed intensifiers. A Gen III filmless intensifier uses a photocathode material doped to optimize the response to particular wavelength ranges, sophisticated gating allows the use also without protective layer.

These intensifiers can be repetitively gated at rates of up to 500 kHz. Although the CCD section of the camera does not feature readout at this rate, there are advantages in operating the optical gating independently. A repetitive signal can be sampled and the output of the intensifier summed on the CCD to integrate an incoming signal, a technique used to generate quality spectra from the little amount of Raman photons gathered for each pulse. Another important aspect of these intensifiers is the choice of phosphor screen used for the conversion of electrons to photons. The standard phos-

phor is of P43 type and has a rather large time constant of 10 ms, meaning that if electrons hit the phosphor screen at any given time, light is emitted from the phosphor over the subsequent period of time. Faster phosphors, usually of type P46, have time constants of a couple of μs . Again, this is not a problem since we are accumulating pulses on the CCD, the same holds true for the phosphor screen. Generally, an iCCD camera has lower spatial resolution than a conventional CCD camera. This is again due to the properties of the image intensifier, where both the MCP and phosphor have major contribution to degrading the spatial resolution.

Noise and sensitivity of the iCCD is governed by the image intensifier [74]. There is still a dark current component originating from thermally generated charge in the photocathode and the CCD, which is generally cooled thermo-electronically to below -20°C . Although electron-multiplying Charge Coupled Device (emCCD) [75], with their additional gain registers to multiply electrons and thereby reduce the readout noise to absolute minimums, have conquered the field of continuous wave Raman instruments, they are not suitable for fast gated operation. Very recently however, combinations of emCCDs with intensifiers became commercially available, promising the best of two worlds, albeit with a considerable price tag.

In the works presented here two different iCCD cameras were used, their properties are summarized in table 3.3.

Vibrational spectroscopy as a tool in process analysis

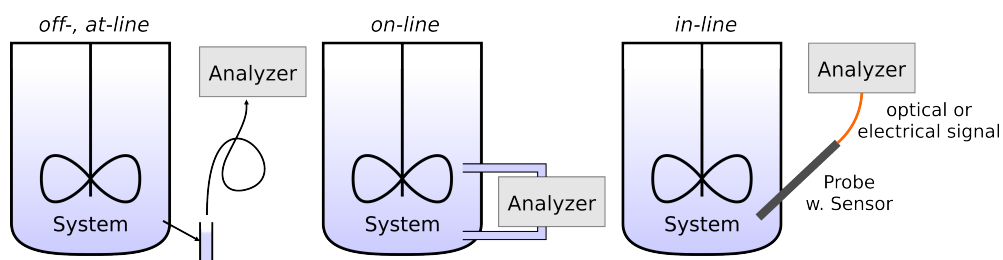
In the following sections a brief overview over analytical techniques based on vibrational spectroscopy and their use in analysis and monitoring of chemical processes will be given. Key concepts of Process Analytical Chemistry (PAC) and Process Analytical Technologies (PAT) will be explored and common implementation will be discussed. The properties of novel mid-infrared process sensors based on tunable Fabry-Pérot will be presented as well as their combination with a supercontinuum laser as a novel light source in the MIR region for enhanced liquid-phase ATR-IR spectroscopy. Additionally, the coupling of Laser Doppler Velocimetry (LDV) and Raman spectroscopy for simultaneous measurement of fluid velocity and chemical composition in a process stream will be discussed.

4.1 A brief introduction into process analytical chemistry

The field of PAC concerns itself mainly with the application of analytical chemistry for chemical processes [76]. The goal is the development of dedicated sensors, which are integrated into the process and deliver continuous and timely information about the state of the process. They do not only comprise the analytical technique itself, but also the calibration and mathematical modeling of the acquired data to derive a figure of merit needed for process control.

Figure 4.1:

Illustration of off-line, on-line and in-line chemical analysis of a process.



The standard approach to control quality in industrial manufacturing processes historically has been to test drawn samples of the final product for compliance with predefined quality criteria. The manufacturing process itself is conducted under a strict set of routine process parameters, commonly referred to as Critical Process Parameters (CPP) that have previously been validated by the manufacturer and approved by the respective authorities. For pharmaceutical and biotechnological processes the Food and Drug administration (FDA) [2] released a guidance report in 2004, where a framework for innovative pharmaceutical development, manufacturing, and quality assurance was presented, which included the use of PAT tools. Similarly to PAC, it considers PAT to be a system for designing, analyzing, and controlling manufacturing through timely and in-process measurements of Critical Quality Attributes (CQA), with the goal of ensuring final product quality. It is important to note that this should be a holistic approach, where PAT is also used to obtain an in-depth understanding of the fundamental workings of a process, for "quality cannot be tested into products; it should be built-in or should be by design" (center-point of Quality by Design (QbD)) [77]. This means creating a deeper understanding through PAC or PAT of the interconnection between CPPs (the cause) and CQAs (the effect). When this causality is known, the strict control of rigid process parameters is no longer necessary and a wider parameter space can be defined. Within these boundaries, product quality can still be assured by monitoring CPPs using suitable PAT or PAC technologies. The advantages of this approach are manifold. Variations in raw material quality can be linked to CQA of the product for a set of CPPs and the process can be guided to the desired product quality by adjusting to the right CPPs. Scrap rates can be significantly reduced by timely knowledge of the process state. Early intervention of the process control might still be able to achieve satisfactory product quality without the need of discarding the product.

An important aspect of PAC and PAT is sampling, which can be done in one of the following ways, as depicted in figure 4.1:

Off-line The sample is drawn at the production facility and analyzed in a dedicated laboratory with a lab-grade analyzer. Results are usually delayed significantly and are of limited use for process control.

At-line The sample is taken and analyzed in close proximity to the process plant. The analyzers here usually have to be more rugged or have to be protected by special housing. It is also of limited use when more than one point has to be sampled.

On-line The analyzer is directly connected to the process usually via a bypass system. Analysis can be performed continuously or in fixed timed intervals. The bypass system has to be designed to allow representative sampling.

In-line Direct contact of the sample with the sensor is facilitated usually via a dedicated probe, which is inserted into the reactor or process line. The analyzer is directly connected to the probe, both are required to be robust regarding the process environment.

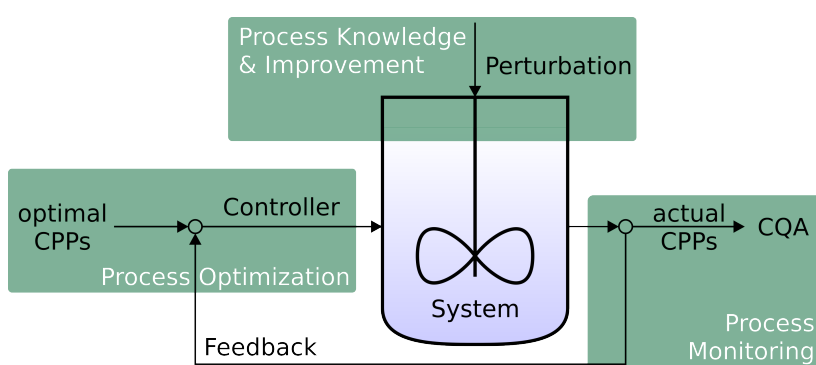


Figure 4.2:

PAT and QbD concept shown for a simplified batch reactor in pharmaceutical applications. CPPs and CQA are critical process parameters and critical quality attributes respectively.

One of the most crucial aspects, that sets these four types apart is the representativity of the taken sample. On one side this indicates that the taken or analyzed aliquot of the process does not differ from the rest, on the other a time delay or alteration because of sample handling, transport and preprocessing could falsify the result and make process control impossible. In this regard, on- and especially in-line implementation are preferable to off- or at-line analysis.

Additionally, in 2012 the German Government [78] declared its ambition in revolutionizing the manufacturing sector with innovative interconnected techniques and coined the term "Industrie 4.0", which is now often used to describe the latest developments in industrial manufacturing. The potential benefits of these developments are the high vertical and horizontal integrability, the individuality in manufacturing tailored products whilst keeping a competitive cost structure and the improved efficiency in both productivity and resource consumption. Creating such a manufacturing structure relies on novel and innovative sensors, which enable the precise and timely control of the process state as well as product quality. These sensors should be easily deployable, cost efficient and most of all, interconnected through standardized network interfaces. This requires a miniaturization of the sensor used for chemical analysis and integration into the process, allowing for real-time quality assurance, making extensive testing of the

final product almost unnecessary.

Several implementations of a wide range of analytical techniques as on- or in-line process analysis instruments exist. Workman et al. give an extensive overview over the topic in multi-issue reviews for the interested reader [79, 80], describing the use of chromatography, mass spectrometry and nuclear magnetic resonance for process monitoring, among others.

4.2 Infrared and Raman spectroscopy in PAC/PAT

At this point it is worth noting that spectroscopic techniques show ample potential for the implementation as process sensors, mainly because of the following reasons: First, they exhibit high selectivity, allowing for simultaneous multi-analyte detection with high sensitivity. Secondly, light can be coupled in and out of the medium of interest, without harming or altering the process. Since light is used to probe the sample, these sensors have very fast response times, making them suitable for detection of fast changes in the reactor. Lastly, they can be integrated into small instruments, capable of being deployed on-site without the need for chemicals or special requirements to perform the analysis. A well-established technique for in-line PAT application is NIR spectroscopy [81]. It offers the advantage of miniaturized spectrometers and a wide-spread availability of optical fibers for guiding the light in and out of the process. Additionally, NIR spectrometers exhibit a moderate price tag compared to MIR and Raman spectrometers. The drawback is certainly the more complex data analysis, which is almost exclusively based on multivariate approaches, since the bands in the NIR are very broad and prone to overlap.

MIR spectrometry mitigates this effect, because the fundamental vibrational transitions are located in this spectral region and as described in section 2.5 and table 2.1 MIR shows stronger absorption features, leading to an increased sensitivity compared to NIR. The disadvantage here are the more difficult instrumentation in terms of light source and detector, the poor availability of robust fibers and the generally higher cost compared to NIR spectrometers. Nevertheless, this spectral region has been the target of numerous applications in PAC and PAT [82, 83].

At last, Raman spectroscopy offers yet again a little different take on the integration of the technique into the process analysis. Since it is based on the scattering of light, in addition to probes and transmission cells, non-invasive measurements by remote collection of the scattered photons is possible. Since the 1980s, Raman spectroscopy has been used as a tool for process analysis for many applications, for instance polymorph identification, crystallization monitoring and real-time release testing [84]. The availability of stable laser sources, low-loss optical fibers, efficient volume holographic grat-

ings, and low-noise charge coupled device detectors enables robust commercial Raman spectrometers. This mitigates the sensitivity issues due to the low Raman cross section (see table 2.1). The benefit of combining Raman spectroscopy with other laser-based measurement techniques will be shown in section 4.4

4.3 Mid-infrared process sensors

In light of PAC/PAT considerations, the design principle behind the spectroscopic MIR sensors described in the following was a fit-for-purpose approach. The limitations of the presented tunable filter based instruments in terms of spectral resolution are offset by the careful definition of the problem at hand and selection of the right optical components. In this way, dedicated optical sensors could be constructed serving a predefined task, which they, upon testing and deployment in actual production plants, fulfilled in a most satisfactory way.

4.3.1 Filtometers using tunable filters

Filtometers can be constructed with a single bandpass filter, commonly using a stack of thin-film interference coatings on a transparent substrate to produce a spectral bandpass, which is tailorable in FWHM and central wavenumber by varying layer thickness and material choice. Although these filters are very efficient, it is seldom enough just to monitor one specific absorption band of target molecule, as variations in IR radiation power or changes in the sample matrix leading to overlapping bands will result in inaccurate concentration values. Therefore it is common practice to use more than one filter (creating a sample and reference channel) or to use tunable filters, where the central wavenumber of the transmission band can be moved through a certain wavelength region. The easiest implementation is to mount different bandpass filters onto a disk, which is rotated through the beam much like a chopper wheel (see figure 4.3). Similarly, by rotating a filter substrate out from behind a screen during the deposition of the different layers will create a wedge, along which the central wavenumber of the bandpass will change. This kind of filters are called Circular Variable Filter (CVF) [85]. The first filtometers based on such CVF and are still used for modern instruments e.g. for fast exhaust gas monitoring [86]. A simpler variant is to move the substrate linearly or to use a wedged substrate from the start. Then, Distributed Bragg Reflector (DBR) are used on the surfaces of the wedge to create a FP cavity with varying inter-mirror distance in one dimension. DBRs are usually created by stacking quarter-wave optical thickness layers

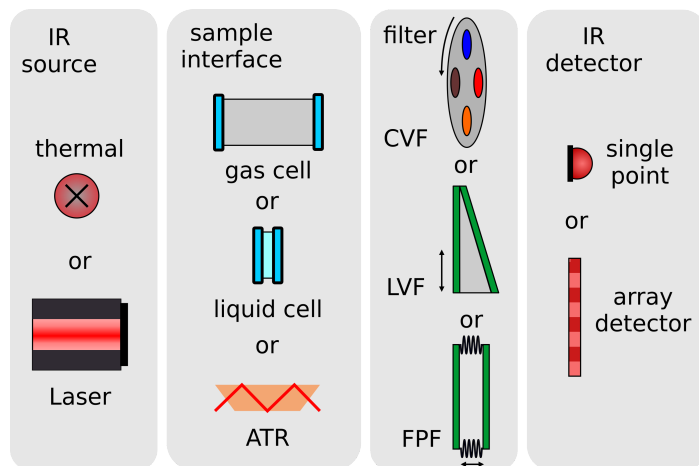


Figure 4.3:

An overview of components used and possible combinations of them for the integration in tunable filtermeter instruments.

with alternating low and high refractive index. This kind of filters are called Linear Variable Filter (LVF) and are used for all kinds of applications from the UV/Vis to IR spectral region. Here, a point detector can be used and the LVF is moved laterally through the beam. Alternatively, a linear array detector can be exploited, detecting the spectrum directly after the filter element. These types of filtermeters are currently produced for several applications, especially for hand-held, battery-powered instruments [87–89]. In figure 4.3 an overview over the different possibilities of combining light sources and sample interfaces with different types of tunable filters and detectors is given. The following section will go into more detail about the use of tunable Fabry-Pérot Filter (FPF) for MIR spectroscopy.

4.3.2 MEMS-based tunable FP-filter

MEMS and Micro-optical-electromechanical Systems (MOEMS) refer to functional machines or optical devices on the micron scale. Such devices became feasible once production was possible using popular modified semiconductor device fabrication technologies, normally used to produce electronics [90]. These fueled the idea of combining the whole optical setup of a typical spectrometer including interferometer, gratings, detector, source etc. into a monolithic silicon-based design, allowing for highly integrated optical sensors [91]. One of the innovations of the last years is the integration of a MEMS based tunable FPF into a IR pyroelectric detector. Here, the tuning of the resonator cavity is achieved by either electro-static or piezo-electric actuation using a parallel plate design. A thorough review of tunable FPF filter applications is given by Ebermann et al.[92]. Electro-static actuators are the most common micro-machined drives based on the fact that they are easily integrated in the micro-machining process [6]. The basic design of the tunable FPF with integrated detector is shown in figure

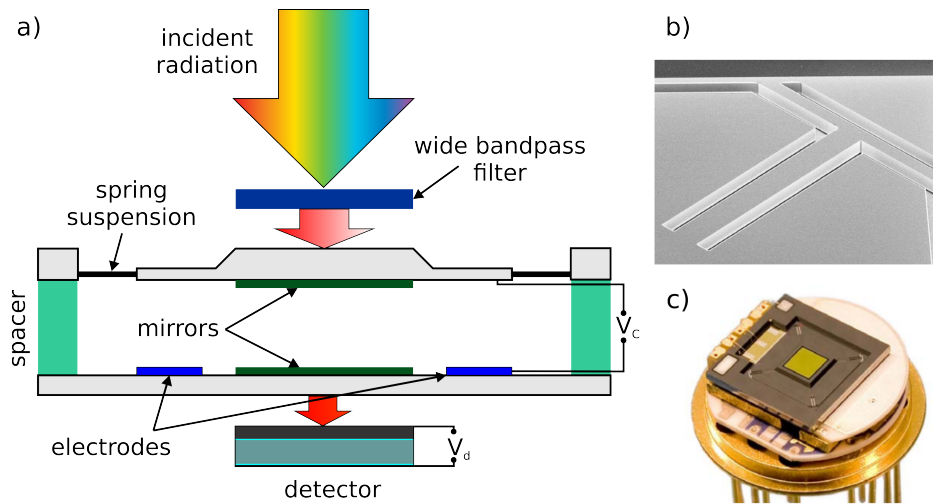


Figure 4.4: **a)** Illustration of the working principle of the MEMS based tunable FPF with integrated detector. **b)** SEM image of the diagonally stress-compensated springs of the mirror suspension. **c)** Photo of the whole optical and electrical structures packaged in a TO-8 housing.

4.4. For the work presented in this thesis, tunable FPF with integrated detectors built by Infratec GmbH were used, where $300\ \mu\text{m}$ thick silicon substrate layers act as reflector carriers, one of them being fixed and the other suspended by springs which allow vertical movement. The fixed reflector is equipped with driving electrodes. The movable reflector is suspended by diagonally arranged springs located in the corners of the outer frame (see figure 4.4b). The optimum spring geometry includes maximum tuning range, low gravity influence on center wavelength and filter bandwidth, low deviation of reflector parallelism by mechanical stress and low fabrication complexity. Both are connected via a spin-coated SU-8 layer, which can produce accurate layer thicknesses by adjusting the rotation speed of the spinning during coating.

The DBRs require to have a broad high reflective zone in the MIR region, achieved with a low stack number. Hence, thin films with as high as possible refractive index ratios between them have to be applied. Silicon dioxide with a refractive index of 1.38 at $4\ \mu\text{m}$ is used as low refractive index material and polycrystalline silicon with a refractive index of 3.33 at $4\ \mu\text{m}$ is used as high refractive index material for the reflectors. With the high ratio of refractive indices, a high-reflective region in the desired spectral zone with an average reflectance of 95 % was obtained already with a double layer stack. The backsides of the silicon substrate were anti-reflection coated to reduce reflection losses with a triple-layer of silicon dioxide and polycrystalline silicon. The following infrared detector is a pyroelectric LiTaO_3 element like described in section 3.1.2 directly hooked up to a transimpedance amplifier. A second equal element, which is connected anti-

parallel and shielded from the radiation, compensates variations due to temperature changes of the surroundings and of the package without reducing the responsivity. A low noise, low power operational amplifier converts the pyroelectric current into a high signal voltage. The whole stack is packaged into a standard TO-8 housing. An additional broad bandpass filter transmits only the interesting order of the transmission of the FP and provides the necessary out-of-band blocking.

4.3.3 Characterization of the tunable FPF-detectors

The tunable filters presented in the previous section are commercially available from the German company InfraTec GmbH. They are available for different regions in the MIR spectrum, table 4.1 summarizes all their properties. During the work in this thesis, these products were also developed towards more user-friendly application by adding an Application-Specific Integrated Circuit (ASIC), which has all the calibration of central wavenumber to control voltage applied to the electrostatic actuator of the tunable FP stored and can be used by sending the target wavenumber via an Universal Asynchronous Receiver-Transmitter (UART) interface.

Before, the dependence of the spectral position of the transmission band of the tunable FPF on the applied control voltage had to be determined. In order to do so, a Bruker Vertex 80v FTIR spectrometer was used, since it offers an external channel, where the light passing the interferometer can be redirected onto the tunable FPF detector. For focusing an off-axis parabolic mirror with a focal length of 156 mm was employed. An aperture of 4 mm was set and 8 scans were averaged per measurement. The scanner frequency of the FTIR was lowered to 1.6 kHz to accommodate the time constant of the pyroelectric detector element. For the analog types of the FPFs the electro-static actuators were controlled via a 0-10 V DAC (NI-9263) promoted to the required control voltages reaching as far as 70 V via a self-built voltage multiplier. The output voltage of the detector element was digitized using an auxiliary ADC of the Bruker FTIR. Figure 4.5 illustrates the setup for the characterization of the tunable FPF detectors. To calculate the transmission, a reference measurement using the same parameters but with a pyroelectric detector of the same type (LME-337) without filter was done. Figure 4.6a shows typical transmission bands from the filters when different control voltages are applied. Figure 4.6b shows the correlation of central wavenumber position and applied voltage as well as FWHM at the respective positions for the LFP5580 spanning a spectral region from 1250 to 1800 cm^{-1} . To check for stability of the FPFs, continuous measurements were undertaken for more than 15 hours. The results are depicted in figure 4.6c and show no greater variation than 0.2 cm^{-1} at either central position and FWHM, which is negligible considering the general broadness of the transmission fea-

Table 4.1: Overview over the specifications for the commercially available tunable FPFs with integrated pyroelectric (and photon) detector.

| | <i>XFP-3137</i> | <i>LFP-3144</i> | <i>LFP-3850</i> | <i>LFP-5580</i> | <i>LFP-80105</i> |
|--|-----------------|--------------------|--------------------|--------------------|--------------------|
| Tuning / cm^{-1} | 3225-2700 | 3225-2270 | 2630-2000 | 1800-1250 | 1250-950 |
| FWHM / cm^{-1} | 25-18 | 56-35 | 41-29 | 32-20 | 20-19 |
| Det. type | PbSe | LiTaO ₃ | LiTaO ₃ | LiTaO ₃ | LiTaO ₃ |
| τ / ms | 1 | 150 | 150 | 150 | 150 |
| D^* / $\text{cm Hz}^{0.5} \text{W}^{-1}$ | 2×10^7 | 3.6×10^6 | 3×10^6 | 4.8×10^6 | 4×10^6 |

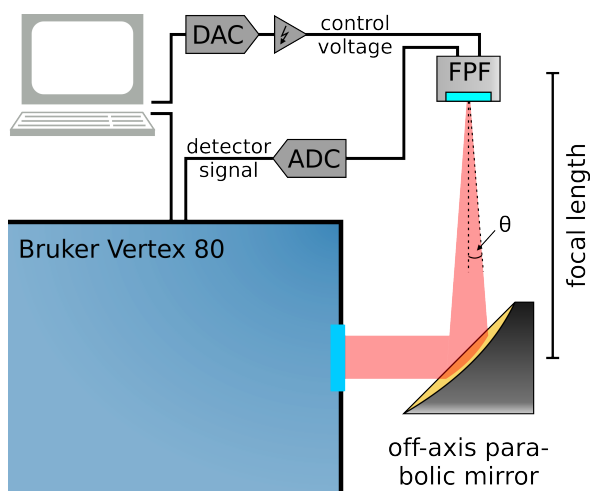


Figure 4.5: Illustration of the setup for characterization of the FPF detectors. The investigations about different focused cone angles was performed by changing the focal length of the off-axis parabolic mirror.

Table 4.2: Reposition stability of the tunable FPF LFP5580 when the same four control voltages are applied multiple times in random order. σ is the standard deviation of the central wavenumber and FWHM, respectively.

| $U_{\text{Control}} / \text{V}$ | $\tilde{\nu}_{\text{Center}} / \text{cm}^{-1}$ | $\sigma_{\text{Center}} / \text{cm}^{-1}$ | $\sigma_{\text{FWHM}} / \text{cm}^{-1}$ |
|---------------------------------|--|---|---|
| 0 | 1296.6 | 0.053 | 0.101 |
| 5 | 1387.6 | 0.059 | 0.146 |
| 7 | 1528 | 0.045 | 0.106 |
| 8 | 1689.5 | 0.048 | 0.151 |

tures with a mean FWHM of 35 cm^{-1} . The stability of the spectral positions of the FPFs was further investigated by changing the control voltage between four different values for ten times each at a randomized order. Subsequently, the center position and the FWHM of each transmission band were determined and the standard deviation σ was calculated. The results are summarized in table 4.2. Again, the stability of the filter after switching between transmission positions is adequate, although it is imperative to use a settling time after the switch before recording of data, in order to let the filter reach stable position. This was determined to be at least 150 ms.

As mentioned in section 3.1.5, the transmission characteristics of a FP cavity changes when instead of perfectly collimated rays a focused beams is employed. Basically, all angles present in the focused cone are allowed to pass, therefore creating a transmission band and featuring a broader FWHM, but also better intensity. To test different incident angles, off-axis parabolic mirrors with focal lengths of 65, 101.6 and 152.4 mm have been used, resulting in maximal incident angles θ of 6.2° , 4° and 2.7° (given a FTIR output beam diameter of 14 mm), respectively. The results of this study are depicted in figure 4.6d. It shows the importance of choosing the right NA when focusing on the tunable FPF. Depending on the application, the change in spectral resolution (a broadening of the FWHM of 1.4 cm^{-1} per degree) will affect the spectral resolution of the instrument. On the other hand, focusing on the detector is essential for generation of adequate signal intensity, important for a sufficient SNR.

4.3.4 Compact gas sensing

The general build-up of the filterometers used in this thesis is depicted in figure 4.7. The gas cell usually consisted of a steel cylinder tube (10 to 30 cm long) equipped with a gas input and output port with the faces of the cylinder closed by IR-transparent windows.

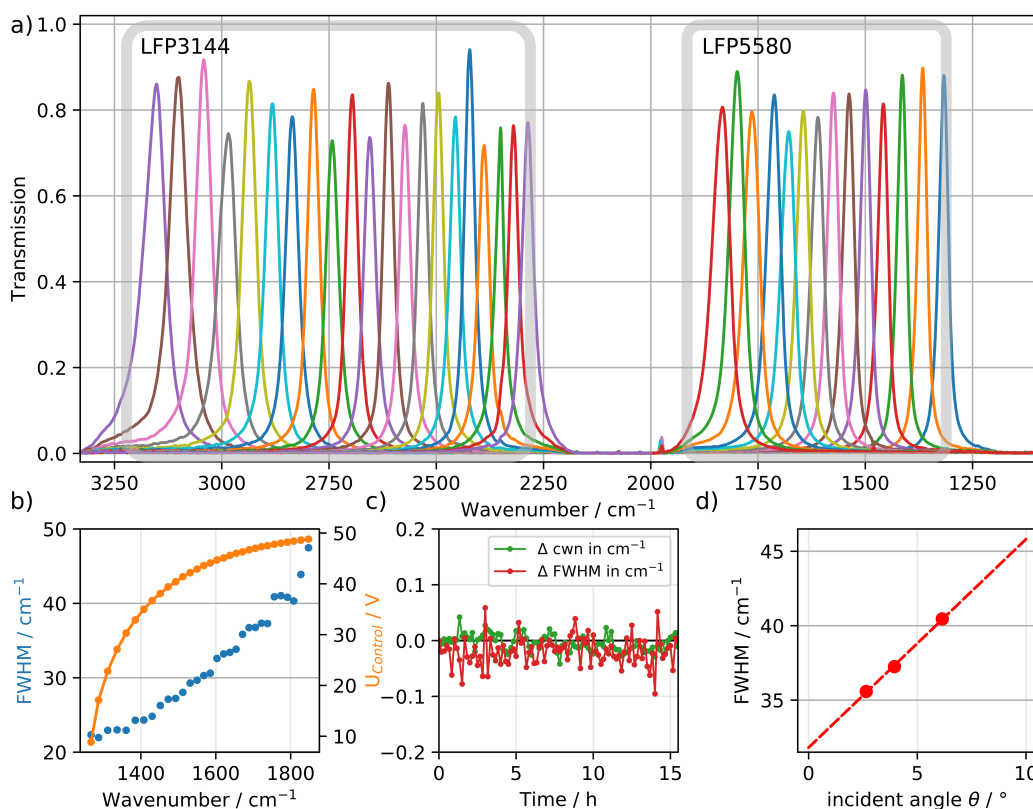


Figure 4.6: **a)** Measured transmission for LFP5580 and LFP3144, when different control voltages are applied. **b)** Tuning behavior of the LFP5580: central wavenumber in dependence of the applied voltage and the change of FWHM with different spectral positions. **c)** Temporal stability of the filter while on a fixed position. The change in central wavenumber and FWHM is plotted in respect to the first measured value. **d)** Change in mean FWHM of the LFP5580 when different mirror focal lengths are used (resulting in different half-angles θ) for focusing on the detector.

The window material was chosen to exhibit appropriate transmission for the spectral region of interest, most often CaF_2 or, if the region under 1000 cm^{-1} had to be measured ZnSe windows were employed. The same holds true for the lenses used to collimate the light beam emitted by the thermal light source and to focus the light back onto the detector after passing the gas cell. Care has to be taken by choosing the focal length of the second lens, since it will influence the spectral resolution of the tunable FPF, as discussed in section 4.3.3. One of the most important aspects is the IR radiation source. Briefly mentioned in section 3.1.1, we employ a pulsed thermal emitters, that can be electrically modulated. Additionally, these emitters usually have a parabolic reflector on top of the TO-39 case, which gives a already directed beam that can easily be collimated and subsequently focused on the detector. The electrical ratings are sufficiently

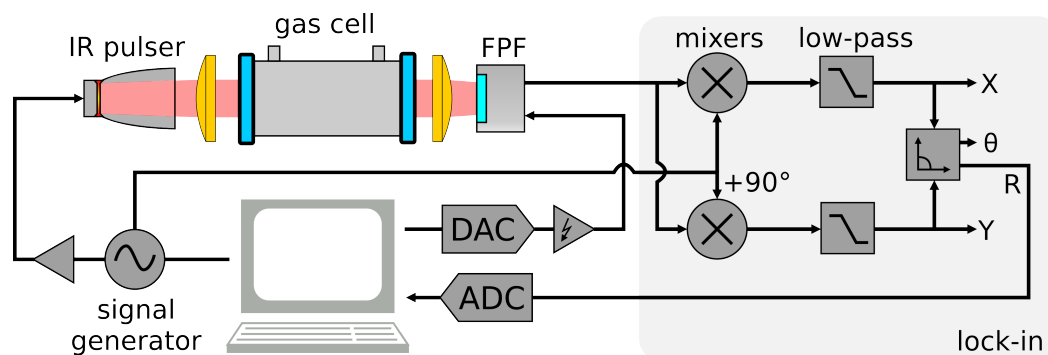


Figure 4.7: Illustration of the optical and electrical setup for the measurement of gas phase components in transmission.

low to keep the requirements for the electronics small, with the maximal voltage at approximately 5 V and no higher current than 100 mA.

Similar to the characterization of the tunable FPF, the analog versions are driven by a DAC (NI-9263) with subsequent voltage multiplication to reach the specified rating for driving the electrostatic actuator in the FPF detector (up to 70 V). For the versions with integrated ASIC, this simplifies to just providing a stable high voltage input. The amplitude (R) of signal output of the detector element inside the FPF is detected using lock-in amplification. Lock-in amplifiers use the knowledge about a signal's time dependence (by knowing the modulation of the signal) to extract it from noisy background. Essentially, the lock-in amplifier takes the detector signal, multiplies it by the reference signal (in this case given by the pulser used for driving the thermal emitter) and integrates it over a specified time. This results in a DC signal, where the contribution from any signal that is not at the same frequency as the reference signal is attenuated drastically [93]. Figure 4.7 illustrates the working principle of the lock-in amplifier with subsequent digitalization of the lock-in detected output signal. The control of all the parts needed for this filterometer can be conveniently facilitated by the use of modern microprocessors based on Central Processing Unit (CPU)s like the Atmel SAM3X8E ARM Cortex-M3 used in the Arduino Due. The modular and easy usability of the Arduino framework allowed the construction of a stand-alone spectroscopic sensor, which was capable of performing the measurement, acquire new background spectra whenever needed, control valves for gas handling and to give out the actual measured parameter to a connected process control system. The addition of a Raspberry Pi in combination of a Wide Area Network (WAN) module allowed for the remote checking of sensor functionality, data transmission and continuous remote improvement of the measurement parameters. This is all in accordance with the concepts of industry 4.0 and PAT, satisfying the need for both a selective chemical sensing and seamless integration into the process control system as well as the process itself.

Absorbance measurements are performed by changing the spectral position of the filter, wait for the filter to reach stable position (settling time) and measure the light intensity as detected with the pyroelectric element (here also averaging may be used to improve the SNR). Stepping through the whole spectral region covered by the tunable FPF allows to gather single-channel spectra, which in turn can be used for the calculation of absorbance spectra. Background spectra were acquired after the gas cell was automatically purged with nitrogen. The time it takes to perform a full scan is therefore a sum of the extent of the spectral range, the chosen step size, settling and integration time at every spectral position. Depending on the magnitude of these factors, acquiring a spectrum can lead to measurement times from several seconds up to tens of minutes. Another possible mode of operation is the continuous sweep of the FPF over the whole spectral range. This makes the settling wait obsolete, as the filter is moving back and forth constantly. This mode is especially useful, if the transmission in the spectral range of FPF has a steep drop-off at one or either end (due to e.g. sample or window absorption). Then, an inherent modulation is also obtained and the thermal emitter can be used in constant heated mode.

As mentioned in section 2.3.1 the concentration of a component can be linearly linked to its absorbance (Beer's law, equation 2.9). However, in practice, the absorption coefficient of the component of interest is not known, hence a calibration step is necessary to link species concentration to the absorbance. After collection of spectra of different concentrated samples, either the height or preferably the integral of a characteristic band of the analyte can be used to determine its concentration. In the simplest case with the tunable FPF, the filter can be positioned on a spectral position where no absorbance (baseline) is observed and then moved to the band of interest, the resulting difference is then a measure for the concentration of the investigated component. This is only the case, if characteristic band of compounds of interest are well isolated (see Publication I). If however, multiple components are present, bands attributed to different substances present in the sample can overlap, making the classical calibration impossible. In this case, multivariate calibration and processing algorithms have to be implemented (see Publication II).

In summary, the combination of the tunable FPF with an integrated detector and the pulsed thermal emitter allow for a spectroscopic sensor, which features high selectivity and sensitivity, robustness, compact size, low electric requirements and smart control features, all at very moderate cost. Compared to process FTIRs, which are still somewhat bulky, electronically more complex, have moving parts and are generally more expensive, these kind of filterometers or chemical sensor show great potential for use on a multitude of different processes. Their size makes them easily integrable, which can lead to a decentralized interconnected web of multiple sensors monitoring any given process and make timely, precise control and optimization of the production process

possible. Publication I shows that for the integration of the developed sensor into a real industrial process, namely the production of formaldehyde through catalytic oxidation over metal silver. Here, two process off-gas components, the by-product methyl formate and the educt methanol were continuously monitored for up to five different reactors with a time resolution of a couple of seconds. Publication II shows how these filterometers can also be used for the analysis of multiple component mixtures using multivariate calibration and modeling.

4.3.5 Enhanced liquid-phase sensing

MIR spectra in the liquid phase typically exhibit much broader band shape due to interactions between close molecules, thus meeting the mediocre spectral resolution of the tunable FPF. Liquid phase IR spectroscopy is therefore more suitable for the use of spectroscopic sensors with reduced spectral resolutions compared to gas phase spectroscopy. The optical setup does not change much compared to the gas setup shown in figure 4.7, except for the gas cell, which is switched for a transmission cell, in which the fluid is passed. One problem associated with transmission cells is their thickness, which is of course also the optical path-length. For highly absorbing fluids, most and foremost water, optical thicknesses of $< 10 \mu\text{m}$ have to be employed [31, 32]. Such transmission cells suffer from several drawbacks, mainly their instability due to pressure change while the liquid is pumped and the affinity to clog or collect and persistently maintain air bubbles at the measurement window. It is a tedious process designing and using such thin flow cells, especially if they should be used in an industrial by-pass measurement. A more elegant solution is to use ATR IR spectroscopy, which was already discussed in section 2.3.3. It allows for the construction of an inline setup, where the probed liquid flows over the ATR crystal. The motivation behind the design and construction of an inline ATR probe for the detection of hydrogen peroxide (H_2O_2) was a novel approach in the desulfurization of biogas. Biogas, which mainly is methane, is produced out of agricultural waste or surplus by decomposition of the available biomass with help of micro-organisms. The thereby produced gas contains a lot of different components, with the most unwanted being dihydrogen sulfide (H_2S). It has to be removed from the biogas before it is inserted into the gas pipelines because of its negative traits, like exhibiting strong odor, toxicity, its corrosive nature and the negative environmental influence. Among other techniques, H_2S in the raw biogas can be removed by oxidative scrubbing, which has recently been developed [94]. Here, dihydrogen sulfide is absorbed into a caustic solution and subsequently oxidized to elemental sulfur and sulfate using hydrogen peroxide as an oxidizing agent. High selectivity towards H_2S removal is achieved and carbon dioxide absorption, which would lead to the consumption of high

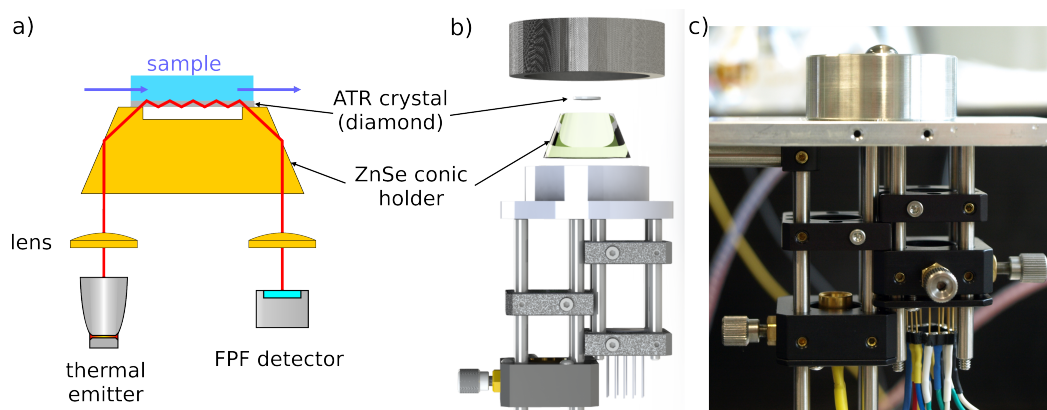
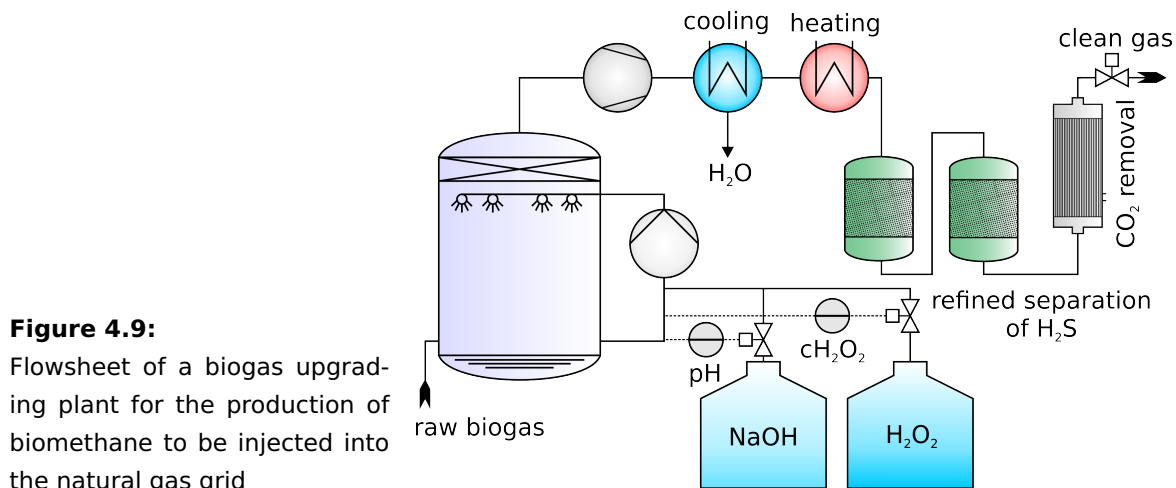


Figure 4.8: **a)** Illustration of the designed ATR optical setup with diamond as the ATR crystal and a ZnSe truncated cone as support and focusing element. **b)** 3D rendering of an exploded view the setup during the planning. **c)** Built prototype with a droplet of water on top.

amounts of caustic solution, is minimized. As a result, this desulfurization process is extremely flexible to fluctuations of operational parameters like gas flow and H_2S content. Additionally, process scaling is straight forward, which makes this process also usable in smaller biogas facilities, allowing for a more distributed production network [95]. Figure 4.9 shows the most essential parts of such a plant. For best achievable H_2S removal at the first gas scrubber, the hydrogen peroxide concentration has to be monitored constantly with a good temporal resolution and precision. Since the end-user application would be rather large scale, a transmission cell featuring a small optical pathlength was rejected. Instead, an ATR sample interface was chosen to be better integrable. Usually, ATR elements are trapezoidal slabs of crystal, which require the coupling of the light at the side faces. Here, it was decided to go a more robust route by using a beam focusing element, which also acts as mechanical holder and fixed angle coupler for the ATR element. Due to its mechanical and chemical stability, diamond was chosen as material for the ATR element. It features a refractive index of approximately 2.4 and can be produced via Chemical Vapor Deposition (CVD) in single crystal form with sizes up to several millimeters. The focusing element is made out of ZnSe, which features a very similar refractive index as diamond and can be matched quite easily. Figure 4.8a and 4.8b shows an illustration (and a CAD rendering) of the optical setup. The diamond disc is glued onto the stainless steel carrier, which is then positioned on top of the ZnSe element. This configuration minimizes space requirements by directing the beams parallel to each other to the back, where radiation source and detector can conveniently be placed.

H_2O_2 has two distinct bands in the MIR spectrum, one is the deformation band of O-H at approximately 1350 cm^{-1} and the other main band is located at approximately



2820 cm^{-1} , belonging to the O-H stretch vibration [96]. The O-H stretch vibration spectral region was found to be better suited for determination of hydrogen peroxide due to the absence of interferences from other constituents. The whole setup was optimized to work around that specific band, this process is described in [97] in more detail. The concentration range of interest is 0.1 to 10 % H_2O_2 content in the caustic washing fluid. The optimal ratio between light throughput and sensitivity could not be reached with a single reflection at the ATR-sample interface (often referred to as bounce). For such situations, it is possible to use a larger ATR element, facilitating more than one bounce and hence increasing the effective thickness. Here, we use a total of 4 bounces. Again, the light radiated by a pulsed thermal emitter was focused into the ATR element and the exiting beam was redirected and focused onto the detector. Although diamond absorbs light between 1800 and 2500 cm^{-1} and the O-H vibration of water forms intense absorption features starting at 3100 cm^{-1} , this ATR configuration has a suitable measurement window for the stretch vibration of H_2O_2 (depicted in figure 2 of Publication III). Hence, quantification of H_2O_2 in solution was possible by just integrating the band and performing univariate calibration (depicted in figure 6 of Publication III).

The biggest downside to ATR spectroscopy is the small effective thickness, which was overcome by using more reflections or bounces. This will inherently affect signal quality, as with every bounce signal intensity at the detector will drop due to absorption and scattering at every interface. With commonly used thermal emitters having a large beam diameter, it is often challenging achieving high optical throughput. Laser sources might be the solution to this problem. Recently, an interesting type of laser is spearheading into the MIR region: the supercontinuum laser (SCL) device. Here, light from a seed laser is converted through non-linear processes in optical fibers and produces a wide emission spectrum. These lasers were discussed in more detail in section 3.1.1.3 and are perfectly suited to the spectral range of the tunable FPF, since the spectral

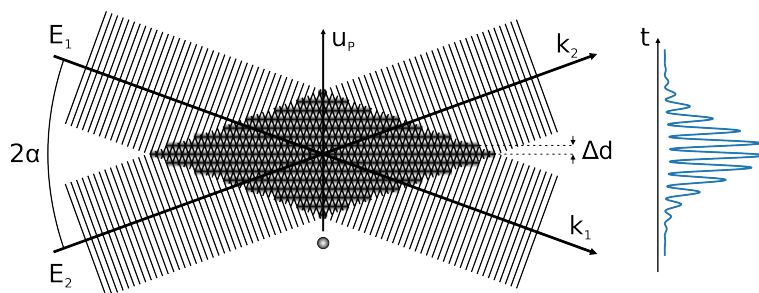


Figure 4.10:

Two beams of equal intensity and wavelength crossing at an angle 2α , creating a fringe pattern with a spacing of Δd . To the right, a typical Doppler burst is shown, i.e. the scattered intensity of a particle moving through the intersecting beams.

position of the absorption band of H_2O_2 is covered in the emission region. The SCL was therefore a perfect match as a high intensity light source for the multi-bounce ATR filometer. The resulting paper (see Publication III) was one of the first shown chemical sensors employing these kind of sources. The intensity at the detector could be substantially improved and the polarized light exiting the SCL enables sensitivity adjustment of the ATR setup by simply rotating the polarization fo the SCL radiation. Recently, the spectrum of applications was widened to stand-off detection [98], imaging using a tunable filter and a micro-bolometer-array [99] and is, hopefully, steadily growing.

4.4 Raman spectroscopy and Laser Doppler Velocimetry

Laser Doppler Velocimetry (LDV) is a laser based measurement technique, which uses the Doppler shift of the reflected light to determine the velocity of fluid flows. Pioneered in the early 1960s [100], it is an established technique for flow research, automation and medical applications [101]. Due to the close cooperation with the institute of chemical engineering at TU Wien, the idea of combining Raman and LDV for simultaneous determination of the flow characteristics and flow composition was born and first experiment followed in suite.

4.4.1 Laser Doppler Velocimetry

Here, a brief introduction into the working principles of LDV will be given. One possibility to describe an LDV experiment is the fringe model [102]. It assumes two plane light waves of equal field amplitudes (E_1, E_2) and frequencies propagating along their wave vectors (k_1, k_2) and intersecting at an angle 2α (see figure 4.10). They superimpose, forming fringe pattern with a fringe spacing of Δd

$$\Delta d = \frac{\lambda}{2 \sin \alpha} \quad (4.1)$$

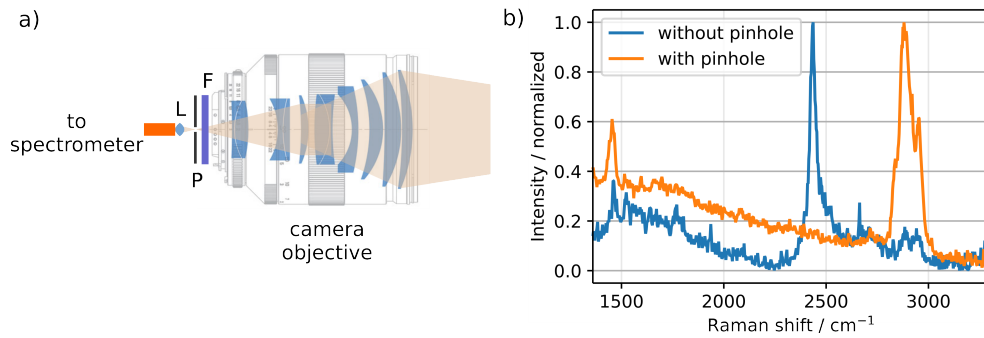


Figure 4.11: **a)** Illustration of the optical setup of the Raman receiver. F...Rayleigh filter, P...pinhole, L...matching lens. **b)** Spectra acquired from a polypropylene target with and without pinhole.

with λ being the wavelength of the beams. If a particle with a diameter smaller than the fringe spacing passes through the measurement volume, the reflected light will create a reflection pattern known as Doppler burst, which is also depicted in figure 4.10. The Doppler burst can now be used to derive the velocity component (the projection perpendicular to the fringe pattern) of the passing particle with

$$u_p = \Delta d \cdot \nu_D \quad (4.2)$$

where ν_D is the Doppler frequency, which can be interpreted as the spacing of the sinusoidal oscillation in the Doppler burst. Due to the laser beams usually exhibiting a Gaussian intensity distribution, the maximum of the Doppler burst is found when the particle passes the center of the measurement volume. When more than one direction in space is to be monitored, a second pair of beams perpendicular to the first beam pair is employed with a shifted wavelength. A dedicated set of detectors, equipped with filters only letting the reflected light attributed to one pair pass, is used to discriminate between the directions. Additionally, often a small wavelength shift between the two beams of a pair is introduced, creating not a static, but a moving fringe pattern. This way, also particles having the same velocity, but opposite flow directions can be distinguished.

4.4.2 LDV-Raman Coupling

Combining LDV and Raman spectroscopy can be challenging, for several reasons. First of all, the employed LDV setup used two wavelengths (488 and 514.5 nm) for probing the measurement volume. This leads to two overlapping Raman spectra of a single compound, because there are two excitation beams in close spectral proximity. To block both laser lines, a edge-filter for the 514 nm laser was used, which blocks also the first

1000 cm^{-1} of the 488 nm Raman spectrum. In figure 6 of Publication IV the Raman band of the O-H stretch vibration can be seen at 2900 cm^{-1} (attributed to the 514 nm) and again at 1900 cm^{-1} (attributed to the 488 nm). This can lead to complications in the analysis of mixtures with several components, as the amount of overlapping bands in the Raman spectrum will be doubled. Secondly, the collection optics had to be adapted to suit the working distance of approximately 0.5 m. Here, a standard zoom objective was used as a variable collection optic. The problem with using lens based collection optics is the backscattered Rayleigh light will create Raman scattering in the lens with an intensity high enough to mask the signal from the intended target. One possibility to solve this issue is to use an edge-filter large enough in size to cover the aperture of the objective, which although possible, is a very costly option. A better approach is to use a confocal concept. A pinhole is introduced into the optical path (see figure 4.11a), which blocks all the light scattered at the lens surfaces or within the objective and lets only photons scattered at the working distance pass into the fiber coupled spectrometer. The effect is shown in figure 4.11b as a comparison of measured spectra with and without pinhole.

The objective was mounted in a perpendicular fashion to the LDV probe head and was fiber-coupled to a standard Czerny-Turner spectrograph. The light was detected using the PI-MAX iCCD described before. Alignment of the LDV measurement volume and the Raman spectrometer was done with a custom built rectangular calibration cell. Both collection optics were mounted on a computer controlled traverse system, which facilitated the movement of the measurement volume through the designed flow system. The whole experimental setup is depicted in figure 2 of Publication IV. After the traverse reached a stable position, both LDV and the Raman spectrometer commenced data acquisition. The proof of principle experiment included a T-mixing channel of rectangular geometry (Figure 3 in Publication IV), where water entered the channel from the straight inlet and ethanol entered the channel from a side inlet. Both fluid streams passed a stratifier for laminarization of the flow. This provided better boundary conditions for simulations before reaching the mixing zone. Validation of the concentration and flow regime was performed with Computational Fluid Dynamics (CFD), which allows the numerical analysis and simulation of process flows.

The innovation in this project was the first-time use of one laser system for both LDV and Raman measurements, which ensured data acquisition from the exact same spot and allowing for simultaneous determination of flow characteristics and process flow composition. This work resulted in a granted patent titled "Methods for the contactless determination of flow parameters and analytes within the flow" and Publication IV, where it is discussed in more detail.

4.5 Publication I: On-line monitoring of methanol and methyl formate in the exhaust gas of an industrial formaldehyde production plant by a mid-IR gas sensor based on tunable Fabry-Pérot filter technology

Authors: Andreas Genner, Christoph Gasser, Harald Moser, Johannes Ofner, Josef Schreiber and Bernhard Lendl

Published in: *Analytical and Bioanalytical Chemistry*, January 2017, Volume 409, Issue 3, Pages 753–761

Status: Published

Reprinted with permission CC BY <https://doi.org/10.1007/s00216-016-0040-9>

Short summary:

This paper is centered around the design and application of a cost-efficient gas sensor for online monitoring of methyl formate and methanol in the gas phase of a formaldehyde production plant using tunable FPF. After careful selection of the interesting spectral region ($950\text{--}1250\text{ cm}^{-1}$) and identification of the suitable tunable FPF (LFP80105), a direct absorption instrument was built employing a temperature controlled gas cell with a length of 30 cm.

The sensor system was calibrated in the research laboratory at TU Wien for measuring both components in the concentration ranges from 100 to 5000 ppmV. The achieved Limit Of Quantification (LOQ) were 184 ppmV and 165 ppmV for methanol and methyl formate, respectively. Subsequently, the prototype was transferred and installed at the industrial project partner Metadynea Austria GmbH and linked to their Process Control System (PCS) (through a 4-20 mA interface) via a dedicated micro-controller and used for on-line monitoring of the process off-gas. Up to five process streams were sequentially monitored in a fully automated manner. The obtained readings for the component concentrations provided useful information on the state of the process plant. Of special interest for industry is the now added capability to monitor the start-up phase and process irregularities with high time resolution, allowing for optimized process control during all phases of production. The timely monitoring of key chemical constituents in an industrial production plant ensures economic operation, guarantees the desired product quality and provides additional in-depth information on the involved chemical processes. The developed sensor delivers rapid, rugged and flexible measurement at very moderate cost.

Here, we present the system design, calibration and implementation into the industrial process as well as several hours worth of process monitoring.

On-line monitoring of methanol and methyl formate in the exhaust gas of an industrial formaldehyde production plant by a mid-IR gas sensor based on tunable Fabry-Pérot filter technology

Andreas Genner¹ · Christoph Gasser¹ · Harald Moser¹ · Johannes Ofner¹ · Josef Schreiber² · Bernhard Lendl¹

Received: 26 July 2016 / Revised: 10 October 2016 / Accepted: 18 October 2016 / Published online: 9 November 2016
© The Author(s) 2016. This article is published with open access at Springerlink.com

Abstract On-line monitoring of key chemicals in an industrial production plant ensures economic operation, guarantees the desired product quality, and provides additional in-depth information on the involved chemical processes. For that purpose, rapid, rugged, and flexible measurement systems at reasonable cost are required. Here, we present the application of a flexible mid-IR filterometer for industrial gas sensing. The developed prototype consists of a modulated thermal infrared source, a temperature-controlled gas cell for absorption measurement and an integrated device consisting of a Fabry-Pérot interferometer and a pyroelectric mid-IR detector. The prototype was calibrated in the research laboratory at TU Wien for measuring methanol and methyl formate in the concentration ranges from 660 to 4390 and 747 to 4610 ppmV. Subsequently, the prototype was transferred and installed at the project partner Metadynea Austria GmbH and linked to their Process Control System via a dedicated micro-controller and used for on-line monitoring of the process off-gas. Up to five process streams were sequentially monitored in a fully automated manner. The obtained readings for methanol and methyl formate concentrations provided useful information on the efficiency and correct functioning of the process plant. Of special interest for industry is the now added capability to

monitor the start-up phase and process irregularities with high time resolution (5 s).

Keywords Formaldehyde production · Fabry-Pérot detector · Mid-infrared · Process analytical chemistry · Methyl formate · Methanol

Introduction

In process analytical chemistry (PAC), there is clear focus on providing dedicated solutions to a given measurement problem. In this regard, emphasis is put on different parameters/features with respect to laboratory equipment. Depending on the installation, in PAC, a number of requirements have to be met. This can involve robustness against environmental conditions (e.g., humidity, vibration, chemical substances in the air), a simple user interface (soft- and hardware), avoiding sample preparation, autonomous operation, and the possibility to forward the gained measurement data to a control center (e.g., Modbus, OPC, 4–20 mA signal [1, 2]). Over the time, many analytical techniques were adopted, optimized, and successfully integrated in industrial processes. The range of different instrumental techniques that were brought on-line includes not only a broad variety of measurement principles such as conductivity-, pH-, and particle-sensors but also highly optimized gas chromatography systems, advanced mass spectrometers, and alike [3, 4]. However, if possible, simple and rugged, sensor-like solutions are the preferred way for efficient on-line monitoring with high time resolution.

A well suited measurement principle for analyzing process streams in the gas phase is infrared spectroscopy. Almost every gaseous analyte (except noble gases and homonuclear diatomic molecules) absorbs radiation in the mid-infrared

Published in the topical collection *Process Analytics in Science and Industry* with guest editor Rudolf W. Kessler.

✉ Bernhard Lendl
bernhard.lendl@tuwien.ac.at

¹ Institute of Chemical Technologies and Analytics, TU Wien, Getreidemarkt 9/164, 1060 Vienna, Austria

² Metadynea Austria GmbH, Hafentrasse 77, 3500 Krems an der Donau, Austria

region (4000–400 cm^{-1}) and both, quantitative and qualitative, measurements are possible. Moreover, different instrumental realizations of mid-IR spectroscopy were developed over time, allowing customers to select the best suiting instrument [5].

Until today, the most generic and thus flexible technology for mid-IR-based gas measurements are Fourier transform infrared (FTIR) spectrometers [6]. Usually, they cover the whole mid-IR range and are capable of recording a full spectrum of the sample. The spectral resolution is typically 1–4 wavenumbers, but it can be reduced if a higher measurement frequency is required. Depending on the analytical problem to be solved either simple integration of characteristic absorption bands or application of chemometric approaches are the preferred modes of data analysis. Concerning applicability in the chemical industry, FTIR spectrometers are available from many different suppliers and in use for in-line as well as on-line monitoring of process gases. The downsides of this technology are, for example, high cost, limited temporal resolution, and, in some cases, the need for especially trained employees, especially when it comes to maintaining multivariate calibration models.

Another group of mid-IR-based analyzers make use of recent advances in laser technology in particular of quantum cascade lasers (QCLs) or intra-cavity lasers (ICLs) [7]. Using these lasers as light sources, concentrations down to the ppb–ppt concentration can be measured at high speed [8–10]. Moreover, it is possible to avoid moving parts, allowing the design of robust and compact instruments. However, their multi-analyte capabilities are still restricted due to the limited tuning range of the corresponding lasers ([11, 12]). An important current disadvantages of these mid-IR laser-based analyzers is their rather high cost.

Alternatively, filter-based mid-IR analyzers are a different, well-established group of mid-IR-based sensors that is characterized by less analytical power but with the advantage of low cost compared to FTIR-based analyzers. Here, a filter transmits infrared radiation only in the region where the analyte of interest is absorbing. These transmission windows can be rather wide ($>20 \text{ cm}^{-1}$ [13]) and cannot compete with the resolution of FTIR spectrometers. Therefore, they are only suited for rather simple applications such as quantifying CO_2 , CO, or ethylene in air [14–17]. In filter-based gas sensors, both absorption measurements based on Beers law as well as photoacoustic measurements have been realized so far.

If several analytes have to be quantified with the same analyzer, multiple filters with distinct transmission windows are needed. In the past, this was realized by mounting filters on a rotating filter wheel. However, the number of installable filters is generally limited, reducing somehow the possibility to fine tune across a certain spectral region as well as to select varying spectral segments with one and the same instrument.

Sensors which employ the gas filter correlation spectroscopy as measurement principle are closely related to the previously mentioned filter-based systems. Hereby, a gas cell filled with the analyte to be measured acts as the optical filter and generates the reference measurement [18, 19]. This technology is not limited to the infrared region ([20]) and typical analytes are CO, CO_2 , and SO_2 .

An approach for realizing filters is to use a Fabry-Pérot interferometer. Its basic principle is that two parallel and reflective surfaces allow only certain wavelengths to transmit. The transmitted wavelength segment depends on the distance between the reflecting mirrors (d), their reflectivity (R), and the interference order (m). The mathematical relation is as follows [21]:

$$\text{FWHM}_\lambda = \frac{2d}{\pi m^2} \frac{(1-R)}{\sqrt{R}}$$

Based on this technique, full widths at half height of typically $10\text{--}20 \text{ cm}^{-1}$ can be achieved.

There are different ways how such FP filters have been implemented in process analyzers so far. FP filters with varying but mechanically fixed distances between the mirrors can be found in circular and linear variable filters [22]. Here, the first method is typically integrated in the respective instrument like a filter wheel, thus requiring a single detector, whereas instruments employing linear variable filters also contain a detector array. In these systems, the optical configuration is such that each detector element is irradiated by a different wavelength segment.

Applying microelectromechanical systems (MEMS) made it possible to develop Fabry-Pérot (FP) interferometers with variable distance between the reflective mirrors. Commercial available detectors employ either piezos (e.g., VTT Technical Research Centre of Finland Ltd. [23]) or mechanical springs (InfraTec GmbH) in combination with an electrical field to establish a certain distance between the mirrors and thus to select a certain wavelength segment. Realization of tunable FP filters using MEMS components allowed downsizing of this functional element. A sensor consisting of a tunable FP filter, a pyroelectric detector and corresponding preamplifier electronics can thus fit in a TO-8 can. Nevertheless, a broadband filter still must be installed to suppress the transmission of harmonics. A basic scheme of such a FP filter-based detector element is illustrated in Fig. 1. A detailed mathematical description of its operation basics is available in [21, 24–26].

Production of formaldehyde

The measurement device presented in this paper was developed to monitor the concentration of side products from chemical reaction plants producing formaldehyde (FA). The

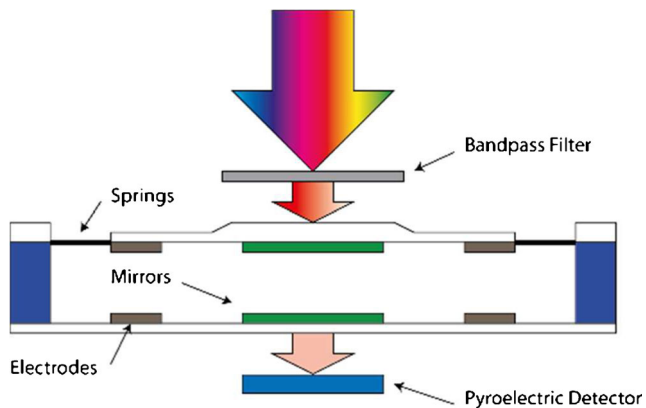
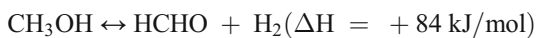
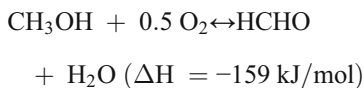


Fig. 1 Scheme of a Fabry-Pérot filter-based detector

underlying catalytic chemical reaction is the partial oxidation of methanol, leading to primarily formaldehyde. Two major processes which differ in the employed catalyst types are used to produce FA on an industrial scale. The first one, which is also known as Formox process, uses metal oxides (e.g., vanadium, molybdenum, or iron oxide) and is operated in the temperature region of 270–400 °C. The other one, which is also used at the investigated production plants of this study, is based on silver crystals and operated at significantly higher temperatures (600–720 °C) [27–30]. The formation of FA can be written as follows:

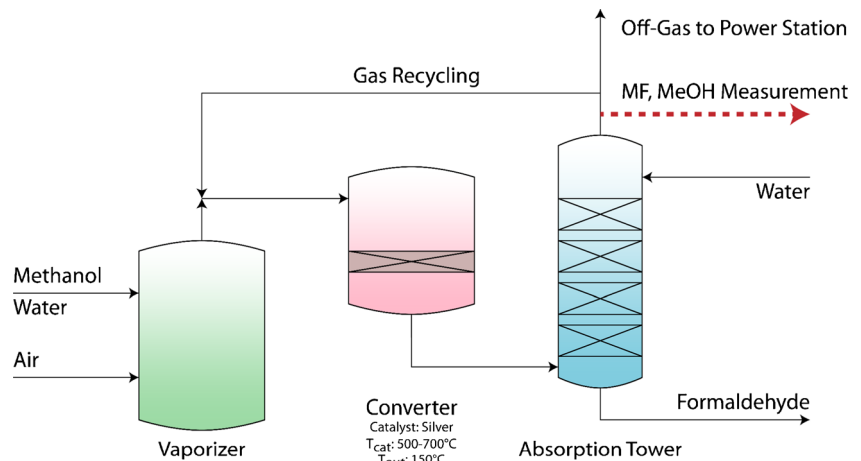


And with oxidation of the hydrogen:



After the catalytic reaction, the product stream is cooled down to approximately 150 °C and washed in counter flow with H₂O in an absorption column (a simplified scheme is given in Fig. 2).

Fig. 2 Simplified scheme of the FA production process based on the silver catalyst. The side product methyl formate (MF) and traces of not converted MeOH are quantified at the top of the absorption tower, indicated with a red arrow [31, 32]



The main part of the off-gas consists of CO₂, CO, and H₂, which are already monitored at Metadynea Austria GmbH with commercial available devices. However, also low concentrations of methanol (MeOH) and methyl formate (MF) (both <5000 ppm) and traces of not absorbed FA (<50 ppm) can be detected. While MeOH originates from not converted reactant, MF is created by a side reaction on the silver catalyst. Investigations with deuterated methanol [33], performed at lower temperatures than in commercial processes, propose the mechanism shown in Fig. 3 (Tischenko mechanism).

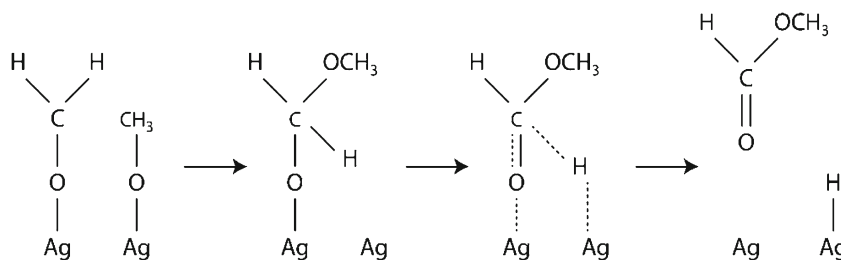
However, Wachs and Madix mention that no MF is found in industrial processes. They argue that the catalyst temperature (>600 °C) would be too high to enable a long enough surface residence time of FA on the silver catalyst to react to MF.

The task of the newly developed mid-IR-based gas sensor is quantification of MeOH and MF in the process off-gas with high time resolution (5 s.). The sensor was developed and implemented with the vision to enable accurate monitoring of the chemical status of the process and therefore to open the possibility for a more economic operation of the FA production plants.

Experimental setup

The installed mid-IR source is a JSIR350-4-AL-R-D6.0-0-0 (Micro Hybrid Electronic GmbH), which is a highly efficient blackbody emitter [34] and produced by applying MEMS processes. It is basically an electrical resistor which heats up when a voltage is applied. Due to its compact design and low thermal mass, amplitude modulation of the emitted radiation up in the hundred Hz region can be achieved. This allows to omit chopper wheels or other modulation techniques usually required by the need of the employed cost-effective pyroelectric detector. For this application, the applied voltage was 5 V and the modulation frequency was set to 3.5 Hz (duty cycle, 50 %) to achieve an optimum detector responsivity.

Fig. 3 Reaction mechanism for the formation of methyl formate as proposed by Wachs and Madix



A ZnSe lens ($f=50$ mm, ThorLabs Inc.) collimates the beam and a flat gold mirror reflects the radiation to a custom built gas cell. Its optical length is 30 cm and its steel body is heated up to 45 °C to avoid possible condensation from the humid off-gas on the cell walls. The limited space requires an additional reflection of the beam from a second plane mirror before it is focused (ZnSe, $f=50$ mm) onto the detector.

The central component of the measurement device is the tunable Fabry-Pérot (FP) filter-detector LFP-80105-337 (InfraTec GmbH) [35]. By applying a control voltage ($V_{\text{range}}=0\text{--}70$ V), the filter can be tuned through the region of $1250\text{--}950$ cm^{-1} , where two vibrational transitions of MF and MeOH can be found (Fig. 5). These bands (MF: CH_3 rocking [36] at ~ 1190 cm^{-1} and MeOH: C-O str. [37] at ~ 1040 cm^{-1}) are spectrally separated well enough for the tunable filter to resolve the bands, although the low spectral resolution of the tunable FP of approximately 10 cm^{-1} (Fig. 4).

As the mid-IR source is modulated, the detector signal has to be demodulated with an in-house developed Lock-In-Amplifier. The resulting signal is digitized with an analog digital converter (ADC, ADS1115, 16 bit, Texas Instruments Inc.) and a microcontroller (ATmega328P, Atmel Corporation) averages 100 measurement points to improve the signal to noise ratio. As the measurement principle is based on the absorption of light, one can

apply the Beer-Lambert Law and calculate the concentration according to

$$A(\lambda) = \log\left(\frac{I_{\lambda}^0}{I_{\lambda}}\right) = \varepsilon(\lambda)cl$$

where $A(\lambda)$ is the absorbance, I_{λ}^0 is the intensity recorded from a reference measurement at a certain wavelength segment, I_{λ} is the intensity recorded from of the sample channel at a certain wavelength segment, $\varepsilon(\lambda)$ is the observed decadic molar absorption coefficient at that wavelength segment, c is the concentration of the analyte, and l is the pathlength.

In order to calculate absorbance and the concentration of the target analyte, one needs to know values for I_{λ} and I_{λ}^0 . Here, the reference value I_{λ}^0 is gained by flushing the gas cell with the IR inactive gas N_2 . This reference measurement, which is also helpful to compensate for long term drifts, is initiated by the microcontroller and performed every 2 h 45 min. The concentrations of the two target analytes have to be quantified consecutively which requires adjusting the filter position periodically. Therefore, a digital to analog converter (DAC, MCP4725, 12 bit, Microchip Technology Inc.) is installed and sets the control voltage of the FP filter-detector.

The concentrations are determined by applying a calibration curve and proportional voltage signals for each analyte are output on additional DACs (2xMCP4725). These analog

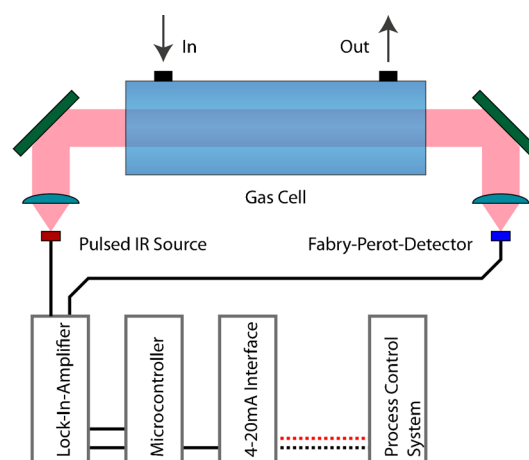


Fig. 4 Left: front side of the developed sensor (19" rack compatible); right: schematic assembly of the optical and electrical parts

signals are connected to two 4–20 mA converters (PXU-20.924/RS, Brodersen Controls A/S) to meet the requirements of the process control system (PCS) at Metadynea Austria GmbH. The 4–20 mA interface is the preferred way to monitor the concentration of the analytes of interest. However, an LCD display (HD44780, Adafruit Industries LLC) is also installed at the front panel of the sensor to check the functionality. An additional single-board-computer (Raspberry Pi 2 Model B, Raspberry Pi Foundation) and a mobile broadband modem (E3531, Huawei Co. Ltd.) allows remote monitoring and firmware upgrades of the microcontroller.

Experimental

Recording spectra of the analytes and calibration curves

Due to the conditions of the gas stream the prototype has to quantify MF and MeOH in the gas phase. At normal temperature and pressure, the analytes of interest are liquids with a significant vapor pressure (MeOH, 13.02 kPa; MF, 63.46 kPa). In order to characterize the device performance and to record calibration curves, gaseous reference samples with similar concentrations as to be expected at the intended application site had to be prepared in the laboratory. The physical properties of MF and MeOH make it difficult to prepare stable calibration gas mixtures of accurately known composition by means of static methods [38]. In addition, static calibration gas mixtures of the readily condensable gases and vapors of MF and MeOH cannot be maintained under a pressure near the saturation limit without the occurrence of condensation. Therefore, the saturation method according to ISO 6145-9:2009 was employed for preparing calibration mixtures of the analytes [39]. Following this standard a saturated gas stream is produced, where the concentration of the desired component can be calculated using pressure and temperature readings logged during the experiments. The resulting saturated gas

stream was then further diluted to the appropriate concentration with N_2 by employing mass flow controllers (MFCs, red-y smart, Vögtlin Instruments AG) and a static mixer. Finally, the sample stream was fed into the developed prototype.

Reference spectra of MeOH and MF were recorded with the prototype to establish calibration curves. To do so, the control voltage of the FP filter was increased to get one data point every 10 cm^{-1} . This led to 31 points per spectrum, taking 2 min.

Online measurements

Operating the prototype at Metadynea Austria GmbH involved a modification of the microcontroller firmware, compared to the reference measurements in the academic laboratory. Instead of recording full spectra with 31 data points, only two filter positions were selected. These were selected at the maximum absorption of the analytes and resulted in one concentration value for MF and MeOH every 5 s.

Multiple FA productions plants are located at the production site. As only one plant can be monitored at a time, the process control system switches the exhaust gas to the prototype automatically. It is intended to analyze each plant at least once per working shift. The result is that in normal operation mode, each plant is monitored for 1–2 h, depending on the number of active plants. This automatic gas stream cycle is overwritten if the plant operators modify process parameters or restart individual production plants.

Results

Spectra of analytes

Two typical spectra of MF and MeOH recorded with the prototype are compared with reference spectra from the PNNL database [40] and shown in Fig. 5a. One can clearly see that the resolution obtained with the FP-interferometer-based

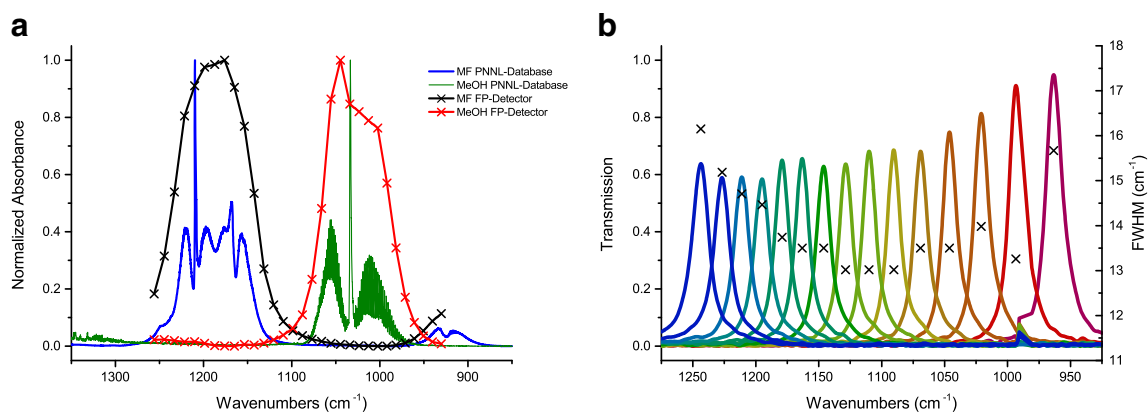


Fig. 5 **a** Comparison of reference spectra (PNNL) and spectra recorded with the FP-detector. All spectra were normalized to a maximum absorbance of one. **b** Transmission behavior and FWHM of the Fabry-Pérot filter at different control voltages

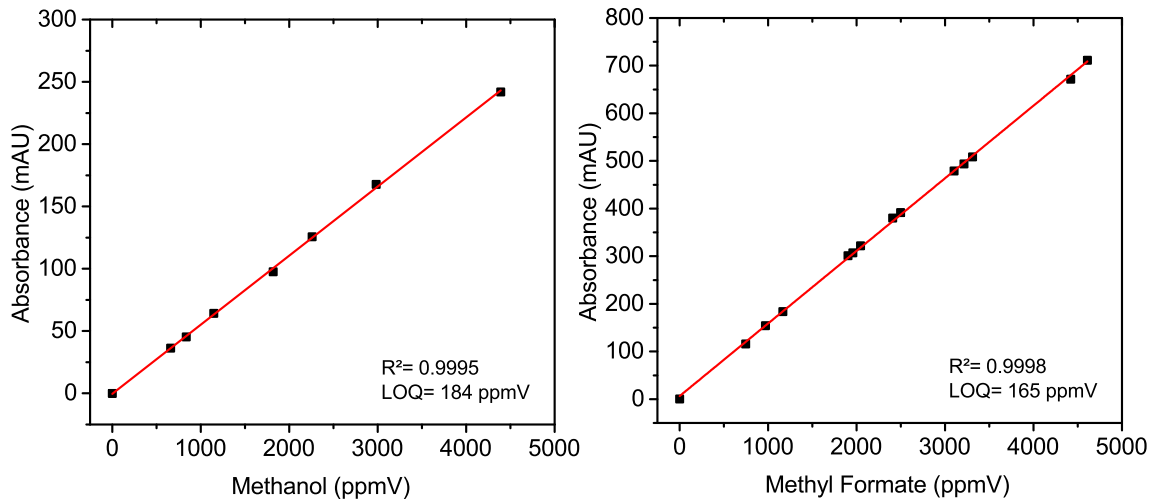


Fig. 6 Calibration curves for MeOH and methyl formate, recorded at wavelength segments centered at 1010 and 1160 cm^{-1}

instrument cannot compete with an FTIR spectrometer. Nevertheless, the absorption bands of the analytes are sufficiently isolated which allows the application of the developed instrument.

Calibration curves

Calibration samples were prepared with the gas mixing rig and spectra were acquired with the prototype. Due to the fact that

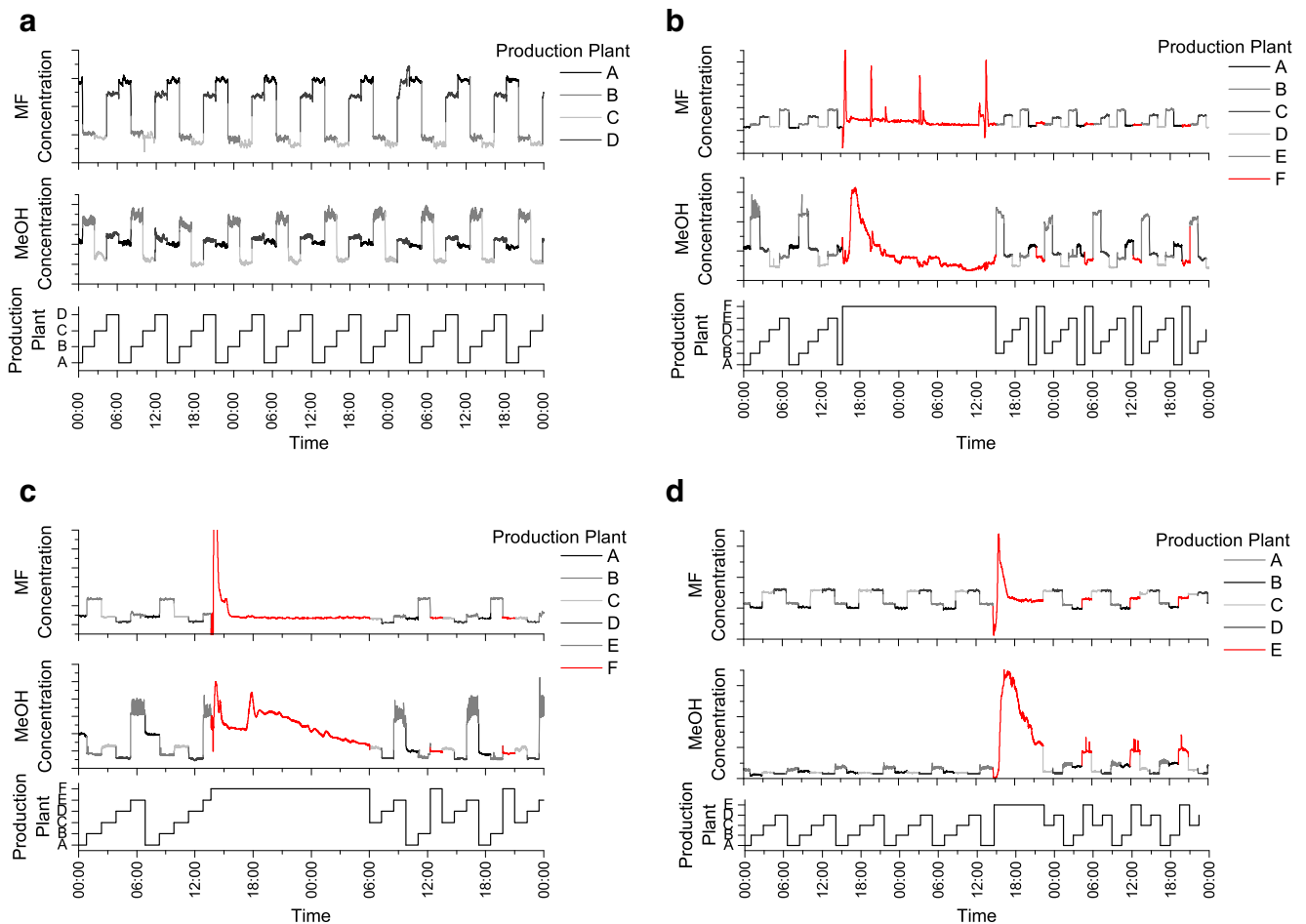
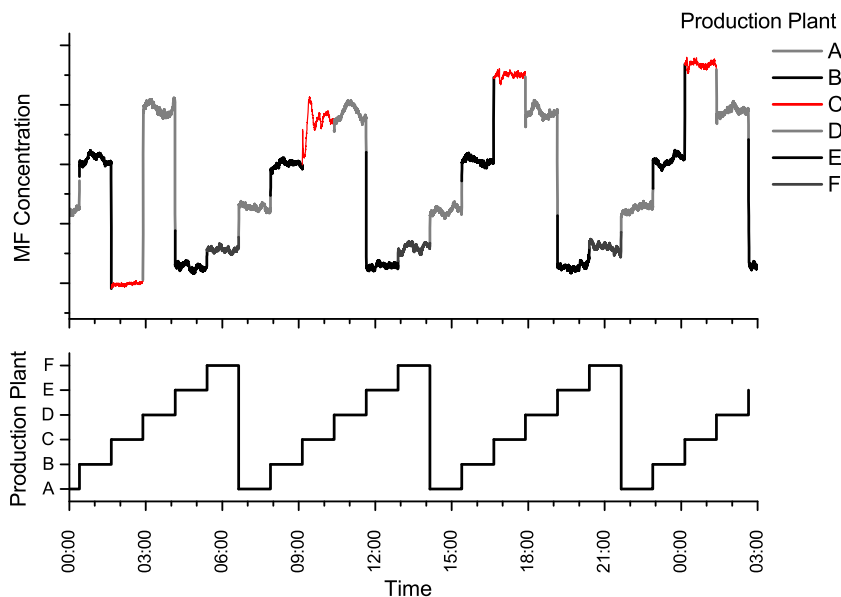


Fig. 7 **a** Methyl formate (MF) and MeOH concentration during 3 days at normal operation. **b–d** Retrieved concentration levels while starting an additional production plant (new plant indicated as red sections)

Fig. 8 Redirecting the exhaust gas to the converter causes an increase of MF as the catalyst temperature decreases



only a single point in the spectrum is used for each analyte during operation at the production plants, wavelength segments with maxima at 1010 cm^{-1} for MeOH and 1160 cm^{-1} for MF were selected as spectral positions to establish the corresponding calibration curves. No significant cross sensitivities were found in the concentration ranges of practical interest.

The resulting calibration curves are plotted in Fig. 6, with achieved limits of quantification of 184 ppmV for MeOH and 165 ppmV for MF.

Experiments at the production plants

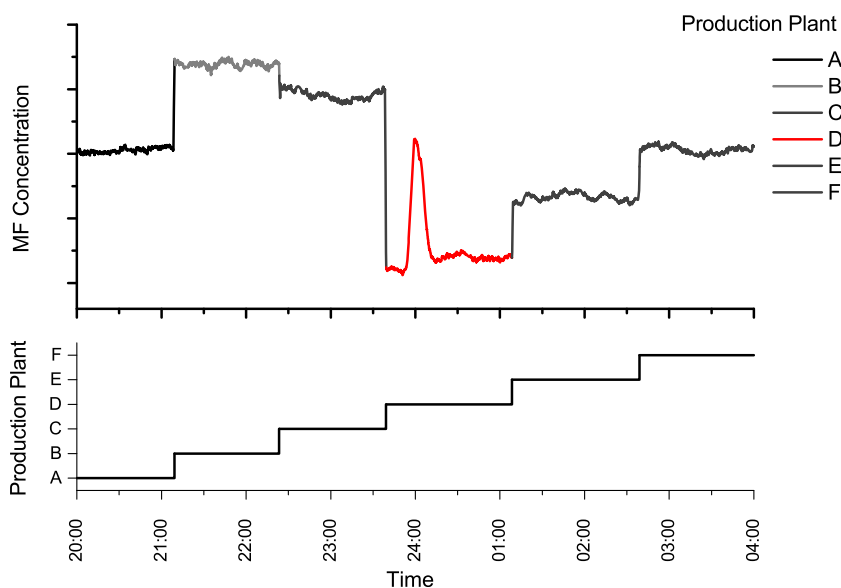
Results from online-measurements at Metadynea Austria GmbH are depicted in the following figures. The exemplary data is

typically plotted over several hours/several days. Due to company regulations absolute values, such as concentration values and production plant IDs (which also change during different experiments) and further additional plant parameters (catalyst temperature, etc.) may not be disclosed.

If the production parameters are constant, the data recorded from the PCS is as shown in Fig. 7a. Here, the periodical switching (approx. every 2 h) between four production plants initiated by the PCS can be observed. The constant production settings lead to almost stable MF and MeOH concentrations during 3 days of operation.

The FA production has to be stopped and restarted at certain intervals. The reasons for that are, for example, degradation of the catalyst caused by sintering effects [27] or test runs for other process optimization experiments. Three examples, where

Fig. 9 A short increase of the MF concentration due to a short change of catalyst temperature



production plants have been restarted, are shown in Fig. 7b–d. During these processes, the automatic switching cycle was deactivated, to gain specific information on the selected reactor during these experiments. According to Wachs and Madix [33], MF can be produced on the silver catalyst at lower temperatures, which is the case when the FA production is started. Reaching the optimum production parameters also leads to a stable and relatively low MF concentration. The MeOH concentration does not stabilize as fast as MF which is very likely caused by its longer retention time in the absorption tower as a consequence of the higher water solubility of MeOH.

A different experiment is shown in Fig. 8. Here, the exhaust-gas was redirected to the converter, leading to a decrease in temperature at the catalyst and an increase of MF at the measurement position. In this case, the automatic switching cycle was not deactivated and the new MF concentration was not accessible until the next repetition.

Another example of the applicability of the developed process analyzer is shown in Fig. 9. An unexpected change of the catalyst temperature resulted in a quick increase of MF. The production parameters were reset within 15 min and the MF concentration stabilized immediately.

Conclusion

A cost-efficient prototype of a process analyzer for on-line monitoring of MF and MeOH in the gas phase of a formaldehyde production plant was developed and implemented. Key components of the developed dedicated process spectrometer were an electrically modulated thermal IR source, a combined Fabry-Pérot interferometer-detector device and a microcontroller for automated measurements. A custom developed gas mixing rig allowed recording reference spectra and calibration curves of the analytes of interest. The achievable limits of quantification were 184 and 165 ppmV for MeOH and MF, respectively. The applicability of the prototype was shown at the production plants of Metadynea Austria GmbH. It provided valuable data on the time-dependent changes of the concentrations of the targeted process gases. After an initial installation phase, it is now considered as a valuable tool for monitoring the production plants and for providing in-depth information on the production process under investigation.

Acknowledgments Open access funding provided by TU Wien (TUW). We would like to thank the employees of our project partner Metadynea Austria GmbH for enabling the cooperation and the access to the production plants. Moreover, we would like to acknowledge the work of Wolfgang Tomischko, for designing the analog electronics and the Lock-In-Amplifier.

Financial support was provided by the Austrian research funding association (FFG) under the scope of the COMET program within the research project “Industrial Methods for Process Analytical Chemistry – From Measurement Technologies to Information Systems (imPACTs)”

(contract # 843546). This program is promoted by BMVIT, BMFWF, the federal state of Upper Austria, and the federal state of Lower Austria.

Compliance with Ethical Standards This paper does not contain any studies with human participants or animals performed by any of the authors.

Conflict of Interest The authors declare that they have no conflict of interest.

Open Access This article is distributed under the terms of the Creative Commons Attribution 4.0 International License (<http://creativecommons.org/licenses/by/4.0/>), which permits unrestricted use, distribution, and reproduction in any medium, provided you give appropriate credit to the original author(s) and the source, provide a link to the Creative Commons license, and indicate if changes were made.

References

- Berrie PG, Gut B, Lindner K-P. Fieldbuses and network protocols. In: Liptak BG, editor. Instrument engineers handbook—process control and optimization. 4th ed. Taylor & Francis Group; 2005. p. 770–789.
- Shimanuki Y. OLE for Process Control (OPC) for new industrial automation systems. IEEE SMC’99 Conf. Proceedings. 1999 I.E. Int. Conf. Syst. Man, Cybern. (Cat. No.99CH37028), vol. 6, pp. 1048–1050; 1999.
- Baakev KA. Process analytical technology. 2nd ed. Oxford: John Wiley & Sons Ltd.; 2010.
- Liptak BG. Process measurement and analysis. 4th ed., vol. 788. CRC Press; 2003.
- Hodgkinson J, Tatam RP. Optical gas sensing: a review. Meas Sci Technol. 2013;24(1):12004.
- Griffiths P, de Haseth JA. Fourier transform infrared spectrometry. 2nd ed. John Wiley & Sons Ltd.; 2007.
- Faist J, Capasso F, Sivco DL, Sirtori C, Hutchinson AL, Cho AY. Quantum cascade laser. Science. 1994;264:553–6 (80-).
- Nelson DD, Shorter JH, McManus JB, Zahniser MS. Sub-part-per-billion detection of nitric oxide in air using a thermoelectrically cooled mid-infrared quantum cascade laser spectrometer. Appl Phys B Lasers Opt. 2002;75(2–3):343–50.
- Curl RF, Capasso F, Gmachl C, Kosterev AA, McManus B, Lewicki R, et al. Quantum cascade lasers in chemical physics. Chem Phys Lett. 2010;487(1–3):1–18.
- Tittel FK, Lewicki R, Lascola R, McWhorte S. Emerging infrared laser absorption spectroscopic techniques for gas analysis. In: Geiger WM, Raynor MW, editors. Trace analysis of specialty and electronic gases. Hoboken: Wiley; 2013. p. 71–110.
- Luo GP, Peng C, Le HQ, Pei SS, Hwang WY, Ishaug B, et al. Grating-tuned external-cavity quantum-cascade semiconductor lasers. Appl Phys Lett. 2001;78(19):2834–6.
- Faist J, Gmachl C, Capasso F, Sirtori C, Sivco DL, Baillargeon JN, et al. Distributed feedback quantum cascade lasers. Appl Phys Lett. 1997;70(20):2670–2.
- InfraTec, “InfraTec - Typical Filter Plots.” [Online]. Available: <http://www.infratec.de/fileadmin/media/Sensorik/pdf/IRFilter-Typical-Plots.pdf>.
- Hodgkinson J, Smith R, Ho WO, Saffell JR, Tatam RP. Non-dispersive infra-red (NDIR) measurement of carbon dioxide at 4.2 μm in a compact and optically efficient sensor. Sensors Actuators B Chem. 2013;186:580–8.

15. Barritault P, Brun M, Lartigue O, Willemin J, Ouvrier-Buffet JL, Pocas S, et al. Low power CO₂ NDIR sensing using a microbolometer detector and a micro-hotplate IR-source. *Sensors Actuators B Chem.* 2013;182:565–70.
16. Frodl R, Tille T. A high-precision NDIR CO₂ gas sensor for automotive applications. *IEEE Sensors J.* 2006;6(6):1697–705.
17. Hildenbrand J, Wöllenstein J, Hartwig S, Eberhardt A, Halford B, Moreno M, et al. A compact optical multichannel system for ethylene monitoring. *Microsyst Technol.* 2008;14(4–5):637–44.
18. Dakin JP, Gunning MJ, Chambers P, Xin ZJ. Detection of gases by correlation spectroscopy. *Sensors Actuators B Chem.* 2003;90(1–3):124–31.
19. Dickerson RR, Delany AC. Modification of a commercial gas filter correlation CO detector for enhanced sensitivity. *J Atmos Ocean Technol.* 1988;5:424–31.
20. Lou XT, Somesfalean G, Zhang ZG, Svanberg S. Sulfur dioxide measurements using an ultraviolet light-emitting diode in combination with gas correlation techniques. *Appl Phys B.* 2009;94(4):699–704.
21. Ebermann M, Neumann N, Hiller K, Gittler E, Meinig M, Kurth S. Recent advances in expanding the spectral range of MEMS Fabry-Perot filters. *Proc. SPIE 7594, MOEMS Miniaturized Syst. IX;* 2010.
22. Ghaderi M, Ayerden NP, Emadi A, Enoksson P, Correia JH, de Graaf G, et al. Design, fabrication and characterization of infrared LVOFs for measuring gas composition. *J. Micromechanics Microengineering.* 2014; 24 Suppl 8.
23. Kantojärvi U, Varpula A, Antila T, Holmlund C, Mäkynen J, Näsiliä A, et al. Compact large-aperture Fabry-Perot interferometer modules for gas spectroscopy at mid-IR. *SPIE Photonics West 2014-OPTO Optoelectron. Devices Mater., vol. 8992, p. 89920C;* 2014.
24. Rossberg D. Silicon micromachined infrared sensor with tunable wavelength selectivity for application in infrared spectroscopy. *Sensors Actuators A Phys.* 1995;47(1–3):413–6.
25. Neumann N, Ebermann M, Kurth S, Hiller K. Tunable infrared detector with integrated micromachined Fabry-Perot filter. *J Micro/Nanolithogr MEMS MOEMS.* 2008;7(2):21004-1–9.
26. Schuler LP, Milne JS, Dell JM, Faraone L. MEMS-based microspectrometer technologies for NIR and MIR wavelengths. *J Phys D Appl Phys.* 2009; 42.
27. Reuss G, Disteldorf W, Gamer AO, Hilt A. Formaldehyde. *Ulmann's Encycl. Industrial Chem., vol. 15, pp. 735–768;* 2012.
28. Weissermel K, Arpe H-J. *Industrial organic chemistry.* 3rd ed. VCH; 1997.
29. Lefferts L, An Ommen JG, Ross JRH. The oxidative dehydrogenation of methanol to formaldehyde over silver catalysts in relation to the oxygen-silver interaction. *Appl Catal.* 1986;23(2):385–402.
30. Yang Z, Li J, Yang X, Wu Y. Catalytic oxidation of methanol to methyl formate over silver—a new purpose of a traditional catalysis system. *Catal Lett.* 2005;100(3–4):205–11.
31. Dynea.com. Silver Catalysed Formaldehyde Plant. 2016. [Online]. Available: <http://www.dynea.com/technology-sales/silver-catalysed-formaldehyde-plant/>.
32. Bahmanpour AM, Hoadley A, Tanksale A. Critical review and exergy analysis of formaldehyde production processes. *Rev Chem Eng.* 2014;30(6):583–604.
33. Wachs IE, Madix RJ. The oxidation of methanol on a silver (110) catalyst. *Surf Sci.* 1978;76(2):531–58.
34. Micro-Hybrid, Infrared Radiation Source JSIR350-4-AL-R-D6.0-0-0. 2013. [Online]. Available: <http://www.microhybrid.de/fileadmin/user/IR-systems-documents/Datenblaetter/Strahler/JSIR350-4-AL-R-D6.0-0-0.pdf>.
35. InfraTec, LFP-80105-337. [Online]. Available: <http://www.infratec.de/fileadmin/media/Sensorik/pdf/LFP-80105-337.pdf>.
36. Wilmshurst JK. A vibrational assignment for methyl formate and methyl acetate. *J Mol Spectrosc.* 1957;1:201–15.
37. Larkin PJ. *IR and Raman spectroscopy—principles and spectral interpretation.* Elsevier; 2011.
38. Pratzler S, Knopf D, Ulbig P, Scholl S, Ulbig P, Scholl S. Preparation of calibration gas mixtures for the measurement of breath alcohol concentration. *J Breath Res.* 2010;4(3):36004.
39. Norm D. ISO6145-9 Herstellung von Kalibriergasgemischen (Sättigungsverfahren). 2010.
40. Sharpe SW, Johnson TJ, James RL, Chu PM, Rhoderick GC, Johnson PA. Gas phase database for quantitative infrared spectroscopy. *Appl Spectrosc.* 2004;58(12):1452–61.

4.6 Publication II: Application of tunable Fabry-Pérot filterometer to mid-infrared gas sensing

Authors: Christoph Gasser, Andreas Genner, Harald Moser, Johannes Ofner and Bernhard Lendl

Published in: *Sensors and Actuators B: Chemical*, April 2017, Volume 242, Pages 9-14

Status: Published

Reprinted with permission <http://dx.doi.org/10.1016/j.snb.2016.11.016>

Short summary:

This paper presents the design and application of a filterometer based on a tunable FPF, covering the spectral range from 1250 to 1850 cm^{-1} (LFP5580), to multiple-component gas sensing. The target analytes were C_4 hydrocarbons, a fraction prominent in the steam cracking process of naphtha (10-12w%). Depending on the cracking severity, the main components in this fraction are 1,3-butadiene (26-47w%), isobutene (22-32w%), 1-butene (14-20w%) and also in lower concentrations, isobutane (1-2w%) [103]. Two showcase the capability of the filterometer to simultaneously detect the main components as well as smaller constituents of this fraction, three components (the used gas mixing rig is limited to 3 components at a time) were chosen, namely 1,3-butadiene, 1-butene and iso-butane. The spectra obtained with the FPF filterometer were compared with spectra recorded on a FTIR spectrometer and successfully validated. Multivariate analysis based on Partial Least Squares (PLS) and Multiple Linear Regression (MLR) for simultaneous quantification of the target analytes were carried out and compared. The PLS model gave best results using 5 factors with a mean Root Mean Square Error of Prediction (RMSEP) of 0.109%. With the selected acquisition parameters, it took about 100 s to collect a full spectrum. Given a defined target application (as a dedicated sensor) it is, however, often not required to record a full spectrum and still achieve multicomponent sensitivity. This was shown here by performing MLR on the obtained dataset. Variable selection was applied to find the most significant descriptors which were then chosen for further analysis. The absence of collinearities was verified by calculating Variance Inflation Factor (VIF) for the selected descriptors. MLR yielded a LOQ of 0.57%, 0.17% and 0.11% for 1,3-butadiene, 1-butene and isobutane, respectively. The advantage of using MLR over PLS in this case lies in the number of data-points to be measured reduces from a full spectrum to seven, which reduces the time of analysis by a factor of 8 to approximately 12 s. Thus we could show that this compact and low-cost sensor paired with chemometric processing methods is able to quantify

gas mixtures composed of three different components. This versatility combined with a small electrical as well as physical footprint pave the way for this technique to establish itself as useful chemical sensors in process monitoring and control.



Application of a tunable Fabry-Pérot filterometer to mid-infrared gas sensing



Christoph Gasser*, Andreas Genner, Harald Moser, Johannes Ofner, Bernhard Lendl

Institute of Chemical Technologies and Analytics, TU Wien, Vienna, Austria

ARTICLE INFO

Article history:

Received 3 July 2016

Received in revised form 3 October 2016

Accepted 3 November 2016

Available online 5 November 2016

Keywords:

Infrared spectroscopy

Gas monitoring

Fabry-Pérot interferometer

Multivariate analysis

Process analytical chemistry

ABSTRACT

The design and application of a versatile, tunable filterometer based on a Fabry-Pérot (FP) tunable filter – detector, covering the spectral range from 1250 to 1850 cm^{-1} at a spectral resolution of approximately 30 cm^{-1} , is presented. The tunable filter was characterized and calibrated using a FTIR spectrometer. Gas mixtures comprising iso-butane, 1-butene, 1,3-butadiene were prepared and measured. The obtained gas spectra were validated by FTIR measurements. Quantitative analysis based on the whole tuning range of the filterometer and employing partial least squares (PLS) calibration revealed fully satisfactory results with root mean square error of prediction (RMSEP) of 0.03, 0.04 and 0.26% for iso-butane, 1-butene and 1,3-butadiene respectively. As the tunable FP filterometer also allows measurements at pre-selected spectral windows a calibration based on multiple linear regression (MLR) was performed as well obtaining similar results. The results clearly show that tunable Fabry-Pérot filters can be used in a new generation of filterometers and provide a low-cost option for the quantitative and fast multicomponent gas sensing.

© 2016 Elsevier B.V. All rights reserved.

1. Introduction

With increasing requirements on monitoring of chemical as well as pharmaceutical processes, the demand for powerful, robust and low priced sensors increases. Trends in PAC (process analytical chemistry) or PAT (process analytical technologies) point towards portable analyzers, which can be used in different environments for at-line, but ideally for on- or in-line analysis. The sensor systems have to be fit for purpose, exhibiting adequate analytical performance for a moderate and reasonable price. In principle infrared and Raman spectroscopies are highly interesting techniques in this regard as they provide direct molecular specific information. Concerning mid-IR spectroscopy, Fourier transform spectrometers present the so far most widely used technique [1,2]. These instruments provide a broad spectral coverage and can be successfully applied to solve a broad variety of different analytical problems often by employing chemometric techniques for data analysis. As of today rugged FT-IR spectrometers for on-line or in-line applications are in generally available in every form factor, albeit at a rather high cost. An interesting alternative to established FTIR spectrometers concern spectrometer developments based on broadly tuning, but still prohibitively expensive laser sources, such as external cavity

quantum cascade lasers (EC-QCLs). Such spectrometers have been used for gas [3,4], as well as liquid sensing [5–7]. This approach, in order to be fit for purpose, needs to target applications where gas traces need to be recorded at high speed or where increased ruggedness for liquid sensing is required to justify the high cost.

For providing an answer to some sensing tasks, however, the spectroscopic performance of an FT-IR spectrometer is not required as a restricted spectral range sometimes can provide the required selectivity to solve a given problem. Furthermore, in many applications the high sensitivities as offered by mid-IR laser spectroscopy are not needed, either. This is often the case when major and minor components of industrial gas mixtures need to be monitored. A cost effective solution for addressing such applications is possible by addressing selected spectral regions by the use of filters instead of using an interferometer or lasers. Thus, analyzers using a small, but constant portion of the IR spectrum, as obtainable with static IR filters, have emerged over the years. Such filter based spectrometers are also known as filterometers, a term coined from “filter” and “photometer”. The commercial success of such filterometers made it apparent, that the compromise between performance and price allows attractive solutions for certain measurement problems. Examples are the oil-in-water analyzers by Wilks Enterprise [8] (Spectro Scientific) or first iterations of filterometers for the determination of casein content in milk and milk products [9]. Also concerning absorption or photoacoustic gas measurements filter based instruments have found their application in the recent past.

* Corresponding author.

E-mail address: christoph.gasser@tuwien.ac.at (C. Gasser).

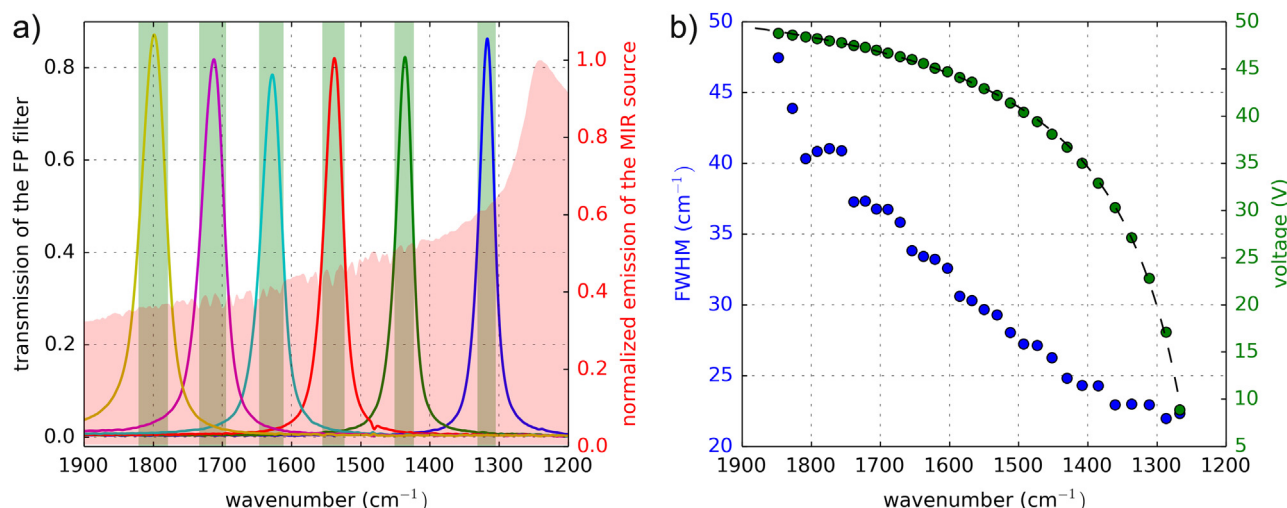


Fig. 1. Transmission windows (a) of the LFP5580 when different voltages are applied and FWHM (b, blue markers) of the transmission curves as a function of wavenumber as well as spectral center (green markers) in dependence of the applied voltage. The fitted curve is indicated as the black dashed line. (For interpretation of the references to colour in this figure legend, the reader is referred to the web version of this article.)

Here, applications of filtometers primarily include gas-phase analysis of simple molecules, such as water and CO₂ [10,11].

Whereas early technological solutions employed a filter wheel for addressing different narrow spectral ranges for measurement, new technological developments are emerging and may change the way modern filtometers operate. New designs respond to the fact that it would often be advisable to monitor more than a single or a set of predefined narrow wavelength ranges. This added capability would increase the flexibility of filtometers and turn them into a more generally applicable analytical tool at remaining low cost and small footprint.

A key enabling technology for this development is Fabry-Pérot (FP) interferometry [12], where the transmitted wavelength is defined among other by the distance between two reflective surfaces. A range of discrete distances can be realized in a small device by circular (CVF) or linear variable filters (LVF). A combination of these with a linear IR detector array [13,14] allows to create compact mid-IR spectrometers, with a spectral resolution of at best 10–20 cm⁻¹, thus approaching the capabilities of a low resolution FT-IR spectrometer but showing sensor-like performance. In these instruments, like those of Pyreos [15], the reflective surfaces of the Fabry-Pérot cavity are kept in place by a wedged spacer in such a way, that the transmission window shifts through the length of the array [14]. Another approach toward compact sensor-like spectrometers consists in changing the distances between the reflective surfaces of the Fabry-Pérot cavity on demand by MEMS (micromechanical systems) fabricated springs or piezo-actuators. These tunable filters also include pyroelectric detector elements and are available in TO8 housings. Compact arrangements of such designs are realized in Infratec's multi-color FP detectors [16] or VTT's integrated solutions [17]. Fabry-Pérot pyro-detectors can therefore be manufactured in large quantities, covering different ranges of the MIR spectrum [18] and are therefore prime candidates for the construction of dedicated spectroscopic sensors. For operation pyro-detectors require modulation of the light intensity. In FT-IR spectrometers this is achieved by using a thermal light source [19], which provides a constant emission of infrared radiation modulated by the interferometer itself. In case of using adjustable Fabry-Pérot cavities for selection of narrow spectral windows practically no intensity modulation is achieved. Therefore, in these miniature, sensor-like spectrometers the intensity of the light source itself has to be modulated. The operation principle of FP-based filtometers permits arbitrary access to selected spectral

regions, in addition to recording the whole spectra by a complete scan.

This work reports on the results obtained with a home-made prototype for gas sensing using a Fabry-Pérot pyro-detector and thermal light source, whose emitting element consists of a thin layer of diamond like carbon (DLC), that can be modulated with up to 100 Hz. A typical gas mixture found at butadiene plants of petrochemical refineries has been selected as target analyte composition (iso-butane, 1-buten, 1,3-butadiene). The obtained spectra are evaluated with multivariate data analysis techniques and the results compared.

2. Materials and methods

2.1. Tunable Fabry-Pérot (FP) filter

For characterization and wavelength calibration, the FP filter (LFP5580, InfraTec GmbH) with a tuning range from 5.5 to 8 μm (1830–1250 cm⁻¹) was coupled to a Bruker Vertex 80v FTIR spectrometer as an external detector using a parabolic off axis mirror (f = 156 mm). Spectra at different driving voltages (5–50 V) were collected by averaging 5 scans and setting the scanner velocity to 1.2 kHz (HeNe frequency). With the resulting transmission windows the filter was calibrated (Fig. 1a). The following relation between driving current and central transmission wavelength was found:

$$V_{driving} = V_{max} - \frac{c}{\tilde{\nu} - \tilde{\nu}_{min}} \quad (1)$$

where $V_{driving}$ is the driving voltage of the tunable FP, V_{max} is the maximum voltage, c is a constant factor and $\tilde{\nu}$ is the central wavenumber. Eq. (1) was fitted (shown in Fig. 1b as the dashed line) to the measured FTIR transmission spectra in order to calibrate the wavenumber axis and enable scanning with equidistant step size.

Furthermore, as shown in Fig. 1b, the full width at half maximum (FWHM, blue markers) of the transmission curves increases with increasing wavenumber.

2.2. FP-based MIR filtometer for gas sensing

The FP-based MIR filtometer (inset in Fig. 2) consisted of a custom built 30 cm gas cuvette employing two circular (diameter

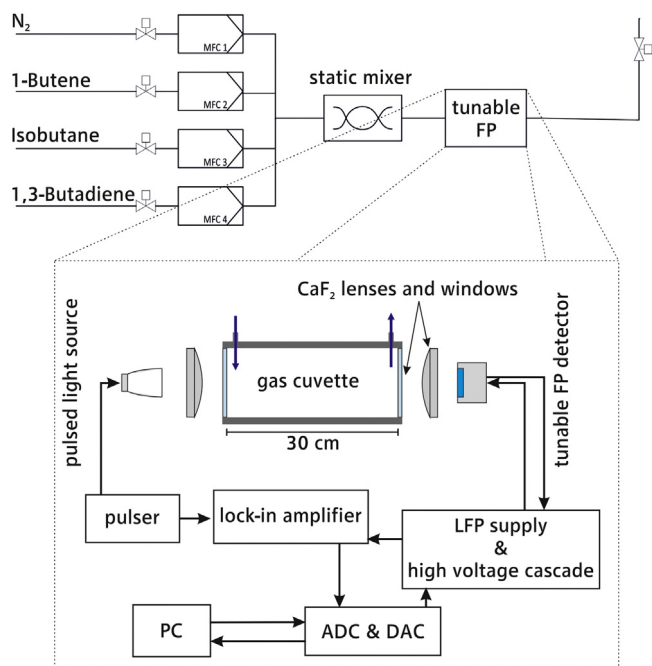


Fig. 2. Setup for the gas measurements including the gas mix rig. The inset shows the instrumentation of the tunable FP filter.

ter: 52 mm) 2 mm thick CaF_2 windows. Light from the pulsed MIR source (JSIR350-4-AL-R-D6 by Micro-Hybrid Electronics GmbH) was collimated with a CaF_2 lens ($f = 50$ mm, ThorLabs GmbH) and after passing the gas cuvette, focused with an equal lens on the active element of the tunable FP filter-detector. The light source was pulsed at 3.52 Hz with 5 V amplitude and a duty cycle of 50%. The electronic signal from the pyroelectric element of the FP filter-detector was processed with a lock-in amplifier and the resulting voltage was digitalized (ADS1115, Texas Instruments, 16-bit resolution) and recorded. Spectra of the samples were collected by stepwise changing the control voltage (MCP4725, Microchip Technology Inc.) for the tunable filter and calculating the resulting mean intensity of an acquisition time of 1.5 s per step. A waiting period of 300 ms was applied when moving to the next position to let the filter settle. The filterometer was thus operated by sampling from one point to the next. A step size of 10 cm^{-1} was chosen over a range of 550 cm^{-1} ($1280\text{--}1830 \text{ cm}^{-1}$). Scanning across the whole spectral range thus took approximately 100 s. For reference measurements of the gases a Tensor 27 FTIR spectrometer (Bruker Optics, Germany) equipped with a 10 cm gas cell was used. For FTIR spectra acquisition 16 scans at a spectral resolution of 1 cm^{-1} were averaged. 3-term Blackman Harris apodization, a zero filling factor of 2 and Mertz phase correction were applied.

2.3. Experimental set-up including gas supply

For providing gas mixtures with defined concentrations a customized gas mixing rig (Fig. 2 top) was used. This rig consisted of four mass flow controllers (MFC red-y smart, Vögtlin Instruments AG, Switzerland), with different operating flows. To ensure homogeneity a helical static mixer was employed before the mixed gas

was directed to the analyzers. Gas lines were made of stainless steel tubing (i.d. 4 mm) and Swagelok connections.

Gases were provided by AirLiquide Austria GmbH with the following purities: 1-butene 99.6 %, isobutane 99.5 % and 1,3-butadiene 99.6 %. The design of experiment was chosen with the built-in function in OPUS 7.2 (Bruker Optics, Germany). 20 measurement points were taken in a range from 0.12 to 1.77 % for 1,3-butadiene and isobutane and from 0.4 to 6.2 % for 1-butene. The composition for each step can be seen in Table 1.

All concentrations are given in volumetric quantities (v/v, in%) unless specified otherwise. All steps had a constant flow of 4 l/min and a duration of 8 min to ensure stable conditions in the gas cell. In addition of measuring gas mixtures spectra of pure gases were measured. The mass flow controllers and all valves switching the gas mix rig were controlled using LabVIEW® (National Instruments).

2.4. Data analysis based on partial least squares (PLS) regression

Multivariate data evaluation was performed using the software package DataLab [20]. Spectra of each concentration step were evaluated. Prior to performing PLS the dataset was mean centered. Cross validation was done by random subsets (using 5 iterations with 2 spectra). The root-mean-square error of prediction (RMSEP) was calculated by Eq. (2),

$$RMSEP = \sqrt{\frac{\sum_{i=1}^N (y_i - \hat{y}_i)^2}{N}} \quad (2)$$

where y_i are the concentrations of the respective components as prepared in the gas mixing rig, \hat{y}_i the values predicted by the PLS algorithm and N the number of samples measured.

2.5. Data analysis based on multiple linear regression (MLR)

Multiple linear regression correlates more than one independent (descriptor) to one dependent (target) variable. Usually spectroscopic methods provide a multitude of descriptors (e.g. different wavenumbers) and only one target variable (e.g. concentration). Additionally, spectra inherently show strong multicollinearities because of spectral features spanning over several wavenumbers. These facts often cause over-optimistic models by applying MLR to spectral data. This can and must be avoided by reducing the number of descriptors. This is usually done by variable selection algorithms, which identify the descriptors that are most important for the analytical problem at hand and use them explicitly to build the model. Absence of collinearities can be tested by calculating and comparing e.g. the variance inflation factor (VIF) for different sets of descriptors.

3. Results and discussion

3.1. System performance

An important parameter indicating the performance of a given experimental set-up are so called 100%-lines. These are obtained by recording two spectra without the analyte being present in the gas cell and calculating the related absorbance spectra, which in absence of any noise would be straight lines. The root-mean-square

Table 1

Comparison of the results of the multivariate models calculated in this study for every component. Additionally, the acquisition time is given for comparison.

| conc. step | 1 | 2 | 3 | 4 | 5 | 6 | 7 | 8 | 9 | 10 | 11 | 12 | 13 | 14 | 15 | 16 | 17 | 18 | 19 | 20 |
|---------------|------|------|------|------|------|------|------|------|------|------|------|------|------|------|------|------|------|------|------|------|
| 1-butene | 0.79 | 1.56 | 1.42 | 1.49 | 4.85 | 0.00 | 4.86 | 2.33 | 3.22 | 1.42 | 2.94 | 0.87 | 3.77 | 1.91 | 2.26 | 4.11 | 1.91 | 6.25 | 0.43 | 0.78 |
| isobutane | 1.39 | 1.13 | 1.51 | 1.07 | 0.31 | 0.89 | 0.49 | 0.69 | 0.12 | 0.88 | 0.19 | 0.06 | 0.00 | 0.63 | 1.12 | 0.06 | 0.94 | 0.06 | 1.77 | 1.70 |
| 1,3-butadiene | 0.77 | 0.85 | 0.34 | 0.94 | 0.50 | 1.72 | 0.22 | 1.10 | 1.43 | 0.94 | 1.52 | 0.35 | 1.26 | 1.28 | 0.51 | 1.09 | 0.85 | 0.33 | 0.43 | 0.43 |

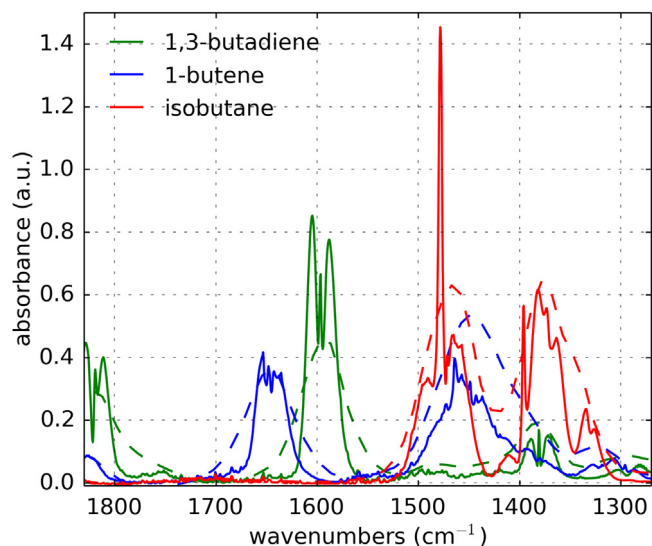


Fig. 3. Pure spectra of the three sample gases collected with the FTIR spectrometer (solid lines) and the tunable FP setup (dashed lines).

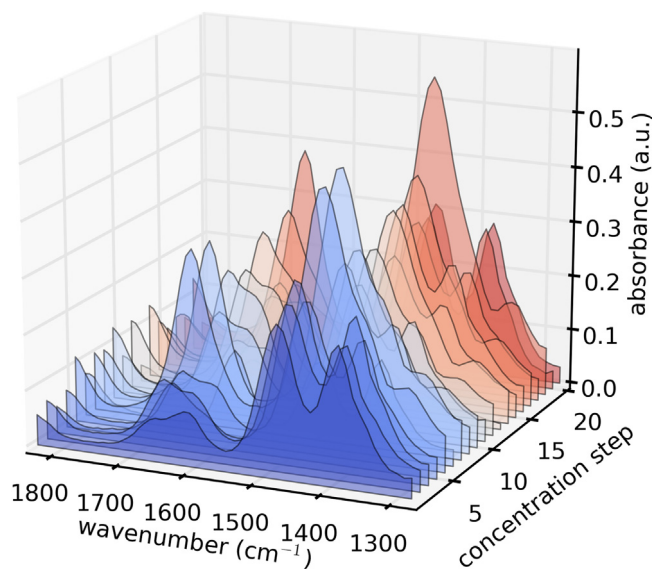


Fig. 4. All spectra of the different 3 component mixtures collected with the tunable FP setup.

(RMS) noise of these 100% lines was calculated. The peak-to-peak (PP) noise on the other hand is the difference of the absolute maximum and absolute minimum absorption value obtained in the respective 100% lines. Under the adopted conditions and covering a spectral range from 1280 to 1830 cm^{-1} the RMS noise was found to be 0.76 mAU (3.1 mAU_{pp}) for the Fabry P erot (FP)-based MIR filterometer. In Fig. 3 the spectra of the pure components collected with the FTIR spectrometer and the tunable filterometer are compared. For the FTIR spectrometer a resolution of 1 cm^{-1} was arbitrarily set, representing the highest resolution this spectrometer can offer. On the contrary, central wavenumbers for the transmission curves of the filter spaced at 10 cm^{-1} were selected considering the FWHM of the corresponding transmission curves being 25–45 cm^{-1} . This difference in the spectral resolution is best observed for isobutene at the band at 1470 cm^{-1} (Fig. 3). This band, assigned to the anti-symmetric deformation of the methyl group [21], should show a distinct peak at the center due to the Q-branch of the rotational transition. While this band is visible in the FTIR spectrum it cannot be observed in the tunable FP spectrum because of the aforemen-

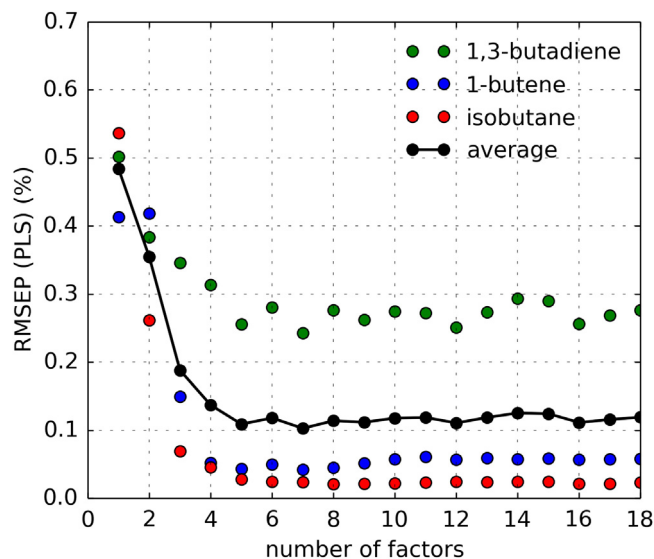


Fig. 5. RMSEP versus number of factors as calculated by cross-validation for the PLS for tunable FP setup. The black line indicates the mean RMSEP of all three components.

Table 2

Composition of each concentration step set by the gas mixing rig and used for multivariate calibration and validation of the tunable FP instrument. All concentrations are given in volumetric quantities (v/v, in%).

| | variable | VIF | R ² | F |
|---------------|-----------|-------|----------------|------|
| 1,3-butadiene | 1577 (32) | 1.047 | 0.97 | 282 |
| | 1448 (18) | 1.047 | | |
| 1-butene | 1612 (36) | 2.625 | 0.992 | 1078 |
| | 1662 (42) | 2.625 | | |
| isobutane | 1367 (10) | 1.36 | 0.9986 | 4561 |
| | 1717 (49) | 3.304 | | |
| | 1812 (62) | 3.788 | | |

tioned lower resolution. The positions of absorption bands of the different analytes are consistent in both spectrometers indicating a proper calibration of the Fabry P erot (FP)-based MIR filterometer.

Using the set-up depicted in Fig. 2 acquisition of FP-based spectra (Fig. 4) for different 3 components mixtures was possible. Care was taken to avoid any carry over from one gas mixture to the next one.

3.2. Quantification employing partial least square (PLS) calibration

PLS models were calculated for the dataset using the gas concentration as set by the mass flow controllers as reference values. When establishing a PLS model the number of factors to be considered has to be selected carefully. It is recommended to choose the least possible amount of factors that describe the sample system sufficiently. For the tunable FP filterometer dataset (Fig. 5) the optimum number of factors was determined using cross-validation (2 spectra left out) to be five. With a mean RMSEP of 0.109% the developed FP filterometer provides highly satisfactory results indicating that spectral resolution as offered by the FP-based MIR filterometer does not limit the analytical performance.

3.3. MLR models for the tunable FP setup

Before setting up the MLR model for each component present in the sample mixture, a reduction of the number of descriptors is necessary. With respect to the FP-based MIR filterometer in this study it

Table 3

Overview of the MLR regression. The results of the variable selection contain the position (in cm^{-1}) and the index of the spectral position (in parenthesis). Additionally, the variable inflation factor (VIF) of each variable, the regression coefficient (R^2) and the F-value of the model is shown.

| | components | | | | | | |
|-----|---------------|---------|----------|---------|-----------|---------|----------------------|
| | 1,3-butadiene | | 1-butene | | isobutane | | acquisition time (s) |
| | LOD (%) | LOQ (%) | LOD (%) | LOQ (%) | LOD (%) | LOQ (%) | |
| PLS | 0.17 | 0.50 | 0.05 | 0.16 | 0.03 | 0.09 | 100 |
| MLR | 0.20 | 0.57 | 0.06 | 0.17 | 0.04 | 0.11 | 12 |

is no longer required to scan the whole spectral range, instead a few positions might be enough to predict the concentrations accurately. This in turn will allow faster measurements.

DataLab has conveniently implemented functions, which automatically select different sets of descriptors, calculate a model and report several parameters (min. t-value, Akaike Information Criterion (AIC), Bayes Information Criterion (BIC), R^2 , etc.) to decide upon the most useful descriptor set for the problem at hand. The variable selection was performed using stepwise regression. Here, the algorithm tries to improve the model by adding more suitable variables and by comparing the minimal t-value. It can also modify its selection by removing the last variable and trying another one, which may yield better results.

With the selected variables multiple linear regressions (MLRs) were performed. To investigate collinearities in the selected variables, the VIF for each selected descriptor was calculated and compared [22]. In general, VIFs should be lower than 10 so that selected variables are not strongly correlated to each other. However, the decision threshold can vary from dataset to dataset [23]. For the spectral descriptors chosen in this study, no VIF (Table 2) was obtained with values above 3.8, so there is no indication for strongly correlated variables. Thus the models can be assessed by their other figures of merit, like the regression coefficient and F value.

The prediction accuracy for the individual components reassembles the trend observed in the PLS models. For 1,3-butadiene and 1-butene two descriptors were chosen, as they gave the best results whilst showing the least correlation among them. Choosing variable sets with more than two descriptors always resulted in high VIFs and were therefore discarded. Isobutane was the only component, which allowed for three descriptors with moderate VIFs. This resulted in a better model and goodness of fit for the regression (Table 2).

3.4. Analytical figures of merit

When comparing different quantitative methods, their ability to quantify a certain component inside a given matrix can be expressed by figures of merit such as the limit of detection (LOD) or the limit of quantification (LOQ). IUPAC defines LOD as the concentration level for which the risk of false non-detects (false negatives) has a probability β [24,25]. Beforehand, a critical concentration level has to be defined, involving a certain risk of false detects (false positives) with a probability α [26]. Whereas these figures of merit are well known and used for a long time in univariate analysis, it is not straight forward to apply these to multivariate datasets. This is because calibration curves obtained from multivariate datasets by different chemometric algorithms may contain different unknown signal contributions for each component. Usually, this is the case when large datasets are generated from complex sample material where the presence of unknown contributions from unknown components cannot be omitted. However, if the sample systems is known to not include such interferences, it is valid to use the IUPAC method for evaluating the resulting calibration curve of each component [27]. Equivalently, the LOQ was determined based on the

standard deviation of the response of the model and the slope of the obtained calibration curve, where the tenfold of the standard deviation is divided by slope.

The LOD and LOQ of the different methods MLR and PLS can now be compared (Table 3). The resulting values for each component are similar, with the PLS having the upper hand by a small margin. This is to be expected, because PLS uses the whole dataset (has a higher information depth) as MLR, where only a couple of descriptors were chosen to represent the components. However, the acquisition time differs quite heavily, with the MLR method only needing 12 s, which in turn significantly improves time resolution. This might be of benefit in fast changing processes, where quick reaction to certain changes is required.

4. Conclusions

A compact, robust and low-cost Fabry Pérot (FP)-based MIR filterometer for gas sensing was built and tested for multicomponent gas analysis on the example of measuring 1,3-butadiene, 1-butene and isobutene. The spectra obtained with the FP filterometer were compared with spectra recorded on a FTIR spectrometer and successfully validated. Multivariate analysis based on partial least squares (PLS) and multiple linear regression (MLR) for simultaneous quantification of the target analytes were carried out and compared. The PLS model gave best results using 5 factors with a mean RMSEP of 0.109 %. Mainly due to the slow response time of the pyroelectric detector employed in the FP-based MIR filterometer, it took about 100 s to collect a full spectrum. Given a defined target application (as a dedicated sensor) it is, however, often not required to record a full spectrum and still achieve multicomponent sensitivity. This was shown here by performing MLR based on the obtained dataset. Variable selection was applied to find the most significant descriptors which were then chosen for further analysis. The absence of collinearities was verified by calculating VIFs for the selected descriptors. MLR yielded a LOQ of 0.57 %, 0.17 % and 0.11 % for 1,3-butadiene, 1-butene and isobutane respectively, which is comparable to the results obtained from PLS analysis. The advantage of using MLR over PLS is that only data from seven positions have to be measured, which reduces the time of analysis by a factor of 8 to approximately 12 s. Thus we could show that this compact and low-cost sensor paired with chemometric processing methods is able to quantify gas mixtures composed of three different analytes. In light of the steadily increasing need for cost effective gas sensing in process applications the presented FP-based MIR filterometer provides an attractive and versatile option. The drawbacks of the FP-based MIR filterometer certainly lay in the restricted range covered and the limited spectral resolution, which can still be sufficient for certain process applications, as shown in this study on selected C_4 hydrocarbons. Apart from the low cost of the employed components a rapid reprogramming allows also adaptation to different measurement problems. This versatility combined with a small electrical as well as physical footprint pave the way for this technique to establish itself as useful chemical sensors in process monitoring and control.

Acknowledgements

We sincerely acknowledge Hans Lohninger from the Vienna University of Technology for providing us with a full version of DataLab [20], which we used to construct the PLS and MLR models. Financial support was provided by the Austrian research funding association (FFG) under the scope of the COMET programme within the research project “Industrial Methods for Process Analytical Chemistry – From Measurement Technologies to Information Systems (imPACTs)” (contract # 843546).

This programme is promoted by BMVIT, BMWFW, the federal state of Upper Austria and the federal state of Lower Austria.

References

- [1] J. Workman, B. Lavine, R. Chrisman, M. Koch, Process analytical chemistry, *Anal. Chem.* 83 (2011) 4557–4578, <http://dx.doi.org/10.1021/ac200974w>.
- [2] D. Landgrebe, C. Haake, T. Höpfner, S. Beutel, B. Hitzmann, T. Scheper, M. Rhiel, K.F. Reardon, On-line infrared spectroscopy for bioprocess monitoring, *Appl. Microbiol. Biotechnol.* 88 (2010) 11–22, <http://dx.doi.org/10.1007/s00253-010-2743-8>.
- [3] M. Brandstetter, A. Genner, K. Anic, B. Lendl, Tunable external cavity quantum cascade laser for the simultaneous determination of glucose and lactate in aqueous phase, *Analyst* 135 (2010) 3260–3265, <http://dx.doi.org/10.1039/c0an00532k>.
- [4] M.C. Phillips, M.S. Taubman, B.E. Bernacki, B.D. Cannon, R.D. Stahl, J.T. Schiffern, T.L. Myers, Real-time trace gas sensing of fluorocarbons using a swept-wavelength external cavity quantum cascade laser, *Analyst* 139 (2014) 2047–2056, <http://dx.doi.org/10.1039/c3an01642k>.
- [5] G.N. Rao, A. Karpf, External cavity tunable quantum cascade lasers and their applications to trace gas monitoring, *Appl. Opt.* 50 (2011) A100–A115, <http://dx.doi.org/10.1364/AO.50.00A100>.
- [6] M.R. Alcaráz, A. Schwaighofer, C. Kristament, G. Ramer, M. Brandstetter, H. Goicoechea, B. Lendl, External-cavity quantum cascade laser spectroscopy for mid-IR transmission measurements of proteins in aqueous solution, *Anal. Chem.* 87 (2015) 6980–6987, <http://dx.doi.org/10.1021/acs.analchem.5b01738>.
- [7] M.R. Alcaráz, A. Schwaighofer, H. Goicoechea, B. Lendl, EC-QCL mid-IR transmission spectroscopy for monitoring dynamic changes of protein secondary structure in aqueous solution on the example of β -aggregation in alcohol-denatured α -chymotrypsin, *Anal. Bioanal. Chem.* (2016), <http://dx.doi.org/10.1007/s00216-016-9464-5>.
- [8] B.P.A. Wilks, In-line infrared sensors covering the mid infrared from 2 to 14 μm (5000–700 cm^{-1}), *Proc. SPIE* 4577 (2002) 76–82.
- [9] W. Luginbu, Evaluation of designed calibration samples for casein calibration in Fourier transform infrared analysis of milk, *Leb. Technol.* 35 (2002) 554–558, <http://dx.doi.org/10.1006/fstl.902>.
- [10] E. Vargas-Rodríguez, H.N. Rutt, Design of CO, CO₂ and CH₄ gas sensors based on correlation spectroscopy using a Fabry–Perot interferometer, *Sens. Actuators B Chem.* 137 (2009) 410–419, <http://dx.doi.org/10.1016/j.snb.2009.01.013>.
- [11] M. Noro, K. Suzuki, N. Kishi, H. Hara, T. Watanabe, H. Iwaoka, CO₂/H₂O gas sensor using a tunable Fabry–Perot filter with wide wavelength range, 2003. 319–322. doi: 10.1109/MEMSYS.2003.1189750.
- [12] G. Chantry, The use of Fabry–Perot interferometers, etalons and resonators at infrared and longer wavelengths—an overview, *J. Phys. E* 3 (1982) (accessed March 31, 2014) <http://iopscience.iop.org/0022-3735/15/1/001>.
- [13] B.R. Wiesent, D.G. Dorigo, Ö. Simsek, A.W. Koch, Linear variable filter based oil condition monitoring systems for offshore wind turbines, *Proc. SPIE* 8105 8105 (2011) 81050D, <http://dx.doi.org/10.1117/12.891505>.
- [14] B.R. Wiesent, D.G. Dorigo, A.W. Koch, Limits of IR-spectrometers based on linear variable filters and detector arrays, *Proc. SPIE* 7767 7767 (2010) 77670L, <http://dx.doi.org/10.1117/12.860532>.
- [15] D.S. Kim, T. Lee, Development of an ultra-compact mid-infrared attenuated total reflectance spectrophotometer, *Opt. Eng.* 53 (2014), <http://dx.doi.org/10.1117/1.OE.53.7.074108>, 74108-1–74108-7.
- [16] N. Neumann, M. Ebermann, K. Hiller, S. Kurth, Tunable infrared detector with integrated micromachined Fabry–Perot filter, *Proc. SPIE* (2007) 646606–646612 <http://dx.doi.org/10.1117/12.698871>.
- [17] J. Antila, M. Tuohiniemi, A. Rissanen, U. Kantojärvi, M. Lahti, K. Viherkanto, M. Kaarre, J. Malinen, MEMS- and MOEMS-Based Near-Infrared Spectrometers, 2000. doi: 10.1002/9780470027318.a9376.
- [18] N. Neumann, M. Ebermann, S. Kurth, K. Hiller, Tunable infrared detector with integrated micromachined Fabry–Perot filter, *J. Micro/Nanolithography MEMS MOEMS* 7 (2008) 21004, <http://dx.doi.org/10.1117/1.2909206>.
- [19] D.A. Long, Handbook of vibrational spectroscopy, vol. 1–5. (Ed.) J.M. Chalmers, P.R. Griffiths. John Wiley & Sons, Chichester, 2002, pp. 3862, J. Raman Spectrosc. 36 (2005) 271–271. doi: 10.1002/jrs.1309.
- [20] H.H. Lohninger, DataLab 3.5, 2000 <http://datalab.epina.at/> (accessed May 6, 2016).
- [21] J.C. Evans, J. Bernstein, The vibrational spectra of isobutane and isobutane-d₁, *Can. J. Chem.* (1956) 1037–1045.
- [22] M.C.U. Araújo, T.C.B. Saldanha, R.K.H. Galvão, T. Yoneyama, H.C. Chame, V. Visani, The successive projections algorithm for variable selection in spectroscopic multicomponent analysis, *Chemom. Intell. Lab. Syst.* 57 (2001) 65–73, [http://dx.doi.org/10.1016/S0169-7439\(01\)00119-8](http://dx.doi.org/10.1016/S0169-7439(01)00119-8).
- [23] R.M. O'Brien, A caution regarding rules of thumb for variance inflation factors, *Qual. Quant.* 41 (2007) 673–690, <http://dx.doi.org/10.1007/s11135-006-9018-6>.
- [24] K. Danzer, L.A. Currie, Guidelines for calibration in analytical chemistry. Part I. Fundamentals and single component calibration (IUPAC Recommendations 1998), *Pure Appl. Chem.* 70 (1998) 993–1014, <http://dx.doi.org/10.1351/pac199870040993>.
- [25] K. Danzer, M. Otto, L.A. Currie, Guidelines for calibration in analytical chemistry part 2 multispecies calibration (IUPAC technical report), *Pure Appl. Chem.* 76 (2004) 1215–1225.
- [26] N.M. Faber, The limit of detection is not the analyte level for deciding between detected and not detected, *Accredit. Qual. Assur.* 13 (2008) 277–278, <http://dx.doi.org/10.1007/s00769-007-0351-9>.
- [27] A.C. Olivieri, Analytical figures of merit: from univariate to multiway calibration, *Chem. Rev.* 114 (2014) 5358–5378, <http://dx.doi.org/10.1021/cr400455s>.

Biographies

Christoph Gasser is a PhD student in the Lendl group. So far he worked on the development of stand-off spatial offset Raman spectroscopy. He is now working on a new infrared sensing technique for process analytical applications.

Andreas Genner is a PhD student in the Lendl group. During his master thesis he worked on the development of a sensor for monitoring cleaning processes in the pharmaceutical industry (CIP) using a broadly tunable EC-QCL as IR source. Moreover, during an internship with G. Strasser at TU Wien him worked on processing and characterization of surface emitting ring structure QCLs. At the moment, Andreas is also developing customized measurement devices for project partners in the chemical industry.

Harald Moser finished his studies on Chemical Engineering at Graz University of Technology in 2009. After a one year stay in the field of mechanics of materials and structures, he joined the Lendl research group in 2011 for his PhD thesis. His current research field includes on-line quantum cascade laser based trace gas analytics for process analytical applications.

Johannes Ofner studied chemistry at Technische Universität Wien from 2001 to 2006. He focused on physical chemistry, especially infrared spectroscopy. In spring 2008 he started his PhD studies at the Atmospheric Chemistry Research Laboratory of the University of Bayreuth (Germany) under the supervision of Prof. Dr. Cornelius Zetzsch and finished his PhD thesis with the title ‘Formation of secondary organic aerosol and its processing by atmospheric halogen species – a spectroscopic study’ in July 2011. He continued his research as a post doc in Bayreuth and joined the Lendl group in December 2012. His work is focused on development and application of spectroscopic methods (Raman and infrared spectroscopy) for atmospheric research on aerosols and trace gases as well as aerosol formation and processing and remote sensing.

Bernhard Lendl studied chemistry at Technische Universität Wien. During his PhD thesis he investigated Flow Injection Analysis coupled to Infrared Spectroscopy for process monitoring and biomedical applications. In 2001 he was appointed associate professor for Analytical Chemistry at Vienna University of Technology. From 2003 to 2004 he was guest professor at the laboratory of Prof. Miguel Valcárcel (Córdoba University, Spain). His current research focuses on the development of novel analytical techniques based on molecular spectroscopy for use in quantitative and qualitative analysis. His group concentrates on emerging new technologies such as mid-IR quantum cascade lasers, waveguide technologies, particle manipulation by ultrasound, as well as performing chemical reactions and separations in micro-fluidic systems. In 2008 he co-founded QuantaRed Technologies as a spin-off company of his research group. In 2015 he chaired the 8th international Conference on Advanced Vibrational Spectroscopy at TU Wien which was attended by 650 people. In 2016 he was appointed full professor for vibrational spectroscopy at TU Wien.

4.7 Publication III: Enhanced mid-infrared multi-bounce ATR spectroscopy for online detection of hydrogen peroxide using a supercontinuum laser

Authors: Christoph Gasser, Jakob Kilgus, Michael Harasek, Bernhard Lendl and Markus Brandstetter

Published in: *Optics Express*, 2018, Volume 26, Issue 9, Pages 12169-12179

Status: Published

Reprinted with permission <http://www.opticsexpress.org/abstract.cfm?URI=oe-26-9-12169>

Short summary:

In this work the design and characterization of a hydrogen peroxide sensors based on an ATR tunable FPF filterometer for use in oxidative gas scrubbing for the desulfurization of biogas. A four bounce ATR system was designed for the sensitive detection of the absorption band of H_2O_2 at approximately 2820 cm^{-1} . Two different light sources were employed and compared: a pulsed thermal emitter and a supercontinuum laser. In both cases, a tunable FPF with integrated detector was used for wavelength discrimination and light detection. The SCL as a light source showed an intensity 38-times higher than the pulsed thermal emitter, which resulted in a noise reduction by a factor of 4 from 5.3 to 1.3 mAU_{RMS} . The ability to quantify aqueous solutions of hydrogen peroxide was tested for both configurations. Here, the SCL showed promising improvements lowering the LOD from 0.38 to 0.13%. Additionally, the effect of the polarization of light relative to the sample interface on the effective pathlength in the employed ATR element was studied. Changing the absorbance of a sample by changing the polarization of the incident light (and therefore the effective path length) allows simple tuning of sensitivity. Furthermore, the temporal resolution could be increased by reducing the amount of averaging needed to gain sufficient SNR in the acquired spectra.

The presented work is to the author's knowledge one of the first shown chemical sensors employing SCL sources. Their unique properties should further spectroscopic applications of SCLs also in the field of MIR spectroscopy.



Enhanced mid-infrared multi-bounce ATR spectroscopy for online detection of hydrogen peroxide using a supercontinuum laser

CHRISTOPH GASSER,¹ JAKOB KILGUS,² MICHAEL HARASEK,³ BERNHARD LENDL,^{1,*} AND MARKUS BRANDSTETTER²

¹Institute for Chemical Technologies and Analytics, TU Wien, Getreidemarkt 9, 1060 Vienna, Austria

²Research Center for Non Destructive Testing GmbH (RECENDT), Science Park 2, Altenberger Straße 69, 4040 Linz, Austria

³Institute of Chemical Engineering, TU Wien, Getreidemarkt 9, 1060 Vienna, Austria

*bernhard.lendl@tuwien.ac.at

Abstract: A compact multi-bounce attenuated total reflection (ATR) probe combined with a Fabry-Pérot filter spectrometer (FPFS) has been developed for detection of hydrogen peroxide used for oxidative gas scrubbing operating in the mid-infrared (MIR) spectral region. A novel MIR supercontinuum light source is employed to enhance the quantification capabilities of the sensor and is compared to a classical thermal emitter. An improvement of a factor of 4 in noise and approximately a factor of 3 in limit of detection is shown in this study allowing fast inline detection of aqueous hydrogen peroxide solutions around 0.1%.

© 2018 Optical Society of America under the terms of the [OSA Open Access Publishing Agreement](#)

OCIS codes: (300.6340) Spectroscopy, infrared; (150.5495) Process monitoring and control; (140.3070) Infrared and far-infrared lasers; (120.2230) Fabry-Perot.

References and links

1. M. Miltner, A. Makaruk, J. Krischan, and M. Harasek, "Chemical-oxidative scrubbing for the removal of hydrogen sulphide from raw biogas: Potentials and economics," *Water Sci. Technol.* **66**(6), 1354–1360 (2012).
2. J. Workman, Jr., B. Lavine, R. Chrisman, and M. Koch, "Process analytical chemistry," *Anal. Chem.* **83**(12), 4557–4578 (2011).
3. N. J. Harrick, "Surface chemistry from spectral analysis of totally internally reflected radiation," *J. Phys. Chem.* **64**(9), 1110–1114 (1960).
4. N. J. Harrick, "Electric Field Strengths at Totally Reflecting Interfaces," *J. Opt. Soc. Am.* **55**(7), 851 (1965).
5. J. Fahrenfort, "Attenuated total reflection," *Spectrochim. Acta* **17**(7), 698–709 (1961).
6. K. R. Kirov and H. E. Assender, "Quantitative ATR-IR Analysis of Anisotropic Polymer Films: Extraction of Optical Constants," *Macromolecules* **37**(3), 894–904 (2004).
7. R. Linker, I. Shmulevich, A. Kenny, and A. Shaviv, "Soil identification and chemometrics for direct determination of nitrate in soils using FTIR-ATR mid-infrared spectroscopy," *Chemosphere* **61**(5), 652–658 (2005).
8. S. Wartewig and R. H. H. Neubert, "Pharmaceutical applications of Mid-IR and Raman spectroscopy," *Adv. Drug Deliv. Rev.* **57**(8), 1144–1170 (2005).
9. S. G. Kazarian and K. L. A. Chan, "ATR-FTIR spectroscopic imaging: recent advances and applications to biological systems," *Analyst (Lond.)* **138**(7), 1940–1951 (2013).
10. M. M. Mossoba, J. K. G. Kramer, H. Azizian, J. Kraft, P. Delmonte, A. R. F. Kia, F. J. Bueso, J. I. Rader, and J. K. Lee, "Application of a novel, heated, nine-reflection ATR crystal and a portable FTIR spectrometer to the rapid determination of total Trans fat," *JAOCS. J. Am. Oil Chem. Soc.* **89**(3), 419–429 (2012).
11. F. K. Tittel, D. Richter, and A. Fried, "Mid-infrared laser applications in spectroscopy," *Solid-State Mid-Infrared Laser Sources* **516**, 445–516 (2003).
12. P. Werle, F. Slemr, K. Maurer, R. Kormann, R. Mücke, and B. Jänker, "Near- and mid-infrared laser-optical sensors for gas analysis," *Opt. Lasers Eng.* **37**(2-3), 101–114 (2002).
13. R. F. Curl, F. Capasso, C. Gmachl, A. Kosterev, B. McManus, R. Lewicki, M. Pusharsky, G. Wysocki, and F. K. Tittel, "Quantum cascade lasers in chemical physics," *Chem. Phys. Lett.* **487**(1-3), 1–18 (2010).
14. M. Brandstetter, A. Genner, K. Anic, and B. Lendl, "Tunable external cavity quantum cascade laser for the simultaneous determination of glucose and lactate in aqueous phase," *Analyst (Lond.)* **135**(12), 3260–3265 (2010).
15. P. Figueiredo, M. Suttinger, R. Go, E. Tsvid, C. K. N. Patel, and A. Lyakh, "Progress in high-power continuous-wave quantum cascade lasers [Invited]," *Appl. Opt.* **56**(31), H15–H23 (2017).
16. J. P. Waclawek, H. Moser, and B. Lendl, "Compact quantum cascade laser based quartz-enhanced photoacoustic

- spectroscopy sensor system for detection of carbon disulfide," *Opt. Express* **24**(6), 6559–6571 (2016).
17. J. P. Waclawek, C. V. Bauer, H. Moser, and B. Lendl, "2 f-wavelength modulation Fabry-Perot photothermal interferometry," *Opt. Express* **24**, 28958–28967 (2016).
 18. H. Moser, W. Pölz, J. P. Waclawek, J. Ofner, and B. Lendl, "Implementation of a quantum cascade laser-based gas sensor prototype for sub-ppmv H₂S measurements in a petrochemical process gas stream," *Anal. Bioanal. Chem.* **409**(3), 729–739 (2017).
 19. J. M. Chalmers and P. R. Griffith, *Handbook of Vibrational Spectroscopy* (Wiley, 2016).
 20. M. Brandstetter, A. Genner, K. Anic, and B. Lendl, "Tunable Mid-IR lasers: A new avenue to robust and versatile physical chemosensors," *Procedia Eng.* **5**, 1001–1004 (2010).
 21. A. Schwaighofer, M. R. Alcaráz, C. Araman, H. Goicoechea, and B. Lendl, "External cavity-quantum cascade laser infrared spectroscopy for secondary structure analysis of proteins at low concentrations," *Sci. Rep.* **6**(1), 33556 (2016).
 22. M. R. Alcaráz, A. Schwaighofer, C. Kristament, G. Ramer, M. Brandstetter, H. Goicoechea, and B. Lendl, "External-Cavity Quantum Cascade Laser Spectroscopy for Mid-IR Transmission Measurements of Proteins in Aqueous Solution," *Anal. Chem.* **87**(13), 6980–6987 (2015).
 23. A. Schwaighofer, M. Brandstetter, and B. Lendl, "Quantum cascade lasers (QCLs) in biomedical spectroscopy," *Chem. Soc. Rev.* **46**(19), 5903–5924 (2017).
 24. R. R. Alfano, *The Supercontinuum Laser Source* (Springer, 2016).
 25. Z. Zhao, B. Wu, X. Wang, Z. Pan, Z. Liu, P. Zhang, X. Shen, Q. Nie, S. Dai, and R. Wang, "Mid-infrared supercontinuum covering 2.0-16 μ m in a low-loss telluride single-mode fiber," *Laser Photonics Rev.* **11**(2), 1700005 (2017).
 26. N. Neumann, M. Ebermann, S. Kurth, and K. Hiller, "Tunable infrared detector with integrated micromachined Fabry-Perot filter," *J. Micro/Nanolithography. MEMS MOEMS* **7**(2), 21004 (2008).
 27. A. Genner, C. Gasser, H. Moser, J. Ofner, J. Schreiber, and B. Lendl, "On-line monitoring of methanol and methyl formate in the exhaust gas of an industrial formaldehyde production plant by a mid-IR gas sensor based on tunable Fabry-Pérot filter technology," *Anal. Bioanal. Chem.* **409**(3), 753–761 (2017).
 28. C. Gasser, A. Genner, H. Moser, J. Ofner, and B. Lendl, "Application of a tunable Fabry-Pérot filtermeter to mid-infrared gas sensing," *Sens. Actuators B Chem.* **242**, 9–14 (2017).
 29. J. Kilgus, P. Müller, P. M. Moselund, and M. Brandstetter, "Application of supercontinuum radiation for mid-infrared spectroscopy," in F. Berghmans and A. G. Mignani, eds. (2016), Vol. 9899, p. 98990K.
 30. J. Kilgus, K. Duswald, G. Langer, and M. Brandstetter, "Mid-Infrared Standoff Spectroscopy Using a Supercontinuum Laser with Compact Fabry-Pérot Filter Spectrometers," *Appl. Spectrosc.* **72**(4), 634–642 (2018).
 31. M. Kumar, M. N. Islam, F. L. Terry, Jr., M. J. Freeman, A. Chan, M. Neelakandan, and T. Manzur, "Stand-off detection of solid targets with diffuse reflection spectroscopy using a high-power mid-infrared supercontinuum source," *Appl. Opt.* **51**(15), 2794–2807 (2012).
 32. X. Zhu and N. Peyghambarian, "High-power ZBLAN glass fiber lasers: Review and prospect," *Adv. Optoelectron.* **2010**, 1–23 (2010).
 33. O. Bain and P. A. Giguère, "Hydrogen peroxide and its analogues: VI. infrared spectra of H₂O₂, D₂O₂ and HDO₂," *Can. J. Chem.* **33**(3), 527–545 (1955).
 34. N. J. Harrick and A. I. Carlson, "Internal Reflection Spectroscopy: Validity of Effective Thickness Equations," *Appl. Opt.* **10**(1), 19–23 (1971).
 35. G. L. Long and J. D. Winefordner, "Limit of detection. A closer look at the IUPAC definition," *Anal. Chem.* **55**, 712A–724A (1983).
 36. P. Werle, R. Mücke, and F. Slemr, "The limits of signal averaging in atmospheric trace-gas monitoring by tunable diode-laser absorption spectroscopy (TDLAS)," *Appl. Phys. B Photophysics Laser Chem.* **57**, 131–139 (1993).
 37. J. M. Dudley, S. Coen, K. L. Corwin, N. R. Newbury, B. R. Washburn, S. A. Diddams, and R. S. Windeier, "Fundamental noise limitations on supercontinuum generation in microstructure fiber," 2003 *Eur. Quantum Electron. Conf. EQEC* **2003**, 203 (2003).

1. Introduction

Chemical-oxidative gas scrubbing has significant potential as a novel method for the desulphurization of biogas [1]. The oxidation and thereby the removal of hydrogen sulphide is facilitated by adding hydrogen peroxide (H₂O₂) to the caustic absorption solution. In this regard, a sensor providing a linear response and covering the concentration range from several percent to tenths of percent H₂O₂ in the absorption solution is needed. A classical redox sensor does not fulfil this requirement as the signal is proportional to the logarithm of the concentration, a significant drawback at higher H₂O₂ concentrations typically set in industrial scrubbers. Chemical oxidative scrubbing offers operational advantages in degree of automation and flexibility towards changes in process conditions. For efficient process control and in view of safety considerations the concentration of hydrogen peroxide in the

absorption solution has to be known promptly and accurately. This results in the need of a sensitive, selective, robust, on- or inline sensor, especially to satisfy requirements in the fields of process analytical chemistry (PAC) or process analytical technologies (PAT) [2]. Mid-infrared (MIR) spectroscopy is a molecular-specific technique which incorporates the aforementioned requirements in regards to sensitivity and selectivity. Additionally, probes can be constructed by using attenuated total reflection (ATR) inside a crystal. This facilitates a robust sample interface between optics and analyzed liquid being an absolute necessity for spectroscopic inline-sensors. ATR spectroscopy was first realized to be an elegant technique to measure MIR reflection spectra of a wide range of samples in the early 60s [3–5]. Since then, numerous applications have emerged ranging from polymer studies [6] to soil characterization [7] as well to a vast variety of analysis in pharmaceutical applications [8]. However, the interaction length of the infrared light with the investigated sample is determined by the evanescent field created at the crystal-sample interface. A measure for the extension of the evanescent field into the sample is the depth of penetration. For most applications it is not larger than a few micrometers [9] per reflection (often referred to as bounce). Small effective path lengths result in a limiting performance in detecting substances with low concentrations or small absorption coefficients. One way to improve the situation is to design a multi-bounce system [10] for increasing the effective light-sample interaction length. This approach however, is limited mainly by strong absorption of the matrix and the low optical throughput when using a thermal light source. For the latter reasons a lower Signal-to-Noise ratio (SNR) is achieved, which will result in lower sensitivities.

Beginning with lead MIR lasers in the mid to late 60s [11,12] laser sources have found their way into the field of MIR spectroscopy [13]. Especially quantum cascade lasers (QCL) offer high optical output power ranging from hundreds of mW [14] to a few W [15] enabling them to be used in long interaction path lengths. Their inherent property of having a narrow linewidth in spectral emission, which can be tuned over a small amount of wavenumbers, allows selective gas sensing using rotational-vibrational transitions in combination with different modulation and detection schemes [16–18]. Nonetheless, broader regions of the MIR spectrum have to be accessed when liquid samples with broader absorption bands are analyzed [19]. Here, external cavity QCLs (EC-QCL) are a better match due to their ability to tune over more than 100 cm^{-1} [14,20], although the spectral information can only be obtained by tuning the laser one wavelength at a time [21–23]. Continued advance and combination of several EC-QCLs already allow for the coverage of even larger spectral ranges.

In recent years another possibility of generating spectrally broad laser light in the mid-infrared region is becoming available. Thereby pulses from seed lasers emitting in the near infrared region are converted by a non-linear device, e.g. certain kinds of optical fibers. The obtained laser pulses with a broad spectral bandwidth can be described as having a super-wide continuous optical spectrum. Hence, the term supercontinuum laser (SCL) was coined [24]. SCLs offer broadband emission up to $16\text{ }\mu\text{m}$ [25] and high optical power up to several watts [26] combined with high spatial coherence and repetition rates in the MHz regime. These properties facilitate the use of the SCL as a novel and highly interesting radiation source for spectroscopic applications. The downside compared to tunable laser sources is the need for wavelength discrimination, analogous to instruments employing thermal emitters as light sources.

Therefore, in this study we propose a combination of a SCL and a tunable Fabry-Perot filter-spectrometer (FPFS) [26] as a high throughput MIR spectrometer with a multi-bounce ATR sample interface for the analysis of aqueous solutions. The ATR probe was designed for optimum performance for the target application of sensing H_2O_2 in water. In this setup the tunable FPFS acts as dispersive spectrometer including already the detector element. Tunable Fabry-Pérot filters (FPF) employing MEMS based, spring suspended movable mirrors are commercially available for the MIR spectral range up to $10\text{ }\mu\text{m}$ and allow the construction of rugged and small optical sensors, which are often referred to as filtometers. Here, we compare

the performance of two filtermeter instruments, one equipped with the SCL as a high-power radiation source to another equipped with a classical thermal emitter, which has shown to be suitable in PAT and PAC applications [27,28]. For SCLs the applicability for transmission and reflection measurements has been demonstrated before [29], as well as for stand-off detection of various compounds [30,31]. Furthermore, the long-term stability and the quantification capability of both configurations for aqueous solutions of hydrogen peroxide was assessed.

2. Materials and Methods

2.1 SCL as source of mid-infrared radiation

The laser source used in this study was a prototype laser built by NKT Photonics (Birkerød, Denmark). It is based on a combination of a pumping diode laser at 1550 nm, which produces sub-nanosecond pulses. Emitted pulses are coupled into a series of erbium-ytterbium doped fiber segments for amplification, before being converted to about 2 μm in a nonlinear silica-based fiber. This light is then amplified again in a Tm-doped fiber while the majority of the light generated by the seed laser is absorbed. The final output spectrum is generated during non-linear processes in a step-index ZBLAN (a glass family containing ZrF_4 - BaF_2 - LaF_3 - AlF_3 - NaF [32]) fiber segment and spans from 1.75 to 4.2 μm . The output power was measured to be 75 mW at a repetition rate of 40 kHz. The emitted average pulse length in this mode was determined to be 3 ns.

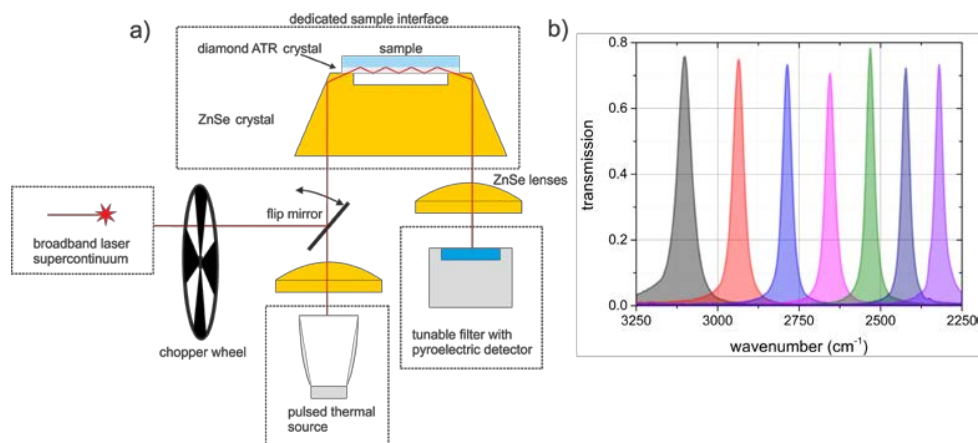


Fig. 1. a) Simplified sketch of the instrumental setup b) Transmission characteristic of the FPFS at different control voltages and tuning behavior.

2.2 ATR-FPFS

Figure 1 shows a simplified sketch of the instrumental setup. The base for the sample interface is a truncated cone (16/25 mm diameter, 10 mm thickness) made of ZnSe (Korth Kristalle, Kiel, Germany), which acts as mechanical holder for the ATR crystal as well as a focusing element, coupling the light efficiently into the ATR crystal. The ATR crystal consisted of a diamond disk (Type IIa, Diamond materials, Freiburg, Germany) with a diameter of 14 mm (flat surfaces were polished, $R_a < 20$ nm) and a thickness of 1 mm, where the light bounces for 4 times between the sample/ZnSe and air/ZnSe interface generated by the bore (4.8 mm in diameter) on top of the ZnSe cone. At the end of the diamond disk the light is coupled out into the ZnSe element, where it is collimated and guided towards the detector. The ZnSe cone and the diamond ATR crystal were integrated into a monolithic aluminum probe head. At the back of the holder, two openings allow the coupling of light. In order to couple light into the ZnSe cone a focusing lens with $f = 25$ mm (positive meniscus

lens ZC-PM-12-25, ISP Optics, New York, USA) was used for the thermal emitter. Since the SCL had a collimated output beam, no lens was required. In order to couple the light out of the ZnSe cone and focus on the detector, again a positive meniscus lens was used (ZC-PM-12-25, ISP Optics, New York, USA, $f = 12$ mm). The detector was mounted in a 16 mm cage system (Thorlabs Inc, New Jersey, USA) using a translational mount (SCP05, Thorlabs Inc, New Jersey, USA) for adjustment. The ATR was designed to have 4 bounces in the desired spectral region. A FPFS with a pyroelectrical detector element (LFP-3144C, InfraTec GmbH, Dresden, Germany) was used for wavelength discrimination. For convenience, the setup incorporating the thermal emitter will be denoted by the prescript PTE (pulsed thermal emitter) and the laser setup with the prescript SCL. Table 1 summarizes the instrumentation of the compared configurations. A flip mirror (SCP05, Thorlabs Inc, New Jersey, USA) was integrated into the optical setup to switch between SCL and thermal emitter.

The thermal emitter (μ Hybrid, Hermsdorf, Germany) was pulsed with a duty cycle of 50%, at 5 V and 120 mA. The SCL was modulated using an optical chopper wheel (MC2000B-EC, Thorlabs Inc, New Jersey, USA) reducing the modulation frequency to 10 Hz in order to adapt to the time constant of the FPFS. A single spectrum with the FPFS was obtained by step-scanning the filter over the whole available spectral range with 2 nm steps. This resulted in an acquisition time of 36 s per spectrum.

Table 1. Overview over the different instrumentation featured in this study.

| Short name | Light source | Type | Detector | Type | Remarks |
|------------|------------------------|-----------------------------------|-----------------------------|-----------|--|
| PTE-FPFS | Pulsed thermal emitter | μ -Hybrid JSIR350-4-AL-R-D6.0 | FP-filter with pyrodetector | LFP-3144C | Tuning range: 3.1 – 4.4 μm (3225 – 2270 cm^{-1}) |
| SCL-FPFS | Supercontinuum laser | SuperK MIR, NKT Photonics | FP-filter with pyrodetector | LFP-3144C | FWHM: 55-70 nm Detectivity @ 10 Hz: 3.6E + 06 $\text{cm}(\sqrt{[\text{Hz}]})/\text{W}$ |

2.3 Chemicals

For the quantitative measurements, aqueous solutions of hydrogen peroxide (Sigma Aldrich) were used. Samples were prepared by dilution from a stock solution with a concentration of 15% for hydrogen peroxide with deionized water.

3. Results and discussion

3.1 Noise evaluation

Figure 2 depicts the raw intensity spectra obtained when the surface of the ATR is wetted with water. Both PTE and SCL show a similar intensity profile, although the PTE for itself should have a much broader and thus smoother emission characteristic (Fig. 2(a), red line). On the higher wavenumber end range of the FPFS, the fall of intensity is caused by the strong absorption of the vibrational O-H stretch oscillations of water for the thermal emitter. The SCL has itself a strong decline on the higher wavenumber end, as indicated by its intensity spectrum. On the lower wavenumber part of the spectrum the absorption of the diamond ATR crystal itself reduces throughput. Only the resulting spectral gap with sufficient transmitted light can be used for MIR spectroscopy of aqueous solutions.

In order to assess the noise characteristic of each configuration, two consecutive spectra over the whole range of the tunable FPFS were obtained, from which absorbance spectra were calculated, thus yielding 100% lines.

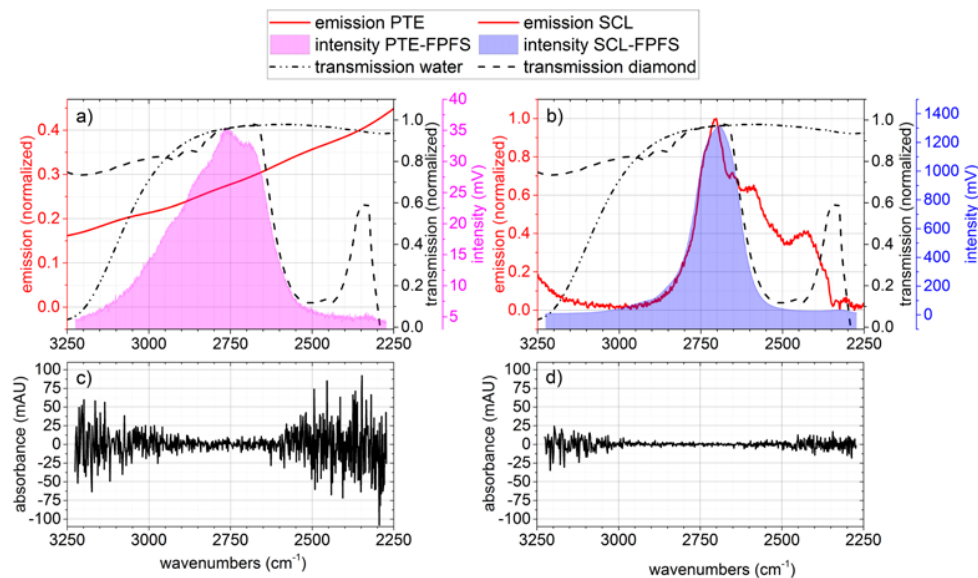


Fig. 2. Single channel spectrum (intensity) of the a) PTE-FPFS setup (magenta filled curve) and the b) SCL-FPFS setup (blue filled curve), showing also the PTE and SCL emission spectrum, the diamond and water transmission spectrum. c) and d) show the 100% lines of the aforementioned setups.

The interesting part of the available spectrum resides between 2620 and 2920 cm⁻¹, as hydrogen peroxide has a characteristic absorption band (O-H stretch vibration) at approximately 2820 cm⁻¹ [33]. This region is covered by both light sources. At the maximum the PTE-FPFS combination only reaches about 35 mV amplitude, whereas the SCL-FPFS comes to 1345 mV, which is an increase by a factor of 38. Here, the much higher light intensity of the SCL shows its strength. Figures 2(c) and 2(d) show the aforementioned 100% lines. In the region of interest the PTE-FPFS exhibits a peak-to-peak (PP) noise of 40 mAU with a root mean square (RMS) of 5.3 mAU. The SCL-FPFS shows less noise with a PP noise of 8 mAU and a RMS noise of 1.3 mAU.

3.2 Quantification of hydrogen peroxide

A standard concentrations series of aqueous hydrogen peroxide solutions was prepared and measured with both instrumentations. Figure 3 depicts the recorded spectra of the 9% hydrogen peroxide solution obtained with PTE-FPFS, SCL-FPFS and a Bruker (Ettlingen, Germany) Tensor 27 FTIR spectrometer equipped with a single bounce diamond ATR element (Platinum ATR, Bruker, Ettlingen, Germany). The PTE-FPFS and the FTIR spectrum show similar absorbance maxima considering the PTE-FPFS ATR is a four-bounce ATR resulting in approximately four-times higher absorption values.

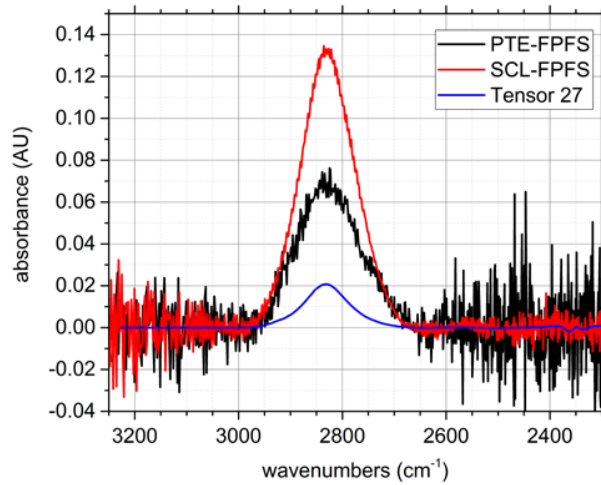


Fig. 3. 9% hydrogen peroxide solution spectra measured with the PTE-FPFS, SCL-FPFS and a Bruker Tensor 27 equipped with a Platinum ATR (single bounce).

The same setup with the SCL as the light source behaves differently by showing an absorbance of twice the value of its thermal powered counterpart. Primarily, this can be explained by the fact that the SCL is emitting polarized radiation, whereas the PTE source emits non-polarized light. This results in a different effective optical path length (also known as effective thickness), which corresponds to the thickness of a material that would result in the same absorbance in a transmission experiment as that obtained in an ATR experiment [34]. Light which is polarized parallel to the plane of incidence (denoted by the subscript p) has a larger effective path length than light which is perpendicular polarized (denoted by the subscript s).

$$d_s = \frac{\lambda}{n_1} \cdot \frac{n_{21} \cos(\theta)}{\pi(1-n_{21}^2)\sqrt{\sin^2(\theta)-n_{21}^2}} \quad (1)$$

$$d_p = \frac{\lambda}{n_1} \cdot \frac{n_{21} \cos(\theta)[2\sin^2(\theta)-n_{21}^2]}{\pi(1-n_{21}^2)[(1+n_{21}^2)\sin^2(\theta)-n_{21}^2]\sqrt{\sin^2(\theta)-n_{21}^2}} \quad (2)$$

Equations (1) and (2) give an approximated solution for the effective path length of parallel (d_p) and perpendicular (d_s) polarized light, where λ is the wavelength, θ is the angle of incidence, n_1 is the refractive index of the sample and n_{21} is the ratio of refractive indices of the ATR crystal and the sample. Figure 4(a) shows the effective path length over the angle of incidence calculated for perpendicular and parallel polarization as well as the ratio between the two. Figure 4(b) depicts the reflectance over the angle of incidence for p-polarization and s-polarization for the case of a non-absorbing sample (solid lines) and an absorbing sample (with an assumed κ of 0.01, dashed lines). Figure 5(a) shows the effective path length calculated for the spectral range used in this study for both polarization states for a one-bounce ATR. It results in 5.2 μm for p-polarization and 2.6 μm for s-polarization at the position of the maximum of the hydrogen peroxide band. When the angle of incidence (at 45°) and the ratio of the refractive indices of the sample/ATR interface are assumed to be constant, the effective path length of the p-polarized light is approximately twice as high as that of the s-polarized light.

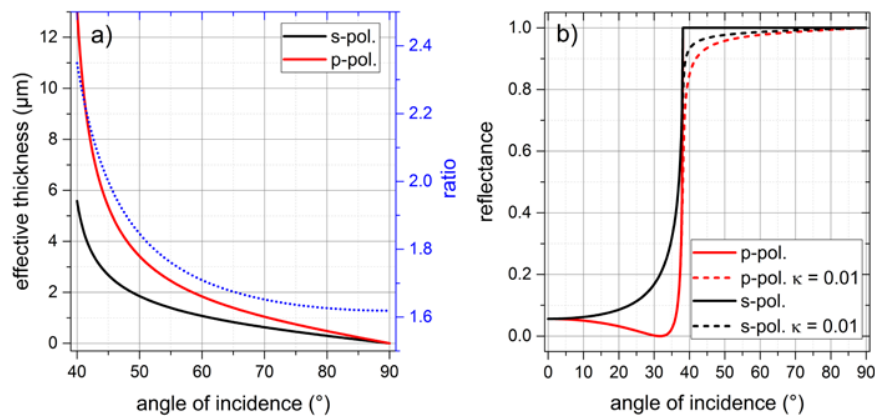


Fig. 4. a) Effective path length (solid lines) over the angle of incidence calculated for perpendicular (s, black) and parallel (p, red) polarization. The ratio of both is depicted as the dotted blue line. b) Reflectance over the angle of incidence for p-polarization and s-polarization for the case of no absorbance in the sample (solid lines) and for a sample absorbance of $\kappa = 0.01$ (dashed lines).

In this case the dispersion of the refractive index around the absorption band of hydrogen peroxide is neglected. Figure 5(a) depicts the raw absorbance spectra for p- and s-polarized light of the SCL, respectively. Figure 5(b) shows the comparison of the theoretical ratio to the ratio of the measured spectra. A good correlation between the calculation and the measurement can be observed. Aside from polarization, the beam characteristics of the two sources also influence the effective path length. The PTE has to be focused into the ATR by means of a lens due to the larger divergence and beam diameter compared to the SCL. The SCL is spatially coherent with a divergence of 1.5 mrad, whereas the PTE has an active area of $2.2 \times 2.2 \text{ mm}^2$ with a reflector cap producing a divergent beam of a diameter of approximately 6 mm. This results in a different coupling with different angle of incidence ranges, which can change the effective path lengths as shown in Fig. 4(a).

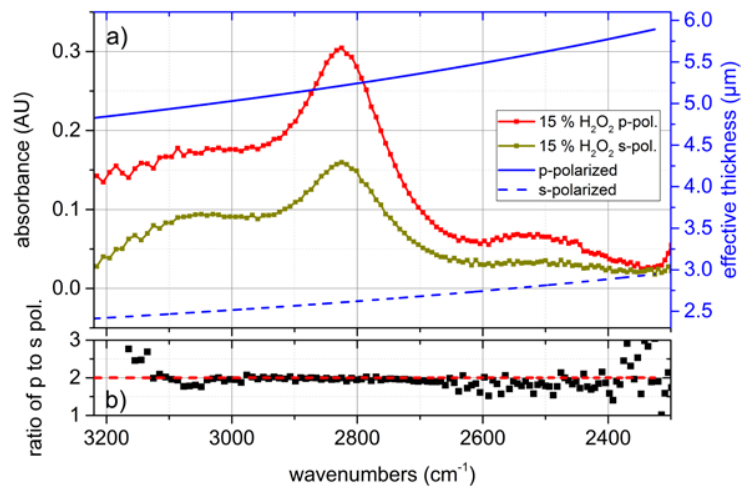


Fig. 5. a) Raw absorbance spectra and effective depth of penetration (blue) calculated for perpendicular (s) and parallel (p) polarization. b) Ratio between the absorbance in the case of p-polarization to s-polarization for measured values (black squares) and theoretical calculation (red dashed line).

For testing the capability of each system in quantifying hydrogen peroxide, several spectra with differently concentrated H_2O_2 standards were measured. The obtained spectra were

filtered using a Savitzky-Golay algorithm with a window size of 19 and a second order polynomial. Furthermore, a baseline correction was performed, before the characteristic band at 2780 cm^{-1} was integrated (between 2720 and 2900 cm^{-1}) and plotted against the concentration of the prepared standard. The resulting calibration curves are displayed in Fig. 6. The slope for the SCL-FPFS configuration is higher by a factor of approximately 1.8 compared to the PTE-FPFS configuration, which can be explained by the aforementioned differences regarding the polarization and coupling of the used light sources.

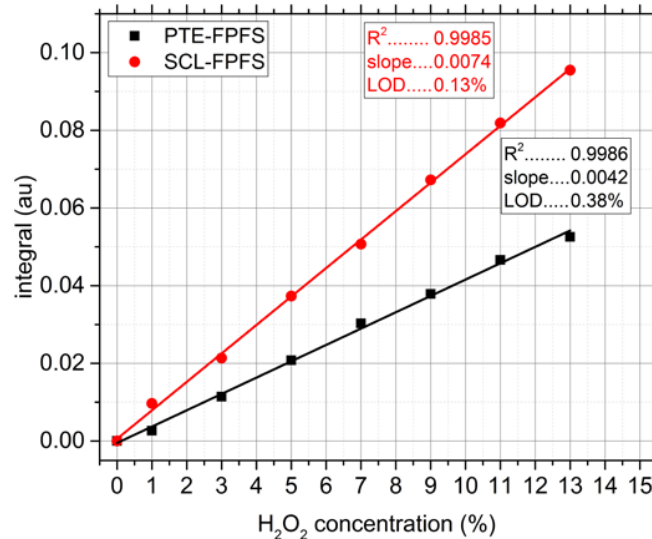


Fig. 6. Integrated areas against the concentration of the standards prepared for hydrogen peroxide for the two different configurations.

Limits of detection (LODs) were calculated using the standard deviation of the blank measurements, a k -value of 3 and the slope of the calibration curve according to the IUPAC definition [35]. Table 2 summarizes the results found for both configurations. The SCL-FPFS outperforms the PTE-FPFS. This can be primarily attributed to the higher sensitivity and to the lower noise of the filterometer employing the supercontinuum laser.

Table 2. Analytical figures of merit for the quantification of hydrogen peroxide in aqueous solution by the two configurations.

| configuration | acquisition time (s) | noise (mAU) | hydrogen peroxide | | |
|---------------|----------------------|-------------|-------------------|----------------|---------|
| | | | slope | R ² | LOD (%) |
| PTE-FPFS | 36 | 5.3 | 0.0042 | 0.9986 | 0.38 |
| SCL-FPFS | 36 | 1.3 | 0.0074 | 0.9985 | 0.13 |

3.3 Long term stability

In order to assess the long term stability of the system, consecutive spectra of a blank (water) were recorded over several hours. The RMS noise of the resulting 100% line was derived in the same spectral region as was used for integration and quantification in section 3.2. This time series was used to calculate an Allan variance, which evaluates the deviation of a measurement in dependence of its integration time τ [36].

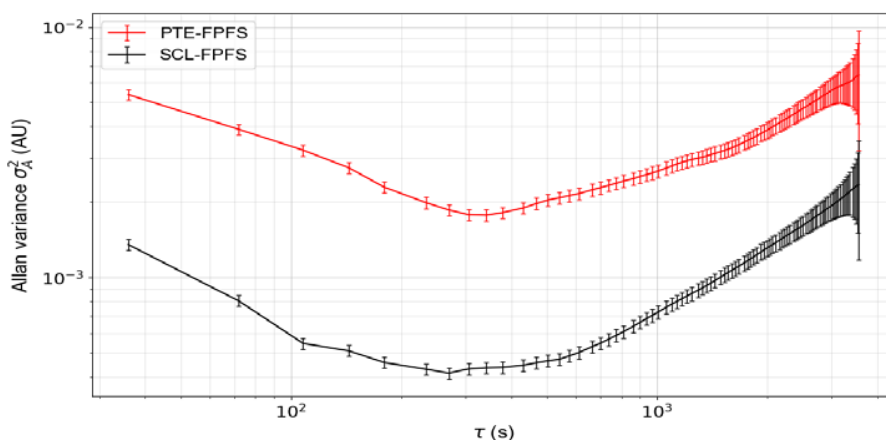


Fig. 7. Allan variances for the different instrument configurations.

The Allan variance plot (Fig. 7) is a particularly suitable tool for the identification of different noise types and the time domains where those noise types are dominant. When normally distributed noise (“white” noise) is assumed, the Allan variance should constantly decrease with increasing integration time. In case of SCLs this type of noise mainly originates from non-linear amplification of the input laser shot noise and spontaneous Raman noise [37]. With increasing integration time Allan plots typically reveal a turning point after which the variance increases again indicating the presence of signal drifts, e.g. due to power fluctuations or thermal drifts. Such a behavior results in a region of minimum Allan variance, which can also be observed in Fig. 7. Here, the use of the SCL as radiation source results in the smaller overall Allan variance which corresponds to the noise behavior discussed before (see 100% lines in Fig. 2). The PTE has a much lower intensity, which results in larger measurement noise and the highest Allan variance. The combination SCL-FPFS appears to have a slightly higher drift, since the minimum of the Allan curve is found earlier at around 280 s compared to the 350 s of the PTE-FPFS. This indicates that the PTE is slightly less affected by intensity drifts than the SCL. However, the SCL-FPFS appears to be superior over the PTE-FPFS in terms of sensitivity with a similar long term stability.

4. Conclusion

In this study a dedicated 4-bounce diamond ATR interface was built for infrared spectroscopic analysis of aqueous solutions of hydrogen peroxide, intended for use in oxidative gas scrubbing, in the wavelength region from 3.1 to 4.4 μm . The coupling of mid-infrared supercontinuum radiation into the ATR was compared to the use of the standard light source in ATR spectroscopy, being a thermal emitter. In both cases, a tunable Fabry-Perot filter with integrated detector was used for wavelength discrimination and light detection. The achievable light throughput through the ATR crystal and the corresponding signal as well as its spectral noise was determined. The PTE-FPFS showed lowest light intensity at the detector. The SCL as a light source produced a signal 38-times higher than the PTE, which resulted in a noise reduction by a factor of 4 from 5.3 to 1.3 mAU, calculated as the RMS noise in the region of interest between 2620 and 2920 cm^{-1} . For both configurations the ability to quantify aqueous solutions of hydrogen peroxide was tested and compared. Here, the SCL showed promising improvements lowering the LOD for hydrogen peroxide detection from 0.38 to 0.13%. Additionally, the effect of the polarization of light on the effective path length in ATR crystals was studied. Changing the absorbance of a sample by changing the polarization of the incident light (and therefore changing the effective path length) allows tuning of sensitivity. This could be used to enhance measurements of low-concentrated

compounds of interest or to reduce the sensitivity if strong infrared absorbers challenge the linearity of the method. Furthermore, the temporal resolution could be increased by reducing the spectral points measured for a spectra. Instead of stepping over the whole available spectral range of the FPFS, only interesting positions could be selected, decreasing the measurement time.

In conclusion, the gained results prove that a promising new type of spectroscopic light source has become available with the advent of MIR SCLs. SCLs combine properties of conventional thermal emitters with those of modern MIR QCLs, resulting in a high-power, spectrally broadband MIR source with laser properties. With these unique properties further spectroscopic applications of SCLs are likely to follow. In this regard, the development and application of dedicated detection schemes is a crucial factor, as was shown in the present study.

Funding

Austrian research funding association (FFG) grant “Industrial Methods for Process Analytical Chemistry - From Measurement Technologies to Information Systems (imPACts)” (843546).

Acknowledgments

Financial support was provided by the Austrian research funding association (FFG) under the scope of the COMET program within the research project “Industrial Methods for Process Analytical Chemistry - From Measurement Technologies to Information Systems (imPACts)” (contract #843546) and by the strategic economic- and research program “Innovative Upper Austria 2020” of the province of Upper Austria.

4.8 Publication IV: Simultaneous Laser Doppler Velocimetry and stand-off Raman spectroscopy as a novel tool to assess flow characteristics of process streams

Authors: Bahram Haddadi, Christoph Gasser, Christian Jordan, Michael Harasek, Bernhard Lendl

Published in: *Chemical Engineering Journal*, 2018, Volume 334, Pages 123-133

Status: Published

Reprinted with permission <http://dx.doi.org/10.1016/j.cej.2017.10.027>

Short summary:

This work describes the first implementation of Raman spectroscopy and LDV using a single laser system as light source for both instruments, ensuring measurement from the same location. The application is primarily focused on the determination of flow characteristics of process streams, which are of utmost importance in industrial chemical plants. Online measurement of physical and chemical properties of such streams like velocity, turbulence, chemical composition and concentration, plays a key role in adjustment and optimization of industrial processes. In this paper, a novel method for simultaneous measurement of velocity, composition, and concentration through combination of Laser Doppler Velocimetry (LDV) and Raman spectroscopy is presented and discussed.

Experiments on mixing of water and ethanol streams in a custom-built T-junction geometry were performed using LDV to obtain velocity and Raman spectroscopy to measure concentration using the suggested method. Results are compared against CFD simulations using models for mixing of miscible, multi-species liquids at different flow regimes. CFD predicts turbulent diffusion to be the dominant phenomena in mixing in the T-junction since the turbulent diffusion coefficient is significantly higher than the molecular diffusion coefficient. A mean deviation of 8% between model and experiment for velocity and 10% for concentration evaluation was determined, which suggests the feasibility of this technique for simultaneous monitoring fluid dynamics and chemical composition in process streams.



Contents lists available at ScienceDirect

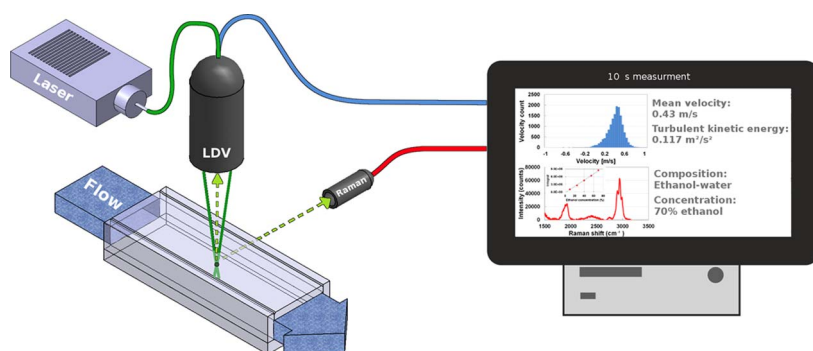
Chemical Engineering Journal

journal homepage: www.elsevier.com/locate/cej

Simultaneous Laser Doppler Velocimetry and stand-off Raman spectroscopy as a novel tool to assess flow characteristics of process streams

Bahram Haddadi^{a,*}, Christoph Gasser^b, Christian Jordan^a, Michael Harasek^a, Bernhard Lendl^b^a Institute of Chemical, Environmental & Biological Engineering, TU Wien, Getreidemarkt 9, 1060 Vienna, Austria^b Institute of Chemical Technologies and Analytics, TU Wien, Getreidemarkt 9, 1060 Vienna, Austria

GRAPHICAL ABSTRACT



ARTICLE INFO

Keywords:

Laser Doppler Velocimetry
Raman spectroscopy
Chemical composition
Velocity measurement
Computational Fluid Dynamics

ABSTRACT

Flow characteristics of process streams are important in industrial chemical plants. Online measurement of physical and chemical properties of such streams like velocity, turbulence, chemical composition, and concentration, plays a key role in adjustment and optimization of industrial processes. In transient processes with steep changes in the concentration and velocity (e.g. mixing of fluid with different viscosities or multiphase flows) it is important to monitor process parameters at the same time and position to be able to interpret them correctly. In this work, a novel method for simultaneous measurement of velocity, composition, and concentration relying on two well-known methods, Laser Doppler Velocimetry (LDV) and Raman spectroscopy is presented and tested. Both techniques were combined using the same laser as light source, thus making sure sampling from exactly the same position at the same time is achieved. Experiments on mixing of water and ethanol streams in a custom-built T-junction geometry were performed using LDV to obtain velocity and Raman spectroscopy to measure concentration using the suggested method. Results are compared against Computational Fluid Dynamics (CFD) simulations using models for mixing of miscible, multi-species liquids at different flow regimes. CFD predicts turbulent diffusion to be the dominant phenomena in mixing in the T-junction since the turbulent diffusion coefficient ($\sim 0.02 \text{ m}^2/\text{s}$) is much higher than the molecular diffusion coefficient ($\sim 10^{-8} \text{ m}^2/\text{s}$). A mean deviation of 8% between model and experiment for velocity and 10% for concentration evaluation was observed, which suggests the feasibility of this technique for simultaneous monitoring of process streams.

* Corresponding author.

E-mail address: bahram.haddadi.sisakht@tuwien.ac.at (B. Haddadi).<http://dx.doi.org/10.1016/j.cej.2017.10.027>

Received 26 May 2017; Received in revised form 28 August 2017; Accepted 5 October 2017

Available online 07 October 2017

1385-8947/© 2017 Elsevier B.V. All rights reserved.

1. Introduction

Process control and optimization are inseparable parts of every industrial process and plant. Regular measurements (e.g. online or offline at a suitable periodic schedule) of the actual status of the process to gain feedback from the system are common and necessary. As more information is provided, a better understanding of the process can be obtained, enabling a more efficient and economic process management. Usually, in process flow streams, velocity, velocity fluctuations (an indicator of mixing and turbulence), compositions and concentrations of key components are of utmost importance. Based on these properties it is possible to predict flow rates and process states. Furthermore, these properties can also be used for validation and calibration of different available models, e.g. the available models used in predictive process control or Computational Fluid Dynamics (CFD) [1].

There exists a variety of techniques for detecting chemical composition and measuring concentration in fluids, among which optical detection approaches are widely applied methods [2,3]. Different spectroscopic detection methods can be used for concentration and composition measurements, e.g. ultraviolet absorption (UV), thermal lens microscopy (TLM) and laser-induced fluorescence (LIF). In general, optical methods are capable of measuring chemical species without interfering with the flow [4]. Among these methods, LIF received special attention because of its accuracy and high sensitivity [5].

Funatani et al. [6] used a particle image velocimetry (PIV) system to measure the velocity field in the thermal flows and simultaneously used a two-color LIF to measure the temperature in a turbulent buoyant plume. Combining planar LIF (PLIF) and PIV, Charogiannis et al. [7] introduced a new method for investigation of hydrodynamic characteristics of thin liquid film flows. They added LIF to a PIV system to mask out particle reflections from raw images and in order to measure spatially and temporally resolved film thickness.

Although LIF as a detection technique is widely used, the main drawback is that usually, the components of the stream itself do not fluoresce and they need to be treated with either fluorescent particles or fluorescence tags, which requires extra effort and is expensive. Especially in multi-phase streams this is problematic, as different markers would be required, which have to follow the flow pattern of the original stream components.

Another well-established method for evaluation of chemical and structural properties of species is Raman spectroscopy. This technique is capable of analyzing non-fluorescent samples [5]. Park et al. [5] used confocal Raman microscopy (CRM) to study the mixing behavior in laminar micro-mixers and they compared the images from CRM to confocal fluorescence microscopy (CFM). Rinke et al. [8] utilized pulsed Raman imaging to analyze the concentration of two components (water and ethanol) at the outlet of a macro mixer. They compared their results with computational fluid dynamics simulations to show the validity of Raman imaging for measuring concentration profiles during a mixing. Beushausen et al. [9] combined two-dimensional molecular tagging velocimetry (2D-MTV) with planar spontaneous Raman scattering (PSRS) to investigate the velocity and concentration fields of water and ethanol in a micro-mixer. They also compared their results with standard μ PIV. Wellhausen et al. [10] used a combination of PIV and Raman scattering to study the mixing in micro-mixers.

Among available velocity measurement techniques Laser Doppler Velocimetry (LDV) has received special attention because of its capability of measuring instantaneous velocity without interfering with the flow, enabling accurate and reproducible measurements at different working conditions (e.g. high temperature) [11–13]. LDV is a direct measurement technique without the need of calibration: It measures the fluid stream velocity and velocity fluctuations based on the detection of scattered light by suitable seeding particles passing between two or more collimated, monochromatic and coherent laser beams [14].

Rottenkolber et al. [15] tried to combine the LDV with Phase Doppler Anemometry (PDA) to investigate the two-phase flow inside

the spray of an SI-engine by adding fluorescent tracer particles to the gas phase. They managed to characterize time-resolved droplet motion and induced air flow. They also compared the results to the PIV. Quinzani et al. [16] combined LDV with Flow Induced Birefringence (FIB) to measure the stress and velocity fields of a viscoelastic solution through a planar abrupt contraction. Lemoine et al. [17] used a combination of LDV and LIF to measure the velocity and concentration in a turbulent submerged free jet and measured the average field of concentration, velocity, and local eddy diffusivity. Dibble et al. [18] did simultaneous LDV-Raman scattering velocity and scalars sampling in the turbulent flames. Using a LDV system with a two-color dual beam, real fringe system laser combined with a dye laser for Raman measurements, they also presented an analytical equation for generating unbiased velocity and scalar distributions using the data from seeding in only one stream. Moss [19] used LDV to study velocity in the open premixed turbulent flame and quantifying the scattered light he also analyzed the liquid concentration in the flame.

From these studies it was found that a combination of LDV and Raman spectroscopy could be capable of providing both velocity and composition of a process stream: LDV is suitable for higher measurement frequencies, which can provide the required turbulence data while Raman spectroscopy delivers composition and concentration information.

Using LDV and Raman spectroscopy integrated into one setup, information about the flow characteristics and the composition for the evaluation of a stream can be obtained at once. However, if these two methods are installed separately there is no guarantee that the process data provided is consistent and from the same fluid element at the same time – even if the focal points of the probes are aimed at the same position within the geometry. The authors believe that especially for more complex flows, including turbulent mixing or multiphase flows, this complicates the interpretation of the measured data and in some cases, may lead to misleading or even wrong results (e.g. considering the slip velocity of two non-mixing components inside a multiphase flow – if the velocity measurement is attributed to the wrong phase the overall evaluation will be degraded or flows with steep velocity or concentration gradients). Therefore, in this work we introduce a new method for combining these two technologies with the goal of obtaining information about the condition of the process at the same position and time. For simplicity, the first test setup for demonstrating the capability of the new approach was run with a single phase two component (water – ethanol) mixing system consisting of a T-junction.

CFD can provide a detailed spatial and temporal representation of the system. CFD is the numerical analysis of systems including fluid flow and related phenomena. CFD provides a powerful tool for having a detailed look inside dynamic streams, which are hard or impossible to experimentally evaluate or very expensive to analyze. Usually, it is used to further analyze phenomena inside a given geometry or optimize the process by adjusting parameters that are difficult to test in laboratories or pilot plants [20,21].

In this study, the T-junction measurement setup was simulated using well established CFD algorithms (e.g. transient simulation of multi-species fluids) and models (e.g. transitional turbulence model). The results of CFD simulations were compared to the measured velocities obtained with LDV and compositions obtained via Raman spectroscopy. Finding a reasonable agreement of the measured flow and concentration profiles with the simulated model supports the feasibility and suitability of the proposed method.

2. Theoretical background

2.1. Laser Doppler Velocimetry (LDV)

In the past, flow patterns were determined using dye injection into the fluid and observing dye streamlines [22]. This method was not applicable to very low and high velocity flows. In 1964 a new method

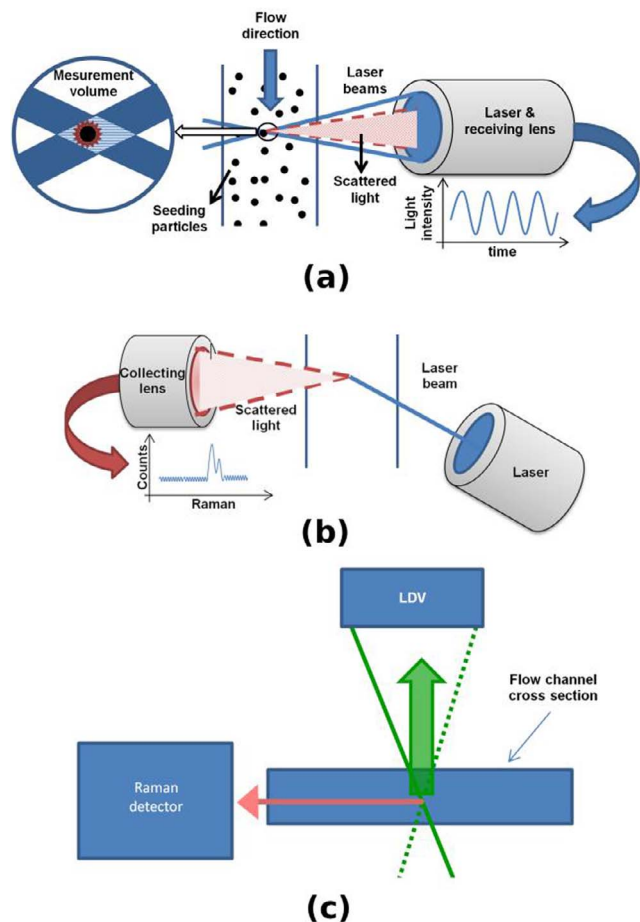


Fig. 1. a – Basic setup for LDV flow measurements (back-scatter mode), b – Basic system setup for Raman scattering measurements, c – Basic sketch of the measurement arrangement: Use of the LDV light source for Raman excitation. LDV signals can be collected in back-scatter geometry, Raman signal perpendicular to main light path.

based on the examination of Doppler shifts using a laser spectrometer was introduced. The new method was named LDV [22,23].

In the LDV method, two coherent laser beams are focused in a small volume, forming a special “fringe” light pattern. When seeding particles travel through this fringe area they pass bright and dark areas and scatter light. The scattered light is collected with a receiver probe and detected using e.g. photomultipliers. Since the distance between the dark and bright areas in the measurement volume is known, the velocity of a particle can be calculated based on the count of fringes traversed by particle per unit time (Fig. 1-a).

$$v = d \times f \quad (1)$$

where v is the particle velocity, d and f are the fringe spacing and the data rate (counts of scattered light per unit time), respectively. Since the seeding particles are chosen to be very small and are used at rather low concentrations it can be assumed that they do not have any effect on the flow pattern and move with flow velocity [24,25]. From the collected velocity data, statistical analysis for mean velocity and turbulence (turbulent intensity, turbulent kinetic energy) can be generated [26].

For measuring the direction of the flow as well as measuring slowly moving or zero velocity particles a Doppler shift is added to one of the laser beams. If the particle is not moving the collected signal will have a frequency equal to the induced frequency shift. When the particle moves in one direction the recorded frequency is the sum of the particle frequency (generated by the velocity of the particle) and the induced frequency shift. The opposite direction will lead to a sum frequency,

which is lower than the induced frequency shift, since the two shifts have different signs. As the induced shift frequency is known and constant, the direction and the velocity of a particle can be calculated [27].

Key advantages of this technique are the possibility to measure fluid flow calibration-free with high sampling frequency without mechanical interference [28]. If measurements are done in the back-scattering mode just one small opening in the system is required. Using a traversing unit, multiple points in the flow can be measured in sequence for profiling or mapping of larger areas of interest. Some drawbacks of the LDV are first the need for seeding particles and second the necessity of optical access to the fluid medium [29,30].

2.2. Raman spectroscopy

Raman spectroscopy is a technique used to observe fundamental vibrational modes in a molecular system [31]. Since the development of lasers as reliable monochromatic light sources, Raman spectroscopy has emerged in a variety of scientific as well as routine analytical applications ranging from medical investigation [32–34] over material characterization [35–37] to food analysis [38–40]. Stand-off or remote Raman spectroscopy describes the same spectroscopic technique with the fundamental difference that the studied sample is located at a certain distance of the detecting instrument [41]. It was originally developed to probe hazardous or dangerous analytes from a safe distance [42]. Usually, a laser is used to excite the sample and an objective to collect the Raman scattered photons, which are then spectroscopically analyzed (Fig. 1-b). The laser light excites the molecules, which will absorb or transfer energy to the photons (Stokes and anti-Stokes scattering) and, for a certain molecule, will cause a characteristic shift in energy. The resulting Raman spectrum is characteristic for a specific molecule (fingerprint) and is used to identify a component. The amount of Raman scattered photons is directly proportional, among other factors, to the number of molecules of a specific component and can be linked to the concentration of the same [31]. Mixtures of several different compounds can lead to complicated Raman signatures with several overlapping bands. For the sake of completeness, it should be mentioned that there are several methods to untangle complex spectra and subsequently gain specific information about very sophisticated samples, e.g. principal component analysis or partial least squares [43]. Here, we prevent this scenario by choosing components with unique Raman bands, which makes identification and quantification as straightforward as possible. The advantages of this technique are the high selectivity towards different chemical compounds as well as the non-destructive nature of the measurement, which makes it viable for in-situ applications. Additionally, it is a laser-based technique using a similar instrumentation as LDV and therefore, the two methods are highly compatible.

2.3. Novel measurement technique

As mentioned in the introduction, it is valuable to have velocity and composition information of the process at the same time from the same sampling position as it gives insight into the current state of the system. A combination of Raman and LDV allows to simultaneously gain velocity in the process stream as well as chemical composition at a specific location with a high time resolution in order to resolve turbulent and mixing phenomena. The most important aspect is to sample light from the same spot at the same time as the velocity measurement is carried out. This is achieved by using the LDV laser light setup (2 or 4 laser beams focused on one spot for 1D or 2D LDV, respectively) as a source for the Raman excitation. The Raman photons can be simultaneously collected in different scattering configurations (for this study 90° was chosen); the LDV signal was collected in backscatter mode with combined sender-receiver optics (Fig. 1-c) [44].

Fluid composition and concentration of the components can be

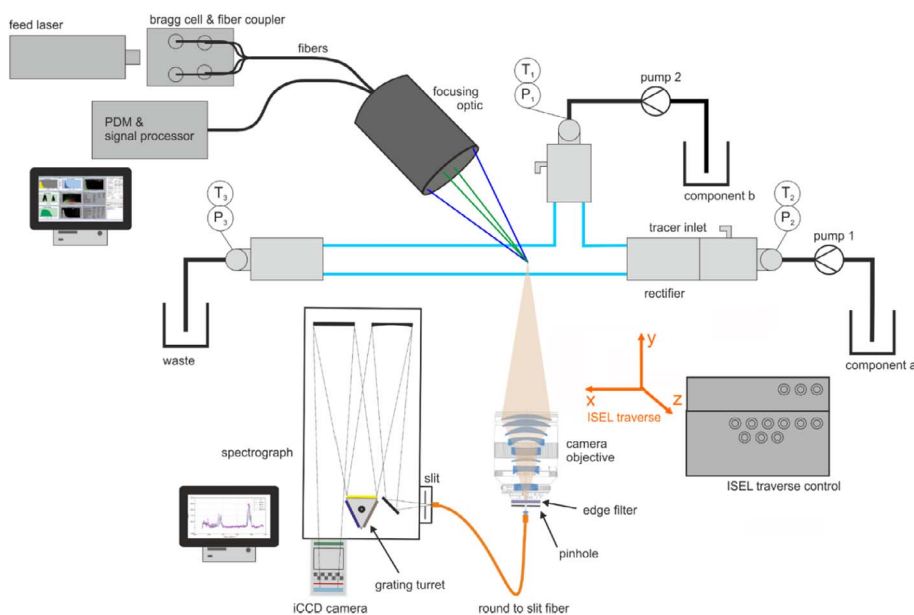


Fig. 2. Schematic of the experimental setup: LDV laser light source and processor in upper left part, Raman spectrometer lower left part. Upper right section: Fluid inlet.

derived from the qualitative and quantitative analysis of the collected Raman spectrum. Generally, if no overlapping spectral features of the involved components are present, it is sufficient to evaluate the strength of a specific band in the Raman spectrum corresponding to the analyte of interest (e.g. band height, area under the band etc.). The investigated fluid stream can be accessed optically either by using a fully transparent part of pipe (or equivalent geometry) or when working in back-scattering configuration, a viewing window made of a transparent material would suffice. This enables this technology to investigate also process facilities already in operation in order to optimize process parameters even further. The critical point is the addition of the two parameters, composition and concentration, to the velocity information. With these, multiphase flow behavior (with low volume fraction of dispersed phase to ensure undisturbed measurements), as well as reactive reagents, can be characterized at once by the same measurement.

3. Experimental

As it can be seen from Fig. 2, the feed laser beam (CVI Melles-Griot Air cooled Argon Ion Laser – 300 mW with a multiline output) is split into two beams (488 nm blue, 514.5 nm green), which are partially shifted by a TSI Fiber-light Wavelength separation module with Bragg cell frequency shift (by 35 MHz) and fiber optics couplers to form a 4 laser beam conglomerate, which is focused at the point of interest. The elastic scattered photons holding the velocity information are collected with the TSI TR260 fiber-optic probe (350 mm focal length, 61 mm dia.) for backscatter signal detection (180° backscattering); probe length volume 0.91 mm, fringe spacing 3.6 μm. The photons are detected with photo-multipliers (TSI PDM 1000 Photomultiplier System) and analyzed at the signal processor (TSI FSA 4000 3-channel digital burst processor, 800 MHz sampling frequency, 175 MHz max. Doppler frequency). Data acquired from the LDV system (TSI Inc. PDPA system, 2-component Phase Doppler Particle Analyzer) was evaluated using TSI FlowSizer (version 3.0.0.0, 2011) software. Raman scattered photons are collected in 90° configuration using a camera objective (Sigma 33–88 mm), which focused the light through a 150 μm pinhole, subsequently the Rayleigh line is filtered out (long-pass edge filter BLP01-514R-25, Semrock) and the Raman spectrum is produced on an iCCD (PI-MAX 1204RB, 1024 × 256 pixel, Princeton Instruments) camera by a Czerny-Turner spectrograph (PI Acton 2750). The CCD chip was thermo-electrically cooled to –20 °C to reduce dark current. Vertical binning was used to extract the spectrum from the CCD chip, thus

increasing signal-to-noise. The whole optical setup can be moved in all three directions by a X,Y,Z traverse (ISEL), which enables the user to collect point-wise profiles in the area of interest as well as 2D cuts and even 3D images.

The test channel was built out of glass with aluminum end parts providing the necessary input streams. Pressure and temperature sensors at each end provided the process data to monitor the stability of the operation. Measurements were performed by stepping through the channel point by point and thus profiling the cross section of interest.

4. CFD models and algorithms

CFD is the numerical study of systems including fluid flow and other relevant phenomena and can be used for detailed spatial and temporal study of the systems. OpenFOAM® (version 4.0, 2016) is a well-established open source CFD code, developed based on verified models and algorithms, which is published under GNU public license (GPL, version 3, 2007). Since the source code is available it is possible to adopt the program for special needs, e.g. adding new solution algorithms or models which are not provided in the main release, e.g. a transitional turbulence model.

4.1. Model formulation

Following momentum balance (Navier-Stokes) and continuity equations were used for calculating pressure and velocity [21]:

$$\frac{\partial \rho}{\partial t} + \nabla \cdot (\rho \mathbf{u}) = 0 \quad (2)$$

$$\frac{\partial \mathbf{u}}{\partial t} + (\mathbf{u} \cdot \nabla) \mathbf{u} = -\frac{1}{\rho} \nabla p + \frac{\mu}{\rho} \nabla^2 \mathbf{u} \quad (3)$$

where ρ [kg/m³] is the density, \mathbf{u} [m/s] is the velocity, p [Pa] is the pressure and μ [kg/(s.m)] is the effective viscosity:

$$\mu = \mu_{mol} + \mu_{turb} \quad (4)$$

where μ_{mol} and μ_{turb} are molecular and turbulent viscosities. Molecular viscosity is a property of the fluid and turbulent viscosity is related to the flow properties and is calculated from turbulent properties [45].

The energy transport and storage is modeled using following equation [21]:

$$\rho \left(\frac{\partial h}{\partial t} + \nabla \cdot (h\mathbf{u}) \right) = -\frac{Dp}{Dt} + \nabla \cdot (K\nabla T) + (\overline{\tau} \cdot \nabla) \mathbf{u} \quad (5)$$

h [J/kg] is enthalpy, t [s] is time, \mathbf{u} [m/s] is velocity, p [pa] is pressure, T [K] is temperature, K [W/(m.K)] is effective thermal conductivity (sum of molecular and turbulent thermal conductivity) of the fluid, τ [Pa] is the shear stress and D/Dt is the material derivative.

Conservation of chemical species i is described using the equation below:

$$\frac{\partial \rho Y_i}{\partial t} + \nabla \cdot (\rho \mathbf{u} Y_i) = \nabla \cdot (D_i \nabla Y_i) + S_M \quad (6)$$

where Y_i is the mass fraction of the species i , ρ [kg/m³] is the density, \mathbf{u} is velocity and S_M is the species source term (e.g. for reactions). D_i [m²/s] is the effective diffusion coefficient which is sum of molecular ($D_{i,mol}$) and turbulent ($D_{i,turb}$) diffusion coefficients:

$$D_i = D_{i,mol} + D_{i,turb} \quad (7)$$

Turbulent diffusion coefficient can be related to turbulent viscosity using turbulent Schmidt (Sc) number [46]:

$$D_{i,turb} = Sc \times \mu_{turb} / \rho \quad (8)$$

In a system with n species for $n-1$ species Eq. (6) is solved and the n th species will be calculated using Eq. (7) for minimizing numerical errors.

$$Y_n = 1 - \sum_{i=1}^{n-1} Y_i \quad (9)$$

The turbulence was modeled using an extension to the already well-established Reynolds Averaged Navier-Stokes (RANS) model $k-\omega$ -SST [45]:

$$\frac{\partial k}{\partial t} + (\mathbf{u} \cdot \nabla) k = P_k - \beta^* k \omega + \nabla \cdot [(\nu + \sigma_k \nu_T) \nabla k] \quad (10)$$

$$\frac{\partial \omega}{\partial t} + (\mathbf{u} \cdot \nabla) \omega = \alpha S^2 - \beta^* \omega^2 + \nabla \cdot [(\nu + \sigma_\omega \nu_T) \nabla \omega] + 2(1-F_1) \sigma_\omega \frac{1}{\omega} \nabla k \nabla \omega \quad (11)$$

where k [J/kg] and ω [1/s] are turbulent energy and specific dissipation rate. P_k is turbulence production term, α , β and σ are closure coefficients and F_1 is the blending function. Since in the simulated and measured flows laminar flow, turbulent flow and transitional zones are expected to be present, the transitional turbulence model was implemented in OpenFOAM® to model all cases using only one solver.

In this transition turbulence model, two more equations are solved beside the k and ω equations. These are used for calculation of source terms to correct the k and ω values to predict the transition between laminar and turbulent flow [47–50]. The first equation is a transport equation for intermittency γ which can be used to trigger transition from laminar to turbulent locally:

$$\frac{\partial \gamma}{\partial t} + (\mathbf{u} \cdot \nabla) \gamma = P_\gamma - E_\gamma + \nabla \cdot [(\nu + \nu_T / \sigma_\gamma) \nabla \gamma] \quad (12)$$

where P_γ is turbulence production term and E_γ is turbulence destruction term.

In the second equation, the transition momentum thickness Reynolds number $\widetilde{Re}_{\theta_t}$ is introduced, which is a measure of nonlocal influence of turbulence intensity and defined using the following transport equation:

$$\frac{\partial \widetilde{Re}_{\theta_t}}{\partial t} + (\mathbf{u} \cdot \nabla) \widetilde{Re}_{\theta_t} = P_{\theta_t} + \nabla \cdot [\sigma_{\theta_t} (\nu + \nu_T) \nabla \widetilde{Re}_{\theta_t}] \quad (13)$$

Mentioned equations were implemented into OpenFOAM® as a new solver (viscoFoam) for simulation of liquid flows and also as a library for modeling of transitional turbulence phenomena.

4.2. Numerical implementation

Using Pressure Implicit with Splitting of Operator (PISO) algorithm first the momentum equations based on the pressure field from the previous time step (first time step: initial conditions) are solved and a velocity field is derived. Using the derived velocity field the first pressure correction equation is solved and based on the pressure corrections, a new pressure field is calculated, from which a new velocity field is derived. With the updated velocity field the second pressure correction equation is solved and pressure and velocities are updated for the next time step [51].

Then based on the new velocity and pressure fields the energy, species and turbulence equations are solved explicitly to calculate new temperatures, mass fractions and turbulent fields. Before going to the next time step fluid properties are updated based on the new fields. Effective viscosities, diffusion coefficients and also thermal conductivities are calculated by adding the turbulent contribution to the molecular properties. The algorithm was implemented in OpenFOAM® as a new solver “viscoFoam” and the turbulence model was implemented as a separate library to be also compatible with other existing solvers. The implemented algorithm can simulate both compressible and incompressible multi-species reacting flows. In this study since the pure fluids’ densities were considered to be constant (temperature and pressure independent) the simulations were performed in incompressible mode with no reactions.

5. Materials and methods

5.1. Experimental

To find appropriate fluid components for convenient LDV/Raman measurements, different liquids were tested. Among available liquids, water (tap water) and diluted ethanol (91.12% ethanol + 8.88% water) were selected for their non-toxicity, easy availability and suitable characteristic Raman spectra. Water was pumped using the straight Inlet one (Fig. 3) into the T-shaped channel and ethanol using side Inlet two. The weight of the supply tanks containing water and ethanol was recorded during the experiments for calculating the actual mass flow

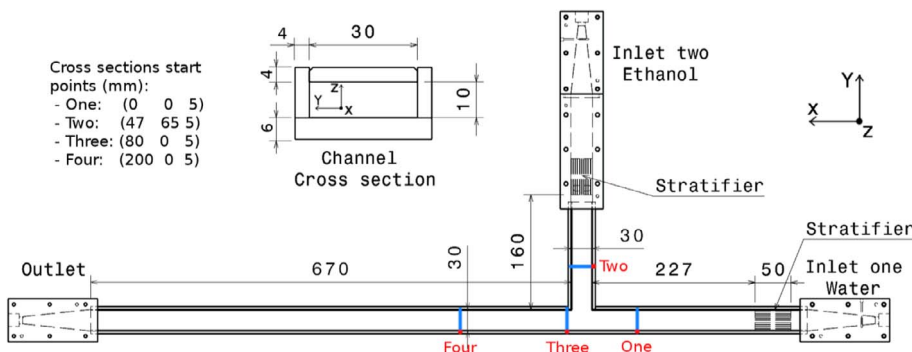


Fig. 3. Design of the T-shaped flow channel for the test system with an overview of the measurement positions (cross sections) for the combined LDV/Raman tests, beginning of each profile is shown with a red dot. Insert upper center: glass channel cross section.

Table 1
LDV measurements settings and parameters.

| Seeding material | Spherical aluminum particles |
|---------------------------------|------------------------------|
| Particle diameter | 0045 mm (maximum) |
| Seeding concentration in feed | 100 ppm |
| Max. measurement time per point | 10 s |
| Max. burst count per point | 100000 |
| LDV burst threshold | 50 mV |
| Band pass filter | 1–10 MHz |
| Downmix frequency | 35 MHz |
| Hardware data coincidence | Yes |
| Software data coincidence | No |

rates. In the inlet of each channel a flow stratifier (stack of 3×10 , 5 cm long, i.d. 2.8 mm tubes) was installed to reduce and dampen inlet effects on the flow providing a homogeneous flow inside the main section channel. The channel had an inner cross section of 10×30 mm.

All measurement points were programmed into the traverse controller. At each measurement point the LDV was set to record up to a maximum time or a maximum particle count, data collection LDV processor settings are listed in Table 1. Seeding particles were added to both liquid storage tanks and dispersed. At the same time the Raman instrument was measuring spectra each second with parameters listed in Table 2. 8 spectra were taken at each point (to stay within the 10 s measurement time frame set by the LDV) and averaged for data evaluation. For comparison with the CFD simulations, data from the LDV and Raman were averaged over the total measurement time of 10 s.

Measurement of the two in-plane velocity components (X and Y) was done at four sections of the channel according to Fig. 3. As there is only homogeneous liquid feed at section one and two, LDV data was collected at just 11 points. In the mixing zone at sections three and four, LDV and Raman datasets were collected at 16 points. All the measurements were done in the center of the channel in the Z direction (5 mm). The experiments were performed at 298 K and ambient pressure.

5.2. Simulations

The experimental setup was modeled using CFD solver viscoFoam to verify the measurement results. The mesh was created with the open source tool cfMesh (version 1.1, 2015) with approximately 3.1 million cells (20×60 cells in the channel cross section, maximum cell size 0.6 mm). A mesh dependency study was also performed to confirm that quality and mesh resolution had no effect on fluid flow (velocity field was analyzed) and mixing phenomena (analyzed by ethanol mass fraction profiles). Boundary conditions (inlet temperature, pressure and mass flows) were set according to the experimental conditions. Important fluid properties and numerical solver parameters are listed in Tables 3 and 4.

Since the Reynolds numbers inside the channel were close to critical Reynolds numbers (inlet one = ~ 3700 , inlet two = ~ 1700 and after mixing $T = \sim 5000$) for modeling turbulence, the transitional turbulence model (see Section 4.1) was used. The buoyancy forces were calculated by considering the gravity ($g = 9.8 \text{ m/s}^2$) in the negative Z direction. Equations were discretized using the second order linear scheme. Transient simulation was performed with adaptive time

Table 2
Raman measurements settings and parameters.

| | |
|-----------------------------|------------------------|
| Laser power | 80 mW (combined beams) |
| Integration time | 1 s |
| Number of spectra per point | 8 |
| Grating | 300 gr/mm |
| Spectral resolution | 15 cm^{-1} |

Table 3
Fluid properties.

| Property | Water | Ethanol |
|---|-----------------------|-----------------------|
| Density [kg/s] | 997.1 | 785.22 |
| Heat capacity [J/kg/K] | 4180 | 2440 |
| Viscosity [Pa.s] | 8.9×10^{-4} | 1.04×10^{-3} |
| Water-ethanol diffusion coefficient [m^2/s] | 8.4×10^{-10} | 8.4×10^{-10} |

Table 4
Numerical solver parameters.

| Numerical schemes | Linear (second order) |
|-----------------------------|-----------------------|
| Turbulent Schmidt number | 1.0 |
| Turbulence model parameters | Standard values [47] |

stepping ensuring a maximum Courant number $Co = 1$. The simulation was continued for 5 s to reach steady state (> 2 residence times of the channel from the low velocity inlet – inlet two, ethanol solution). Water – ethanol mixtures properties were calculated using mixture fraction based laws from the pure fluids. Changes in density due to non-ideality of the mixture were omitted since they would not contribute significantly (below 2.5% density deviation) [52].

5.3. Data analysis

5.3.1. Velocity evaluation using LDV

Fig. 4 shows a sample of data collected from an LDV measurement (10th point on the profile three in Fig. 3 and velocity components in the x and y directions). From the LDV dataset average velocities were calculated and plotted.

5.3.2. Composition and volume fraction evaluation using Raman spectroscopy

Detecting different chemical compounds using their respective Raman spectrum can be done easily by identifying characteristic vibrational bands, if the sample matrix is simple enough. The intensity of these bands correlates to the volume fraction of the compound of interest. However, the intensity of the band at the iCCD camera is also a function of laser power, the collection efficiency of the lens, throughput through the spectrograph, exposure or integration time, aperture of the lens, etc. Therefore, it is necessary to perform a calibration, where the volume fraction of a species is directly linked to the intensity of a characteristic band. For this study, a small cell incorporating the same geometry as the test channel was constructed. It was filled with six different calibration standards. Before Raman spectra were collected, the intensity of the laser beams was measured using a laser power meter (ThorLabs PM100D with S121C probe). This was done for the

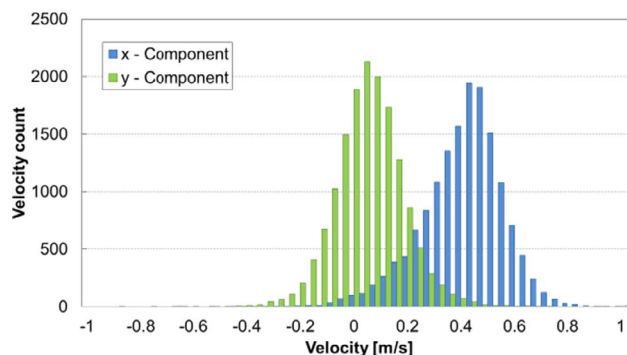


Fig. 4. Distribution of measured velocities for the 10th point (80, 20, 5) on the profile three: x-component and y component.

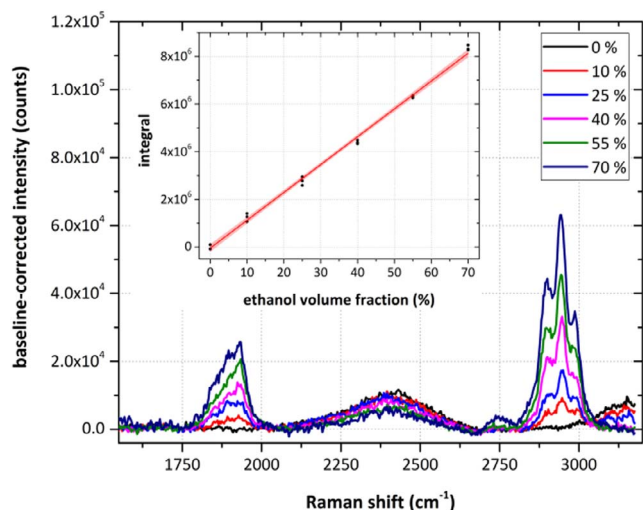


Fig. 5. Raman spectra of the calibration standards. Inset: Calibration curve with linear fit and confidence bands (95%).

calibration as well as for the test channel measurements to adjust for power fluctuations due to preparation steps before each experiment. Also, the possible interference of the seeding particles was tested with the calibration cell. The resulting spectra (with and without seeding particles) were compared and no influence of the seeding particles could be found. Spectra were taken by integrating over 1 s. This procedure was repeated 3 times. The resulting spectra (Fig. 5) were baseline-corrected, the band between 2800 and 3040 cm^{-1} associated with ethanol was integrated and correlated to the volume fraction of the prepared standards. Fig. 5 shows the resulting spectrum with the bands associated with the C–H stretch vibrations of ethanol around 2900 cm^{-1} resulting from Raman scattering of 514 nm laser beams. The bands appearing at 1900 cm^{-1} are related to the same vibrational transitions, although excited by the 488 nm laser beams. Because of the close spectral proximity of the two laser beams, Raman spectra obtained with this combination will show overlapping features from both lasers, complicating the spectrum. However, for this investigation good spectral separation can be observed. The calculated limit of detection (LOD 3σ) for this calibration was 1.9%, with a correlation coefficient R^2 of 0.995 for the calibration curve.

An example of data collected by Raman spectroscopy at profile 3 (Fig. 3) can be seen in Fig. 6. The collected spectra were evaluated against the calibration curve and the volume fraction of ethanol or water was calculated and plotted for each point. Each Raman measurement lasted 1 s and in total eight measurements per point were

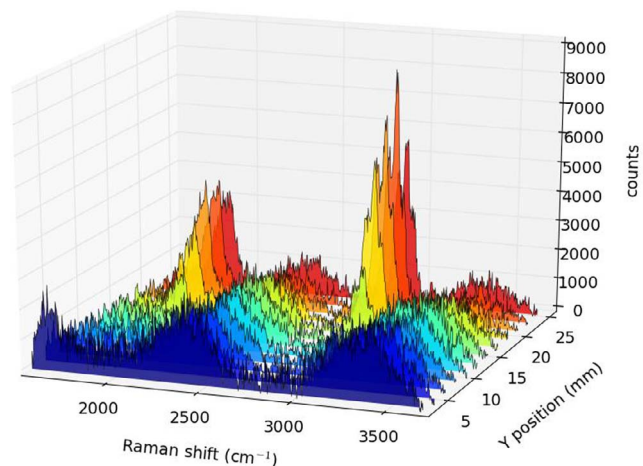


Fig. 6. Example of Raman spectra, collected at different positions on profile three.

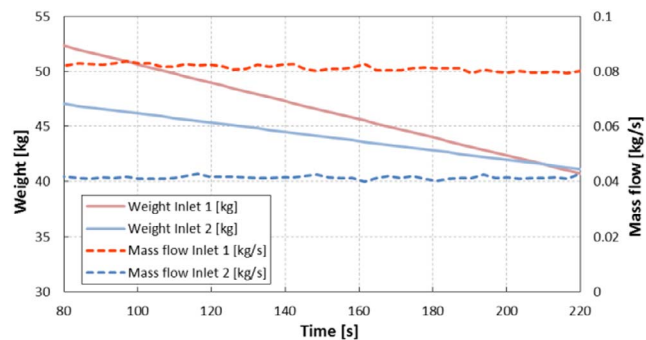


Fig. 7. Mass of fluid storage tanks and fluid flow rates during the experiment.

done (during 10 s of measurement per point).

5.3.3. Flow rates evaluation

Gravimetric flow rate determination was carried out for both liquid streams by calculating the first derivative of the time-resolved weight signals (measurement frequency: 0.3 Hz) from the liquid storage vessels (Kern DE 60K1D balances). As can be seen in Fig. 7, average flow rates for Inlet one (water) was 0.08 ± 0.0021 kg/s and for Inlet two (ethanol) it was 0.04 ± 0.0013 kg/s.

6. Results and discussion

6.1. CFD simulations

For a better understanding of the flow behavior, results of CFD simulations will be analyzed in this section. The key parameters considered here are the pressure, the velocity information and the ethanol mass fraction field.

6.1.1. Pressure

Fig. 8 shows the pressure profile in the simulated channel. The pressure drop from both inlets relative to the outlet is about 1000 Pa. As can be observed in Fig. 8 the highest-pressure zones are located between the inlet tube and the stratifiers. There is a higher pressure drop at Inlet one (straight inlet), as Δp is proportional to the higher flow rate at this inlet. Also a low pressure zone right after T-junction can be observed.

6.1.2. Velocity

A contour plot of the velocity magnitude can be seen in Fig. 9. The highest velocities can be found at the channel outlet, as both inlet flows are accumulating. Inlet one with the higher volume flow rate shows higher velocity compared to inlet two ($\sim 2\times$). The velocity in the stratifier tubes is higher due to the smaller flow cross section. The stratifiers manage to remove flow disturbances (e.g. the flow profile at the inlet section and before the stratifiers) and turbulence structures larger than the inner diameter of the stratifier tubes (2.8 mm). At the exit of the stratifier tubes small free jets can be observed, which decay after approximately 25 mm and as it is known turbulent jets decay within 7–10 jet diameters [53], after that a homogenous flow is

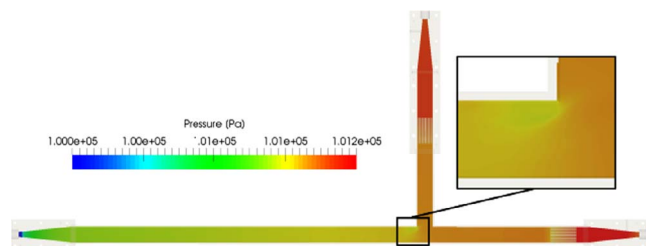


Fig. 8. Pressure contour plot on the symmetry plane after reaching steady state.

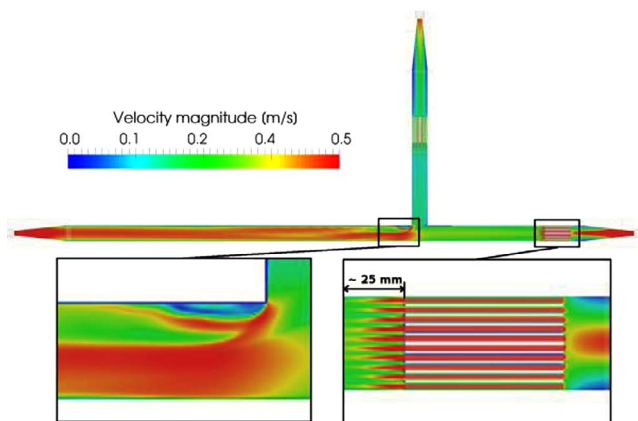


Fig. 9. Velocity magnitude contour plot on the symmetry plane after reaching steady state.

developed, which can propagate through the channel. When the two streams join at the T-junction, the fluid velocity fluctuates across the channels cross section. Close to the wall opposite to the T-junction the velocity starts increasing; adjacent to the T-inlet a local recirculation zone can be observed. This swirling flow is generated right after the T-junction and causes some fluctuations in the velocity field further downstream.

6.1.3. Ethanol mass fraction distribution

Fig. 10 shows flow path-lines colored with ethanol mass fraction and the velocity contours on five cut planes spaced equally (5 cm) from each other. The recirculation zone close to the T-junction strongly affects the fluid flow, which in turn affects mixing. As the density of the stream with higher ethanol mass fraction is lower, the flow is guided above the water stream by buoyant forces before the two streams eventually mix. This has an adverse influence on the mixing performance after the T-junction.

For a quantitative analysis of mixing progress in the channel a series of evaluation planes have been selected along the channel from the mixing point to the outlet. For each of the planes, the minimum, maximum and median of ethanol mass fraction as well as their standard deviations are calculated as a parameter for quantifying the extent of mixing. Calculated values are plotted in Fig. 11 over the length of the channel [54] (standard deviation of zero shows ideal mixing). Fig. 11

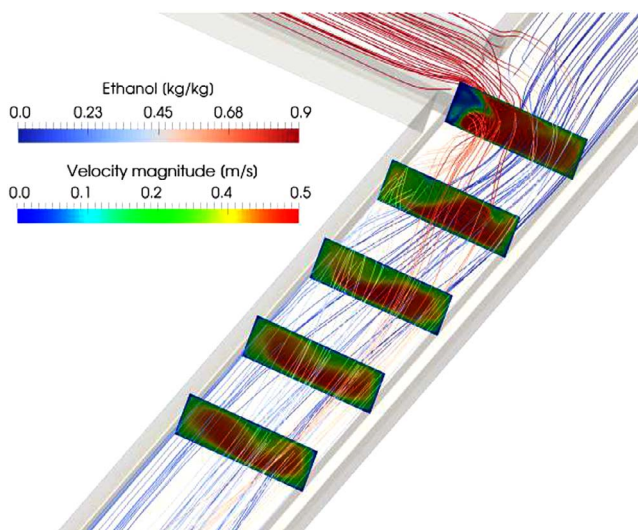


Fig. 10. Flow path-lines colored with ethanol mass fraction and also velocity magnitude contour plots on the equally spaced (5 cm) cut planes after the T-junction after reaching steady state.

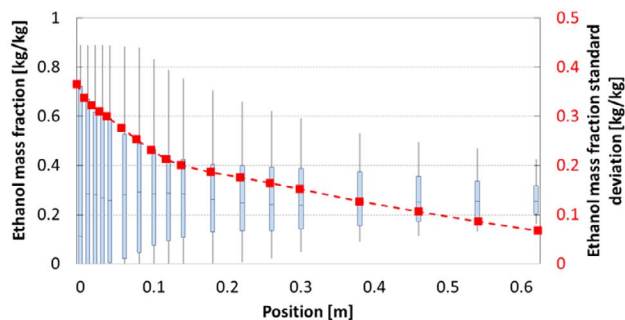


Fig. 11. Ethanol mass fraction box plots and standard deviation of ethanol mass fraction (red dotted line) after the T-junction – embedded figure shows the starting and end positions of box plots.

shows the minimum ethanol mass fraction right after the T-junction is zero while the maximum mass fraction is still the ethanol inlet mass fraction (~0.889 kg/kg). These values stay constant for about 10 cm (~7 hydraulic diameters), then the minimum starts increasing and maximum starts decreasing. Finally, they converge towards average mass fraction of ethanol. As mixing progresses, 1st quartile, median and 3rd quartile of the ethanol mass fraction also converge towards the average mass fraction. However, complete mixing does not occur within the length of the channel: At the outlet still some non-uniformity in the ethanol mass fraction profiles can be observed.

The quality of mixing along the length of the channel can be examined by evaluating the standard deviation of the ethanol mass fraction as a fast and reliable measure for the mixing progress [55]. Fig. 11 shows the standard deviation of ethanol mass fraction along the mixing zone. The data is extracted from the same positions as box plots. In the first 15 cm the standard deviation decreases with a bigger slope compare to the rest of the length, which suggests stronger mixing in this region. This can be explained by the production of more turbulence at the contact region of the two separate streams (shear layer – Fig. 12) and consequently a higher turbulent diffusion coefficient. Fig. 13 shows the turbulent diffusion coefficient in the mixing region, as expected the turbulent diffusion coefficient is lower in the laminar inlet compared to the turbulent inlet. The highest turbulent diffusion coefficients can be found after the T-junction where the two fluids join which is the region where the flow has highest fluctuations. Since the turbulent diffusion coefficient (~0.02 m²/s) is much higher than molecular diffusion coefficient (~10⁻⁸ m²/s), the turbulent diffusion is the dominant phenomena in mixing.

6.2. LDV measurements

Measurements over all four profiles were performed and LDV

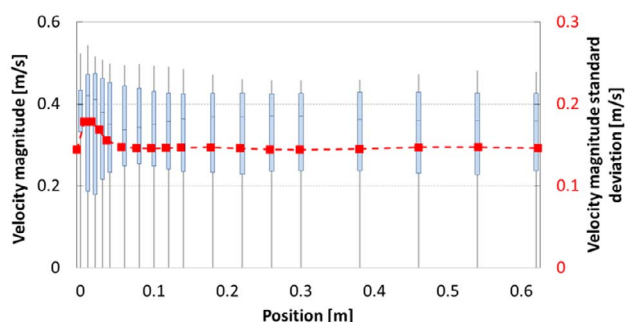


Fig. 12. Velocity magnitude box plots and standard deviation of velocity magnitude (red dotted line) after the T-junction – for positions check the embedded picture in Fig. 11.

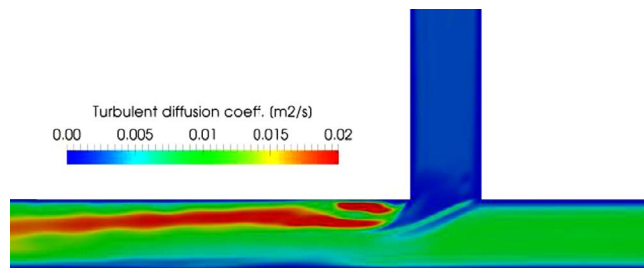


Fig. 13. Turbulent diffusion coefficient in the mixing region after reaching steady state.

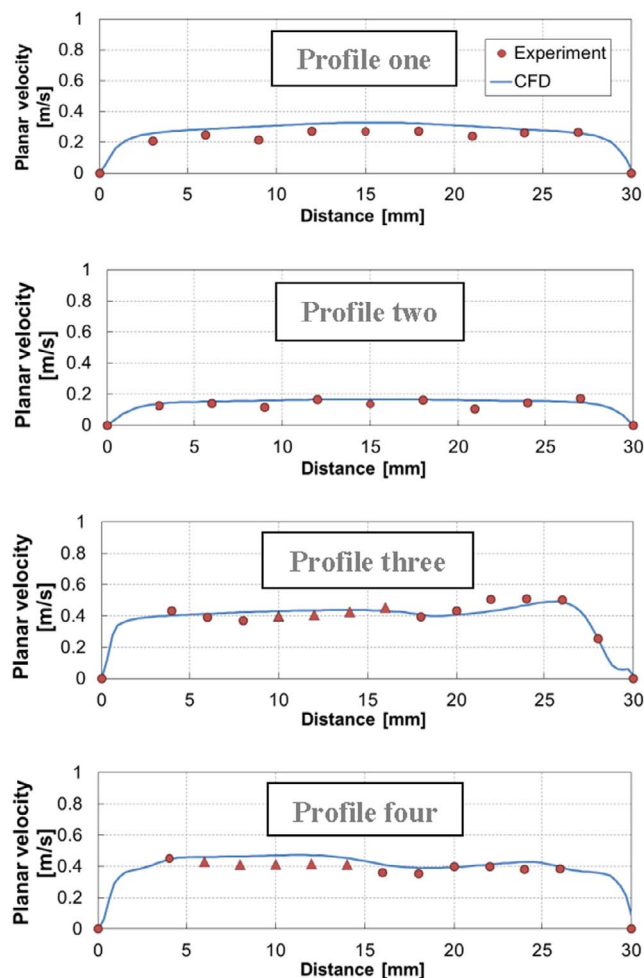


Fig. 14. Measured and simulated velocity magnitudes (x and y components) profiles at different cross sections. In profile three and four some experimental points (shown with triangles) were replaced by data from another experiment under the same condition due to low LDV data rates because of scratched channel glass.

velocities were analyzed and plotted. In Fig. 14 points indicate the experimental measurement spots along the y-axis depicted in Fig. 3. The simulation results and the experimental findings match within the estimated measurement uncertainty, e.g. at profile three in Fig. 14 the velocity increase close to the wall (at position ~ 27 mm) can be observed in both simulation and experiment. Overall, the mean deviation between the measured and simulated velocities over all measured profiles is 8%.

6.3. Raman measurements

Volume fraction data derived from Raman spectra was evaluated at profiles three and four only, since no volume fraction changes were

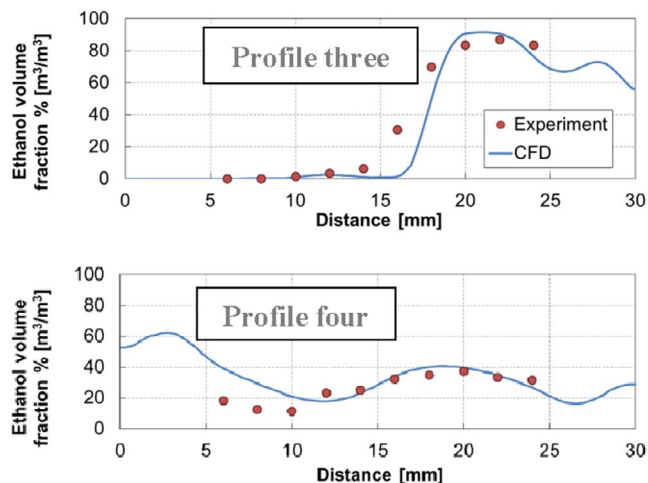


Fig. 15. Measured and simulated volume fraction profiles at different cross sections.

observed in the inlet flow profiles one and two. The points in the plot indicate the mean experimental values (time-averaged Volume fraction). Fig. 15 shows that the measured data compares reasonably well to the CFD simulation. In profile three, at the starting position, both CFD and experiment show low volume fraction values close to zero. For both methods, the volume fraction starts rising at around 15 mm and reaches a maximum of 90% ethanol volume fraction at approximately 20 mm. The slope of the ethanol volume fraction gradient differs in both simulation and experiment, but it is still reasonably resolved. In profile four the trend, the maximum and minimum volume fractions are in good agreement between simulation and experiments, except for the first three measurement points, where the volume fraction derived from Raman spectroscopy is consistently smaller than predictions from CFD indicate. Here, the mean deviation between the measured and simulated volume fraction is 23%, which is a higher margin of error than obtained for velocity. This is primarily caused by the discrepancies in profile three, where CFD predicts a steeper slope in volume fraction than measured with Raman spectroscopy, which results in high deviations for points located in this region, although the position of the transition is predicted correctly within the limits of the spatial resolution. Excluding points at this region, the mean deviation between model and experiment reduces to less than 10% in predicting volume fraction.

Generally, deviations between simulated model predictions and experiments are to be expected. The reasons are manifold: part of the discrepancy comes from the assumption of ideal behavior in CFD simulation, such as boundary conditions and the models. Examples include velocity inlet or pressure outlet boundary conditions which are considered to be uniform with fixed values and are influenced by practical limitations (e.g. fluctuations in flow caused by the pumps, etc.), that cannot be controlled or fully eliminated experimentally. Using ideal models (e.g. ideal mixing behavior of the components) can also lead to differences between simulation and experiment. Furthermore, the inaccuracies in dimensions of experimental setup can also contribute to these deviations. The other point, which has to be considered, is the different spatial resolution in the simulation and experiment. In the simulation, the resolution is limited by the discretization of the domain for the numerical solution of the flow, contrary to experiments, where the resolution is defined by physical parameters, e.g. depth of focus of the optics used.

7. Conclusion

A new method for simultaneous measurement of velocity and concentration of different substances in a process stream is proposed. The new technique is based on the combination of two already well-established methods in the respective fields: LDV and stand-off Raman

spectroscopy. The laser source from the LDV was used for multiple purposes: The back scattered light from the seeding particles in the fluid flow was collected and analyzed for the velocity evaluation. In addition to that, Raman spectra were collected simultaneously from the same focal position of the LDV measurement volume at the same exact time. Using a traverse system both optical systems were translated in space in order to capture profiles inside the flow geometry. A proof of concept study in lab scale was successfully carried out on a T-junction transparent channel (rectangular cross section, 1×3 cm) using ethanol solution and water as mixing fluids at ambient conditions (298 K, 1.025 bar). Flow rates were adjusted to 0.08 kg/s for the water stream and to 0.04 kg/s for the ethanol stream. Profiles were acquired at four different positions in the T-junction: one profile for each inlet (3 mm steps, 10 points per profile), one profile close to the junction (2 mm, 15 points) and one profile down the stream (2 mm, 15 points). At each point data was collected for ten seconds.

Additionally, the measurement geometry was simulated using CFD. A multi-species solver for simulating miscible fluids was developed based on the open-source CFD package OpenFOAM®. The simulation was set up with boundary and operating conditions derived from the experiments. Because of different flow regimes in the channel (Reynolds number between 1700 and 5000), a transitional turbulence model was applied. The simulation was run for 5 s (exceeding twice the volumetric residence time).

Based on the analysis of the simulation results it was found the turbulent diffusion coefficient ($\sim 0.02 \text{ m}^2/\text{s}$) is much higher than the molecular diffusion coefficient ($\sim 10^{-8} \text{ m}^2/\text{s}$) and turbulent diffusion is the dominant phenomena in the mixing region. Simulation results were also compared to measurements and good agreement of measured features and the simulation results could be observed (minimum, maximum and changes in velocity and Volume fraction), which affirms the feasibility and suitability of the suggested method. However, discrepancies between experiment and simulation were observed for both velocities and Volume fraction, in the order of 8% for predicted velocities and 23% for Volume fraction. The higher deviations in the Volume fraction evaluation mainly can be attributed to the different slope predicted by CFD and measured by the experiment in the transitional region from low to high ethanol Volume fraction, although the position of the transition is predicted correctly. Excluding these points, the mean deviation between model and experiment reduces to less than 10%. The observed differences can be explained by applying ideal boundary conditions and models in the CFD and uncertainties in the experimental parameters and setup. Furthermore, the inaccuracies in dimensions of experimental setup can also contribute to these deviations. Another point, which has to be considered, is the different spatial resolution in the simulation and experiment. In the simulation, the resolution is limited by the discretization of the domain for numerical solution of the flow, contrary to experiments, where the resolution is defined by physical parameters, e.g. depth of focus of the optics used.

The presented concept of combining LDV and Raman can provide valuable information on flow properties and composition of a process stream whilst maintaining spatial and temporal accuracy. In this study a proof of concept experiment is shown, with measurement data averaged over 10 s per point. The integration time for Raman spectra was set to 1 s in order to achieve sufficient high signal to noise ratios, which is imperative for accurate quantification of a chemical component. Accumulating spectra and using averages is a commonly used technique to improve signal to noise in Raman spectroscopy and in this case allows the study of fluctuations of the Raman measurement, as each spectra can be compared to the next one. However, faster measurements would be desirable and are definitely possible through optimization of several used components, like collection optics, power of the excitation laser, throughput of the spectrograph etc. This could result in integration times well below 1 s and in consequence increase the temporal resolution of the whole combination. Generalization of measurement time for Raman is hard to estimate as it depends on

mentioned reasons amongst others, e.g. the Raman cross section of the compound of interest, which can change drastically and is therefore best adjusted by experiment. The optimal situation would be that the presented combined technique has a higher measurement frequency as the phenomena present in the fluid stream. This would allow for an instantaneous exploration of velocity and concentration in the process of interest.

8. Outlook

Using the same laser source for both Raman and LDV evaluation of the streams ensures identical positioning and local accordance of the collected information. Additionally, this method shows potential to measure the slip or drift flux velocity of multiphase mixtures with low volume fraction of dispersed phase, e.g. pipe flows, where gas and liquid can flow in different directions [56]. An alternative construction of the instrumentation with back-scatter detection for LDV and Raman are possible, allowing for only one optical opening being necessary. Using optical fibers, the size of these optical access points can be further reduced. This construction would be also attractive for industrial applications since it could be integrated within one single case.

Although the interpretation of Raman spectra can be more challenging at times because of overlapping spectral features due to dual-color excitation, using a full Raman spectrum provides the possibility of examining multi-component streams in terms of concentrations and compositions. Here, chemometric approaches can help untangle complex spectra and deliver information of the participating compounds with high selectivity and sensitivity. New Raman devices or techniques like time-gated spectroscopy can allow for much faster acquisition of Raman spectra and thus be used for identifying turbulent fluctuations of the concentrations of the components. It would also allow for differentiating of micro- (diffusion based) and macro mixing (convective).

It is proposed that this combination of methods can deliver advantageous insight into processes not only in scientific research but also in industrial plants. However, more investigations are required to make the new approach suitable for industrial applications.

Acknowledgements

Financial support was provided by the Austrian research funding association (FFG) under the scope of the COMET program within the research project “Industrial Methods for Process Analytical Chemistry – From Measurement Technologies to Information Systems (imPACTs, www.k-pac.at)” (contract # 843546).

A patent application for this method has been submitted by TU Wien under the title “Verfahren zur kontaktlosen Bestimmung von Strömungsparametern”, Application ID: A161/2017.

The authors would also like to acknowledge all the helps and guides from Johannes Frank and thank him for sharing his experience.

References

- [1] W.L. Oberkamp, T.G. Trucano, C. Hirsch, Verification, validation, and predictive capability in computational engineering and physics, *Appl. Mech. Rev.* 57 (2004) 345–384.
- [2] K.B. Mogensen, H. Klank, J.P. Kutter, Recent developments in detection for microfluidic systems, *Electrophoresis* 25 (2004) 3498–3512.
- [3] P.J. Viskari, J.P. Landers, Unconventional detection methods for microfluidic devices, *Electrophoresis* 27 (2006) 1797–1810.
- [4] J.C. Fister, S.C. Jacobson, J.M. Ramsey, Ultrasensitive cross-correlation electrophoresis on microchip devices, *Anal. Chem.* 71 (1999) 4460–4464.
- [5] T. Park, M. Lee, J. Choo, Y.S. Kim, E.K. Lee, D.J. Kim, S.-H. Lee, Analysis of passive mixing behavior in a poly (dimethylsiloxane) microfluidic channel using confocal fluorescence and Raman microscopy, *Appl. Spectrosc.* 58 (2004) 1172–1179.
- [6] S. Funatani, N. Fujisawa, H. Ikeda, Simultaneous measurement of temperature and velocity using two-colour LIF combined with PIV with a colour CCD camera and its application to the turbulent buoyant plume, *Meas. Sci. Technol.* 15 (2004) 983.
- [7] A. Charogiannis, J.S. An, C.N. Markides, A simultaneous planar laser-induced fluorescence, particle image velocimetry and particle tracking velocimetry technique for the investigation of thin liquid-film flows, *Exp. Therm. Fluid Sci.* 68

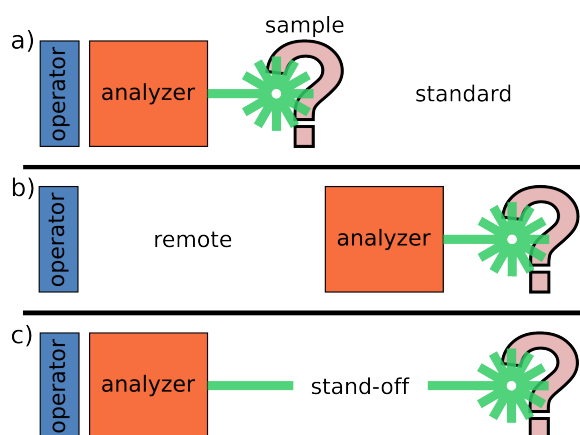
- (2015) 516–536.
- [8] G. Rinke, A. Wenka, K. Roetmann, H. Wackerbarth, In situ Raman imaging combined with computational fluid dynamics for measuring concentration profiles during mixing processes, *Chem. Eng. J.* 179 (2012) 338–348.
- [9] V. Beushausen, K. Roetmann, W. Schmunk, M. Wellhausen, C. Garbe, B. Jähne, 2D-measurement technique for simultaneous quantitative determination of mixing ratio and velocity field in microfluidic applications, *Imag. Meas. Meth. Flow Anal.* (2009) 155–164.
- [10] M. Wellhausen, G. Rinke, H. Wackerbarth, Combined measurement of concentration distribution and velocity field of two components in a micromixing process, *Microfluid. Nanofluid.* 12 (2012) 917–926.
- [11] S. Eckert, A. Cramer, G. Gerbeth, Velocity measurement techniques for liquid metal flows, *Magneto hydrodynamics* 275–294 (2007).
- [12] F. Durst, A. Melling, J.H. Whitelaw, Principles and practice of laser-Doppler anemometry, NASA STI/Recon Tech. Rep. A 76 (1976).
- [13] Y. Zhang, K. Gong, S. He, Y. Huo, Progress in laser Doppler velocity measurement techniques, *Laser Infrared* 11 (2010) 2.
- [14] L. Drain, *The laser Doppler techniques*, Chichester, Sussex, England and New York, 1980.
- [15] G. Rottenkolber, R. Meier, O. Schäfer, K. Dullenkopf, S. Wittig, Combined “Fluorescence” LDV (FLDV) and PDA technique for non-ambiguous two phase measurements inside the spray of a si-engine, *Part. Part. Syst. Charact.* 18 (2001) 216–225.
- [16] L.M. Quinzani, R.C. Armstrong, R.A. Brown, Birefringence and laser-Doppler velocimetry (LDV) studies of viscoelastic flow through a planar contraction, *J. Nonnewton. Fluid Mech.* 52 (1994) 1–36.
- [17] F. Lemoine, M. Wolff, M. Lebouche, Simultaneous concentration and velocity measurements using combined laser-induced fluorescence and laser Doppler velocimetry: application to turbulent transport, *Exp. Fluids* 20 (1996) 319–327.
- [18] R.W. Dibble, V. Hartmann, R.W. Schefer, W. Kollmann, Conditional sampling of velocity and scalars in turbulent flames using simultaneous LDV-Raman scattering, *Exp. Fluids* 5 (1987) 103–113.
- [19] J.B. Moss, Simultaneous measurements of concentration and velocity in an open premixed turbulent flame, *Combust. Sci. Technol.* 22 (1980) 119–129.
- [20] J.D. Anderson, J. Wendt, *Computational Fluid Dynamics*, Springer, 1995.
- [21] H.K. Versteeg, W. Malalasekera, *An introduction to computational fluid dynamics: the finite volume method*, Pearson Education, 2007.
- [22] Y. Yeh, H.Z. Cummins, Localized fluid flow measurements with an He–Ne laser spectrometer, *Appl. Phys. Lett.* 4 (1964) 176–178.
- [23] J. Foreman, E. George, J. Jetton, R. Lewis, J. Thornton, H. Watson, 8C2-fluid flow measurements with a laser Doppler velocimeter, *IEEE J. Quantum Electron.* 2 (1966) 260–266.
- [24] P.K. Rastogi, *Photomechanics*, Springer Science & Business Media, 2003.
- [25] R. Goldstein, *Fluid Mechanics Measurements*, CRC Press, 1996.
- [26] D.F.G. Durao, M.V. Heitor, J.C.F. Pereira, Measurements of turbulent and periodic flows around a square cross-section cylinder, *Exp. Fluids* 6 (1988) 298–304.
- [27] S. Kato, H. Ito, T. Ichikawa, M. Kagami, *Laser doppler velocimeter*, United States Patent US 5,587,785, 1996.
- [28] R. Beauvais, *Laser-Doppler Velocimetry (LDV)*, Opt. Meas. Springer, 1994, pp. 179–193.
- [29] H.-E. Albrecht, N. Damaschke, M. Borys, C. Tropea, *Laser Doppler and Phase Doppler Measurement Techniques*, Springer Science & Business Media (2013).
- [30] M. Nabavi, K. Siddiqui, A critical review on advanced velocity measurement techniques in pulsating flows, *Meas. Sci. Technol.* 21 (2010) 42002.
- [31] D.A. Long, *The Raman effect: a unified treatment of the theory of raman scattering by molecules*, Wiley Online Library (2002), <http://dx.doi.org/10.1002/0470845767.ch27>.
- [32] K. Buckley, J.G. Kerns, A.W. Parker, A.E. Goodship, P. Matousek, Decomposition of in vivo spatially offset Raman spectroscopy data using multivariate analysis techniques, *J. Raman Spectrosc.* 45 (2014) 188–192.
- [33] G. Falgayrac, S. Facq, G. Leroy, B. Cortet, G. Penel, New method for Raman investigation of the orientation of collagen fibrils and crystallites in the Haversian system of bone, *Appl. Spectrosc.* 64 (2010) 775–780.
- [34] Y. Oshima, H. Sato, H. Kajiura-Kobayashi, T. Kimura, K. Naruse, S. Nonaka, Light sheet-excited spontaneous Raman imaging of a living fish by optical sectioning in a wide field Raman microscope, *Opt. Express.* 20 (2012) 16195–16204.
- [35] M. Tanaka, R.J. Young, Review Polarised Raman spectroscopy for the study of molecular orientation distributions in polymers, *J. Mater. Sci.* 41 (2006) 963–991.
- [36] M. Becker, H. Scheel, S. Christiansen, H.P. Strunk, Grain orientation, texture, and internal stress optically evaluated by micro-Raman spectroscopy, *J. Appl. Phys.* 101 (2007) 63531.
- [37] M. Bauer, *Raman spectroscopy of laser induced material alterations*, lmu, 2010.
- [38] E.C.Y. Li-Chan, The applications of Raman spectroscopy in food science, *Trends Food Sci. Technol.* 7 (1996) 361–370.
- [39] Y. Liu, K. Chao, M.S. Kim, D. Tuschel, O. Olkhovoyk, R.J. Priore, Potential of Raman spectroscopy and imaging methods for rapid and routine screening of the presence of melamine in animal feed and foods, *Appl. Spectrosc.* 63 (2009) 477–480.
- [40] N. Dupuy, J. Laureyns, Recognition of starches by Raman spectroscopy, *Carbohydr. Polym.* 49 (2002) 83–90.
- [41] X. Zhu, T. Xu, Q. Lin, Y. Duan, Technical development of Raman spectroscopy: from instrumental to advanced combined technologies, *Appl. Spectrosc. Rev.* 49 (2014) 64–82.
- [42] B. Zachhuber, G. Ramer, A.J. Hobro, B. Lendl, Stand-off Raman Spectroscopy of Explosives, *Secur. Def.* (2010) pp. 78380F–78380F.
- [43] S. Kokot, M. Grigg, H. Panayiotou, T.D. Phuong, Data interpretation by some common chemometrics methods, *Electroanalysis* 10 (1998) 1081–1088.
- [44] B. Haddadi, C. Gasser, C. Jordan, M. Harasek, B. Lendl, Verfahren zur kontaktlosen Bestimmung von Strömungsparametern, Patent application submitted: A161/2017, n.d.
- [45] F. Menter, Zonal two equation kw turbulence models for aerodynamic flows, AIAA J. (1993), <http://dx.doi.org/10.2514/6.1993-2906>.
- [46] G. Brethouwer, The effect of rotation on rapidly sheared homogeneous turbulence and passive scalar transport. Linear theory and direct numerical simulation, *J. Fluid Mech.* 542 (2005) 305–342.
- [47] F.R. Menter, R.B. Langtry, S.R. Likki, Y.B. Suzen, P.G. Huang, S. Völker, A correlation-based transition model using local variables—Part I: model formulation, *J. Turbomach.* 128 (2006) 413–422.
- [48] R.B. Langtry, F.R. Menter, S.R. Likki, Y.B. Suzen, P.G. Huang, S. Völker, A correlation-based transition model using local variables—part II: test cases and industrial applications, *J. Turbomach.* 128 (2006) 423–434.
- [49] R.B. Langtry, F.R. Menter, Correlation-based transition modeling for unstructured parallelized computational fluid dynamics codes, AIAA J. 47 (2009) 2894–2906.
- [50] R. Langtry, F. Menter, Transition Modeling for General CFD Applications in Aeronautics, 43rd AIAA Aerosp. Sci. Meet. Exhib. 2005, p. 522.
- [51] J.H. Ferziger, M. Peric, *Computational methods for fluid dynamics*, Springer Science & Business Media, 2012.
- [52] T.A. Scott Jr, Refractive index of ethanol-water mixtures and density and refractive index of ethanol–water–ethyl ether mixtures, *J. Phys. Chem.* 50 (1946) 406–412.
- [53] M. Miltner, C. Jordan, M. Harasek, CFD simulation of straight and slightly swirling turbulent free jets using different RANS-turbulence models, *Appl. Therm. Eng.* 89 (2015) 1117–1126.
- [54] A. Soleymani, E. Kolehmainen, I. Turunen, Numerical and experimental investigations of liquid mixing in T-type micromixers, *Chem. Eng. J.* 135 (2008) S219–S228.
- [55] M. Engler, N. Kockmann, T. Kiefer, P. Woias, Numerical and experimental investigations on liquid mixing in static micromixers, *Chem. Eng. J.* 101 (2004) 315–322.
- [56] P.F. Vassallo, R. Kumar, Liquid and gas velocity measurements using LDV in air–water duct flow, *Exp. Therm. Fluid Sci.* 19 (1999) 85–92.

Stand-off Hyperspectral Raman Imaging

Raman spectroscopy is usually a non-invasive and non-destructive way of analyzing a wide range of substances based on the inelastic scattering of photons. The scattering nature of the Raman effect implies the efficient collection of scattered photons from the sample, which contain molecule specific information of the vibrational transitions excited by the incident radiation and can be done in several ways. Raman microscopes use the optical setup of reflected light microscopes to create small focal points and collect from high numerical apertures, whereas hand-held devices use close contact to efficiently detect the Raman light. Both are not suitable when the sample is located in remote distances. Stand-off applications, where the instrumentation is physically separated from the target, offer several advantages for such endeavors, especially if dangerous or hard to reach samples are of interest. The following sections will give an overview over the developments of stand-off Raman spectroscopic instruments, their working principle and performance for the remote detection of explosives. Advancements in stand-off Raman imaging will be presented, where both mapping and hyperspectral imaging techniques will be explored, discussed and compared. Finally, the use of chemometrics and image processing on the datasets acquired with stand-off Raman imaging will be shown and the benefits of this combination will be discussed.

Figure 5.1:

Different detection scheme employed in Raman spectroscopy. **a)** Standard configuration with operator, instrument and sample in close proximity. **b)** Remote configuration, where the instrument is deployed to the sample and transmits the analysis result. **c)** Stand-off configuration, where the instrument and operator are located distant from the investigated sample.



5.1 Stand-off Raman spectroscopy

Stand-off Raman spectroscopy describes a technique, where the instrument and operator are located at a certain distance from the sample under investigation (see figure 5.1). The principle of stand-off analysis using Raman spectroscopy was first proposed in the 1960s [104]. The problems identified at the time were mainly concerned with the adequacy of sensitivity arising from the inherently low signal levels, long-distance ranges and usually low sample concentrations [105, 106]. With the advent of small, high powered lasers the problem of long distances between sample and spectrometer was partially solved, as the laser beams stay collimated across large beam paths. Further technological development in the field of lasers and learnings from optimizations during the 1960-70s, in the early 1990s the first compact prototypes for the detection of solid and liquid samples at distance ranging from 6 to 16 m were reported [107]. The first major identified field of application for such systems was the planetary exploration. Minerals have distinct and often quite strong Raman signals and also organic material, if present, may be detected. Hence, several efforts have been made to show the capability of stand-off Raman instruments for the identification of minerals over distances greater than 200 m [108], even 400 m [109]. These developments culminated in the integration of stand-off Raman into the mast camera suite known as SuperCam of the 2020 Mars rover, where among Laser Induced Breakdown Spectroscopy (LIBS) and IR also stand-off Raman plays a crucial role for the identification of minerals and organic material [110].

The second most investigated application is the safe detection of hazardous and/or explosive materials at a safe distance. Several studies have assessed the applicability of stand-off Raman systems for remote identification of these compounds. A wide range of explosives, including RDX, TATP, PETN, TNT and urea nitrate and additionally, more easily accessible explosive inorganic salts such as several nitrates and perchlorates have

been detected [111]. The most used technique thereby is spontaneous Raman scattering. There are however also nonlinear techniques used for Raman spectroscopy, namely Coherent anti-Stokes Raman Spectroscopy (CARS) and Stimulated Raman Spectroscopy (SRS). CARS is a third-order non-linear optical process involving three laser beams: a pump beam, a Stokes beam and a probe beam. These beams interact at the sample and generate a coherent optical signal, which is resonantly enhanced when the frequency difference between the pump and the Stokes beams coincides with the frequency of a vibrational transition [112, 113]. For SRS, which is also the underlying principle of Raman lasers, a Stokes beam is employed stimulating a specific vibrational transition. When the difference in energy between both pump and Stokes beam coincides with the energy of a specific vibrational transition, the occurrence of this transition is resonantly enhanced. The analyzed signal is equivalent to changes in the intensity of the pump and Stokes beams. SRS and CARS show orders of magnitude stronger signals than spontaneous Raman emission due to their coherent nature. This is of course very attractive for the low signals expected for stand-off applications, since the sample-detector distance is high and laser powers can be reduced. The major drawback is however the increase in complexity of the optical and electronic instrumentation and the need of having coherent light over large distances, which is challenging in itself.

Although there are several different laser based sensing methods available for the remote detection of explosives, Raman spectroscopy has some key advantages: It is non-destructive, instrumentally straight-forward and can be designed compact in size. The first is especially important if sensitive samples like explosives are investigated. Some compounds are of limited stability and can be triggered by intense focused laser beams, such as needed for LIBS. It has to be noted however, that with advances of suitable laser sources in the MIR spectral region, also stand-off MIR reflection techniques are now able to detect small amounts of explosive at reasonable distances [114].

The notion that one particular remote laser sensing technique will give a complete picture of the chemical composition of a target has to be dismissed. Instead, approaches comprising a combination of more than one laser spectroscopic technique will most likely result in a more in-depth analysis. This concept is well documented for planetary exploration with the prime example being the SuperCam on the Mars 2020 rover. For the detection of explosives, the same approach has been undertaken during the OPTIX (Optical Technologies for the Identification of Explosives) project [115], a EU-FP7 funded international research program, where a combination of Raman, LIBS and IR was sought after and in which also part of the work presented here was supported.

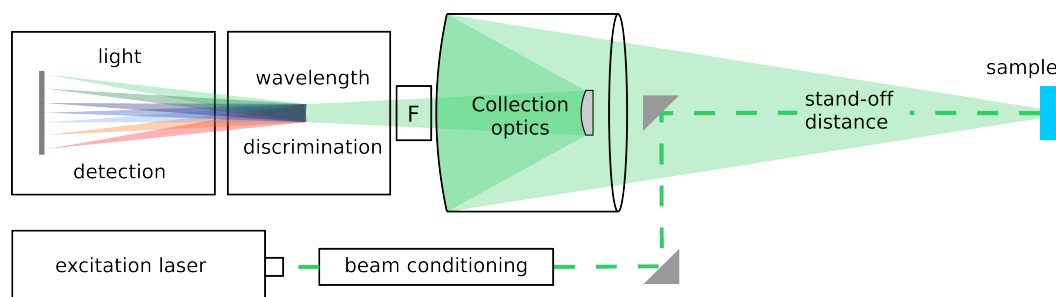
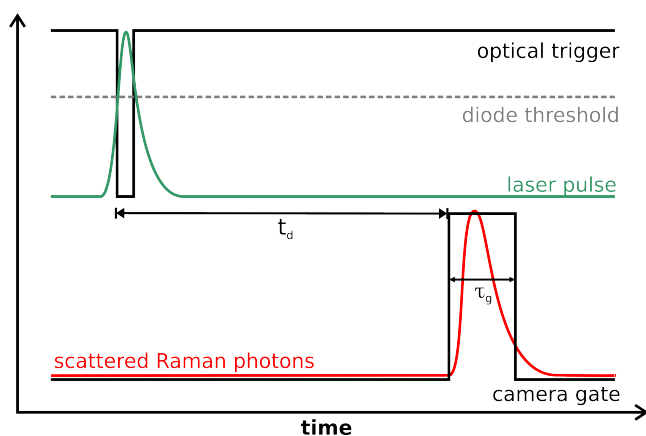


Figure 5.2: Illustration of the general built-up of a stand-off Raman spectrometer. The laser beam is directed at the sample, where the inelastically backscattered light is collected by an appropriate collection optic. Subsequently, the laser light is blocked by a Rayleigh filter (F), after that the light is spectrally analyzed and detected.

5.1.1 Stand-off Raman instrumentation

Figure 5.2 shows a principal set of components necessary for stand-off Raman spectroscopy. The light exiting the excitation laser is usually focused on the sample of interest and the backscattered light is collected by an appropriate optics. Since in stand-off configuration large distances between the instrument and the detector are desirable, long focal lengths of the collection optics are favorable. The most used optical component fulfilling this requirement are telescopes. Available in vast variety of geometries, they are based either on solely lenses (refractive telescopes, historically the first available) or on mirrors (reflective telescopes) or a combination of both (catadioptric telescopes). For optical systems with large focal lengths, very large diameters D are necessary to achieve high light gathering powers. The first refractive telescopes employed lenses, which were increased in size until approximately 1 m. Lenses with greater diameter were so heavy, that due to gravitational deformation no satisfactory image quality could be achieved. Mirrors on the other hand could be produced in a stable manner much bigger in size, although at the beginnings the lack of manufacturing prowess to produce complex shapes limited their use, because of spherical aberrations. The saving grace was a combination of both lenses and mirrors, creating catadioptric telescopes. The main advantage of reflective telescopes, besides bigger diameters, is the possibility to construct them smaller in size. The employed Cassegrain-geometry "folds" the beam by using a primary mirror with a hole, through which the image is projected with the help of a second mirror (see figure 5.2). To correct the spherical errors of this arrangement, a Schmidt corrector plate is introduced as entrance window, forming the Schmidt-Cassegrain telescope variant. It is one of the most popular commercial designs of amateur astronomical optics and is therefore already optimized for use in the visible region of the EM spectrum, available at a very moderate price. Additionally,

**Figure 5.3:**

Timing diagram of a pulsed excitation with synchronized detection. The laser pulse is detected by a photodiode (or internally given) producing a synchronization pulse. After a certain delay time t_d the gate of the camera is opened for a given period (τ_g).

it is important to keep in mind that the collection optics properties should be closely matched to the input requirements of the wavelength discrimination and light detection unit in order to maximize the light throughput.

Taking another look at equation 2.29, we can see that the choice of excitation wavelength heavily influences the Raman scattering cross section, namely by the inverse fourth power. This means shorter wavelength are significantly more effective. This is one of the reasons why Raman spectroscopy to this day is mostly performed in the visible region of the EM spectrum. However, one can imagine, with a stand-off apparatus used in open field or on the surface of a planet under solar irradiance will not yield satisfactory results, as the low intensity of Raman scattering will make it impossible to distinguish interfering light (e.g. daylight) from the photons containing information about the target. If however, a pulsed laser is used and the dedicated photon detector possesses the ability to gate at the time frame of the pulse-length of the laser, a synchronized detection scheme can be applied, which is illustrated in the time diagram in figure 5.3. The basic steps are the following: First, a reference pulse triggers a laser pulse of a certain pulse duration or the laser fires and produces a trigger, which acts as a starting point. After a specific delay time t_d , which corresponds to the time of flight of the photons traveling towards and backwards from the target, the detector opens its gate for the duration of the incoming, backscattered photons. The gate time τ_g should be optimized to get as many photons, specifically scattered from the target, as possible, which will be in the range of the pulse-length. This process can then be repeated a number of times with a repetition rate equal to the emission rate of the pulsed laser, which will increase the SNR significantly. It has been shown, that this way quality spectra can be acquired even in broad daylight, which would not have been possible in a continuous wave measurement [116]. Another important part of any Raman spectrometer is the Rayleigh filter (denoted as F in figure 5.3). Since the Rayleigh scattering cross section is orders of magnitude greater than the Raman scattering cross section, the very intense elastically backscattered light has to be blocked out for the detector

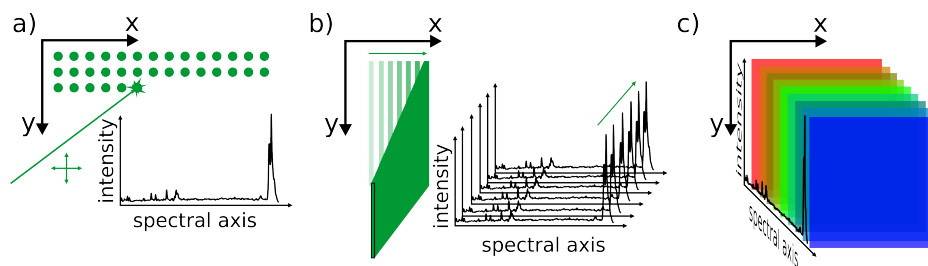


Figure 5.4: Different principles of Hyperspectral imaging. a) Mapping or Whiskbroom imaging. b) Line-scanning or pushbroom imaging. c) Staring or Spectral scanning imaging.

not to be over-saturated with light. This is either done by high-pass edge-filters, which have a steep cut-off at wavelengths a little higher than the excitation wavelength and let the red-shifted light pass or by notch filters, which exhibit strong absorption exactly at the laser wavelength and thereby efficiently blocking it. Afterwards a wavelength discrimination device analyzes the light spectrally, before it's detected on the photon detector.

5.2 Remote chemical detection using Hyperspectral Raman Imaging

The following section will explore the different possibilities of building a stand-off Raman imaging system. The main motivation is the need for spatial resolved measurements for a number of applications. If a larger area has to be scanned for hazardous or potential explosive residues, a single point measurement will not suffice. Two different approaches will be discussed in more detail: one is mapping the laser point over the target, the other is using a tunable filter to acquire a direct image. The result is in both cases a 3D dataset, where two axis are populated with local coordinates and the third is a spectral axis. This is usually called a Hyperspectral Image (HSI) cube and the associated measurement techniques are known as Hyperspectral Imaging techniques. Both approaches will be compared. The latter system is also designed to be used as a mobile stand-off Raman analyzer, which can be operated off a small vehicle. It should be noted at this point, that this system is not limited to the detection of explosives and similar compounds, but can also be used in arts and cultural heritage analysis or geological investigations, among other.

5.2.1 Hyperspectral Imaging: an overview

The term *Hyperspectral Imaging* (HSI) first originated in the 1980s in remote sensing with airborne imaging spectrometers used for mineral mapping [117]. Nowadays, HSI describes an ever increasing and constantly evolving field of chemical and structural image analysis, which provides spatial and spectral information at the same time for a given sample of interest. Popular applications range from airborne remote sensing over food quality and safety [118] to microbiology [119]. As already mentioned, the result of HSI devices are three-dimensional datasets, which consist of the two-dimensional spatial information and an additional spectral dimension. Generally, two different methodologies of HSI measurements can be differentiated: spatial and spectral methods. Spatial scanning methods, where the image is created by mapping the point of measurement over the target surface, can be divided into two groups: point-by-point mapping (whiskbroom imaging, shown in figure 5.4a) and line-scanning (pushbroom imaging, shown in figure 5.4b). Whiskbroom imaging, a spectrum of a specific spatial position of the sample is obtained and then the area of interest is scanned by moving pointwise to generate a mapping of the sample surface. This is the most common method of modern Raman microscopy (often also called micro-spectroscopy), the obvious integration of a Raman spectrometer into a confocal microscope.

Using a cylindrical lens on a Gaussian beam, especially Powell lenses, otherwise known as laser line generation lenses, laser lines with uniform intensity distribution can be created. If such a laser line is employed for excitation, a whole line of spectra can be recorded at the same time and when scanned laterally over the sample a HSI can be created. Known as the pushbroom approach, it utilizes the fact that most detectors used for spectroscopy are two-dimensional arrays with one free dimension (which is usually binned vertically), which can be used to image one dimension of the sample surface. This leads usually to a considerably increase in acquisition speed.

Spectral scanning methods collect a two-dimensional spatial image for a given wavelength band at a time. Therefore, the HSI cube is built by stacking spectral snapshots on top of each other (see figure 5.4c). This requires selecting a certain wavelength and image it onto the detector array, which can be facilitated by tunable bandpass filters. Depending on the application, the filters have to provide an adequate width of the bandpass, good optical throughput, a large optical aperture for passing the image and fast and reliable tuning. A wide range of possible technologies exist, where acousto-optical tunable filters (AOTFs), tunable Fabry-Perot interferometers and liquid crystal tunable filters (LCTFs) are most commonly used.

A special mention should be given to techniques that capture the full HSI in one shot. Analogous to color image sensors, mosaic filters are applied to the whole sensor giving adjacent pixels distinct sensitivities. These devices promise the fastest acquisition

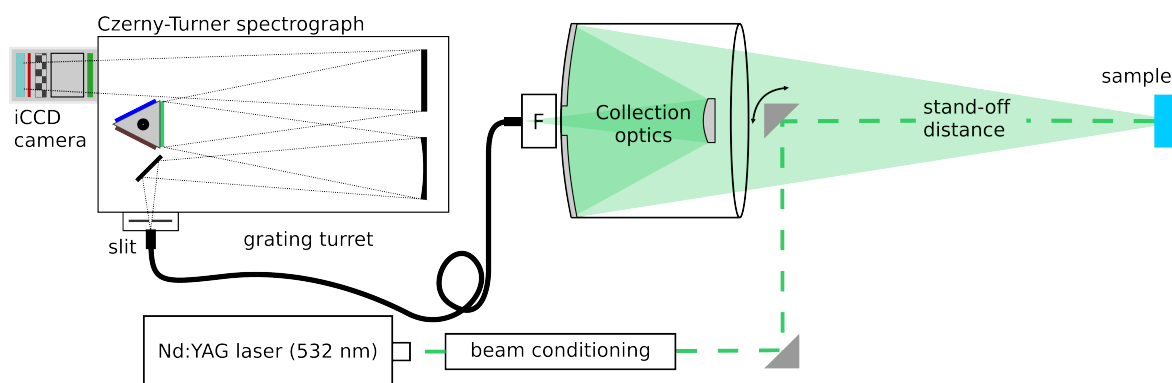


Figure 5.5: Optical setup for the mapping stand-off Raman instrument. The final coaxial mirror is mounted on a motorized kinematic mount for computer controlled movement of the laser beam at the target.

rates, although the number of spectral bands and the spatial resolution might be somewhat limited [120, 121].

5.2.2 Stand-off Raman mapping

In 2010 during my bachelor thesis working for the OPTIX project, it was shown that a peculiar effect used in some standard Raman applications can also be used in stand-off Raman spectroscopy. Spatially Offset Raman Spectroscopy (SORS) describes a method, where the laser beam is spatially translated from the collection point [122, 123], enabling the detection of Raman signals originating from matter inside the sample. We could show that using SORS, signals from explosive material inside various containers could be acquired and that fluorescence originating from surface layers could be considerably reduced, making the stand-off measurement of different substances concealed in diverse containers possible [124, 125]. This work needed precise positioning of the laser beam at stand-off distances of over 10 m. It was facilitated by using a kinematic mirror holder (Thorlabs KM100), actuated by stepper motors (Thorlabs ZST213). With their positioning accuracy of $<2.5 \mu\text{m}$, the biggest positional error in 15 m distance would be below 1 mm. Compared to the spot size of the EKSPLA NL301HT of approximately 6 mm, this was considered satisfactory. In order to correlate the laser beam position on the target to the mirror position, which was actuated by the stepper motors, a bilinear calibration in the form of

$$\begin{aligned} P_x &= a_0 + a_1x + a_2y + a_3xy \\ P_y &= b_0 + b_1x + b_2y + b_3xy, \end{aligned} \tag{5.1}$$

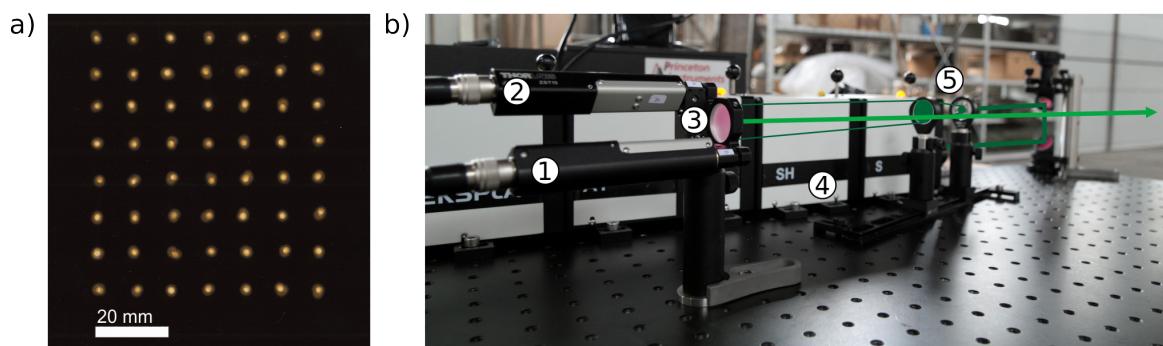


Figure 5.6: **a)** Pattern of 9x9 1 mm spaced points, produced by accumulating ten laser pulses on a piece of photo-paper at a distance of 15 m. **b)** Photo of the mirror setup including the two stepper motors (1,2), the kinematic mirror holder (3), the beam conditioning unit (5) and the laser (4).

was applied, where P_i are the motor position and a_i , b_i the parameters of the respective coordinate, which have to be determined through a calibration process. Usually 8 points were chosen and positioned to with the actuators, while every position was marked on the target surface. Then the correlation parameters a_i and b_i could be calculated. With this a very regular pattern could be produced, shown in figure 5.6 along with a photo of the setup.

The telescope used is a Celestron C6-XLT, a 6 inch (152.4 mm) Schmidt-Cassegrain type tube featuring a focal length of 1500 mm (f/9.9). Connection to the spectrograph was facilitated by an optical fiber, namely an Avantes round-to-slit fiber bundle (200 19 μm fibers) with an NA of 0.22 (f/2.23). A f-number matching lens with a focal length of 50 mm was used after a long-pass edge-filter was put in place to block out the Rayleigh scattered light. The slit end of the fiber was positioned collinear to the entrance slit of the spectrograph for maximum light throughput. The spectrograph was of Czerny-Turner configuration and acquired from Princeton Instrument (Acton SP2750) with a focal length of 750 mm and a aperture of f/9.7. The triple grating turret was equipped with a 300, 600 and 1800 grooves/mm blazed gratings. The output of the spectrograph was directed onto a Princeton Instruments PI-MAX iCCD camera, already featured in the first column of table 3.3. Spectra were acquired by binning the vertical pixels columnwise. Stand-off Raman mappings were acquired by setting specific location and then fire a certain amount of pulses onto the sample, whilst the camera detected the backscattered photons after a specific delay. To increase the SNR level, several pulses were co-added onto the CCD chip, accumulating more signal. The spectra was then recorded and saved on disk. The next position of the mapping was subsequently started. This process was repeated until the map was completed. For easier handling all of these step were automated using LabVIEW.

The achievable Field Of View (FOV) of optical components can be calculated according to [126]

$$AFOV = \tan^{-1}\left(\frac{h}{2bf}\right) \quad \text{with} \quad b = 1 + \frac{|m|}{m_p} \quad \text{and} \quad |m| = \frac{f}{d-f}, \quad (5.2)$$

where AFOV is the angular FOV, h is the sensor height (or aperture diameter), b is the bellows factor, f the focal length, $|m|$ the perpendicular magnification, m_p the pupil magnification and d the distance to the object plane equal to the working distance. The horizontal FOV is then calculated as

$$HFOV = 2d \tan\left(\frac{AFOV}{2}\right). \quad (5.3)$$

To calculate the HFOV for the fiber coupled telescope, a diameter of 1.5 mm for the fiber bundle was measured, the effective focal length of the telescope and matching lens was calculated to be 1000 mm, resulting in an AFOV of 0.08°. The HFOV then amounts to approximately 22 mm at a distance of 12 m, which was also measured and can be seen in figure 2a of Publication V.

Generally, the performance of this type of mapping stand-off Raman imager is discussed in Publication V. As one can imagine, 22 mm is a rather limited FOV, hence the mapping of the laser beam relative to the telescope is not suitable for larger images. Here, a collinear approach would exceed this limitation, but would also require the movement of the whole telescope setup. This means setting and stabilizing a new point for measurement will take a considerable amount of time, which is clearly the time consuming step in this kind of imager. Similarly, the required spatial resolution for a map will increase the measurement time, since each additional point has to be recorded in sequence. So it seems cumbersome for imaging a larger area without prior knowledge of the location of a desired target substance. Here, imaging techniques using the whole FOV of the collection optics should be better suited, which will be discussed in the following sections.

5.2.3 Building a stand-off HSRI

To decrease the time necessary for imaging a given area of interest, a bigger FOV is desirable. The only reasonable choices for achieving that are either using different optics or, as proposed here, use a bigger sensor size. Since the diameter of commonly available fiber bundles is limited and achieving a greater FOV with a fiber coupled system would not really achieve acceptable spatial resolution without extensive mapping, direct imaging onto a iCCD seems to be the logical choice. For that, as previously mentioned, a tunable filter with a large enough aperture is needed to select a certain

5.2. Remote chemical detection using Hyperspectral Raman Imaging

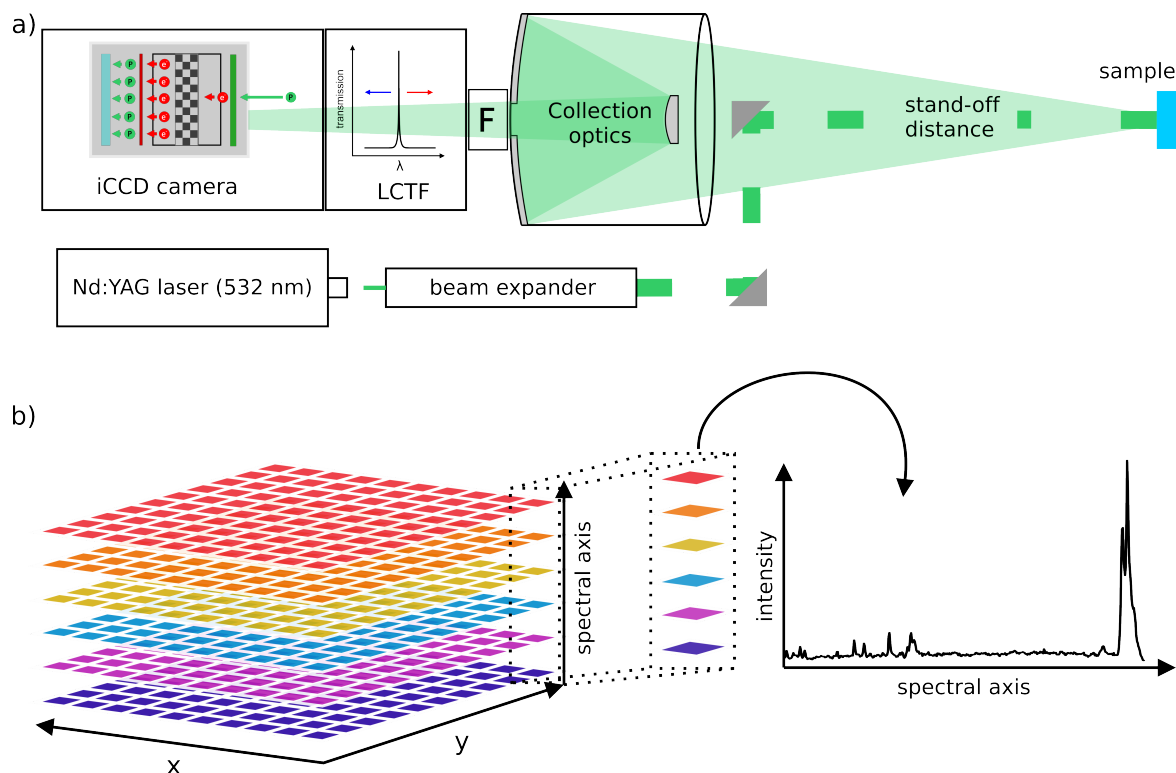


Figure 5.7: **a)** Illustration of the principle setup for a staring stand-off HSRI instrument. **b)** The general structure of the HSI in the staring HSRI type with stacked spectral snapshots, where the same pixel on every stack represent the measured Raman spectrum.

spectral band and pass the corresponding image to the array detector. One suitable technique, the AOTF, consists of a birefringent crystal attached to a piezoelectric transducer. These devices diffract transmitted light by the refractive index pattern created by the standing acoustic wave and thus provide a programmable grating. The spectral position of the bandpass is selected by changing the frequency of the transducer i.e. the sound wave [127]. The main drawbacks of AOTFs are the image degradation due to image shift during tuning, image dispersion in the direction of diffraction and the relative broad spectral bandwidth. Nevertheless, AOTFs have been used for Raman spectroscopy [128, 129]. Another possibility is the use of tunable Fabry-Pérot cavities, as described in section 3.1.5. Here, previous studies used piezo-actuated, large aperture tunable cavities to achieve a tunable filter in the UV region, but there is still room of improvement regarding spectral resolution and throughput [130]. Yet another suitable candidate is the liquid crystal tunable filter (LCTF). It is based on the concept of a birefringent interferometer discussed in section 3.2.4 and features fast electronic tuning, very good spectral resolution with a decent optical throughput. The fact that it is also

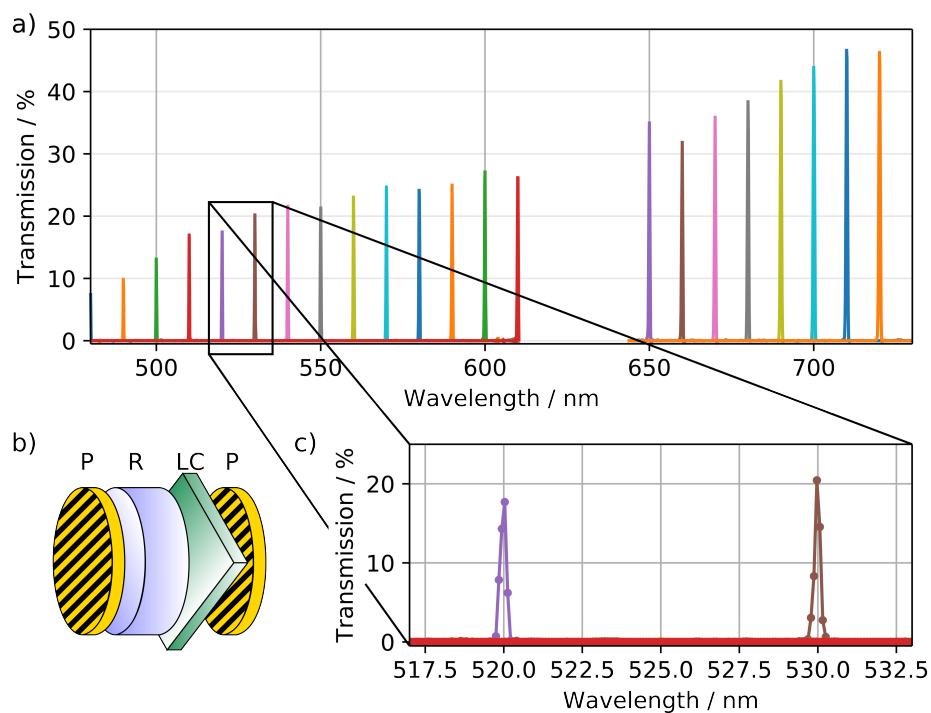
Table 5.1: Different commercially available LCTFs and their characteristic properties. VS stands for VariSpec.

| | <i>VS VIS/VISR</i> | <i>VS SNIR/NIRR</i> | <i>VS LNIR</i> | <i>VS XNIR</i> |
|------------------|--------------------|---------------------|----------------|----------------|
| Spectral range | 400/480-720 nm | 650-1100 nm | 850-1800 nm | 1200-2450 nm |
| Bandwidth | 7, 10, 20/ 0.25 nm | 7, 10/ 0.75 nm | 6, 20 nm | 9 nm |
| Aperture | 20/ 35 mm | 20 mm | 20 mm | 20 mm |
| Acceptance angle | 7.5°/ 3.5° | 7.5°/ 3.5° | 3.5° | 3.5° |
| Response time | 50 ms/ 150 ms | 150 ms | 150 ms | 150 ms |

commercially available made it the candidate of choice for the design of a stand-off HSRI. The properties of commercialized LCTFs are listed in table 5.1 and a illustration of a single stage can be seen in figure 5.8b. The LCTF used in this thesis was the VariSpec VISR because of its spectral resolution of 0.25 nm. The manufacturer assures a wavelength stability of 0.03 ± 0.5 nm, stable operation from 10 to 40°C and a maximum input power of 500 mW/cm². It provides an easy to use serial interface, is also powered over the USB bus and has no mechanical moving parts, which allows rugged sensing in difficult environments. The included software development kit (SDK) allowed a fast programming and integration into the LabView environment.

5.2.4 Characterization of the HSRI

Figure 5.8a shows the transmission of the LCTF at different spectral positions over the whole tuning range. With 50 % being the theoretical maximum of transmission, this is only achieved in the longer wavelength range of the useful spectral range. Figure 5.8c shows a zoomed part of two transmission bands at 520 and 530 nm, which both feature bandpasses narrower than the specified 0.25 nm. During the assembly of the LCTF, telescope and the camera, a test object was scanned for evaluation of the optical arrangement. A fluorescent light bulb was chosen as first analysis target, a monochrome picture is shown in figure 5.9a. A HSI of the turned on bulb was acquired starting at 480 to 720 nm with a step size of 3 nm, with the intensifier of the camera being at 5 % and the gate at 10 ms. A fluorescent lamp is a form of low-pressure mercury discharge lamp, with a cathode at each end consisting of a coiled tungsten heater coated with special oxides of barium and strontium, which emit electrons when heated. These electrons ionize noble gas atoms inside the bulb surrounding the filament to form a plasma through impact ionization. Then also the mercury atoms are ionized through

**Figure 5.8:**

a) Measured transmission of the VISR LCTF. **b)** Illustration of a single Lyot type cell used in the VISR LCTF with P...polarizer, R...fixed retarder and LC...liquid-crystal. **c)** Zoom in of two transmission bands at 520 and 530 nm.

avalanche ionization and emit in the UV region of the EM spectrum. The inner surface of the lamp is coated with a fluorescent coating made of varying blends of metallic and rare-earth phosphor salts to shift the spectrum of the lamp into the visible. Depending on the composition and doping of the phosphor components, the perceived spectrum (and the measured one of course) changes. A "cool white" labeled fluorescent lamp utilizing two rare-earth-doped phosphors, Tb^{3+} , $\text{Ce}^{3+}:\text{LaPO}_4$ for green and blue emission and $\text{Eu}:\text{Y}_2\text{O}_3$ for red. Figure 5.9d shows the spectrum of a position on the center of the fluorescent tube of the lamp (P1) and one spectrum at the position of the cathodes (P2). Except intensity-wise, the spectra are nearly identical, showing the main emission peak from the $^5\text{D}_0-^7\text{F}_2$ transition from $\text{Eu}:\text{Y}_2\text{O}_3$ [131]. Figure 5.9b depicts the intensity distribution for this emission line, which follows nicely down the fluorescent tube. All of the most prominent emission lines can be attributed to either Hg, Tb or Eu using the NIST atomic spectra database [132]. Interestingly enough, at 697 nm (see figure 5.9c and e) in the intensity distribution only the cathode areas light up, meaning that we see a specific emission probably coming from the cathode material, although it is hard to pinpoint which one it is (Tungsten has a line there, as has Ba and Sr per NIST database). Nevertheless, it shows the ability of the setup to record sharp images of a target at a distance of 12 m and the ability to measure sharp spectral lines (the maximal resolution of the system was not exhausted, as only every 3 nm a point was measured due to file size restrictions.)

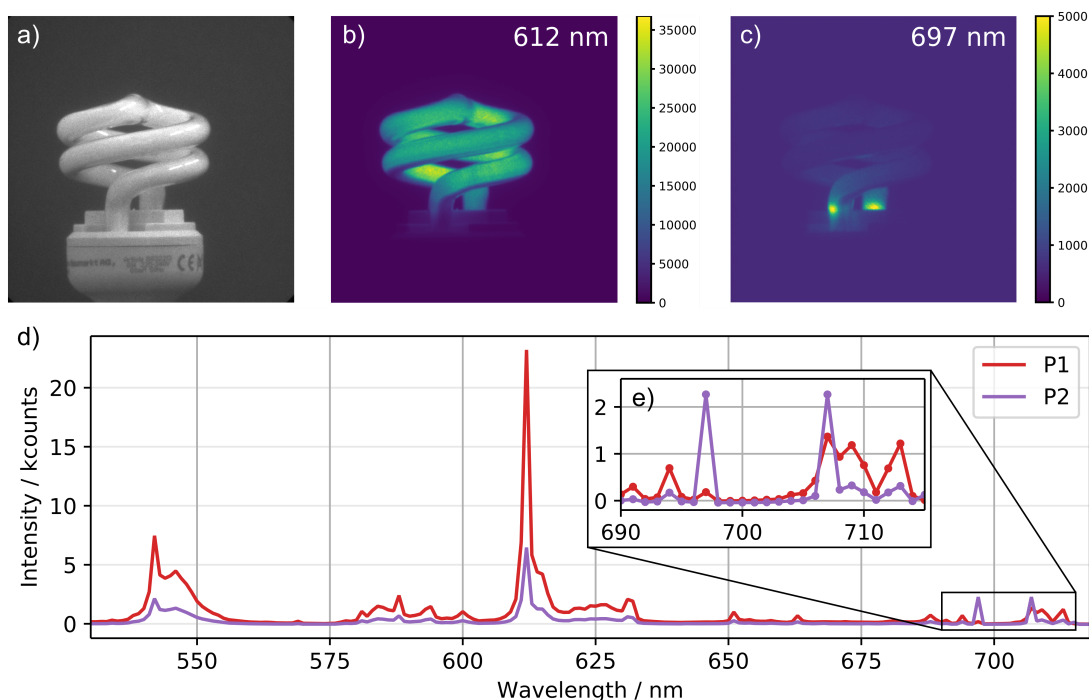


Figure 5.9: **a)** Black & white image of the fluorescent light bulb. **b)** Intensity distribution at the most intense emission band at 612 nm. **c)** Intensity distribution at 697 nm. **d)** Raw spectra of point P1 at the center of the light bulb and of point P2 located at the electrodes. **e)** Inset showing zoomed version of the spectral range showing the most significant differences between point P1 and P2.

5.2.5 Characterization of the pulsed, air-cooled laser

For laser power and pulse energy measurements of the Explorer One HE 532 pulsed laser a Gentec SOLO 2 powermeter was used. Different laser repetition rates and diode currents were applied. The repetition rate investigations were carried out with a diode current of 7.54 A, which is the highest nominal rating for the current and delivers the highest light output. Figure 5.10c shows this behavior, where when higher diode currents are applied, pulse energy as well as average power increase. Change in repetition rate of the laser has a somewhat different effect: With lower frequencies, the pulse energy increases, but the average power is reduced, which should be expected since power is pulse energy times repetition frequency (see figure 5.10a). The average power reaches a maximum at a repetition rate of approximately 18 kHz, before decreasing again due to ever lower pulse energies. Laser pulses were examined using a Thorlabs DET10A Silicon biased detector and a LeCroy 64Xi oscilloscope with a maximal sample rate of 10 GS/s. As pulses are expected to be 10 to 100 ns long, the bandwidth and rise time of the photodiode must be good enough to resolve the pulses in the time domain.

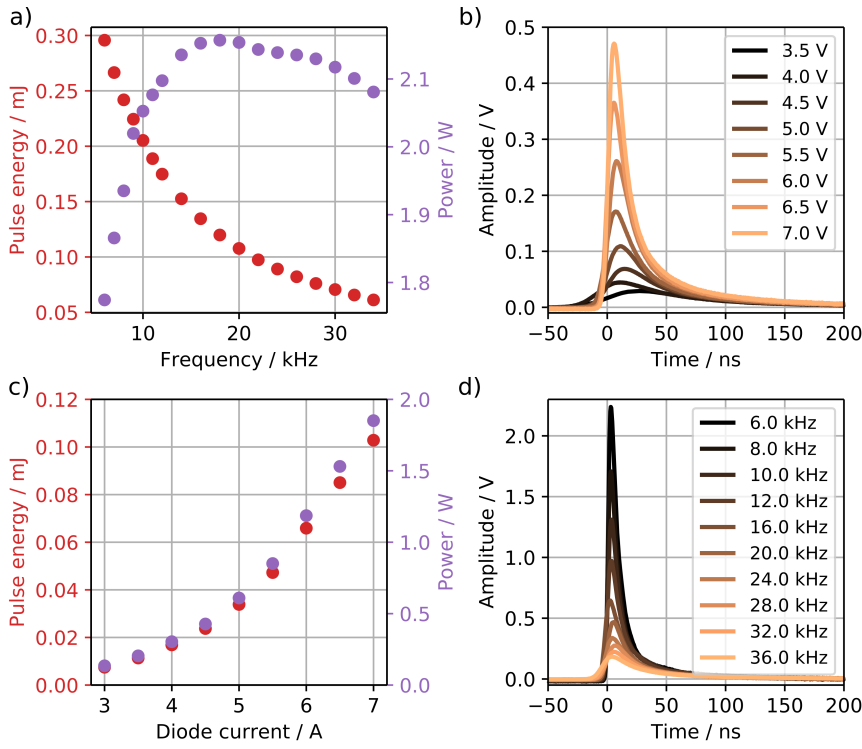


Figure 5.10: Characterization of the Explorer One HE 532. **a)** Pulse energy and average power for different repetition rates. **b)** Laser pulses for different diode currents. **c)** Pulse energy and average power for different diode currents. **d)** Laser pulses for different repetition rates.

The bandwidth can be approximated as follows:

$$\begin{aligned}
 BW &= \frac{1}{2\pi RC_j} \\
 \tau_r &= \frac{0.35}{BW},
 \end{aligned}
 \tag{5.4}$$

with BW being the bandwidth, R the load resistance, C_j the junction capacitance and τ_r the rise time of the diode. In this study the diode was terminated with 50Ω at the input of the oscilloscope. The junction capacitance has a value of 6 pF , so the bandwidth amounts to approximately 530 MHz and the rise time to approximately 0.7 ns . This is sufficient to resolve the laser pulses, as figures 5.10b and 5.10d show. Laser pulses at lower repetition rates show steeper pulses, which is related to the higher pulse energies seen before. The change in form of the pulse with both repetition rate and diode current is important to know, as the trigger signal is coming from a built-in photodiode and emits a trigger pulse when a certain threshold is reached, which depends heavily on the pulse shape. Hence, determining the perfect delay and gate time is to be redone whenever one of those two parameters are changed.

5.2.6 Design of a mobile, rugged and versatile stand-off HSRI

To build a mobile, field deployable stand-off HSRI, the first important component is the laser. In this case, we used the DPSS Explorer One HE with a emission wavelength of 532 nm. It features air-cooling, small electrical and mechanical footprint and a trigger output with very little jitter, important for correct and stable triggering in gated stand-off Raman spectroscopy. The same telescope as in the mapping type instrument is used, namely the f/9.9 Celestron C6 XLT with an aperture of 6 inch (152.4 mm) and a focal length of 1500 mm. Since the whole scenery is to be acquired at once, an iCCD with squared detector is employed. The Princeton Instruments PI-MAX 4 HbF offers high detectivity and fast gating down to 0.5 ns, with a pixel size of 13 μm and a sensor format of 1024x1024 px. Using equations 5.2 and 5.3, the AFOV when focused to infinity is 0.508°, resulting in a HFOV of 133 mm. Since we are focusing closer than infinity, the bellows factor surmounts to approximately 1.2, reducing the HFOV of our optics to approximately 110 mm. This was also experimentally measured by putting a ruled target at 15 m and evaluating the image at the iCCD. The LCTF has an acceptance angle (half-angle) of 3.5° and an aperture of 22 mm. The f/9.9 telescope has a maximal half-angle of 2.9°, although the aperture with the physical extend of the filter (100 mm) produces some vignetting at the sensor, which can be seen faintly in figure 5.9a at the edges. To excite Raman signals over the whole FOV, the laser beam has to cover the whole area. The laser output beam has a diameter of 0.8 mm with a divergence of 3.9 mrad. Natively, this would result in a beam diameter of 22 mm at a working distance of 15 m, which is not enough. Hence, a beam expander based on a Galilean telescope was constructed. It consists of a concave lens, which widens the beam before a convex lens collimates the beam again, but with a new beam diameter. The ratio in focal length determines the change in diameter of the output beam. Here, two lenses with focal lengths of $f_1 = -50$ mm and $f_2 = 150$ mm with a inter-lens distance of 100 mm would give a 3-times widened beam with the same divergence as the input beam. That would give us 59 mm beam diameter at 15 m, which is still not enough. So the beam expander was slightly defocused, increasing the beam divergence of the output beam. Now the beam was widened to fit the FOV of the camera/telescope optic. Nevertheless, the output beam of the laser has a Gaussian profile, meaning the intensity towards the edges falls off significantly. It is therefore more adequate to define an effective FOV, given by the area with sufficient illumination to produce adequate Raman signals. To determine this, a flat uniform polymer sheet was used as a target and the intensity distribution was assessed. From this measurement we deduced that the effective FOV is smaller than the visually illuminated diameter and by using a FWHM criterion, it was determined to be 70 mm in diameter (see Publication V, Figure 2). Widening the beam to this extend also decreases the power, which is radiated onto the sample. The effect is

quite drastic: Let's assume a typical confocal Raman microscope with 532 nm excitation laser has a focus point of about 500 nm in diameter and a power output of 20 mW. The power density at the sample will be $102 \text{ mW}/\mu\text{m}^2$, whereas the 2 W output power of the pulsed laser are distributed over a diameter of 70 mm, resulting in a power density of $5 \cdot 10^{-7} \text{ mW}/\mu\text{m}^2$. This equals a decrease of $2 \cdot 10^8$. Together with the challenge of detecting the backscattered photons with smaller solid angles than when microscope optics are employed, one can understand the skeptical demeanor of many scientist at the beginning of stand-off or remote Raman applications. Nevertheless, the quality of the acquired spectra is sufficient for most use cases and very well comparable to standard techniques, as is shown in Publication V, Figure 3.

Another important issue is the stability and quality of the spectral resolution achieved with the HSRI (primarily a function of the LCTF). To test this, a flat sheet of Teflon was positioned at 15 m distance and a HSI was acquired. Subsequently, the intense and sharp band at 746 cm^{-1} was analyzed by fitting a pseudo-Voigt profile and evaluating the maximum and the FWHM. Inside the FOV of the system, good spectral stability both ind position and bandwidth was obtained (see figure 2, Publication VI).

A more detailed comparison between the stand-off mapping and direct stand-off HSRI is given in Publication V. Some features of the prototype should be highlighted here. The LabVIEW user interface allows to control all of the components and the most important functionalities involved in this technique. All laser parameters can be set, as well as the lasing element temperature checked, which is of utmost importance for stable emission. Additionally, a stepper motor was installed, which was connected to the focus knob of the telescope. Hence, stable focusing inside the software is possible. Direct control over the LCTF and monitoring of the elements temperature is also integrated. The most important parameters to set during a measurement are:

Sequential or repetitive gating Sequential Gating allows for steady change of either delay or gate time and is necessary for finding the best synchronization between laser and camera. The repetitive mode allows for on-CCD accumulations to increase the SNR.

Gate and delay time The parameters for the time of flight measurement.

On-CCD accumulations To increase SNR, more than one shot is averaged, usually a measurement time of seconds for a single frame is chosen.

Internal or external trigger The internal triggering is used for monochrome photos of the target or VIS spectroscopy. The external trigger is used for synchronization with the laser.

Intensifier gain Sets the gain of the MCP inside the intensifier of the ICCD.

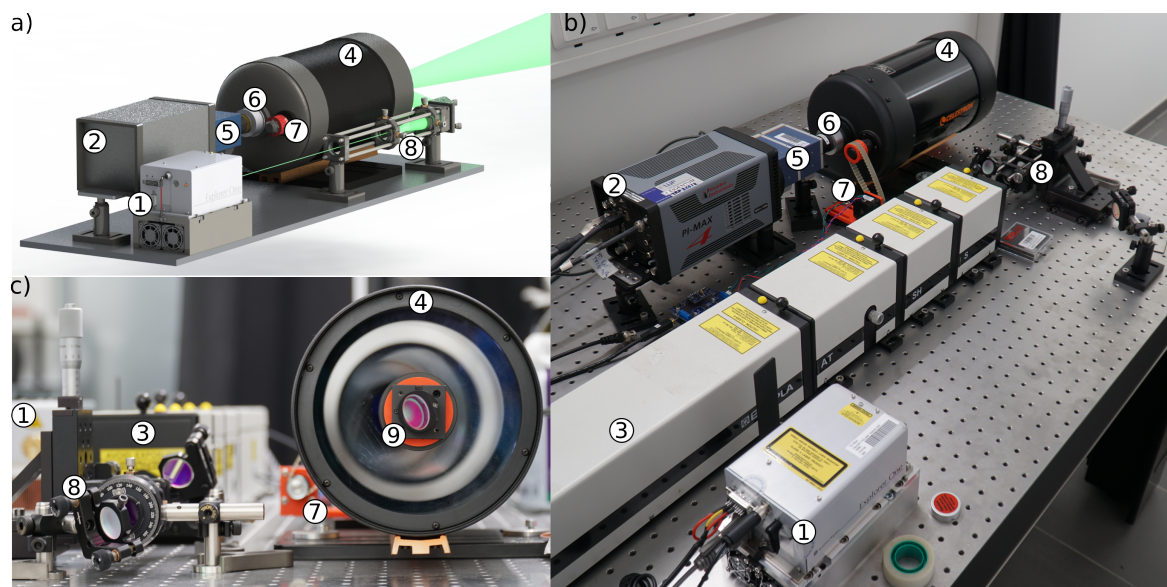


Figure 5.11: **a)** Rendering of the compact, mobile instrument setup. **b)** Photo of an overview of the prototype build on the optical table. **c)** Photo of the front of the prototype build on the optical table. 1...Explorer One DPSS, 2...iCCD (1024x1024), 3...EK-SPLA laser, 4...Celestron C6 telescope, 5...VariSpec LCTF, 6...Rayleigh filter, 7...Focus motor control, 8...Galilean beam expander, 9...custom made, front-mounted collinear laser mirror holder.

In the developed software, there are three different measurement modes:

VIS Mode Here, either a fixed wavelength can be set to acquire a monochrome picture of the sample (for focusing or as a reference) or a VIS spectrum over any spectral range with a chosen stepsize within the specifications of the LCTF can be acquired.

Raman Mode As the name suggests, this mode acquires Raman HSIs. It can be set to a specific Raman shift, very useful when searching for the perfect delay or gate time. Additionally, a full HSRI can be measured starting at an arbitrary Raman shift with a spectral resolution of the users choosing within the specifications of the LCTF.

Region selector Mode Most often, for the successful identification of a unknown sample it is not necessary acquiring the whole Raman spectrum, but instead various important regions where the most important Raman bands reside. This mode allows the user to set any number of regions with different spectral steps sizes, to adapt the measurement protocol to the problem at hand. This can significantly reduce the time needed for completion of the measurement.

Lastly, the handling and processing of the acquired data has to be mentioned. A single frame of the camera has about 5 MB in size, for 600 spectral positions (which mimics a typical spectrum from a commercial spectrometer) the minimal space requirement is 2.9 GB. One can easily see, how fast actually disk space can be filled when measuring several HSIs. Therefore, the acquired HSI was directly saved as binary datacube, which can be directly opened with the commercial HSI processing software ImageLab. This way, efficient storing and easy processing of the HSIs is guaranteed, an important aspect for the following sections.

5.3 Chemometrics and HSI: a perfect fit

Chemometrics, a term coined by Wold in the beginnings of the 1970s [133], is concerned with the application of mathematical and statistical techniques to extract chemical and physical information from complex data. It has now a firm footing in most applications in spectroscopy, especially in quantitative multivariate process analysis [79, 82]. The most important techniques for quantitative analysis of MIR and NIR spectra are PLS and Principal Component Regression (PCR) [134, 135]. It can also be used to disentangle information of a singular sample measured with different vibrational and elemental spectroscopic techniques, increasing the information depth which ultimately leads to a complete understanding of the chemical structure of the sample [136]. As discussed in the previous section, HSIs can feature considerable sizes, making interpretation of the measured data very difficult, even for experts. Chemometrics can help reducing the amount of information into digestible pieces, especially when it can get rid of excess noise and instrument caused artifacts. For the qualitative analysis of the HSI, in problems posing the question if substance A is present or not, classification techniques are the most suitable fit. Classification algorithms are automated procedures which identify patterns in data sets in order to assign a property (class) to each sample. The patterns are first identified using data with known classes (training data) and can then be used to make predictions for future data with unknown class label. For these models, the raw intensities of the acquired spectra are the input features or variables. However, raw intensities may not be very selective in some cases because they are prone to noise and may be highly correlated (different wavenumbers around a vibrational band will behave very similarly). Furthermore, spectra may cover a large range of wavenumbers, leading to a high number of variables and the resulting high dimensional dataspace is problematic for many mathematical models. This can be mitigated by using spectral descriptors, which incorporate the chemical information inside the descriptor, thereby reducing the amount of variables.

One of the more used classifiers is the Random Decision Forest (RDF), which can be

used for fast classification as well as for efficient variable selection. It will be discussed in more detail in the following section.

5.3.1 Random decision forest

A Random Forest (RF) is an ensemble classifier based on a set of binary decision trees [137]. Decision trees belong to the most trivial classifiers and consist of a sequence of binary decisions along a certain threshold. After each node, the data is split into two subsets which separate the samples in a best possible way (see dotted lines in the training phase shown in figure 5.12). With every nodal point the tree grows deeper and the purity of the nodes increases. The growing process is finished when all the samples in a node belong to the same class. This terminal node is also called leaf. With each node, the model adapts better to the training data, hence deep decision trees exhibit low bias, but show at the same time high variance. To mitigate this, the idea behind the RDF is to build a large number of uncorrelated trees. Then, by averaging their results, the variance is reduced while the bias remains low. This procedure is called bootstrap aggregation or bagging. Figure 5.12 shows the training process: Each of the N_T trees is grown with a bootstrap sample, which is a randomly selected subset of the training set. The bootstrap sample is drawn with replacement, which means that within a given training set some samples can occur multiple times while others are not represented at all. This ensures that all decision trees are trained with different training data.

The main parameter on the RDF to be optimized is the number of trees N_T . With N_T too small, the variance may still be high and the model is prone to noise. The upper limit for N_T is computation time during training, which increases with larger numbers of N_T , but does usually not yield considerable improvement. Here, RDF can be parameter-optimized without the use of external validation, like cross-validation, by using the so-called Out-Of-Bag (OOB) error, a procedure similar to cross-validation. Thereby, a bootstrap sample smaller than the original subset is chosen for growing the n -th tree [138]. The remaining (OOB) samples are classified by the n -th tree and the deviation is determined. After growing all trees the mean error can be estimated.

The main advantages of the RDF is that it doesn't need extensive preprocessing of the data, it is robust concerning the parameter settings, it inherently performs multi-class tasks and proofed to be robust in high dimensions [139]. The main disadvantage is relatively high computation time during training when a large number of trees is used. Another big advantage is the possibility of determining a variable importance. This can be done by computing the discrepancy between OOB errors resulting from a subset obtained through random permutations of the values of the different variables and the OOB error of the original dataset [140]. This can be used in a n exploratory study to

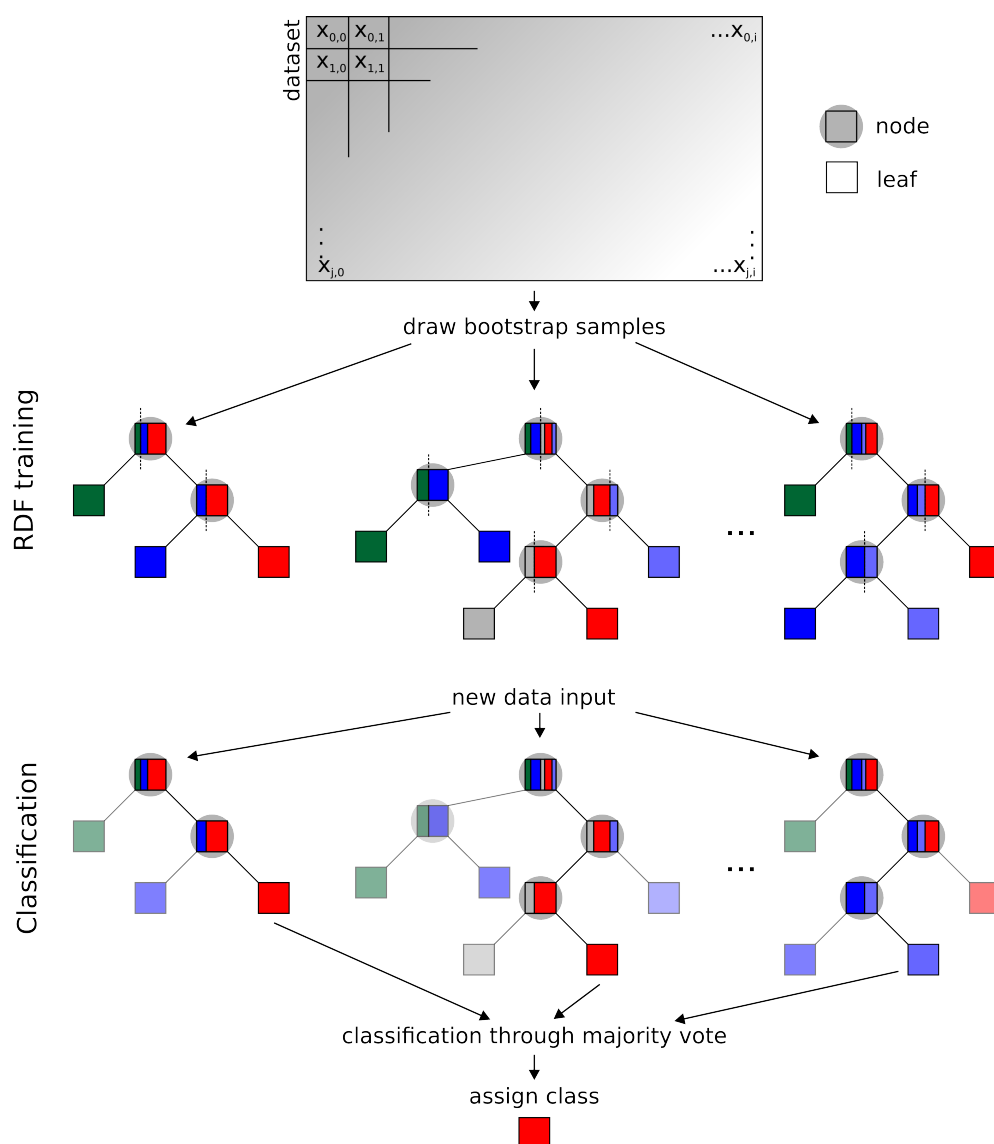


Figure 5.12: Illustration of the principle of a Random Decision Forest. Out of the complete training data matrix, bootstrap samples are drawn randomly, for each a decision tree is grown in the training phase. Once the RDF is complete, a new sample is classified by majority vote of all decision trees.

find the most suitable spectral regions for the identification of certain compounds. During this thesis, the RDF and especially the variable importance was used to create a reliable and fast stand-off HSRI scheme for the detection of explosives at a distance of 15 m. Therefore, a training sample was created by putting mg-amounts of explosives on a Aluminum substrate in random positions. A full HSRI was acquired, which after spike removal and baseline correction was used to train a RDF using all spectral

positions measured. The resulting variable importance (Publication VI, Figure 6) showed which parts of the Raman spectrum were important for the classification. Subsequently these regions were selected and special descriptors were used to create a more selective and stable signal. With this new spectral descriptors another RDF was created, with a dataset showing smaller dimensionality due to the smaller variable count. This is especially useful for the HSRI instrument built here, because if the number of measured spectral positions is reduced, the acquisition speed of the prototype increases rapidly. The process and the results are given in more detail in Publication VI.

5.4 Publication V: Comparing mapping and direct hyperspectral imaging in stand-off Raman spectroscopy for remote material identification

Authors: Christoph Gasser, María González-Cabrera, María José Ayora-Cañada, Ana Domínguez-Vidal and Bernhard Lendl

Published in: *Journal of Raman Spectroscopy*

Status: Accepted, in press

Short summary:

This work is aimed at a thorough comparison between stand-off Raman mapping (called pointwise imager) and the direct Hyperspectral Raman imager (HSRI). The design and performance figures of merit are presented for both imagers. The setup of the direct HSRI is presented, where a defocused laser beam illuminates a wide area of the sample and the Raman scattered light is collected from the whole field of view (FOV) at once as a spectral snapshot filtered by a liquid crystal tunable filter to select a specific Raman shift. Both techniques are compared in terms of achievable field of view, spectral resolution, signal to noise performance and time consumption during a measurement at stand-off distance of 15 m. The HSRI showed superior spectral resolution and signal to noise ratio, while more than doubling the FOV of the PI at laser power densities reduced by a factor of 277 at the target.

Additionally, the application of chemometrics is shown on the output HSI dataset. Vertex component analysis is employed to get a simple deterministic false color image showing the chemical composition of the simple test target. This is shown for an artificial polymer sample, measured at a distance of 15 m.

1 Comparing mapping and direct hyperspectral imaging 2 in stand-off Raman spectroscopy for remote material 3 identification

4 Christoph Gasser¹, María González-Cabrera², María José Ayora-
5 Cañada², Ana Domínguez-Vidal², Bernhard Lendl¹

6 ¹Institute of Chemical Technologies and Analytics, TU Wien, Vienna, Austria

7 ²Department of Physical and Analytical Chemistry, Universidad de Jaén, Campus Las
8 Lagunillas, s/n 23071, Jaén, Spain

9 Abstract

10 Stand-off Raman spectroscopy offers a highly selective technique to probe unknown
11 substances from a safe distance. Often, it is necessary to scan large areas of interest. This
12 can be done by pointwise imaging (PI), that is spectra are sequentially acquired from an
13 array of points over the region of interest (point-by-point mapping). Alternatively, in this
14 paper a direct Hyperspectral Raman imager (HSRI) is presented, where a defocused laser
15 beam illuminates a wide area of the sample and the Raman scattered light is collected from
16 the whole field of view (FOV) at once as a spectral snapshot filtered by a liquid crystal
17 tunable filter (LCTF) to select a specific Raman shift.

18 Both techniques are compared in terms of achievable field of view, spectral resolution,
19 signal to noise performance and time consumption during a measurement at stand-off
20 distance of 15 m. The HSRI showed superior spectral resolution and signal to noise ratio
21 (SNR), while more than doubling the FOV of the PI at laser power densities reduced by a
22 factor of 277 at the target. Further, the output hyperspectral image (HSI) data cube can be
23 processed with state of the art chemometric algorithms like vertex component analysis in
24 order to get a simple deterministic false color image showing the chemical composition of
25 the target. This is shown for an artificial polymer sample, measured at a distance of 15 m.

26 **Keywords:** stand-off, remote detection, Raman spectroscopy, hyperspectral imaging
27

28 Introduction

29 Stand-off Raman spectroscopy is a highly versatile remote detection technique, which
30 combines the advantages of Raman spectroscopy with the benefit of separating physically
31 the instrumentation from the sampling point. Illumination via laser light and collection of
32 primarily backscattered Raman photons allow for a remote detection scheme, as long as
33 free propagation of photons is possible. This makes stand-off Raman spectroscopy a potent
34 analytical solution for a variety of applications. The exploration of different materials
35 located on planetary surfaces is one of the most prominent studied application possibilities,
36 given its advantages in terms of accessibility of remote objects also when the rover is
37 stationary^[1]. A wide range of samples, such as minerals, organics and inorganics have been
38 detected before by using remote Raman instruments^[2-4]. The possibility of maintaining a
39 distance from the target whilst obtaining relevant analytical information without

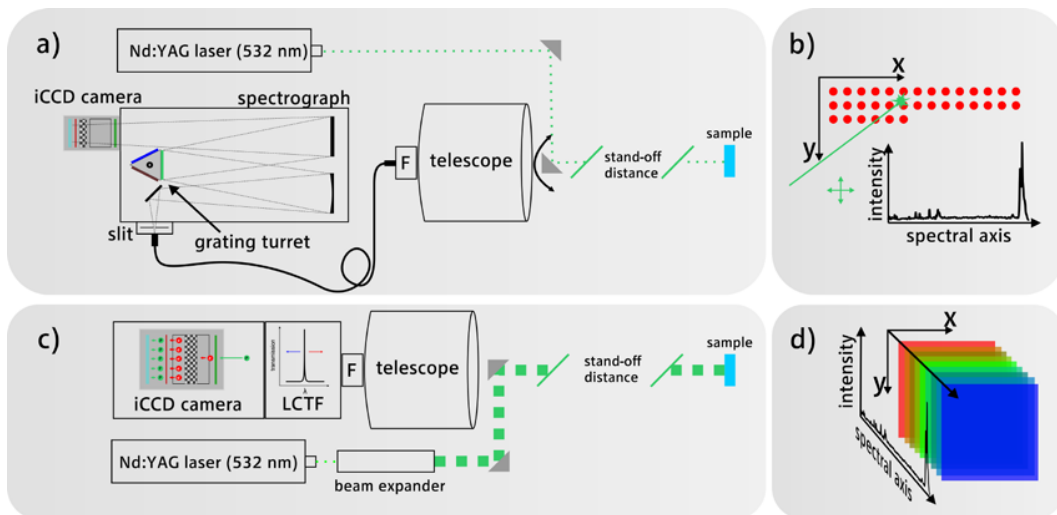
1 compromising the safety of the operator or the instrument makes stand-off Raman
2 spectroscopy also the ideal tool for detection of hazardous or harmful materials. This has
3 been demonstrated with different types of explosives^[5,6] and possible concealed threats in
4 several kind of containers^[7,8]. Moreover, art, heritage and restoration applications could
5 also benefit from the use of stand-off instrumentation, due to the considerable reduction of
6 the risk of producing contaminations or alterations in the composition of original works of
7 artistic value and the improved accessibility to hard-to-reach areas such as ceilings or high
8 walls.

9 Hyperspectral imaging describes a wide range of increasingly used and constantly evolving
10 techniques for chemical and structural analysis, which provides both spatial and spectral
11 information for a given sample of interest^[9,10]. The result of these measurements is a three-
12 dimensional dataset, which consists of the two-dimensional spatial information and an
13 additional spectral dimension, thus forming a hyperspectral image (HSI) cube. Generally,
14 two different techniques of obtaining this HSI cube can be differentiated: spatial and
15 spectral methods. Regarding spatial scanning methods, two-different approaches can be
16 distinguished: point-by-point mapping (whiskbroom imaging) and line-scanning
17 (pushbroom imaging)^[11]. In whiskbroom imaging, a spectrum of a specific spatial position
18 of the sample is obtained and then the area of interest is scanned by moving pointwise to
19 generate a mapping of the sample surface. Most of Raman-based hyperspectral imaging
20 techniques use microscopes and accurate translation stages to move the sample in order to
21 achieve Raman maps^[12]. If however, a whole line of spectra is recorded at the same time
22 and is scanned laterally over the sample a HSI can be created much faster. This is generally
23 known as pushbroom approach, which utilizes the fact that most detectors used for Raman
24 spectroscopy are two-dimensional arrays with one free dimension, which in turn can be
25 used to image one dimension of the sample surface onto the detector thus considerably
26 increasing the acquisition speed^[9]. On the other hand, spectral scanning methods collect a
27 two-dimensional spatial image for each wavelength band at a time. Therefore, the HSI cube
28 is built by stacking spectral snapshots on top of each other. This requires the possibility of
29 selecting a certain wavelength and image it onto the detector array, which can be facilitated
30 by tunable bandpass filters. Such filters have multiple prerequisites, they have to provide
31 an adequate width of the bandpass in order to ensure sufficient spectral resolution, good
32 transmission characteristics, large optical aperture for passing the image and fast tuning.
33 Among several possible technologies, acousto-optical tunable filters (AOTF), tunable
34 Fabry-Perot cavities (TFPC) and liquid crystal tunable filters (LCTF) are the most
35 commonly used^[13]. AOTFs, which usually consist of a birefringent crystal attached to a
36 piezoelectric transducer, provide a programmable grating, thus acting like a tunable filter.
37 The transmitted light is diffracted by the acoustic wave and the spectral position of the
38 bandpass is selected by changing the frequency of the transducer i.e. the sound wave^[14].
39 The main drawbacks of AOTFs are the image degradation due to image shift with tuning,
40 image dispersion in the diffraction direction and the bigger bandwidth compared to LCTFs.
41 ^[15]TFPCs consist of two reflective surfaces, which's transmission characteristics depend
42 on, among others, the distance between the surfaces^[16]. Piezoelectric crystals can be used
43 to facilitate the spectral tunability of TPFCs with large optical apertures by changing the
44 distance of the reflective surfaces^[17]. LCTFs are based on Lyot filters, where a filter stage
45 is based upon one birefringent crystal plate sandwiched by orthogonal polarizers^[18].
46 Multiple stacks with varying thickness of plate retarders create a narrowband bandpass,

1 which can be tuned by using a liquid crystal panel^[19,20]. Since LCTFs offer fast and reliable
 2 tuning with good spectral bandwidth at a small footprint, they have been used for several
 3 HSI applications^[21], among them Raman spectroscopic imagers^[22].
 4 In this study we compare the performance of two different stand-off Raman imaging
 5 approaches: a pointwise or whiskbroom imager (PI), where the HSI is created by scanning
 6 the laser point over the sample; and a direct HSRI, where the HSI is created by stacking
 7 spectral snapshots on top of each other. The PI system employs a classical diffracting
 8 spectrometer, coupled to the telescope by an optical fiber with the laser point being scanned
 9 over the sample by means of an electronically controlled mirror. The HSRI uses a LCTF
 10 to select a specific Raman shift and collect a spectral image, while the laser illuminates the
 11 whole field of view (FOV) of the telescope or rather the camera ^[23]. In order to suppress
 12 unspecific light (originating from e.g. daylight) the emission of the laser pulse and the
 13 acquisition of the backscattered photons were synchronized. Both configurations are
 14 compared in terms of achievable FOV, signal to noise ratio (SNR) and time consumption
 15 during a measurement at a stand-off distance of 15 m. Furthermore, the importance of
 16 spatial resolution is explored for the purpose of chemical identification of small amounts
 17 of substances at stand-off distances.

18 Materials and methods

19 In this study two different optical setups were employed, which are displayed in Figure 1a
 20 and c. The first includes a collimated laser beam creating an illuminated point with a
 21 diameter of 6 mm, which is mapped over the target area with the help of a motorized mirror.
 22 The whole Raman spectrum is collected from each measurement point and then combined
 23 into a HSI cube (Figure 1b). The second setup employs a widened and unfocused laser
 24 beam, which illuminates an area with an apparent diameter of approximately 100 mm. The
 25 scattered Rayleigh light is filtered and directly imaged onto the camera, thus generating the
 26 HSI cube, one image at a time, along the spectral axis (Figure 1d).



27

28 *Figure 1: Simplified sketch of the instrumentation used in this study for (a) pointwise stand-off*
 29 *Raman spectroscopy and (c) direct stand-off Raman imaging setup with an illustration*
 30 *of the hyperspectral image generation for both methods respectively in (b) and (d).*

1 In both systems, a Q-switched, frequency doubled (532 nm) Nd:YAG NL301HT laser
2 (EKSPLA, Lithuania) with a pulse energy of 50 mJ, a pulse length of 4.4 ns and a repetition
3 rate of 10 Hz was used as an excitation source. The beam profile is specified exhibiting a
4 top-hat beam profile in the near field and a near-Gaussian profile in the far-field with a
5 beam divergence lower than 0.6 mrad.

6 ***Pointwise stand-off Raman imager (PI)***

7 For the pointwise stand-off Raman system the laser was aligned coaxially to a 6" Schmidt-
8 Cassegrain telescope (C6-A-XLT, $f = 1.5$ m, $f/9.9$, Celestron, USA) for the collection of
9 Raman scattered light using a motorized kinematic mirror mount (KS1-Z8, Thorlabs,
10 USA), which allowed for the mapping of the laser onto the sample area. The backscattered
11 Rayleigh light was filtered using a long pass filter (LP03-532RE, Cut-off wavelength
12 533.3 nm, OD > 6, Semrock, USA) and the Raman photons were guided to an Acton
13 standard series SP-2750 spectrograph (slit 120 μm , $f/10$, 300 grooves/mm, Princeton
14 Instruments, Germany) via a round-to-slit fiber optical bundle cable consisting of nineteen
15 200- μm diameter optical fibres (FCRL 19UV200, NA 0.22, Avantes, Netherlands). To
16 match the F number of telescope and fiber bundle, a $f = 50$ mm lens was used. Finally, the
17 backscattered light was detected by a PIMAX 1024RB intensified CCD (iCCD) camera
18 (QE 7.5% @ 600nm, Princeton Instruments, USA). The outgoing laser pulse and the gate
19 of the iCCD camera were synchronized so that the measurement window coincided with
20 the maximum Raman signal. Data acquisition and mapping was automated using
21 LabVIEW[®] (National Instruments, USA).

22 ***Direct stand-off hyperspectral Raman imager (HSRI)***

23 The direct stand-off imager (Figure 1c) employed an expanded laser beam, generated using
24 a defocused Galilean type beam expander in order to achieve an apparent beam diameter
25 of approximately 100 mm at the sample. This was done by The backscattered Rayleigh
26 photons were again filtered through a long pass filter (LP03-532RE, Cut-off wavelength
27 533.3 nm, OD > 6, Semrock, USA). Subsequently, the Raman photons were filtered using
28 a tunable LCTF filter (VariSpec VISR, Perkin-Elmer, USA) with a spectral resolution of
29 0.25 nm and directly imaged onto an iCCD equipped with a quadratic sensor (PIMAX 4
30 1024f-HBf iCCD. 1024x1024 pixels, 13 μm pixels, QE 45% @ 600nm, Princeton
31 Instruments, USA). The VariSpec LCTF is of the Evans Split element variety, which
32 requires only half as many polarizers as an equivalent Lyot filter type^[24]. The LCTF has a
33 clear aperture of 20 mm, a free spectral range of 480-720 nm, an angle of acceptance of 7°
34 and a response time of 150 ms. The transmission of the LCTF varies over the whole
35 spectral range, with a mean transmission of 22.5 % in the area of interest. Each acquired
36 spectral image was stacked in order to build the hyperspectral data cube. This process was
37 automated using LabVIEW[®] (National Instruments, USA).

38 ***Chemometric methods***

39 Vertex component analysis (VCA) was used for the evaluation of the generated HSI data
40 cubes. VCA is a technique for unsupervised endmember extraction assuming the data is a

1 linear mixture of pure components, also called endmembers^[25]. For the analysis, the
2 commercial software ImageLab (Epina GmbH, Austria) was used.

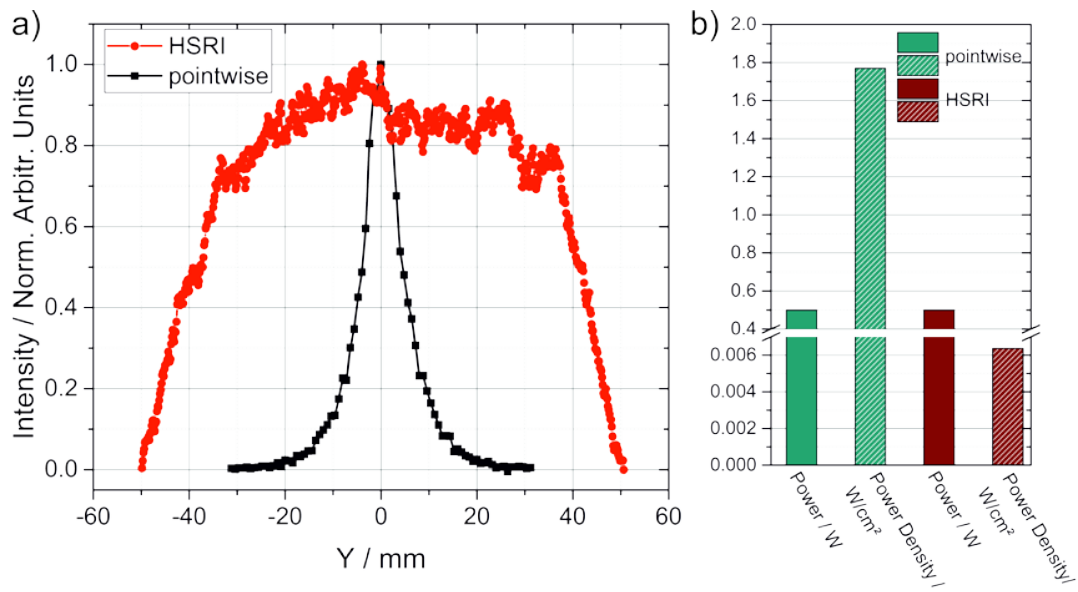
3 ***Chemicals***

4 Plates of different chemical composition and thickness were acquired from RS
5 Components (United Kingdom), namely polypropylene (PP, 2 mm), polyethylene (PE,
6 4 mm), polytetrafluoroethylene (PTFE or Teflon, 6 mm) and Nylon (N6, 4 mm). Pieces
7 were cut out and glued together using small amounts of cyanoacrylate on the edges of the
8 cut pieces. Sulfur (>99.98%) was obtained from Sigma-Aldrich and for the spatial
9 resolution experiments, polylactic acid (PLA) plates were designed as samples containers
10 on the computer and 3D printed afterwards.

11 **Results and discussion**

12 ***Illumination system***

13 Illumination and FOV differ greatly between the two systems. Figure 2a depicts the FOV
14 of both configurations over the horizontal axis Y, measured on a PP plate of 2 mm
15 thickness at a distance of 15 m. For the PI setup this was done by scanning the laser point
16 laterally step by step away from the center and recording a spectrum at every point.
17 Afterwards, the intensity of the band at 2890 cm^{-1} was assessed in dependence of the
18 horizontal position of the illumination point. The resulting curve (black) shows a distinct
19 fall off with increasing offset from the central point, reaching the 10 % mark at a diameter
20 of approximately 24 mm. To assess the field of view of the HSRI prototype, the same PP
21 plate was used at 15 m distance as a target. A spectral image at 2890 cm^{-1} was acquired
22 and the intensity was evaluated along the same horizontal axis Y as before. The HSRI
23 configuration shows a broader intensity profile, mainly influenced by the emission
24 characteristics of the laser beam. Normally, the FOV of a telescope and CCD chip
25 combination is influenced by the focal length of the telescope, the stand-off distance and
26 the size of the CCD chip itself. For the employed HSRI system, this surmounts to a
27 theoretical FOV of approximately 110 m. Ideally, for the HSRI the laser beam has an ideal
28 top-hat structure also in the far-field, which means the energy density within the beam is
29 uniform. This leads to a uniform intensity distribution in aberration-free optical systems,
30 which enables the usage of the whole image without loss of SNR in less illuminated border
31 regions. For the HSRI presented in this study the effective FOV with adequate Raman
32 intensity amounts to a diameter of approximately 70 mm.



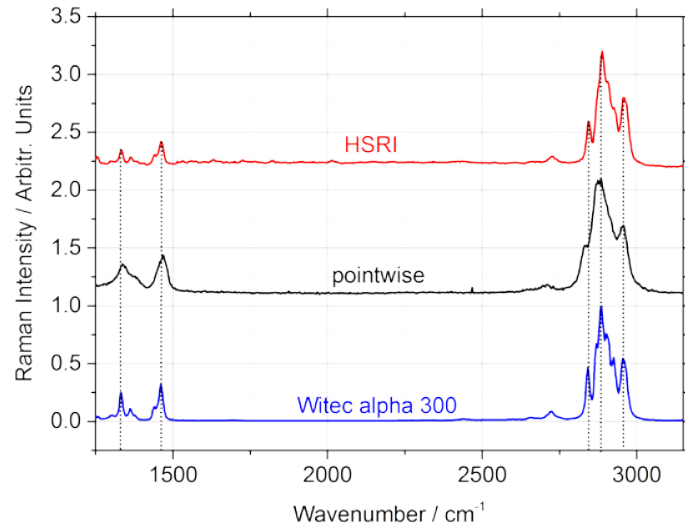
1

2 *Figure 2: a) Measured field of view for both configurations on the horizontal axis Y. b)*
 3 *Laser power and power density used in this study for both configurations.*

4 In the PI system the numerical aperture and the diameter of the fiber bundle limit the FOV.
 5 In contrast to the HSRI, the PI system with its fiber bundle with a numerical aperture of
 6 0.22 and a diameter of 1.5 mm, the effective FOV is reduced to an area with a diameter of
 7 24 mm. This means that the maximal useful area that can be illuminated for the PI is
 8 452 mm² and for the HSRI it is 3848 mm², a less than tenfold increase.

9 *Spectral investigations*

10 Spectra obtained with both systems were compared to spectra taken with a commercially
 11 available Raman microscope (alpha300rsa, Witec, Germany) with the same excitation
 12 wavelength of 532 nm used throughout this study. Again, a PP plate was the target of
 13 choice and Figure 3 shows the obtained spectra.



1

2 *Figure 3: Exemplary spectra of PP obtained with the HSRI system (red) and with the*
 3 *pointwise stand-off imager (black) at 15 m distance. Reference PP spectrum (blue) taken*
 4 *with a commercial instrument (Witec alpha300rsa).*

5 On the high Raman shift range from 2840 to 2950 cm^{-1} typical bands arising from the
 6 symmetric and asymmetric stretch vibrations of the methyl and methylene group can be
 7 found. Additionally, the bands attributed to the symmetric and asymmetric bending of the
 8 methyl and methylene group present in PP are visible between 1260 and 1500 cm^{-1} in the
 9 chosen spectral range. Both configurations of stand-off Raman imagers show the same
 10 bands as the reference taken by the Raman microscope and the spectral positions are in
 11 good agreement. The biggest difference in the shown spectra is their respective resolution.
 12 The Raman microscope uses a 600 gr/mm grating, which results in a spectral resolution of
 13 approximately 4 cm^{-1} with the spectrograph and camera built into the instrument. The PI
 14 system with a 300 gr/mm grating and a 750 mm focal length f/10 spectrograph has the
 15 lowest spectral resolution of the compared systems with approximately 15 cm^{-1} . The HSRI
 16 imager does not use a classical spectrograph as the dispersive element, but the LCTF.
 17 Hence, the spectral resolution is a function of the width of the transmission curve, which
 18 is specified by the manufacturer to be constant over the complete visible range at 0.25 nm.
 19 This amounts to a mean spectral resolution of 7.4 cm^{-1} in the observed spectral range.
 20 Additionally, the relative intensities vary between spectrograph and filter systems. The
 21 tunable filter has lower throughput at shorter wavelengths, which becomes apparent when
 22 comparing bands at higher Raman shifts with bands at lower Raman shifts for the
 23 spectrograph and the filter configuration in Figure 3. Nevertheless, the resolution is
 24 sufficient for most common applications, even exceeding the PI setup, which already
 25 showed its usefulness in previous works^[4].

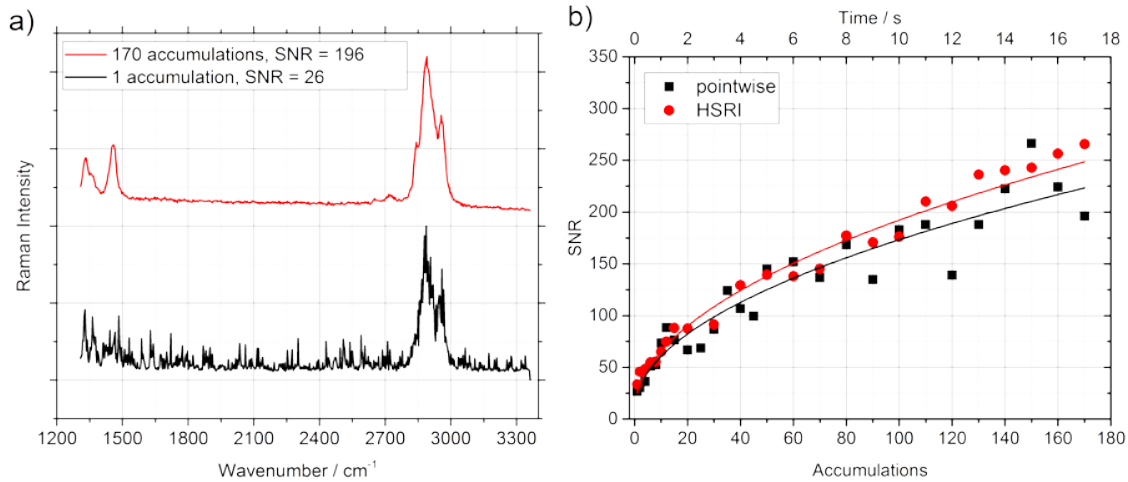
26 The tunable filter in the HSRI is mainly used because of the ability to perform direct
 27 imaging. Hence, in this system it is important to evaluate the uniformity of the transmission
 28 window in terms of spectral position and spectral resolution over the field of view.

29 To do this, a PTFE plate with an appropriate size was measured using the HSRI prototype.
 30 The region from 700 to 1500 cm^{-1} with spectral steps of 2 cm^{-1} was acquired, thereby
 31 oversampling the theoretical resolution of the HSRI of approximately 7 cm^{-1} . PTFE shows

1 several bands in this region, the two most important ones are the skeletal stretching at
2 approximately 746 cm^{-1} and the symmetric CF_2 stretching modes at approximately
3 1380 cm^{-1} [26]. Since the band at 746 cm^{-1} shows higher intensity and narrow linewidth, it
4 was chosen to be the indicator for spectral resolution and position accuracy of the filter. To
5 assess these parameters, a fit of the band using a pseudo-Voigt profile [27] was performed
6 and the full width at half maximum (FWHM) and the center of the fitted function were
7 determined. Figure S3b displays an exemplary fit. This was done for the whole HSI cube,
8 the distribution of the center position and FWHM over the imaged surface are represented
9 in Figure S3c and d, respectively. In the central circle with a diameter of 70 mm the center
10 position varies around 746 cm^{-1} by no more than 2 cm^{-1} with a standard deviation of
11 0.28 cm^{-1} . An aggregation of extreme values at the edges of the image is observed.
12 Similarly, the calculated FWHM ranges from 10 to 14 cm^{-1} in the inner circle, with
13 considerable outliers at the edges of the image. These extreme values are due to the lower
14 intensity of the exciting laser at the edges of the imaged area, reducing the SNR of the
15 resulting spectra and preventing a regular fit for center position and especially for FWHM
16 evaluation. Overall, the reported deviations of both center position and FWHM are within
17 the expected error margin, given that the spectral resolution of the filter is specified to be
18 around 7.5 cm^{-1} . This means that adequate Raman spectra collection using the tunable filter
19 is viable for the whole aperture given a strong enough laser excitation

20 *Signal to noise*

21 To investigate the signal to noise performance of PI and HSRI, a PP plate was mounted at
22 15 m and measured with the systems. Both instrumentations work in a pulsed and time-
23 gated mode, meaning that after a laser pulse is emitted, a trigger signal is sent to the camera.
24 After a set time delay of typical a few hundreds of nanoseconds (depending on the sample-
25 telescope distance), the gate of the intensifier is opened for 5 ns. This way, otherwise
26 interfering light sources can be suppressed and the Raman signal from the sample can be
27 maximized. The SNR in this study was calculated by using the mean intensity between
28 2890 and 2905 cm^{-1} (at the center of the C-H stretch vibrational band) divided by the
29 standard deviation between 3090 and 3200 cm^{-1} (baseline noise). When only one-shot
30 measurements are performed, spectra tend to be of low quality as can be observed in Figure
31 4a. Therefore, usually more than one pulse is accumulated on the CCD in order to increase
32 the SNR. With increasing number of accumulations the quality of the spectra improves
33 considerably.

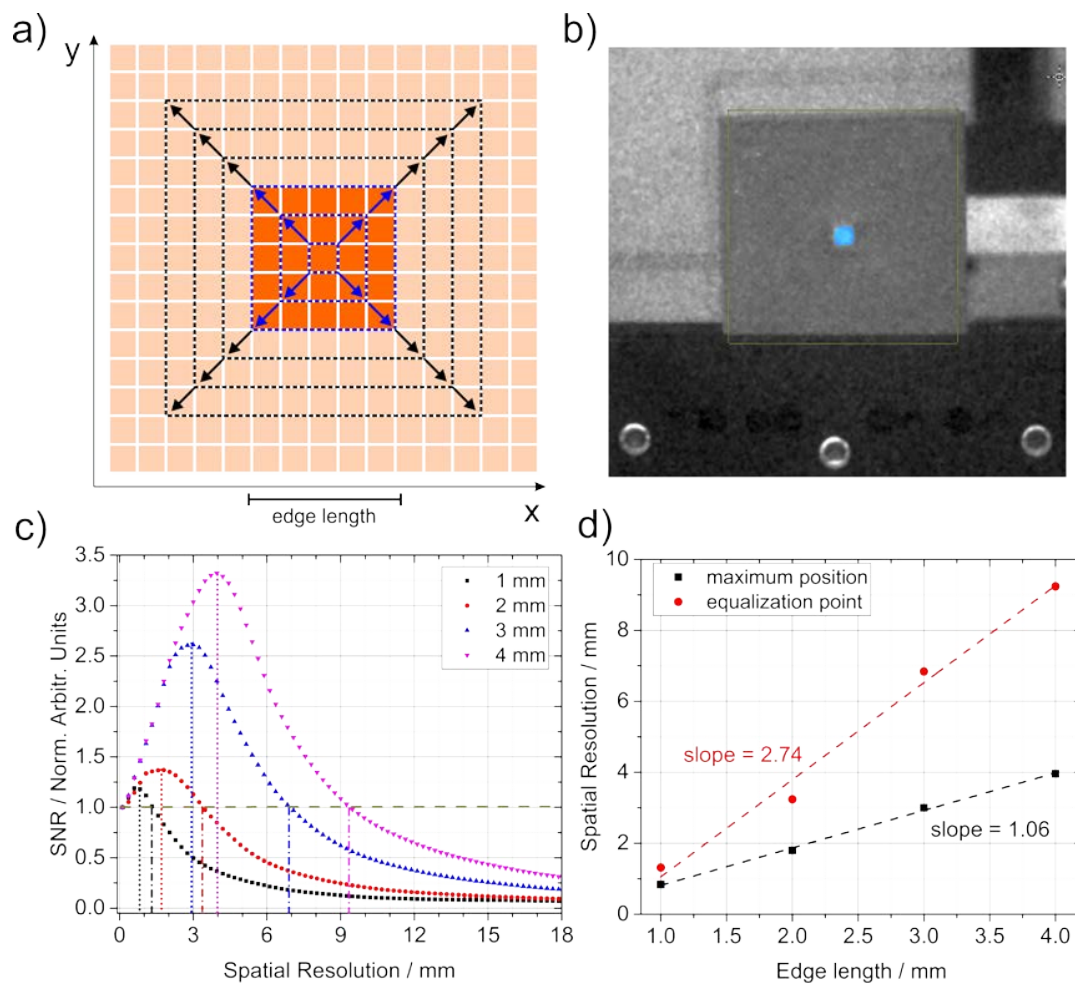


1

2 *Figure 4: a) Spectra of PP acquired with the PI system for two different number of*
 3 *accumulations with calculated SNRs. b) Signal to noise for both setups over the number of*
 4 *accumulations, i.e. acquisition time.*

5 Figure 5b shows the increase of SNR with increasing numbers of accumulation in the
 6 expected way of the square root of accumulations (fitted curves). For the HSRI, an area of
 7 pixels equaling the excitation area of the PI imager was averaged (28 mm²) in order to
 8 calculate the SNR. As visualized in Figure 4b the PI imager and the HSRI show similar
 9 results in SNR. This favors the HSRI setup, when comparing the laser power impinging
 10 onto the sample. The laser sends out an energy of 50.8 mJ/pulse, which yields an averaged
 11 power of 0.5 W and considering a beam diameter of 6 mm results in power density of
 12 1.77 W/cm² for the PI system. The HSRI uses an expanded beam to an effective diameter
 13 of approximately 100 mm, which leads to a power density 6.4 mW/cm², a 277-fold
 14 decrease compared to the PI system. The possibility of using lower laser power densities
 15 is beneficial for practical use of such stand-off Raman systems, where moderate power
 16 density levels are sought after due to eye-safety concerns in civil and also military
 17 applications. Since the intensity of scattered Raman photons is directly proportional to the
 18 input of laser power onto the sample, the much lower power density for the HSRI should
 19 cause a significant drop-off in SNR. Instead, a comparable SNR performance of both
 20 systems was observed. This can be explained by the higher optical throughput of the optical
 21 system, e.g. higher throughput of the LCTF compared to the spectrograph, on one side and
 22 a difference in detection efficiency of the iCCD cameras. The PIMAX 1024 RB used in
 23 the PI imager has a quantum efficiency of about 7.5 %, whereas the GenIII intensifier of
 24 the PIMAX4 1024HBf used in the HSRI has one of 45 %, six times more. Additionally,
 25 the étendue, a measure for the gathering power of an optical system, which is equal to the
 26 source emitting area multiplied by the solid angle from which the light is collected, is
 27 different. Due to the small diameter of the single fibers used in the bundle, the PI has an
 28 étendue of 0.27 mm²sr, whereas the HSRI can use up to the full sensor size of the CCD
 29 camera, amounting to an étendue of 1.09 mm²sr. This is an increase of a factor of 4 and
 30 shows one of the downsides of fiber coupled stand-off Raman instruments^[28]. The
 31 throughput of the PI system could however be optimized by using a spectrograph with a F-
 32 number more suitable to the used fiber bundle. Launching the f/2.2 fiber bundle into the
 33 f/10 spectrograph approximately 40 % of the light are lost.

1 Additionally, it is especially useful if larger potentially contaminated or hazardous areas
2 have to be scanned. The studied instrumentations behave differently for this task. The time
3 consuming step for the PI is to move from point to point in order to map the area of interest.
4 So the total measurement time scales with size of the investigated area and the spatial
5 resolution defined by the excitation laser beam diameter. The time consuming step for
6 HSRI is to collect spectral images at each desired Raman shift in order to build up the HSI
7 cube. Here, the total measurement time scales with the number of spectral images necessary
8 for spectroscopic determination of the analytes of interest that is the extension of the
9 spectral range. Additionally, if the area under investigation is bigger than the FOV of the
10 HSRI, further images have to be taken. Figure S1 shows a comparison of the total
11 measurement time for both setups. It assumes a FOV for the HSRI of 70x70 mm² at 15 m,
12 the green and blue solid lines are the calculated time values for the respective prototype
13 with the configuration used in this study. The dashed lines are calculated for a low spatial
14 resolution for the PI and for a small number of spectral images for the HSRI. The dashed-
15 dotted lines represent the opposite situation, where high spatial resolution is needed for the
16 PI system and a high number of spectral images are needed for the HSRI system. The semi-
17 transparent areas represent the possible or working span of both techniques (Figure S1).
18 Generally, the PI instrument will outperform the HSRI for small areas of interest, since
19 only a few or, in the best case, a single measurement will suffice to complete the assessment
20 of the target. For areas greater than 45 cm² the HSRI starts to be faster than the pointwise
21 acquisition, however after reaching areas over 49 cm² the HSRI has to retake another image
22 outside its FOV, which creates a massive increase in time consumption reflected in the step
23 of graph. Finally, for greater image sizes than approximately 200 cm² the HSRI will always
24 be faster than the PI. Overall, looking at the span stretched over the maxima of both
25 techniques, the HSRI imaging speed scales more advantageously with time.



1

2 *Figure 5: a) Simplified drawing of the CCD chip with an arbitrary feature on top of it. The*
 3 *dashed squares indicate different spatial resolutions. b) Greyscale image of the sample at*
 4 *15 m with a blue overlay of the intensity of the sulfur band at 480 cm⁻¹. c) SNRs calculated*
 5 *for the sulfur for different spatial averaging (simulating different spatial resolutions) and*
 6 *different feature sizes. The pointed lines are the position of the maximum SNR. d) Spatial*
 7 *resolution for which the maximum of the SNR and the equalization point can be observed*
 8 *for different feature sizes i.e. edge lengths.*

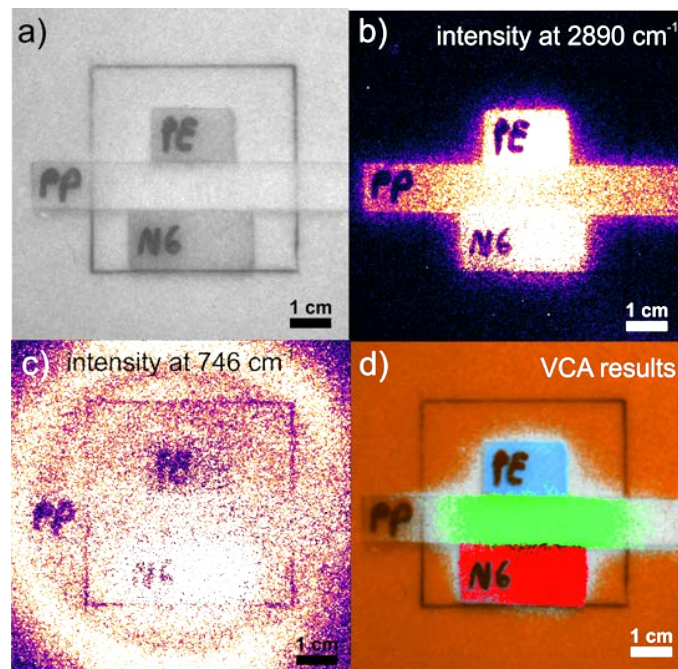
9 In order to highlight the importance of spatial resolution, samples with a sulfur feature of
 10 different sizes have been prepared by 3D printing polymer plates holding different sizes of
 11 cavities filled with sulfur powder. Square cavities with an edge length in the range of 1 to
 12 4 mm and a thickness of 0.3 mm were measured at a distance of 15 m by employing 2 s
 13 acquisition time per spectral snapshot (20 accumulations), 140 ns gate delay and 5 ns gate
 14 width using the HSRI system. The influence of spatial resolution was explored post-
 15 measurement by choosing a central pixel inside the feature and averaging adjacent pixel
 16 spectra to decrease the spatial resolution. Then, the SNR was calculated through the
 17 maximum band intensity between 478 and 482 cm⁻¹ (at the center of the sulfur band)
 18 divided by the standard deviation of the baseline between 510 and 580 cm⁻¹ (baseline
 19 noise). The concept of this study is depicted in Figure 5a, where the reproduction of an

1 arbitrary sample feature (dark orange) on an array detector (light orange) through the
2 imaging optics is indicated. The stepwise variation of the spatial resolution is achieved by
3 spatially averaging spectra of adjacent pixels. As long as the sample feature is bigger than
4 the spatial resolution, spatial averaging (blue arrows in Figure 5a) will result in an increase
5 of SNR following a square root function, since the noise in the baseline is reduced with
6 every averaging step, but the signal level stays constant. In Figure 5c the SNRs for different
7 feature sizes are depicted in dependence of the spatial resolution, normalized to the first
8 value for each series. In the beginning the SNR increases according to the previous stated
9 decrease of noise. When the spatial resolution surpasses the feature size, the situation
10 changes dramatically (indicated by the black arrows in Figure 5a), as new pixels containing
11 solely noise are added and the signal is diluted over the whole pixel area. This still leads to
12 a reduction of noise, however the signal intensity is also heavily reduced, which results in
13 a significant reduction of SNR. The tipping point should coincide with the spatial
14 resolution being of the same size as the sample feature, which was also observed in the
15 experiments (Figure 5d, black curve). Another interesting point is the equalization point,
16 the spatial resolution where the SNR of the different sized features drops down to the
17 original value observed at the highest spatial resolution possible and after which a decrease
18 in spatial resolution always results in lesser quality spectra. It is more than double the value
19 of the feature size in the studied cases (Figure 5d, red curve). This shows in general the
20 importance of having adequate spatial resolution, especially when small amounts of sample
21 are to be detected on large background materials. The concept is also valid for other HSI
22 techniques, but whiskbroom systems are more prone to difficulties, since the time-
23 consuming step is the measurement with adequate spatial resolution. The stand-off HSRI
24 shows its strength here, since producing adequate spatial resolution is not the time-
25 consuming task and can even be changed during the measurement and in post-processing
26 on a software basis.

27 *Chemometric image analysis*

28 The HSRI approach usually leads to large datasets, which in most cases is not
29 informative for the user nor required to solve the given analytical problem. Hence, efforts
30 are made to simplify data interpretation by using a variety of algorithms to deconvolute
31 and classify the recorded data in order to facilitate the extraction of the required
32 information needed to provide a meaningful result. Linear unmixing algorithms are
33 commonly used for hyperspectral datasets, when the presence of pure pixels can be
34 assumed. Among these methods, VCA is advantageous because the VCA algorithm
35 competes with state-of-the-art methods whilst exhibiting a computational complexity
36 between one and two orders of magnitude lower than the best available method^[25]. It
37 additionally involves noise characterization in order to reduce the sensitivity to noise by
38 applying a singular value decomposition. VCA calculates endmembers of the vertices of
39 a simplex spanned by the spectral differences within the dataset. The endmembers
40 represent the most varying spectra with nonnegative intensities and concentrations and
41 can be assigned to chemical constituents in most cases. An example is given in Figure 6,
42 where a sample consisting of four different polymers (PTFE, PE, PP and nylon) is
43 depicted (Figure 6a). It was placed at a distance of 15 m to the telescope and measured
44 using the HSRI prototype. The intensity images of the bands 746 and 2890 cm^{-1} are
45 shown. The effects of polymer thickness and reflectivity can then be observed in Figure

1 6c. Since PTFE is the background material, the intensity at 746 cm^{-1} reflects the laser
2 beam intensity distribution, except for the area blocked by the PE. In the case of PE,
3 which is thicker and less transparent, a drop-off in intensity can be observed. For the
4 nylon however, which is of the same thickness as the PE, a stronger signal is obtained,
5 which is attributed to the fluorescence of the material, which results in an elevated
6 baseline. The signal at 2850 cm^{-1} is very intense for all polymers, except for PTFE,
7 exhibiting the CH stretch vibration at this spectral region. Figure S2 provides a
8 comparison of spectra of selected pixels of the respective polymer measured with the
9 HSRI with a confocal Raman microscope. The VCA is able to find most pixels associated
10 with the respective polymers, except towards some boundary regions between them,
11 where because of mixed spectra the algorithm does not correlate correctly. Nevertheless,
12 as shown in 7d, VCA finds PE (marked in blue), PP (marked in green), Nylon (marked in
13 red) and PTFE (marked in orange). This fast classification of the image can prove useful
14 to a variety of applications.



15

16 *Figure 6: a) Monochrome image of the sample consisting of the 4 polymers. b) Intensity*
17 *distribution at 2850 cm^{-1} (PE). c) Intensity distribution at 746 cm^{-1} (PTFE). d) Overlay for*
18 *VCA endmembers correlation to the different polymers in different colors.*

19 Conclusion

20 In this study, a comparison of a pointwise stand-off Raman imager and a direct
21 hyperspectral Raman imager in terms of achievable field of view, signal to noise, spectral
22 and spatial resolution and total measurement time is reported. The investigated prototypes
23 differ in maximal possible FOV, which for the PI is limited by the numerical aperture of
24 the optical fiber coupling the telescope with the spectrograph and for the HSRI by the FOV
25 of the telescope and CCD size. The HSRI exhibits a FOV of roughly $70\times 70\text{ mm}$, which is

1 nearly ten times more than the FOV of the PI. The stability of the spectral resolution of the
2 tunable filter over the open aperture was investigated and determined to be better than 2 cm^{-1}
3 1 for the central position and better than 4 cm^{-1} for the FWHM of the PTFE band at 746 cm^{-1} .
4 1 . This proves the viability of the filter as a dispersive element for direct Raman imaging.
5 The excitation beam has to be expanded in order to illuminate the whole scene for the
6 HSRI, which leads to significantly lower power density at the sample. For the tested
7 scenario the difference in power density amounts close to 277 fold increase with the PI
8 imager. Nevertheless, the HSRI setup shows similar SNR values over the same
9 measurement time, although the PI system would benefit substantially from a better
10 matched fiber bundle-spectrograph matching.

11 A significant contributor to the time needed for data acquisition is the size of the area to be
12 investigated. A bigger FOV helps with screening larger areas faster. Inversely, the higher
13 the spatial resolution of the imager has to be, the more time a mapping instrument would
14 need, since the diameter of the excitation laser beam would need to be small and the number
15 of mapping points would substantially increase. Spatial resolution is better suited for the
16 HSRI, since the whole FOV of the collection optics can be used with a spatial resolution
17 defined by the pixel size of the CCD chip. In time-gated configuration like stand-off
18 applications, the required time is proportional to the repetition rate of the laser and
19 inversely proportional to the number of accumulations, which holds true for both
20 configurations.

21 In summary, two stand-off Raman imagers were constructed and compared, one relying on
22 mapping of the excitation laser beam, the other directly imaging the scene for single Raman
23 shifts in order to create a HSI cube. The HSRI instrument showed better suitability for large
24 area scanning, especially if a small number of spectral snapshots are required and offers a
25 smaller electric and mechanic footprint, making it the better choice for mobile applications
26 in the field.

27 Acknowledgements

28 Financial support was provided by the Austrian Science Fund (FWF) under the scope of
29 the Translational-Research programme within the research project “Advanced stand-off
30 Raman spectroscopy for chemical identification from safe distances” (TRP-265). M.
31 Gonzalez-Cabrera acknowledged the Ministry of Education, Culture and Sports
32 (FPU15/03119 fellowship) for a mobility grant during her doctorate studies.

33 References

- 34 [1] S. M. Angel, N. R. Gomer, S. K. Sharma, C. McKay, *Appl. Spectrosc.* **2012**, *66*,
35 137.
36 [2] T. E. Acosta-Maeda, A. K. Misra, L. G. Muzangwa, G. Berlanga, D. Muchow, J.
37 Porter, S. K. Sharma, *Appl. Opt.* **2016**, *55*, 10283.
38 [3] A. K. Misra, S. K. Sharma, T. E. Acosta, J. N. Porter, D. E. Bates, *Appl. Spectrosc.*
39 **2012**, *66*, 1279.
40 [4] B. Zachhuber, G. Ramer, A. Hobro, E. t. H. Chrysostom, B. Lendl, *Anal. Bioanal.*
41 *Chem.* **2011**, *400*, 2439.
42 [5] K. L. Gares, K. T. Hufziger, S. V Bykov, S. A. Asher, *J. Raman Spectrosc.* **2016**,

- 1 47, 124.
- 2 [6] S. Wallin, A. Pettersson, H. Ostmark, A. Hobro, *Anal. Bioanal. Chem.* **2009**, 395,
3 259.
- 4 [7] B. Zachhuber, C. Gasser, E. t. H. Chrysostom, B. Lendl, *Anal. Chem.* **2011**, 83,
5 9438.
- 6 [8] M. L. Ramírez-Cedeño, W. Ortiz-Rivera, L. C. Pacheco-Londoño, S. P.
7 Hernández-Rivera, *IEEE Sens. J.* **2010**, 10, 693.
- 8 [9] A. A. Gowen, Y. Feng, E. Gaston, V. Valdramidis, *Talanta* **2015**, 137, 43.
- 9 [10] A. A. Gowen, C. P. O'Donnell, P. J. Cullen, G. Downey, J. M. Frias, *Trends Food*
10 *Sci. Technol.* **2007**, 18, 590.
- 11 [11] Y. J. Hsu, C.-C. Chen, C.-H. Huang, C.-H. Yeh, L.-Y. Liu, S.-Y. Chen, *Biomed.*
12 *Opt. Express* **2017**, 8, 3005.
- 13 [12] T. Dieing, O. Hollricher, J. Toporski, *Confocal Raman Microscopy*, **2010**, vol.
14 158.
- 15 [13] P. J. Lapray, X. Wang, J. B. Thomas, P. Gouton, *Sensors (Switzerland)* **2014**, 14,
16 21626.
- 17 [14] S. E. Harris, R. W. Wallace, *J. Opt. Soc. Am.* **1969**, 59, 744.
- 18 [15] H. R. Morris, C. C. Hoyt, P. J. Treado, *Appl. Spectrosc.* **1994**, 48, 857.
- 19 [16] C. Calaza, L. Fonseca, M. Moreno, S. Marco, C. Cané, I. Gracia, *Sensors*
20 *Actuators A Phys.* **2004**, 113, 39.
- 21 [17] M. Kaarre, S. Kivi, P. E. Panouillot, H. Saari, J. Mäkynen, I. Sorri, M. Juuti, J.
22 Mäkynen, I. Sorri, M. Juuti, *AIP Conf. Proc.* **2013**, 1537, 231.
- 23 [18] J. W. Evans, *J. Opt. Soc. Am.* **1949**, 39, 412.
- 24 [19] G. Shabtay, E. Eidingen, Z. Zalevsky, D. Mendlovic, E. Marom, *Opt. Express*
25 **2002**, 10, 1534.
- 26 [20] J. Staromlynska, S. M. Rees, M. P. Gillyon, *Appl. Opt.* **1998**, 37, 1081.
- 27 [21] N. Gat, in *Proc. SPIE*, (Eds: H. H. Szu, M. Vetterli, W. J. Campbell, J. R. Buss),
28 **2000**, vol. 4056, pp. 50–64.
- 29 [22] H. R. Morris, C. C. Hoyt, P. Miller, P. J. Treado, *Appl. Spectrosc.* **1996**, 50, 805.
- 30 [23] H. Östmark, M. Nordberg, T. E. Carlsson, *Appl. Opt.* **2011**, 50, 5592.
- 31 [24] J. W. Evans, *J. Opt. Soc. Am.* **1949**, 39, 229.
- 32 [25] J. M. P. Nascimento, J. M. B. Dias, *IEEE Trans. Geosci. Remote Sens.* **2005**, 43,
33 898.
- 34 [26] C. J. Peacock, P. J. Hendra, H. A. Willis, M. E. A. Cudby, *J. Chem. Soc. A*
35 *Inorganic, Phys. Theor.* **1970**, 2943.
- 36 [27] F. Sánchez-Bajo, F. L. Cumbreira, *J. Appl. Crystallogr.* **1997**, 30, 427.
- 37 [28] A. K. Misra, S. K. Sharma, C. H. Chio, P. G. Lucey, B. Lienert, *Spectrochim. Acta*
38 *Part A Mol. Biomol. Spectrosc.* **2005**, 61, 2281.
- 39
- 40

5.5 Publication VI: Stand-off hyperspectral Raman imaging and random decision forest classification: a potent duo for the fast, remote identification of explosives

Authors: Christoph Gasser, Michael Göschl, Johannes Ofner and Bernhard Lendl

Published in: *Analytical Chemistry*

Status: Submitted

Short summary:

As mentioned in the last section, this study is centered around the idea of the combination of a random forest classifier with the stand-off hyperspectral Raman imager (HSRI) for the fast detection and classification of different explosives at a distance of 15 m. Therefore, the collected hyperspectral image cube (HSI) is evaluated and classified using a random decision forest (RDF) algorithm. The RDF is trained with a training set of mg-amounts of different explosives i.e. TNT, RDX, PETN, NaClO₃ and NH₄NO₃ on an artificial aluminum substrate. The resulting classification is validated and variable importance is used to optimize the RDF using spectral descriptors, effectively reducing the dimensionality of the dataset. Using the gained information, a faster acquisition and calculation mode can be designed, giving improved results in classification at a much higher repetition rate.

Stand-off hyperspectral Raman imaging and random decision forest classification: a potent duo for the fast, remote identification of explosives

Christoph Gasser, Michael Göschl, Johannes Ofner and Bernhard Lendl*

Institute of Chemical Technologies and Analytics, TU Wien, Getreidemarkt 9/164, 1060 Vienna, Austria

ABSTRACT: In this study we present a stand-off hyperspectral Raman imager (HSRI) for the fast detection and classification of different explosives at a distance of 15 m. The hyperspectral image cube is created by using a liquid crystal tunable filter (LCTF) to select a specific Raman shift and sequentially imaging spectral images onto an intensified CCD camera. The laser beam is expanded to illuminate the field of view of the HSRI and thereby improves large area scanning of suspicious surfaces. The collected hyperspectral image cube (HSI) is evaluated and classified using a random decision forest (RDF) algorithm. The RDF is trained with a training set of mg-amounts of different explosives i.e. TNT, RDX, PETN, NaClO₃ and NH₄NO₃ on an artificial aluminum substrate. The resulting classification is validated and variable importance is used to optimize the RDF using spectral descriptors, effectively reducing the dimensionality of the dataset. Using the gained information, a faster acquisition and calculation mode can be designed, giving improved results in classification at a much higher repetition rate.

The advance in computer or machine vision over the last decades fueled a wide range of new and exciting possibilities for automated recognition, classification and control in medical^{1,2}, industrial^{3,4} as well as military⁵ areas. At the same time, the need of rapid detection of localized traces of harmful substances such as explosives at safe distances increased due to the rise of domestic attacks and the accompanying elevated security risk and screenings. It is imperative then, to distinct the chemical composition of a target substance in an area of interest, deciding whether or not it poses a threat. This can most effectively be done by adding another layer of information to an ordinary image by means of spectroscopy, a technique known as Hyperspectral Imaging (HSI). Continuous advancements in instrumentation led to a plethora of different combinations of spectroscopic and imaging techniques with the goal of creating spatially resolved chemical maps for various different applications, ranging from food quality and safety analysis⁶ to biomedical engineering⁷. Raman spectroscopy (RS) seems to be particularly suited as a spectroscopic technique to be implemented in such HSI screening devices, since it offers high chemical selectivity whilst being a non-destructive method and features the ability to be used at remote distances due to its scattering nature. Lasers allow light to be transported over significant distances without high losses, hence, probing distant samples via stand-off RS is viable. In stand-off RS applications, the instrument is physically separated from the sample⁸, which is especially useful if dangerous or harmful substances are the target of an investigation or the target area is poorly accessible. The detection of explosives and explosive residues using stand-off RS became prominent due to the successful endeavor of this kind of instruments to detect tiny amounts of explosive material at significant distances, shown in several studies over the last years⁹⁻¹¹.

The result of a HSI experiment is a data cube, where two axis represent the local information and an additional axis is occupied by the spectral variables. Most spectroscopic techniques are suitable for obtaining HSI, generally the recording mechanism can be divided into three techniques: whiskbroom¹², pushbroom¹³ and staring or spectral scanning¹⁴ measurement. The whiskbroom scanner uses a single point detection scheme,

which mapped over a certain area produces the HSI. The first RS HSI instruments were based on this scheme using microscope systems, where the implementation of RS due to its scattering nature and ability to work in the visible spectral range is preferable¹⁵. High spatial resolution is a direct benefit of using an optical microscope as both excitation and collection optic, which can even dissect samples optically into μm thin slices when a confocal arrangement is used¹⁶. Similarly, in the pushbroom approach, a line is scanned over area of interest with an array detector, where one axis is dedicated to the spectral axis¹⁷. Lastly, the staring or spectral scanning techniques utilizes a tunable filter to select a specific spectral feature and acquire an image. The HSI is built by consecutively stacking spectral images. The first implementation again employed microscopes in combination with acousto-optical (AOTFs) and liquid crystal tunable filters (LCTFs)¹⁸.

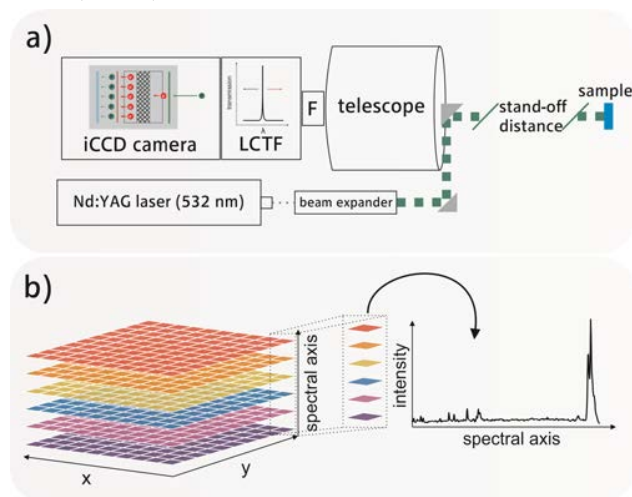


Figure 1. a) Illustration of the optical setup. The beam emitted by the laser (532 nm, Nd:YAG) is expanded in order to illuminate the field of view of the telescope at the stand-off distance. The Raleigh line is filtered by an edge filter (F), before a tunable liquid crystal filter (LCTF) selects a Raman shift for the spectral image. The image is taken by an iCCD camera synchronized to the pulsed laser

output. b) Sketch of the structure of the resulting hyperspectral image cube.

Recently, even Bragg tunable filters have been used in Raman microspectroscopy¹⁹. A comparison of all techniques of Hyperspectral Raman Imaging (HSRI) was performed by Schlücker et al.²⁰. Regarding stand-off HSRI instruments, most are designed as whiskbroom imagers and are therefore of limited use when large areas should be investigated, as mapping the excitation laser over the whole area is a tedious process. Pushbroom systems have been tested as stationary screening devices¹⁷. Staring or spectral scanning stand-off Raman imagers have been proposed and tested over the last years²¹, where the dispersive element is a tunable filter with a large enough aperture to transmit the whole field of view (FOV) of the collecting optic as an

image directly onto the detector array. Here, LCTFs can facilitate narrow bandpass filters suitable for RS, which can be tuned electronically in a fast and reliable manner, whilst on a small footprint. In combination with a suitable intensified CCD (iCCD) camera and a small, air-cooled, pulsed laser it is possible to design a stand-off HSRI system, which can be field deployable. The limitation of the LCTFs is the usable spectral range, especially regarding the UV region, where the absorbance of the incorporated materials in LCTFs hinders their application. Hence, recently, custom built tunable filters based on Fabry-Pérot interferometers have been studied as viable alternatives for UV excitation²². These are however, still not available commercially.

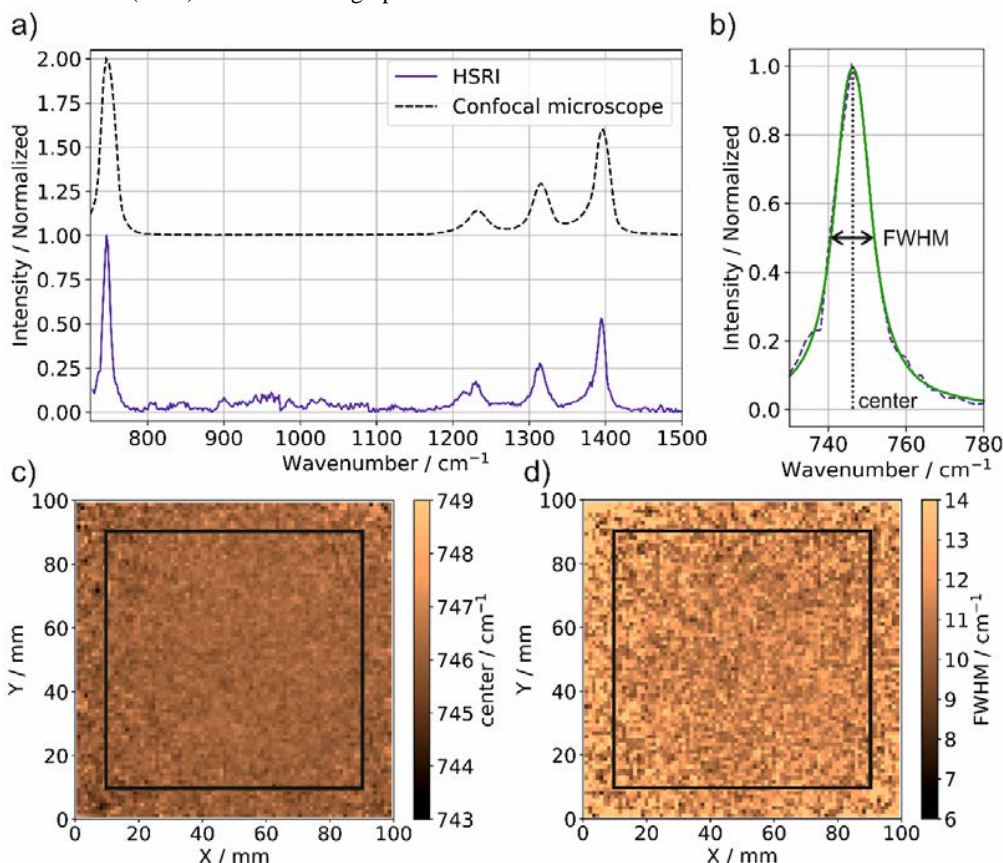


Figure 2. a) Sample spectra of PTFE compared to a reference measurement using a confocal Raman microscope. b) Illustration of the curve fit of the band at 746 cm^{-1} with a pseudo-Voigt profile (green curve). c) Distribution of the center position of the fitted band over the FOV of the HSRI. d) Distribution of the FWHM of the fitted band over the FOV of the HSRI.

The resulting HSI datasets are usually highly dimensional and complex, challenging even experts with their evaluation. Therefore, chemometric algorithms found their way into the field of RS as handy tools for breaking down thousands of complex spectra into digestible information²³. In regards to detection of explosives, a fast and robust classification of the obtained HSRI would result in easily understandable false color images, which can be also interpreted by trained non-experts. Here, we propose the usage of a random forest classifier (RDF), due to its ability to perform high quality classification with efficient use of processing power²⁴. The RDF consist of an ensemble of decision trees, which are trained by randomly selecting and using a subset of the available dataset (defined by the

ratio R , in-bag samples), thus growing into a forest of user defined size (N_T). Classification is reached by majority vote of the class assignment probabilities of each tree, which carry low bias and high variance due to the random pick of samples during training²⁵. A major advantage represents the use of the previously left out subset as internal cross-validation on the performance of the RDF by calculating an error estimate known as out-of-bag (OOB) error²⁶. Similarly, this can be exploited to investigate on the variable importance (VIP). When comparing OOB errors from the trained RDF with OOB errors from RDFs with randomly permuted sample variables, the effect of each variable can be assessed. This is a useful tool in decreasing the dimensionality of the obtained data whilst keeping quality classification²⁷.

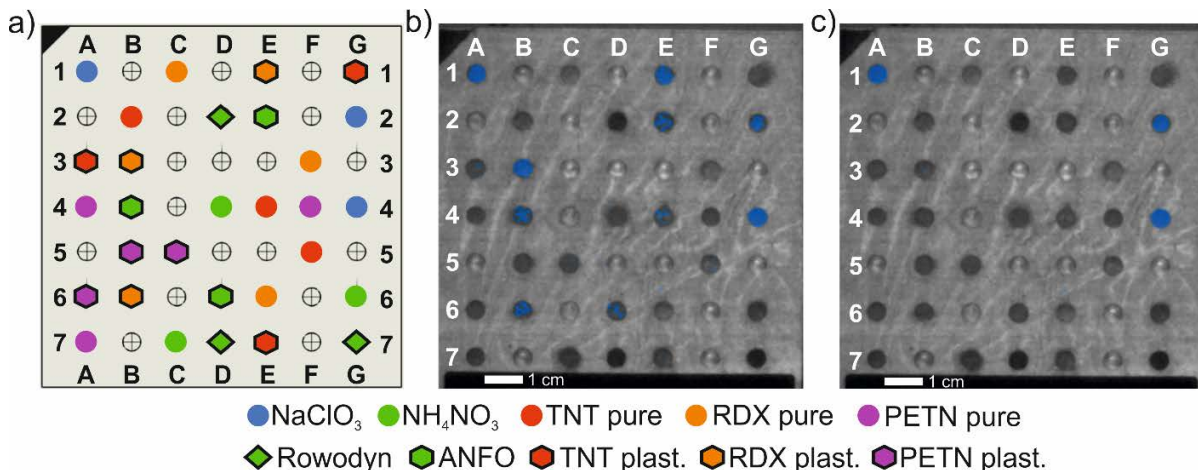


Figure 3. a) Illustration of the randomly chosen and filled positions of each sample on the sample holder. b) Overlay of the intensity of the spectral image at 941 cm^{-1} corresponding to the symmetric stretch vibration of NaClO_3 on a greyscale image of the sample. c) Overlay of the intensity of a correlation to a template triangle as the spectral descriptor for the band associated with NaClO_3 on a greyscale image of the sample.

Table 1: Results of the RDF classifiers for the different explosive classes. Calculation time is given as a relative number.

| | OOB average error in % | | | | | # Var. | Meas. time | Calc. time |
|-------------|------------------------|--------------------------|------|------|------|--------|-------------|------------|
| | NaClO_3 | NH_4NO_3 | PETN | RDX | TNT | | | |
| RDF1 | 1.44 | 1.82 | 7.82 | 5.94 | 3.67 | 768 | 51 min 15 s | 3 |
| RDF2 | 0.37 | 0.85 | 5.2 | 2.63 | 1.1 | 80 | 5 min 20 s | 1 |

This results in a considerable reduction of measurement time, especially for the staring HSRI system, as the amount of spectral images to be acquired as the time consuming step can be reduced significantly.

In this study we present an air-cooled, mobile stand-off HSRI system in the visible spectral range. Accidental detonation or photo-degradation of the sample was avoided by using an excitation laser with low pulse energies, but high repetition rates with a defocused beam to illuminate an area corresponding to the field of view of the collection optics. The HSRI works in staring or spectral scanning mode, where an LCTF is used to discriminate a certain Raman shift and collect the image. Different explosive materials are measured at a distance of 15 m. The obtained HSI is the basis to train a RDF, which is used to identify the most important variables and create designated spectral descriptors (SPDCs)²⁸, reducing the dimensionality of the dataset and subsequently improving measurement and calculation time. A second RDF is trained using these SPDCs, showing improved performance, whilst highlighting the benefits of the synergy between stand-off HSRI and RDF classification for the fast, remote detection of explosives.

MATERIALS AND METHODS

Stand-off hyperspectral Raman imager

The direct stand-off imager (Figure 1a) used an air-cooled, Q-switched, frequency-doubled (532 nm) Nd:YAG Explorer One (EONE 532-200, Spectra-Physics, USA) laser with a Gaussian beam profile and adjustable pulse energies ranging from 30 to 300 μJ and repetition rates from single shot to 60 kHz. The laser beam was expanded using a defocused Galilean type beam expander to a diameter of approximately

100 mm at the stand-off distance of 15 m. The backscattered Rayleigh photons eliminated using a long pass filter (LP03-532RE, Semrock, USA). Afterwards, a specific Raman shift was selected using a tunable LCTF filter (VariSpec VISR, Perkin-Elmer, USA) with a spectral resolution of 0.25 nm and directly imaged onto an iCCD equipped with a quadratic sensor (PIMAX 4 1024f-HBf iCCD, 1024x1024 pixels, 13 μm pixels). The spectral images were stacked in order to build the hyperspectral data cube as depicted in Figure 1b. This process was automated using LabVIEW® (National Instruments, USA).

Chemicals

Explosives

An appropriate rectangular sample holder in aluminum with an edge length of 80 mm was designed. 49 wells with a diameter of 4 mm and a depth of 1 mm were cut into the aluminum acting as a holder for the explosives. The wells were randomly filled with 10 mg of the different available explosives or precursors so that every class was represented three times (Figure 3a). Three pure explosive components, trinitrotoluene (TNT), pentaerythritol tetranitrate (PETN) and 1,3,5-Trinitro-1,3,5-triazinane (research department explosive, RDX) were used in this study. At the same time, the three pure components were also added as plastic variants i.e. the pure explosives with added binders, desensitizers, waterproof coatings and plasticizers, which help increase their usability and storability²⁹. Rowodyn is a commercially available explosive, mostly composed of NH_4NO_3 , nitroglycerine, ethylene glycol dinitrate and fuel. Ammonium nitrate fuel oil (ANFO) is a mixture of NH_4NO_3 and fuel oil. All these samples were acquired from the Austrian Armed Forces. Finally, NaClO_3 and NH_4NO_3 were acquired

from Sigma Aldrich as examples of explosive substances often found in improvised explosive devices³⁰.

Other

A 3 mm thick polytetrafluoroethylene (PTFE) plate was acquired from RS Components GmbH (Austria) as a reference material for the test of the stand-off HSRI.

Table 2: Associated band (labeled as Band) of the different classes of explosives, their band assignment (Assign.) and a respective reference. Parameters of the triangle correlation (TC) spectral descriptor (c means center; b1, b2 baseline points 1 and 2, respectively) used in this study for every class. All numbers have the unit cm^{-1} .

| Class | Band | Assign. | Spectral descriptor: TC | | |
|---------------------------------|--------------------|-----------------------------|-------------------------|------|------|
| | | | c | b1 | b2 |
| NaClO ₃ | 940 ³¹ | $\nu^s \text{ClO}_3^-$ | 941 | 917 | 959 |
| NH ₄ NO ₃ | 1044 ³² | $\nu^s \text{NO}_3^-$ | 1045 | 1031 | 1062 |
| PETN | 2987 ³³ | $\nu^s \text{CH}_2$ | 2993 | 2976 | 3017 |
| RDX | 2959 ³⁴ | $\nu^{\text{as}} \text{CH}$ | 2957 | 2939 | 2978 |
| TNT | 1356 ³⁵ | $\nu^s \text{NO}_2$ | 1361 | 1331 | 1407 |

Measurement parameters

The sample was placed at a distance of 15 m to the telescope. The repetition rate of the laser was set to 10 kHz emitting pulses with a pulse width of approximately 10 ns and pulse energies of 0.21 mJ, giving an average power of 2.1 W, yielding an average radiant energy of 2.7 $\mu\text{J}/\text{cm}^2$ and an average irradiance of 26.7 mW/cm^2 due to the widened beam. The laser pulses are synchronized to the gate of the intensifier of the iCCD in order to maximize Raman signal and suppress ambient light. The gate of the camera was set to 10 ns to coincide with the laser pulse width. Signal to noise was improved by accumulating 30.000 pulses on the CCD per spectral image, resulting in a total measurement time of 3 seconds per image. HSI cubes were started at 800 cm^{-1} and ended at 3101 cm^{-1} Raman shift with a spectral image every 3 cm^{-1} , resulting in 768 different spectral layers.

Reference Raman spectra of all components were measured using a confocal Raman microscope (Horiba LabRAM HR, Japan) equipped with frequency-doubled Nd:YAG (532 nm) laser with 20 mW, a 20x objective, 2 seconds integration time, 10 accumulations and a grating of 300 gr/mm .

Random decision forest

In order to train the RDF^{25,26}, a list of training data points was created. 40 pixels with pure explosives (TNT, PETN, RDX, NaClO₃ and NH₄NO₃) were selected manually and associated to their respective class. Preprocessing of the dataset included spike removal and baseline correction using Euler's method³⁶ over 15 iterations with a smoothness of 10,000 and an asymmetry of 0.001. First, an RDF was trained with all the spectral images as input variables (RDF1). The ratio (R) between used and unused samples (in-bag and out-of-bag OOB samples) was optimized by computing several forests and choosing the ratio which yielded the lowest OOB average errors. Similarly, the optimal number of trees (N_T) was established. Afterwards, a feature selection was done via the variable importance of each class. Spectral descriptors, in this case correlation to a template triangle peak (TC descriptor), were chosen as the new input.

The second RDF was trained using those as input variables (RDF2). Both classification are compared regarding their classification and OOB errors. All calculations were performed using ImageLab[®] (Epina GmbH, Austria).

RESULTS AND DISCUSSION

To assess the capability of the stand-off HSRI to produce quality HSIs (single pixel spectra) over the whole FOV, a PTFE plate was placed at a distance of 15 m and imaged starting at 680 cm^{-1} to 1500 cm^{-1} with steps of 3 cm^{-1} . An acquired single pixel example spectra is displayed in Figure 2a and compares correctly to the given reference spectrum. An important factor for correct and accurate interpretation of the obtained HSI is the wavelength stability of the dispersive element, in this case the LCTF filter, over the whole FOV. The band of PTFE at 746 cm^{-1} corresponding to the skeletal stretch³⁷ was chosen because of its high intensity and narrow linewidth for an in-depth analysis of the stability and accuracy of the LCTF as wavelength discriminator. Both center position and full width at half maximum (FWHM) of the band were assessed by fitting the band with a pseudo-Voigt profile³⁸ as shown in Figure 2b and extracting the respective parameters. Due to low intensities at the edges of the image because of the Gaussian beam profile only values inside the rectangular indicated in Figure 2b and c were taken for further analysis, as this was also the size of the test sample. The median center position was found to be 746.2 cm^{-1} with a standard deviation of 0.3 cm^{-1} . The median FWHM was located at 11.3 cm^{-1} with a standard deviation of 0.8 cm^{-1} . Both parameters are well within the specifications of the LCTF and exhibit no drift or inconsistencies over the whole FOV. This is crucial for the device to act as reliable dispersive element in this HSRI application.

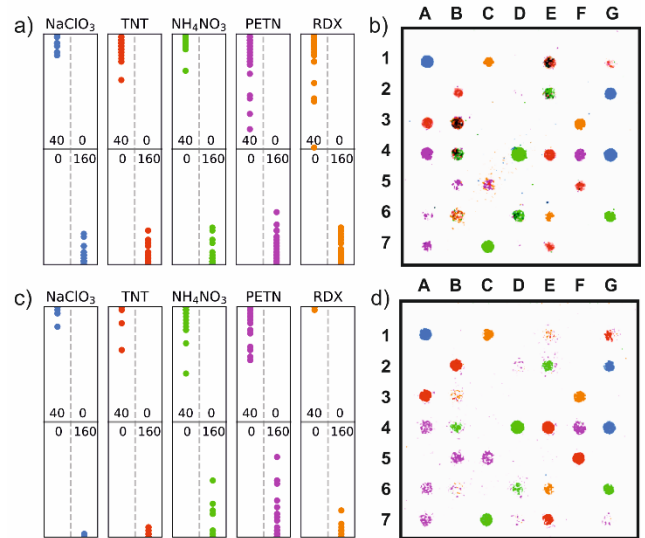


Figure 4. a) Confusion matrix for the training data set of the RDF1 classification, when all acquired intensities are used as variables b) RDF1 classifier with all variables applied over the whole sample, each class is color-coded. c) Confusion matrix for the training data set of the RDF2, when only the spectral descriptors are used. d) RDF2 classifier with only spectral descriptors applied over the whole sample, each class is color-coded.

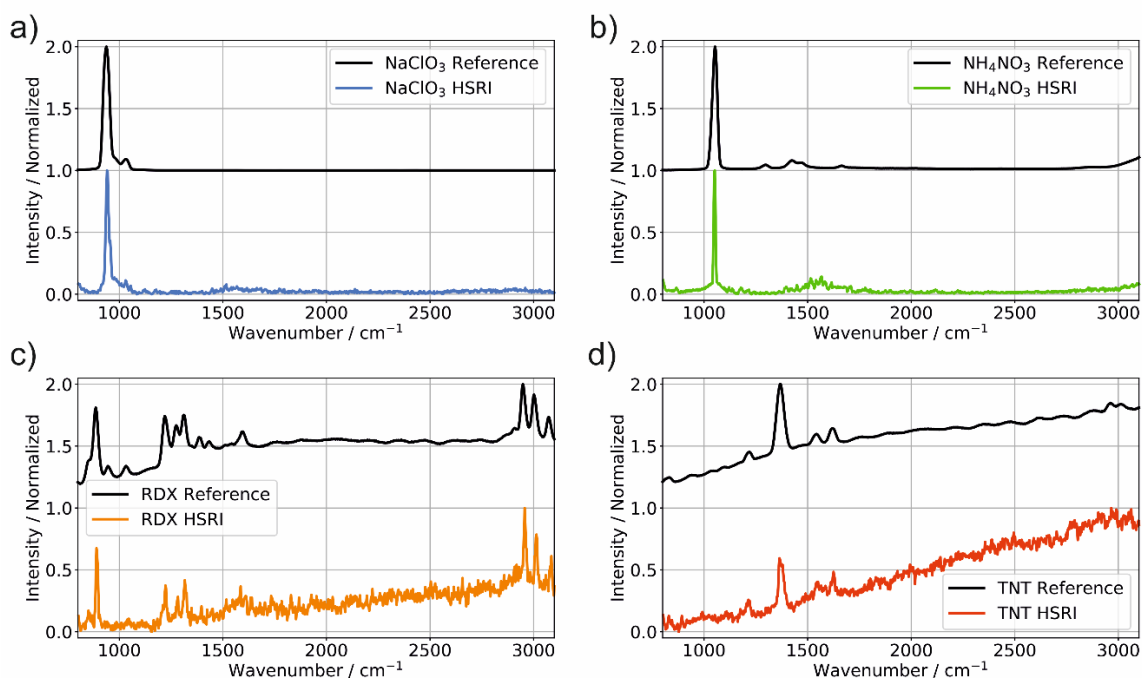


Figure 5. Reference spectra of four different explosives (NaClO_3 , NH_4NO_3 , RDX, TNT, black curves) obtained via confocal Raman microscope with the spectrum of a pixel recorded with the stand-off HSRI at a distance of 15 m. These spectra are not preprocessed, except normalization.

The capability to detect the amounts of explosives put into the sample holder at a distance of 15 m is shown exemplary in Figure 5, where raw single pixel spectra chosen from the respective sample positions are compared against reference spectra obtained via measurement using a Raman microscope. The pure components NaClO_3 and NH_4NO_3 show quality spectra (Figure 5a and b) both when measured with the stand-off HSRI and the Raman microscope. Analogously, the spectra of RDX and TNT are in good agreement with the respective reference spectrum. Both components exhibit an elevated background, which can be attributed to fluorescence. This leads to fluctuating baseline features (e.g. between 2500 and 2800 cm^{-1} in Figure 5d), which are not sample related and are caused by the transmission characteristics of the Rayleigh edge filter used to block the incoming laser light. The main difference in the spectra obtained with the HSRI and the Raman microscope is the signal-to-noise ratio (SNR). It is higher for the reference spectra, due to the longer integration time and significantly higher incident irradiance when using the microscope. At 532 nm a 20x objective (NA=0.4) on a confocal microscope system gives a theoretical spatial resolution of approximately 500 nm. Assuming an area of that diameter, the irradiance under the microscope amounts to 10^{10} mW/cm^2 , an increase of approximately 8 orders of magnitude compared to the irradiance of the widened beam. Given that the intensity of a Raman signal is direct proportional to the impinging laser intensity onto the sample, it speaks for the throughput and detectivity of the stand-off HSRI to still show acceptable spectra, even at stand-off distances.

To build an able classifier, the first step taken in this study was to train a RDF classifier (RDF1) using the baseline corrected intensities of each spectral image as input variables. The training set included 200 reference points per pure class of explosive, manually selected from the 3 possible positions on the sample (Figure S1). To select an optimal R (0.66) and N_T (50),

a scan for both parameters was performed, taking the OOB average error as the indicating measure for when optimal classification is reached (Figure S2-S5).

The results of RDF1 are shown in Figure 4a and b. The confusion matrix shows that for the training set can be distinguished without any false positives or false negatives. However, the OOB errors reveal differences in the quality of classification between the different explosives. NH_4NO_3 and NaClO_3 are better characterized than the other pure components, which is feasible, because of their strong, single standing spectral features. An even more differentiated image is given in Figure 4b, where the RDF1 classifier is applied to the whole dataset. Here, various misclassifications can be identified, with sample position B3 showing the biggest error. On this spot, pixels classified as TNT, RDX and NaClO_3 neighbor each other, whereas B3 was prepared with plasticized RDX. Aggregations of false classification on positions with fluorescent samples like E1, E2, B3, B4, B6 and C5 are also found. The evidence is hardened when Figure 3a and b are compared. Even after baseline correction, the intensity distribution of the band of NaClO_3 at 941 cm^{-1} (Figure 3b) does not only cover the areas A1, G2 and G4, as prepared, but also e.g. B3, B4, B6 and E2. It is apparent that another tool which gives a more selective measure for the abundance of the respective compound has to be found. This challenge was approached by first evaluating the VIP scores of every class when all variables are used i.e. the VIP scores of RDF1. Figure 6a and b depict the VIP scores and the respective spectra from a pure pixel for two selected classes, namely sodium chlorate and TNT. High VIP scores for RDF1 for sodium chlorate are situated around the maximum band intensity at 941 cm^{-1} , which was expected. For TNT the same situation is true with the highest VIP score around the main band associated with the symmetric stretch of the NO_2 at 1361 cm^{-1} , albeit the presence of other bands.

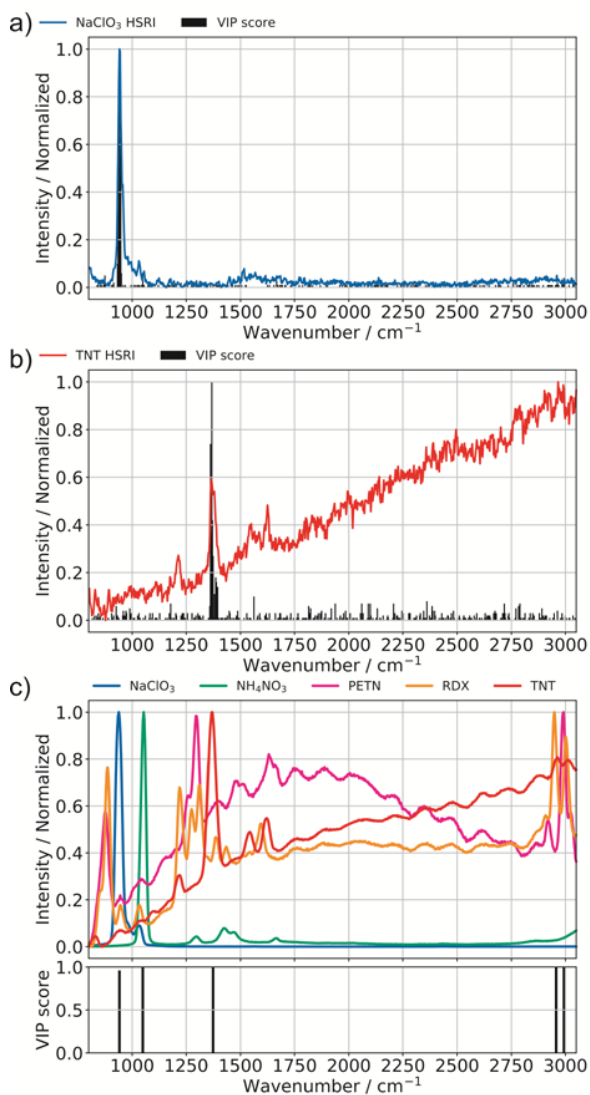


Figure 6. a) Variable importance (VIP) scores of the NaClO_3 class for the RDF using all spectral images as variables. b) VIP scores of the TNT class for the RDF using all spectral images as variables. c) VIP scores of all explosive classes for the RDF using only spectral descriptors as variables.

Similarly, it was found that for all other classes, one spectral feature was predominantly represented in the VIP scores. This spurred the idea of using these small parts of the spectrum for classification. However, the fact that elevated baselines with heavy fluorescent backgrounds (e.g. RDX as shown in Figure 7) heavily affected pure intensities, another spectral descriptor less prone to noise was needed to describe band intensity. Here, a triangle correlation (TC) descriptor was used. The descriptor is characterized by a triangle template with the parameters b_1 and b_2 as baseline points and c as center point. The strength of the descriptor is calculated by the positive significant correlation (significance level 0.01) to the data points within the chosen range multiplied by the baseline corrected integral as a measure of band intensity³⁹. This descriptor tends to be less sensitive to noise, since for noise it's unlikely to produce a significant correlation to the triangle template. In comparison of Figure 3b and c, the effect of choosing a TC descriptor with appro-

appropriate parameters (Table 2) for sodium chlorate is clearly visible. The TC descriptors intensity is only observable for the prepared NaClO_3 positions, instead of also highlighting points with highly fluorescent background. The TC descriptor was subsequently also applied to all other regions where the RDF1 gave high VIP scores for the different classes. This resulted in 5 different TC descriptors for the 5 explosive classes investigated in this study, which are summarized in Table 2. Now, the same parameters as in RDF1 were taken to train a second RDF, RDF2, except for the input variables, which in case of RDF2 consisted of the five TC descriptors. A R and N_T scan revealed similar behavior of this RDF, so the same values as in RDF1 were used. Again OOB errors were calculated and show an overall improved performance of the classifier (Table 1). Especially the detection and recognition of sodium chlorate profited from the new spectral descriptors, as was discussed before comparing Figure 3b and c, but is confirmed by the OOB errors found in RDF1 and RDF2. Overall, the OOB errors are reduced for all classes of explosives, which in turn results in a much cleaner assessment of the whole sample, when the RDF2 is applied to the whole FOV imaged by the HSRI, shown in Figure 4d.

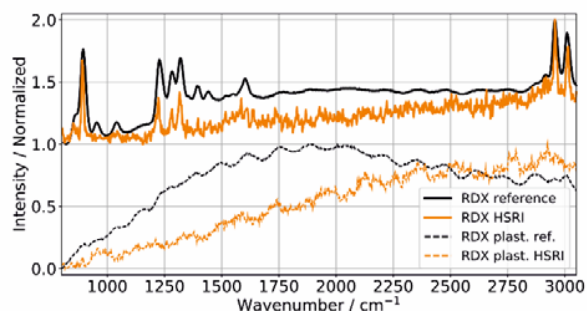


Figure 7. Reference (black, solid line) and stand-off HRSI (orange, solid line) spectra of pure RDX compared to a reference (black, dashed line) and HSRI (orange, dashed line) spectrum of RDX with plasticizer.

CONCLUSION

A stand-off hyperspectral Raman imager working at 532 nm excitation wavelength with 15 m distance to the sample position was designed, constructed and tested for its capability to produce quality spectra at low laser irradiance at the target. The stability and correctness of the produced spectra was assessed for every pixel in the FOV of the imager. Different types of explosive samples, namely ammonium nitrate, sodium chlorate, PETN, RDX and TNT were prepared in the mg-range on an aluminum substrate. Additionally, plasticized variants of the explosives as well as a commercial explosive (Rowodyn) were prepared on the same substrate and measured at 15 m. Two RDFs were trained: the first RDF (RDF1) was trained by using all the available pixel intensities of all spectral images of a defined test set. With the help of the variable importance in RDF1, triangle correlation (TC) descriptors for the pure components in the test set were constructed and used in the training of a second RDF (RDF2). Both RDFs were compared regarding their out-of-bag errors and classification performance of the whole sample. It is shown, that the TC spectral descriptor can significantly increase the selectivity and specificity of the signal response and therefore improve the classification prowess of the RDF. Additionally, since for the TC descriptor fewer spectral positions are needed, the measurement time decreases by a factor of

10, whilst the computation time is reduced by a factor of 3 due to the reduction of variables. Fluorescence remains a challenge in this spectral region, possible solutions include moving the excitation either to the near infrared or to deep UV wavelengths⁴⁰ or use faster gating to discriminate fluorescence in the time domain⁴¹. In conclusion, we show that the combination of direct HSRI and RDF with an improved selection of spectral descriptors enable a fast large area detection of mg-amounts of explosives at a distance of 15 m using Raman spectroscopy in the visible regime.

ACKNOWLEDGMENT

Financial support was provided by the Austrian Science Fund (FWF) under the scope of the Translational-Research programme within the research project “Advanced stand-off Raman spectroscopy for chemical identification from safe distances” (TRP-265). The authors thank Prof. Johannes Lohninger for his support while using ImageLab.

REFERENCES

- Capitán-Vallvey, L. F.; López-Ruiz, N.; Martínez-Olmos, A.; Erenas, M. M.; Palma, A. J. Recent Developments in Computer Vision-Based Analytical Chemistry: A Tutorial Review. *Anal. Chim. Acta* **2015**, *899*, 23–56.
- Opitz, J.; Parsia, B.; Sattler, U. Using Ontologies for Medical Image Retrieval - An Experiment. *CEUR Workshop Proc.* **2009**, *529* (5), 858–872.
- Yan, T. S.; Cui, D. W. The Method of Intelligent Inspection of Product Quality Based on Computer Vision. *2006 7th Int. Conf. Comput. Ind. Des. Concept. Des. CAIDC* **2006**.
- Brosnan, T.; Sun, D. W. Improving Quality Inspection of Food Products by Computer Vision - A Review. *J. Food Eng.* **2004**, *61* (1 SPEC.), 3–16.
- Al-Kaff, A.; Martín, D.; García, F.; Escalera, A. de la; María Armingol, J. Survey of Computer Vision Algorithms and Applications for Unmanned Aerial Vehicles. *Expert Syst. Appl.* **2018**, *92*, 447–463.
- Gowen, A. A.; O'Donnell, C. P.; Cullen, P. J.; Downey, G.; Frias, J. M. Hyperspectral Imaging – an Emerging Process Analytical Tool for Food Quality and Safety Control. *Trends Food Sci. Technol.* **2007**, *18* (12), 590–598.
- Li, Q.; He, X.; Wang, Y.; Liu, H.; Xu, D.; Guo, F. Review of Spectral Imaging Technology in Biomedical Engineering: Achievements and Challenges. *J. Biomed. Opt.* **2013**, *18* (10), 100901.
- Hobro, A. J.; Lendl, B. Stand-off Raman Spectroscopy. *TrAC Trends Anal. Chem.* **2009**, *28* (11), 1235–1242.
- Misra, A. K.; Sharma, S. K.; Acosta, T. E.; Porter, J. N.; Bates, D. E. Single-Pulse Standoff Raman Detection of Chemicals from 120 m Distance during Daytime. *Appl. Spectrosc.* **2012**, *66* (11), 1279–1285.
- Zachhuber, B.; Ramer, G.; Hobro, A. J.; Lendl, B. Stand-off Raman Spectroscopy of Explosives. *Quantum* **43** (0).
- Wallin, S.; Pettersson, A.; Ostmark, H.; Hobro, A. Laser-Based Standoff Detection of Explosives: A Critical Review. *Anal. Bioanal. Chem.* **2009**, *395* (2), 259–274.
- Adão, T.; Hruška, J.; Pádua, L.; Bessa, J.; Peres, E.; Morais, R.; Sousa, J. J. Hyperspectral Imaging: A Review on UAV-Based Sensors, Data Processing and Applications for Agriculture and Forestry. *Remote Sens.* **2017**, *9* (11).
- Boldrini, B.; Kessler, W.; Rebnera, K.; Kessler, R. W. Hyperspectral Imaging: A Review of Best Practice, Performance and Pitfalls for in-Line and on-Line Applications. *J. Near Infrared Spectrosc.* **2012**, *20* (5), 483–508.
- Li, Q.; He, X.; Wang, Y.; Liu, H.; Xu, D.; Guo, F. Review of Spectral Imaging Technology in Biomedical Engineering: Achievements and Challenges. *J. Biomed. Opt.* **2013**, *18* (10), 100901.
- Delhaye, M.; Dhameincourt, P. Raman Microprobe and Microscope with Laser Excitation. *J. Raman Spectrosc.* **1975**, *3* (1), 33–43.
- Dieing, T.; Hollricher, O.; Toporski, J. *Confocal Raman Microscopy*; 2010; Vol. 158.
- Zachhuber, B.; Östmark, H.; Carlsson, T. Spatially Offset Hyperspectral Stand-off Raman Imaging for Explosive Detection inside Containers; Fountain, A. W., Ed.; 2014; p 90730J.
- Morris, H. R.; Hoyt, C. C.; Treado, P. J. Imaging Spectrometers for Fluorescence and Raman Microscopy: Acousto-Optic and Liquid Crystal Tunable Filters. *Appl. Spectrosc.* **1994**, *48* (7), 857–866.
- Gaufrès, E.; Marcet, S.; Aymong, V.; Tang, N. Y. W.; Favron, A.; Thouin, F.; Allard, C.; Rioux, D.; Cottenye, N.; Verhaegen, M.; et al. Hyperspectral Raman Imaging Using Bragg Tunable Filters of Graphene and Other Low-Dimensional Materials. *J. Raman Spectrosc.* **2018**, *49* (1), 174–182.
- Schlücker, S.; Schaeberle, M. D.; Huffman, S. W.; Levin, I. W. Raman Microspectroscopy: A Comparison of Point, Line, and Wide-Field Imaging Methodologies. *Anal. Chem.* **2003**, *75* (16), 4312–4318.
- Östmark, H.; Nordberg, M.; Carlsson, T. E. Stand-off Detection of Explosives Particles by Multispectral Imaging Raman Spectroscopy. *Appl. Opt.* **2011**, *50* (28), 5592–5599.
- Glimtoft, M.; Bååth, P.; Saari, H.; Mäkynen, J.; Näsälä, A.; Östmark, H. Towards Eye-Safe Standoff Raman Imaging Systems; Bishop, S. S., Isaacs, J. C., Eds.; 2014; Vol. 9072, p 907210.
- Ofner, J.; Brenner, F.; Wieland, K.; Eitenberger, E.; Kirschner, J.; Eisenmenger-Sittner, C.; Török, S.; Döme, B.; Konegger, T.; Kasper-Giebl, A.; et al. Image-Based Chemical Structure Determination. *Sci. Rep.* **2017**, *7* (1), 1–11.
- Pal, M. Random Forest Classifier for Remote Sensing Classification. *Int. J. Remote Sens.* **2005**, *26* (1), 217–222.
- Breiman, L. Random Forests. *Mach. Learn.* **2001**, *45* (1), 5–32.
- Cutler, A.; Cutler, D. R.; Stevens, J. R. Ensemble Machine Learning. **2012**, No. January.
- Belgiu, M.; Drăgu, L. Random Forest in Remote Sensing: A Review of Applications and Future Directions. *ISPRS J. Photogramm. Remote Sens.* **2016**, *114*, 24–31.
- Ofner, J.; Kamilli, K. A.; Eitenberger, E.; Friedbacher, G.; Lendl, B.; Held, A.; Lohninger, H. Chemometric Analysis of Multisensor Hyperspectral Images of Precipitated Atmospheric Particulate Matter. *Anal. Chem.* **2015**, *87* (18), 9413–9420.
- Meyer, R.; Khler, J.; Homburg, A. *Explosives*; Wiley-VCH Verlag GmbH & Co. KGaA: Weinheim, Germany, 2007.
- Kavicky, V.; Figuli, L.; Jangl, S.; Ligasová, Z. Analysis of the Field Test Results of Ammonium Nitrate: Fuel Oil Explosives as Improvised Explosive Device Charges; 2014; pp 297–309.
- Bates, J. B. Polarized Vibrational Spectra of Potassium Chlorate. *J. Chem. Phys.* **1971**, *55* (2), 494–503.
- Ghosh, M.; Wang, L.; Asher, S. A. Deep-Ultraviolet Resonance Raman Excitation Profiles of NH₄NO₃, PETN, TNT, HMX, and RDX. *Appl. Spectrosc.* **2012**, *66* (9), 1013–1021.
- Gruzdtkov, Y. a.; Gupta, Y. M. Vibrational Properties and Structure of Pentaerythritol Tetranitrate. *J. Phys. Chem. A* **2001**, *105* (25), 6197–6202.
- Infante-Castillo, R.; Pacheco-Londoño, L.; Hernández-Rivera, S. P. Vibrational Spectra and Structure of RDX and Its¹³C-And¹⁵N-Labeled Derivatives: A Theoretical and Experimental Study. *Spectrochim. Acta - Part A Mol. Biomol. Spectrosc.* **2010**, *76* (2), 137–141.
- Daniel, N. W.; Lewis, I. R.; Griffiths, P. R. Interpretation of Raman Spectra of Nitro-Containing Explosive Materials. Part II: The Implementation of Neural, Fuzzy, and Statistical Models for Unsupervised Pattern Recognition. *Appl. Spectrosc.* **1997**, *51* (12), 1868–1879.
- Eilers, P. H. C. A Perfect Smoother. *Anal. Chem.* **2003**, *75* (14), 3631–3636.
- Peacock, C. J.; Hendra, P. J.; Willis, H. A.; Cudby, M. E. A. Raman Spectrum and Vibrational Assignment for Poly(Tetrafluoroethylene). *J. Chem. Soc. A Inorganic, Phys. Theor.* **1970**, 2943.
- Sánchez-Bajo, F.; Cumbera, F. L. The Use of the Pseudo-Voigt Function in the Variance Method of X-Ray Line-Broadening Analysis. *J. Appl. Crystallogr.* **1997**, *30* (4), 427–430.
- Lohninger, H.; Varmuza, K. Selective Detection of Classes of Chemical Compounds by Gas Chromatography / Mass

- Spectrometry / Pattern Recognition: Polycyclic Aromatic Hydrocarbons and Alkanes. *Anal. Chem.* **1987**, *59* (2), 236–244.
- (40) Nagli, L.; Gaft, M.; Fleger, Y.; Rosenbluh, M. Absolute Raman Cross-Sections of Some Explosives: Trend to UV. *Opt. Mater. (Amst)*. **2008**, *30* (11), 1747–1754.
- (41) Johansson, I.; Zachhuber, B.; Nordberg, M.; Östmark, H. Rejection of Fluorescence from Raman Spectra of Explosives by Picosecond Optical Kerr Gating. *Proc. SPIE Vol. 8710* **2013**, *8710*, 87100R–87100R–8.

AUTHOR INFORMATION

Corresponding Author

* Prof. Dr. Bernhard Lendl
bernhard.lendl@tuwien.ac.at

ASSOCIATED CONTENT

Supporting Information

The Supporting Information is available free of charge on the ACS Publications website.

Supporting information (PDF) containing:

Figure S1: a) Prepared sample positions with the different explosives. b) Manually selected sample positions for the RDF training dataset.

Figure S2: OOB average error in dependence of the selected in-bag to OOB ratio for RDF1.

Figure S3: OOB average error in dependence of the selected forest size (N_T) for RDF1.

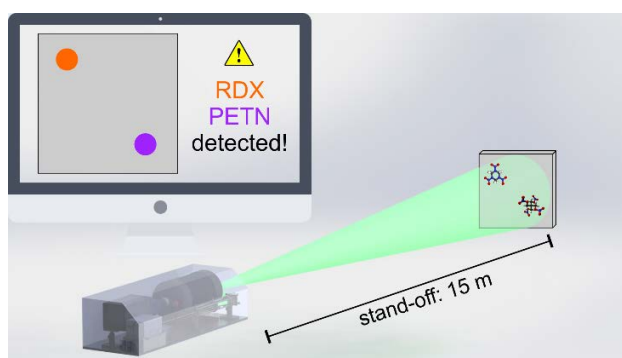
Figure S4: OOB average error in dependence of the selected in-bag to OOB ratio for RDF2.

Figure S5: OOB average error in dependence of the selected forest size (N_T) for RDF2.

Author Contributions

C. Gasser, J. Ofner and B. Lendl designed the HSRI prototype and the experiment, C. Gasser and M. Göschl did the measurements and evaluated the obtained dataset, C. Gasser, J. Ofner and B. Lendl wrote the manuscript. All authors have given approval to the final version of the manuscript.

TOC figure



Bibliography

- [1] Norman Sheppard. "The Historical Development of Experimental Techniques in Vibrational Spectroscopy". In: *Handbook of Vibrational Spectroscopy*. Ed. by John M. Chalmers and Peter R. Griffiths. John Wiley & Sons, 2001.
- [2] Food and Drug Administration. *Guidance for Industry: PAT — A Framework for Innovative Pharmaceutical Development, Manufacturing, and Quality Assurance*. Tech. rep. September. 2004.
- [3] Richard Jackson. "Continuous Scanning Interferometers for Mid-infrared Spectrometry". In: *Handbook of Vibrational Spectroscopy*. John Wiley & Sons Ltd, 2002.
- [4] Erik R. Deutsch et al. "High-resolution miniature FTIR spectrometer enabled by a large linear travel MEMS pop-up mirror". In: ed. by Mark A. Druy, Christopher D. Brown, and Richard A. Crocombe. May 2009, 73190J.
- [5] Yoshihisa Warashina et al. "MEMS based miniature FT-IR engine with built-in photodetector". In: ed. by Wibool Piyawattanametha and Yong-Hwa Park. Mar. 2014, 89770E.
- [6] Norbert Neumann et al. "Tunable infrared detector with integrated micromachined Fabry-Perot filter". In: *Journal of Micro/Nanolithography, MEMS and MOEMS* 7.2 (2008), p. 021004.
- [7] Christoph Gasser et al. "Application of a tunable Fabry-Pérot filterometer to mid-infrared gas sensing". In: *Sensors and Actuators, B: Chemical* 242 (2017), pp. 9–14.
- [8] Robert F. Curl et al. "Quantum cascade lasers in chemical physics". In: *Chemical Physics Letters* 487.1-3 (Feb. 2010), pp. 1–18.

-
- [9] Johannes P. Waclawek, Harald Moser, and Bernhard Lendl. "Compact quantum cascade laser based quartz-enhanced photoacoustic spectroscopy sensor system for detection of carbon disulfide". In: *Optics Express* 24.6 (2016), p. 6559.
- [10] Harald Moser et al. "Implementation of a quantum cascade laser-based gas sensor prototype for sub-ppmv H₂S measurements in a petrochemical process gas stream". In: *Analytical and Bioanalytical Chemistry* 409.3 (2017), pp. 729–739.
- [11] Andreas Schwaighofer et al. "External cavity-quantum cascade laser infrared spectroscopy for secondary structure analysis of proteins at low concentrations". In: *Scientific Reports* 6.April (2016), p. 33556.
- [12] Mirta R. Alcaráz et al. "External-Cavity Quantum Cascade Laser Spectroscopy for Mid-IR Transmission Measurements of Proteins in Aqueous Solution". In: *Analytical Chemistry* 87.13 (July 2015), pp. 6980–6987.
- [13] Mirta R. Alcaráz et al. "EC-QCL mid-IR transmission spectroscopy for monitoring dynamic changes of protein secondary structure in aqueous solution on the example of β -aggregation in alcohol-denatured α -chymotrypsin". In: *Analytical and Bioanalytical Chemistry* (2016).
- [14] Andreas Schwaighofer, Markus Brandstetter, and Bernhard Lendl. "Quantum cascade lasers (QCLs) in biomedical spectroscopy". In: *Chem. Soc. Rev.* 46 (2017), pp. 5903–5924.
- [15] Robert R. Alfano. *The Supercontinuum Laser Source*. New York, NY: Springer New York, 2016. arXiv: [arXiv:1011.1669v3](https://arxiv.org/abs/1011.1669v3).
- [16] Zheming Zhao et al. "Mid-infrared supercontinuum covering 2.0-16 μ m in a low-loss telluride single-mode fiber". In: *Laser & Photonics Reviews* 11.2 (Mar. 2017), p. 1700005.
- [17] Jiang Liu et al. "Recent progress in high-power ultrafast thulium-doped fiber lasers and mid-infrared supercontinuum sources". In: 9466 (2015), p. 946605.
- [18] Christoph Gasser et al. "Enhanced mid-infrared multi-bounce ATR spectroscopy for online detection of hydrogen peroxide using a supercontinuum laser". In: *Optics Express* 26.9 (2018), pp. 12169–12179.
- [19] Christian Jordan et al. "Simultaneous Laser Doppler Velocimetry and stand-off Raman spectroscopy as a novel tool to assess flow characteristics of process streams". In: *Chemical Engineering Journal* 334.August 2017 (Feb. 2017), pp. 123–133.
- [20] S. Michael Angel et al. "Remote Raman Spectroscopy for Planetary Exploration: A Review". In: *Applied Spectroscopy* 66.2 (Feb. 2012), pp. 137–150.
- [21] Alison J. Hobro and Bernhard Lendl. "Stand-off Raman spectroscopy". In: *TrAC Trends in Analytical Chemistry* 28.11 (Dec. 2009), pp. 1235–1242.

- [22] A.A. Gowen et al. "Hyperspectral imaging – an emerging process analytical tool for food quality and safety control". In: *Trends in Food Science & Technology* 18.12 (Dec. 2007), pp. 590–598.
- [23] Judith M. Fonville et al. "Hyperspectral Visualization of Mass Spectrometry Imaging Data". In: *Analytical Chemistry* 85.3 (Feb. 2013), pp. 1415–1423.
- [24] T. Dieing, Olaf Hollricher, and J. Toporski. *Confocal Raman Microscopy*. Ed. by Thomas Dieing, Olaf Hollricher, and Jan Toporski. Vol. 158. Springer Series in Optical Sciences. Berlin: Springer Berlin Heidelberg, 2011, pp. 1–20.
- [25] Harald Moser. "Development and Implementation of an Industrial Process Gas Monitoring System for H₂S based on Mid-Infrared Quantum Cascade Laser Spectroscopy". PhD thesis. TU Wien, 2015, p. 193.
- [26] Peter F. Bernath and Alexander Dalgarno. "Spectra of Atoms and Molecules". In: *Physics Today* 49.3 (Mar. 1996), pp. 94–94. arXiv: [arXiv:1011.1669v3](https://arxiv.org/abs/1011.1669v3).
- [27] John E. Bertie and Zhida Lan. "Infrared Intensities of Liquids XX: The Intensity of the OH Stretching Band of Liquid Water Revisited, and the Best Current Values of the Optical Constants of H₂O(l) at 25°C between 15,000 and 1 cm⁻¹". In: *Applied Spectroscopy* 50.8 (Aug. 1996), pp. 1047–1057.
- [28] August Beer. "Bestimmung der Absorption des rothen Lichts in farbigen Flüssigkeiten". In: *Ann. Phys. Chem* (1852).
- [29] Pramod Kumar Verma et al. "The Bend+Libration Combination Band Is an Intrinsic, Collective, and Strongly Solute-Dependent Reporter on the Hydrogen Bonding Network of Liquid Water". In: (2018).
- [30] Philip L. Hanst. "Long Path Gas Cells". In: *Handbook of Vibrational Spectroscopy*. 2002, pp. 994–1002.
- [31] Huayan Yang et al. "Obtaining information about protein secondary structures in aqueous solution using Fourier transform IR spectroscopy". In: *Nature Protocols* 10.3 (Mar. 2015), pp. 382–396.
- [32] Andreas Schwaighofer et al. "Beyond Fourier Transform Infrared Spectroscopy: External Cavity Quantum Cascade Laser-Based Mid-infrared Transmission Spectroscopy of Proteins in the Amide I and Amide II Region". In: *Analytical Chemistry* 90.11 (June 2018), pp. 7072–7079.
- [33] Georg Ramer and Bernhard Lendl. "Attenuated Total Reflection Fourier Transform Infrared Spectroscopy". In: *Enc. Anal. Chem.* (2013), pp. 1–27.
- [34] N. J. Harrick. "Surface chemistry from spectral analysis of totally internally reflected radiation". In: *The Journal of Physical Chemistry* 64.9 (Sept. 1960), pp. 1110–1114.

-
- [35] Nicolas James Harrick. *Internal Reflection Spectroscopy*. John Wiley & Sons, Inc, 1967.
- [36] Rudolf W. Kessler, Waltraud Kessler, and Edith Zikulnig-Rusch. "A Critical Summary of Spectroscopic Techniques and their Robustness in Industrial PAT Applications". In: *Chemie Ingenieur Technik* 88.6 (June 2016), pp. 710–721.
- [37] Max Planck. *The Theory of Heat Radiation*. P. Blakiston's Son & Co., 1914.
- [38] Henry Bujis. "Incandescent Sources for Mid- and Far-infrared Spectrometry". In: *Handbook of Vibrational Spectroscopy*. 2002, pp. 367–370.
- [39] S. Carpenter et al. "Pulsed wideband IR thermal source". In: *IEE Proceedings - Optoelectronics* 144.5 (Oct. 1997), pp. 315–322.
- [40] M. U. Pralle et al. "Photonic crystal enhanced narrow-band infrared emitters". In: *Applied Physics Letters* 81.25 (2003), pp. 4685–4687.
- [41] Takuya Inoue et al. "High-Q mid-infrared thermal emitters operating with high power-utilization efficiency". In: *Optics Express* 24.13 (2016), p. 15101.
- [42] J Puton et al. "Optimisation of a pulsed IR source for NDIR gas analysers". In: *Opto-Electronics Review* 10.2 (2002), pp. 97–103.
- [43] Frank K Tittel, Dirk Richter, and Alan Fried. "Mid-infrared laser applications in spectroscopy". In: *Solid-State Mid-Infrared Laser Sources* 516.7 (2003), pp. 445–516.
- [44] Peter Werle et al. "Near- and mid-infrared laser-optical sensors for gas analysis". In: *Optics and Lasers in Engineering* 37.2-3 (2002), pp. 101–114.
- [45] P. A. Budni et al. "Efficient mid-infrared laser using 19 μm -pumped Ho:YAG and ZnGeP₂ optical parametric oscillators". In: *Journal of the Optical Society of America B* 17.5 (May 2000), p. 723.
- [46] D. Richter et al. "Development of a tunable mid-IR difference frequency laser source for highly sensitive airborne trace gas detection". In: *Applied Physics B: Lasers and Optics* 75.2-3 (Sept. 2002), pp. 281–288.
- [47] J. Faist et al. "Quantum Cascade Laser". In: *Science* 264.5158 (Apr. 1994), pp. 553–556.
- [48] Rui Q. Yang. "Infrared laser based on intersubband transitions in quantum wells". In: *Superlattices and Microstructures* 17.1 (Jan. 1995), pp. 77–83.
- [49] D Caffey and MB Radunsky. "Recent results from broadly tunable external cavity quantum cascade lasers". In: *SPIE* 858 (2011).
- [50] Markus Brandstetter et al. "Tunable external cavity quantum cascade laser for the simultaneous determination of glucose and lactate in aqueous phase." In: *The Analyst* 135.12 (Dec. 2010), pp. 3260–5.

- [51] H Y Holman et al. "IR spectroscopic characteristics of cell cycle and cell death probed by synchrotron radiation based Fourier transform IR spectromicroscopy." In: *Biopolymers* 57.6 (2000), pp. 329–35.
- [52] Xiushan Zhu and N. Peyghambarian. "High-power ZBLAN glass fiber lasers: Review and prospect". In: *Advances in OptoElectronics* 2010 (2010).
- [53] R. Clark Jones. "Proposal of the Detectivity D^{**} for Detectors Limited by Radiation Noise†". In: *Journal of the Optical Society of America* 50.11 (Nov. 1960), p. 1058.
- [54] Bernhard Schmidt et al. "Longitudinal Bunch Diagnostics using Coherent Transition Radiation Spectroscopy". In: (2018). arXiv: [1803.00608](https://arxiv.org/abs/1803.00608).
- [55] E Theocharous and J R Birch. "Detectors for Mid- and Far-infrared Spectrometry: Selection and Use". In: *Handbook of Vibrational Spectroscopy*. 2002, pp. 379–397.
- [56] A Rogalski. "HgCdTe infrared detector material: history, status and outlook". In: *Reports on Progress in Physics* 68.10 (Oct. 2005), pp. 2267–2336.
- [57] Daniel Hofstetter, Mattias Beck, and Jérôme Faist. "Quantum-cascade-laser structures as photodetectors". In: *Applied Physics Letters* 81.15 (Oct. 2002), pp. 2683–2685.
- [58] J. Cooley, P. Lewis, and P. Welch. "Historical notes on the fast Fourier transform". In: *IEEE Transactions on Audio and Electroacoustics* 15.2 (June 1967), pp. 76–79.
- [59] Pierre Jacquinot. "The Luminosity of Spectrometers with Prisms, Gratings, or Fabry-Perot Etalons". In: *Journal of the Optical Society of America* 44.10 (Oct. 1954), p. 761.
- [60] Janine Connes and Pierre Connes. "Near-Infrared Planetary Spectra by Fourier Spectroscopy I Instruments and Results". In: *Journal of the Optical Society of America* 56.7 (July 1966), p. 896.
- [61] Georg A. Reider. *Photonics*. Cham: Springer International Publishing, 2016.
- [62] J. J. Zayhowski and C. Dill. "Diode-pumped passively Q-switched picosecond microchip lasers". In: *Optics Letters* 19.18 (2008), p. 1427.
- [63] B Braun and F X K. "56-ps passively Q -switched diode-pumped microchip laser". In: 22.6 (1997), pp. 381–383.
- [64] M. J. Pelletier. "Raman Monochromators and Polychromators". In: *Handbook of Vibrational Spectroscopy*. 2002, pp. 496–510.
- [65] H Owen. "Volume Phase Holographic Optical Elements". In: *Handbook of Vibrational Spectroscopy*. 2002, pp. 511–518.

-
- [66] Peter R. Griffiths and James A. De Haseth. *Fourier Transform Infrared Spectrometry: Second Edition*. Hoboken, NJ, USA: John Wiley & Sons, Inc., Apr. 2006, pp. 1–529.
- [67] Matthias Lenzner and Jean-claude Diels. “Concerning the Spatial Heterodyne Spectrometer”. In: *Optics Express* 24.2 (Jan. 2016), p. 1829.
- [68] T. L. van Raalte. “Chain Birefringent Filters”. In: *Journal of the Optical Society of America* 57.10 (Oct. 1967), p. 1217.
- [69] John W. Evans. “The Birefringent Filter”. In: *Journal of the Optical Society of America* 39.3 (Mar. 1949), p. 229.
- [70] Peter Miller. *Optical Filter Assembly with Selectable Bandwidth and Rejection*. 2010. arXiv: [arXiv:1208.5721](https://arxiv.org/abs/1208.5721).
- [71] Carolyn J.S. Pommier et al. “Array Detectors for Raman Spectroscopy”. In: *Handbook of Vibrational Spectroscopy*. 2012, pp. 536–550.
- [72] Lucrezia Cester et al. “Time-of-Flight Imaging at 10 ps Resolution with an ICCD Camera”. In: *Sensors* 19.1 (Jan. 2019), p. 180.
- [73] Joseph P. Estrera and Michael Saldana. “High-speed photocathode gating for generation III image intensifier applications”. In: *Helmet- and Head-Mounted Displays VIII: Technologies and Applications*. Ed. by Clarence E. Rash and Colin E. Reese. Vol. 5079. 2003. Sept. 2003, p. 212.
- [74] Leon A. Bosch. “Image intensifier tube performance is what matters”. In: *Image Intensifiers and Applications II*. Ed. by C. Bruce Johnson. Vol. 4128. Nov. 2000, p. 65.
- [75] Donal J. Denvir and Emer Conroy. “Electron-multiplying CCD: the new ICCD”. In: *SPIE Low-Light-level and Real-Time Imaging Systems, Components and Applications*. Ed. by C. Bruce Johnson, Divyendu Sinha, and Phillip A. Laplante. Vol. 4796. Cic. Feb. 2003, p. 164.
- [76] Jerome Workman et al. “Process Analytical Chemistry”. In: *Analytical Chemistry* 81.12 (June 2009), pp. 4623–4643.
- [77] Dirk C. Hinz. “Process analytical technologies in the pharmaceutical industry: The FDA’s PAT initiative”. In: *Analytical and Bioanalytical Chemistry* 384.5 (2006), pp. 1036–1042.
- [78] Wolfgang Kagermann, Helbig Henning, and Johannes Wahlster. *Recommendations for implementing the strategic initiative INDUSTRIE 4.0*. Tech. rep. May 2013.
- [79] Jerome Workman et al. “Process Analytical Chemistry”. In: *Analytical Chemistry* 83.12 (June 2011), pp. 4557–4578.

- [80] Jerome Workman et al. "Process Analytical Chemistry". In: *Analytical Chemistry* 71.12 (June 1999), pp. 121–180. arXiv: [14356007](#) [[10.1002](#)].
- [81] Yves Roggo et al. "A review of near infrared spectroscopy and chemometrics in pharmaceutical technologies". In: *Journal of Pharmaceutical and Biomedical Analysis* 44.3 SPEC. ISS. (2007), pp. 683–700. arXiv: [1607.04893](#).
- [82] N D Lourenço et al. "Bioreactor monitoring with spectroscopy and chemometrics: a review." In: *Analytical and bioanalytical chemistry* 404.4 (Oct. 2012), pp. 1211–37.
- [83] Daniel Landgrebe et al. "On-line infrared spectroscopy for bioprocess monitoring." In: *Applied microbiology and biotechnology* 88.1 (Oct. 2010), pp. 11–22.
- [84] Karen A. Esmonde-White et al. "Raman spectroscopy as a process analytical technology for pharmaceutical manufacturing and bioprocessing". In: *Analytical and Bioanalytical Chemistry* 409.3 (Jan. 2017), pp. 637–649.
- [85] Paul Wilks. "Infrared Filometers". In: *Handbook of Vibrational Spectroscopy*. 2002, pp. 285–293.
- [86] Cambustion. *Cycle-by-cycle AFR measurement of a cold start using an NDIR500 and HFR500*. Tech. rep. 2015, pp. 1–12.
- [87] A. Emadi et al. "IR microspectrometers based on linear-variable optical filters". In: *Procedia Engineering* 25 (2011), pp. 1401–1404.
- [88] Nada A. O'Brien et al. "Miniature near-infrared (NIR) spectrometer engine for handheld applications". In: May (2012), p. 837404.
- [89] Benjamin R. Wiesent et al. "Linear variable filter based oil condition monitoring systems for offshore wind turbines". In: *Proceedings of SPIE 8105* 8105 (2011), p. 81050D.
- [90] J Angell, S Terry, and P Barth. "Silicon Micromechanical Devices". In: *Scientific American* 248.4 (1983), pp. 44–55.
- [91] R. F. Wolffenbuttel. "MEMS-based optical mini- and microspectrometers for the visible and infrared spectral range". In: *Journal of Micromechanics and Micro-engineering* 15.7 (2005).
- [92] Martin Ebermann et al. "Tunable MEMS Fabry-Pérot filters for infrared microspectrometers: a review". In: 9760 (2016), 97600H.
- [93] JH Scofield. "Frequency-domain description of a lock-in amplifier". In: *American Journal of Physics* (1994).
- [94] J. Krischan, A. Makaruk, and M. Harasek. *Design and scale-up of an oxidative scrubbing process for the selective removal of hydrogen sulfide from biogas*. 2012.

-
- [95] M. Miltner et al. "Chemical-oxidative scrubbing for the removal of hydrogen sulphide from raw biogas: Potentials and economics". In: *Water Science and Technology* 66.6 (2012), pp. 1354–1360.
- [96] Osias Bain and Paul A. Giguère. "Hydrogen peroxide and its analogues: VI. infrared spectra of H₂O₂, D₂O₂ and HDO₂". In: *Canadian Journal of Chemistry* 33.3 (Mar. 1955), pp. 527–545.
- [97] Christoph Gasser. "Characterisation and Application of Fabry-Pérot Tunable Detectors and Pulsable MIR Sources for Novel Sensor Elements". Master Thesis. TU Wien, 2013.
- [98] Jakob Kilgus et al. "Mid-Infrared Standoff Spectroscopy Using a Supercontinuum Laser with Compact Fabry-Pérot Filter Spectrometers". In: *Applied Spectroscopy* 72.4 (Apr. 2018), pp. 634–642.
- [99] Jakob Kilgus et al. "Diffraction limited mid-infrared reflectance microspectroscopy with a supercontinuum laser". In: *Optics Express* 26.23 (2018), p. 30644.
- [100] Y. Yeh and H. Z. Cummins. "Localized Fluid Flow Measurements with an He-Ne Laser Spectrometer". In: *Applied Physics Letters* 4.10 (May 1964), pp. 176–178.
- [101] Michael D. Stern. "Laser Doppler velocimetry in blood and multiply scattering fluids: theory". In: *Applied Optics* 24.13 (July 1985), p. 1968.
- [102] Zhengji Zhang. *LDA Application Methods*. Springer Berlin Heidelberg, 2010.
- [103] K. Weissermel and J.A. Arpe. *Industrial Organic Chemistry*. Weinheim, Germany: Wiley-VCH Verlag GmbH, May 2003.
- [104] John Cooney. "Remote sensing of the earth". In: *Proceedings of the Symposium on Electromagnetic Sensing of the Earth from Satellites*. New York, NY, 1965.
- [105] Tomas Hirschfeld et al. "Remote spectroscopic analysis of ppm-level air pollutants by Raman spectroscopy". In: *Applied Physics Letters* 22.1 (Jan. 1973), pp. 38–40.
- [106] T Hirschfeld. "Range Independence of Signal in Variable Focus Remote Raman Spectrometry". In: *Appl. Opt* 13.6 (1974), pp. 1435–1437.
- [107] SM Angel, T.J. Kulp, and T.M. Vess. "Remote-Raman spectroscopy at intermediate ranges using low-power cw lasers". In: *Applied Spectroscopy* 46.7 (1992), pp. 1085–1091.
- [108] Teng Chen et al. "Remote Raman spectra of benzene obtained from 217 meters using a single 532 nm laser pulse." In: *Applied spectroscopy* 61.6 (June 2007), pp. 624–9.

- [109] Tayro E Acosta-Maeda et al. "Remote Raman measurements of minerals, organics, and inorganics at 430 m range". In: *Applied Optics* 55.36 (Dec. 2016), p. 10283.
- [110] Rene Perez et al. "The supercam instrument on the NASA Mars 2020 mission: optical design and performance". In: *International Conference on Space Optics — ICSSO 2016*. Ed. by Nikos Karafolas, Bruno Cugny, and Zoran Sodnik. Vol. 10562. October 2016. SPIE, Sept. 2017, p. 266.
- [111] Alison J. Hobro and Bernhard Lendl. "Stand-off Raman spectroscopy". In: *TrAC Trends in Analytical Chemistry* 28.11 (Dec. 2009), pp. 1235–1242.
- [112] Haowen Li et al. "Standoff and arms-length detection of chemicals with single-beam coherent anti-Stokes Raman scattering." In: *Applied optics* 48.4 (Feb. 2009), B17–22.
- [113] Arthur Dogariu and Alex Pidwerbetsky. "Coherent anti-stokes Raman spectroscopy for detecting explosives in real time". In: *SPIE Defense, Security, and Sensing*. Ed. by Augustus W. Fountain. Vol. 8358. May 2012.
- [114] Mark F. Witinski et al. "Portable standoff spectrometer for hazard identification using integrated quantum cascade laser arrays from 65 to 11 μm ". In: *Optics Express* 26.9 (Apr. 2018), p. 12159.
- [115] *OPTIX - Optical Technologies for the Identification of Explosives*. 2008.
- [116] S Sharma. "Stand-off Raman spectroscopic detection of minerals on planetary surfaces". In: *Spectrochimica Acta Part A: Molecular and Biomolecular Spectroscopy* 59.10 (Aug. 2003), pp. 2391–2407.
- [117] Alexander F.H. Goetz et al. "Imaging Spectrometry for Earth Remote Sensing". In: *Science* 228.4704 (June 1985), pp. 1147–1153.
- [118] Di Wu and Da Wen Sun. "Advanced applications of hyperspectral imaging technology for food quality and safety analysis and assessment: A review - Part I: Fundamentals". In: *Innovative Food Science and Emerging Technologies* 19 (2013), pp. 1–14.
- [119] Aoife A. Gowen et al. "Recent applications of hyperspectral imaging in microbiology". In: *Talanta* 137 (May 2015), pp. 43–54.
- [120] Grégory Vincent et al. "Pixel-sized infrared filters for a multispectral focal plane array". In: *Applied Optics* 57.3 (2018), p. 391.
- [121] Pierre-Jean Lapray et al. "Multispectral Filter Arrays: Recent Advances and Practical Implementation". In: *Sensors* 14.11 (Nov. 2014), pp. 21626–21659.
- [122] Pavel Matousek and Nicholas Stone. "Emerging concepts in deep Raman spectroscopy of biological tissue." In: *The Analyst* 134.6 (June 2009), pp. 1058–66.

-
- [123] Benjamin Gardner, Nicholas Stone, and Pavel Matousek. “Noninvasive Determination of Depth in Transmission Raman Spectroscopy in Turbid Media Based on Sample Differential Transmittance”. In: *Analytical Chemistry* 89.18 (2017), pp. 9730–9733.
- [124] Bernhard Zachhuber and Christoph Gasser. “Stand-off Spatial Offset Raman Spectroscopy for the detection of concealed content in distant objects”. In: *Analytical ...* 83.24 (Dec. 2011), pp. 9438–42.
- [125] Bernhard Zachhuber et al. “Stand off spatial offset Raman spectroscopy: a distant look behind the scenes”. In: *Proceedings of SPIE*. Ed. by Roberto Zamboni et al. Vol. 8189. Oct. 2011, p. 818904.
- [126] Andy Rowlands. *Physics of Digital Photography*. IOP Publishing, 2017.
- [127] S. E. Harris and R. W. Wallace. “Acousto-Optic Tunable Filter*”. In: *Journal of the Optical Society of America* 59.6 (June 1969), p. 744.
- [128] H. Trey Skinner et al. “Remote Raman microimaging using an AOTF and a spatially coherent microfiber optical probe”. In: *Applied Spectroscopy* 50.8 (1996), pp. 1007–1014.
- [129] Ramy Abdlaty et al. “High Throughput AOTF Hyperspectral Imager for Randomly Polarized Light”. In: *Photonics* 5.1 (2018), p. 3.
- [130] Martin Glimtoft et al. “Towards eye-safe standoff Raman imaging systems”. In: ed. by Steven S. Bishop and Jason C. Isaacs. Vol. 9072. May 2014, p. 907210.
- [131] The Long Phan et al. “Luminescent properties of Eu-doped Y2O3 nanophosphors”. In: *Physica Status Solidi (A) Applied Research* 201.9 (July 2004), pp. 2170–2174.
- [132] A. Kramida, Ru. Ralchenko, and J. Reader. *NIST Atomic Spectra Database*. NIST Atomic Spectra Database (ver. 5.6.1), [Online]. Available: <https://physics.nist.gov/asd> [2019, March 14]. National Institute of Standards and Technology, Gaithersburg, MD. 2018.
- [133] Svante Wold. “Chemometrics and Bruce: Some Fond Memories”. In: *ACS Symposium Series*. Vol. 1199. Jan. 2015, pp. 1–13.
- [134] Svante Wold, Michael Sjöström, and Lennart Eriksson. “PLS-regression: A basic tool of chemometrics”. In: *Chemometrics and Intelligent Laboratory Systems* 58 (2001), pp. 109–130. arXiv: [S0169-74390100155-1](https://arxiv.org/abs/50169-74390100155-1).
- [135] Nouna Kettaneh, Anders Berglund, and Svante Wold. “PCA and PLS with very large data sets”. In: *Computational Statistics and Data Analysis* 48 (2005), pp. 69–85.

- [136] Johannes Ofner et al. "Image-Based Chemical Structure Determination". In: *Scientific Reports* 7.1 (2017), pp. 1–11.
- [137] Leo Breiman. "Random forests". In: *Machine Learning* 45.1 (2001), pp. 5–32. arXiv: [/dx.doi.org/10.1023/A:1010933404324](https://doi.org/10.1023/A:1010933404324) [http:].
- [138] Mariana Belgiu and Lucian Drăgu. "Random forest in remote sensing: A review of applications and future directions". In: *ISPRS Journal of Photogrammetry and Remote Sensing* 114 (2016), pp. 24–31.
- [139] Adele Cutler, D Richard Cutler, and John R Stevens. "Ensemble Machine Learning". In: January (2012).
- [140] Bjoern H Menze et al. "A comparison of random forest and its Gini importance with standard chemometric methods for the feature selection and classification of spectral data". In: *BMC Bioinformatics* 10.1 (2009), p. 213.

List of Figures

| | | |
|-----|---|----|
| 2.1 | Illustration of the electromagnetic spectrum over several orders of magnitude in frequency, energy as well as wavelength. The two most important regions for this work are highlighted, namely the IR and VIS range. Additionally, the light-matter interactions are broadly depicted. RS is used as an abbreviation for Raman spectroscopy and shows the region where RS is mostly performed. Illustration adapted from [25]. | 6 |
| 2.2 | a) Illustration of a simple model of a harmonic oscillator, where k is the stiffness of the spring connecting the two masses m_1 and m_2 . b) Potential energy of a diatomic molecule as a function of the atomic displacement (R) during a vibration of a harmonic oscillator. The eigenfunctions of the vibrational energies are depicted as solid lines, the corresponding eigenvalues as dashed lines. c) Potential energy of a diatomic molecule as a function of the atomic displacement (R) during a vibration as a Morse potential. Ground state and first electronic excited state are depicted. Rotational energies are drawn in light grey. The term schemata for IR spectroscopy and Stokes-, as well as anti-Stokes-Raman spectroscopy are shown. | 8 |
| 2.3 | a) 3D model of the water molecule with all possible symmetry operations. C_2 denotes the axis of rotation and $\sigma_v(xz)$ and $\sigma'_v(yz)$ denote the mirror planes. b) The normal modes of the water molecule with their respective fundamental frequencies. | 10 |

| | | |
|------|--|----|
| 2.4 | The three normal vibrational modes of CO ₂ with the corresponding variation of the dipole moment μ_i and polarizability α along the normal coordinate Q . Additionally, the change of both parameters in equilibrium are given, which determines their IR or Raman activity. | 12 |
| 2.5 | Molar absorption coefficient of water in liquid phase for the IR region. The inset shows a zoomed part of the NIR region with the associated molecular vibrations. Data taken from Bertie et al. [27] | 13 |
| 2.6 | a) Reflected and transmitted beam at a surface between two dielectric media with the refractive indices $n_1 > n_2$. b) When the angle θ reaches θ_c , total internal reflection occurs. | 15 |
| 2.7 | a) Reflectance for both parallel and perpendicular polarized light for different angles of incidence with absorbing and non-absorbing medium. n_1 was chosen to be 2.43, n_2 was 1.5 with absorption indices ranging from 0 to 0.03, calculated for a wavelength of 3.5 μm . b) Effective thickness for both parallel and perpendicular polarized light and the ration between them. c) Refractive index and absorption index for the bending vibration band of liquid water. Data taken from Bertie et al. [27] | 16 |
| 2.8 | Measured Raman spectrum of sulfur with Stokes and Anti-Stokes region in wavelength, wavenumber and Raman shift. The spectrum was acquired using a confocal Raman microscope (Horiba LabRam 800) using a excitation wavelength of 532 nm. | 20 |
| 2.9 | a) Raman shift conversion for the second, third and fourth harmonic of a Nd:YAG laser used as excitation laser. b) Extend of the Raman spectrum (400-4000 cm^{-1}) in wavelength over the excitation wavelength. | 21 |
| 2.10 | Top: Simple illustration of a common IR absorption experiment. A broadband IR light source is shined through the sample and the transmitted radiation is spectrally analyzed and detected. Bottom: Simple illustration of a Raman experiment. A monochromatic light source is directed at the sample and the scattered photons (Stokes is depicted in red, Anti-Stokes in blue) are spectrally analyzed and detected. | 23 |
| 3.1 | a) Planck's law for black-body surfaces heated to different temperatures. b) Image of a SiC (Globar) incandescent light source for the MIR. c) Illustration of the pulsed emitter membrane, suspended on a silicon frame. d) Packaged pulsed emitter with a parabolic reflector. | 26 |
| 3.2 | Illustration of a pyroelectric detector. The sensing element LaTiO ₃ is sandwiched between nm-thin NiCr electrodes. The top side is coated with a black polymer, acting as an absorbing layer. Adapted from [54] | 30 |

| | |
|--|----|
| 3.3 Schematic illustration of the working principle of the FTIR spectrometer with BS...beamsplitter, DM...dichroic mirror, FFT...Fast Fourier Transform. The movement of the translated mirror is indicated with Δl | 32 |
| 3.4 Illustration of the simplest form of a Fabry-Pérot resonator. θ indicates the angle of incidence of the beam, d the distance between the two mirrors, E the field strength and r and t are the reflectivity and transmittance coefficient respectively. | 34 |
| 3.5 Calculated transmission of a Fabry-Pérot interferometer with starting parameters of $n = 1.3$, $d = 2.5\mu m$, $R = 0.95$ and the incident angle θ of 0° . a) The reflectivity R and with it, the Finesse, is altered. b) The effect of a change in refractive index is shown. c) The shift of the center position when changing the distance between the two reflective surfaces. d) The effect of different angles of incidence with the convolution (dotted lines, normalized) between them to show how a focused beam affects the transmission window. | 36 |
| 3.6 a) Active Q-switched laser module as used in the EKSPLA laser. b) Passive Q-switched microchip laser architecture employing a saturable absorber. M are mirrors, P is a polarizer. | 40 |
| 3.7 a) Linearly polarized light at the angle θ and the respective components. b) Right circularly polarized light forming a helix illustrated with the respective components. | 43 |
| 3.8 Illustration of linearly polarized light entering the birefringent crystal of length L with the ordinary axis n_o along the z-axis and the extraordinary axis n_e along the y-axis. | 45 |
| 3.9 Transmission of a stack of Lyot filters. Every Lyot element has double the extend of its predecessor and their cumulative transmission is also shown for every additional element. Calculated with $n_e = 1.51$, $n_o = 1.47$ and a crystal length L of 10 mm. | 46 |
| 3.10 Illustration of the working principle of an intensified CCD camera. The photocathode creates an electron, which is accelerated towards the MCP. The MCP acts as spatially resolved secondary electron amplifier. Afterwards the electrons are accelerated toward a phosphor screen, where they are converted back to photons and detected by a cooled CCD. | 48 |
| 4.1 Illustration of off-line, on-line and in-line chemical analysis of a process. . . | 52 |
| 4.2 PAT and QbD concept shown for a simplified batch reactor in pharmaceutical applications. CPPs and CQA are critical process parameters and critical quality attributes respectively. | 53 |

| | | |
|------|---|-----|
| 4.3 | An overview of components used and possible combinations of them for the integration in tunable filterometer instruments. | 56 |
| 4.4 | a) Illustration of the working principle of the MEMS based tunable FPF with integrated detector. b) SEM image of the diagonally stress-compensated springs of the mirror suspension. c) Photo of the whole optical and electrical structures packaged in a TO-8 housing. | 57 |
| 4.5 | Illustration of the setup for characterization of the FPF detectors. The investigations about different focused cone angles was performed by changing the focal length of the off-axis parabolic mirror. | 59 |
| 4.6 | a) Measured transmission for LFP5580 and LFP3144, when different control voltages are applied. b) Tuning behavior of the LFP5580: central wavenumber in dependence of the applied voltage and the change of FWHM with different spectral positions. c) Temporal stability of the filter while on a fixed position. The change in central wavenumber and FWHM is plotted in respect to the first measured value. d) Change in mean FWHM of the LFP5580 when different mirror focal lengths are used (resulting in different half-angles θ) for focusing on the detector. | 61 |
| 4.7 | Illustration of the optical and electrical setup for the measurement of gas phase components in transmission. | 62 |
| 4.8 | a) Illustration of the designed ATR optical setup with diamond as the ATR crystal and a ZnSe truncated cone as support and focusing element. b) 3D rendering of an exploded view the setup during the planning. c) Built prototype with a droplet of water on top. | 65 |
| 4.9 | Flowsheet of a biogas upgrading plant for the production of biomethane to be injected into the natural gas grid | 66 |
| 4.10 | Two beams of equal intensity and wavelength crossing at an angle 2α , creating a fringe pattern with a spacing of Δd . To the right, a typical Doppler burst is shown, i.e. the scattered intensity of a particle moving through the intersecting beams. | 67 |
| 4.11 | a) Illustration of the optical setup of the Raman receiver. F...Rayleigh filter, P...pinhole, L...matching lens. b) Spectra acquired from a polypropylene target with and without pinhole. | 68 |
| 5.1 | Different detection scheme employed in Raman spectroscopy. a) Standard configuration with operator, instrument and sample in close proximity. b) Remote configuration, where the instrument is deployed to the sample and transmits the analysis result. c) Stand-off configuration, where the instrument and operator are located distant from the investigated sample. | 120 |

| | | |
|------|--|-----|
| 5.2 | Illustration of the general built-up of a stand-off Raman spectrometer. The laser beam is directed at the sample, where the inelastically backscattered light is collected by an appropriate collection optic. Subsequently, the laser light is blocked by an Rayleigh filter (F), after that the light is spectrally analyzed and detected. | 122 |
| 5.3 | Timing diagram of a pulsed excitation with synchronized detection. The laser pulse is detected by a photodiode (or internally given) producing a synchronization pulse. After a certain delay time t_d the gate of the camera is opened for a given period (τ_g). | 123 |
| 5.4 | Different principles of Hyperspectral imaging. a) Mapping or Whiskbroom imaging. b) Line-scanning or pushbroom imaging. c) Staring or Spectral scanning imaging. | 124 |
| 5.5 | Optical setup for the mapping stand-off Raman instrument. The final coaxial mirror is mounted on a motorized kinematic mount for computer controlled movement of the laser beam at the target. | 126 |
| 5.6 | a) Pattern of 9x9 1 mm spaced points, produced by accumulating ten laser pulses on a piece of photo-paper at a distance of 15 m. b) Photo of the mirror setup including the two stepper motors (1,2), the kinematic mirror holder (3), the beam conditioning unit (5) and the laser (4). | 127 |
| 5.7 | a) Illustration of the principle setup for a staring stand-off HSRI instrument. b) The general structure of the HSI in the staring HSRI type with stacked spectral snapshots, where the same pixel on every stack represent the measured Raman spectrum. | 129 |
| 5.8 | a) Measured transmission of the VISR LCTF. b) Illustration of a single Lyot type cell used in the VISR LCTF with P...polarizer, R...fixed retarder and LC...liquid-crystal. c) Zoom in of two transmission bands at 520 and 530 nm. d) | 131 |
| 5.9 | a) Black & white image of the fluorescent light bulb. b) Intensity distribution at the most intense emission band at 612 nm. c) Intensity distribution at 697 nm. d) Raw spectra of point P1 at the center of the light bulb and of point P2 located at the electrodes. e) Inset showing zoomed version of the spectral range showing the most significant differences between point P1 and P2. | 132 |
| 5.10 | Characterization of the Explorer One HE 532. a) Pulse energy and average power for different repetition rates. b) Laser pulses for different diode currents. c) Pulse energy and average power for different diode currents. d) Laser pulses for different repetition rates. | 133 |

5.11 **a)** Rendering of the compact, mobile instrument setup. **b)** Photo of an overview of the prototype build on the optical table. **c)** Photo of the front of the prototype build on the optical table. 1...Explorer One DPSS, 2...iCCD (1024x1024), 3...EKSPILA laser, 4...Celestron C6 telescope, 5...VariSpec LCTF, 6...Rayleigh filter, 7...Focus motor control, 8...Galilean beam expander, 9...custom made, front-mounted collinear laser mirror holder. 136

5.12 Illustration of the principle of a Random Decision Forest. Out of the complete training data matrix, bootstrap samples are drawn randomly, for each a decision tree is grown in the training phase. Once the RDF is complete, a new sample is classified by majority vote of all decision trees. 139

List of Tables

| | |
|--|-----|
| 2.1 Overview over interaction cross sections (σ in $\text{cm}^2/\text{molecule}$) selected spectroscopic techniques. Adapted from [36] | 23 |
| 3.1 Overview over a selection of light detectors for the MIR region. Typical values are given for the detectivity D^* in $\text{cm Hz}^{0.5} \text{W}^{-1}$, the time constant τ , the usable spectral range and the operating temperatures. | 31 |
| 3.2 Pulsed solid state lasers used in the works presented in this thesis and their respective properties. | 41 |
| 3.3 iCCD cameras used in the works presented in this thesis. Both devices were manufactured by Princeton Instruments. | 49 |
| 4.1 Overview over the specifications for the commercially available tunable FPFs with integrated pyroelectric (and photon) detector. | 59 |
| 4.2 Reposition stability of the tunable FPF LFP5580 when the same four control voltages are applied multiple times in random order. σ is the standard deviation of the central wavenumber and FWHM, respectively. | 60 |
| 5.1 Different commercially available LCTFs and their characteristic properties. VS stands for VariSpec. | 130 |

Peer-reviewed research articles

1 Stand off spatial offset Raman spectroscopy: a distant look behind the scenes

B. Zachhuber, C. Gasser, A. J. Hobro, E. T. H. Chrysostom, B. Lendl, in *Proceedings of SPIE*, (Eds: R. Zamboni, F. Kajzar, A. A. Szep, C. Lewis, D. Burgess, M. T. Gruneisen, M. Dusek, J. G. Rarity), **2011**, vol. 8189, p. 818904.

2 Stand-Off Spatial Offset Raman Spectroscopy for the Detection of Concealed Content in Distant Objects

B. Zachhuber, C. Gasser, E. t. H. Chrysostom, B. Lendl, *Anal. Chem.* **2011**, 83, 9438.

3 Depth profiling for the identification of unknown substances and concealed content at remote distances using time resolved stand off Raman spectroscopy

B. Zachhuber, C. Gasser, G. Ramer, E. t. H. Chrysostom, B. Lendl, *Appl. Spectrosc.* **2012**, 66, 875.

4 Stand-off Spatial Offset Raman Scattering

B. Zachhuber, C. Gasser, E. H. Chrysostom, B. Lendl, *Lasers, Sources, Relat. Photonic Devices, OSA Tech. Dig.* **2012**, 8.

5 On-line monitoring of methanol and methyl formate in the exhaust gas of an industrial formaldehyde production plant by a mid-IR gas sensor based on tunable Fabry-Pérot filter technology

A. Genner, C. Gasser, H. Moser, J. Ofner, J. Schreiber, B. Lendl, *Anal. Bioanal. Chem.* **2017**, 409, 753.

6 Application of a tunable Fabry-Pérot filter to mid-infrared gas sensing

C. Gasser, A. Genner, H. Moser, J. Ofner, B. Lendl, *Sensors Actuators, B Chem.* **2017**, 242, 9.

7 Simultaneous Laser Doppler Velocimetry and stand-off Raman spectroscopy as a novel tool to assess flow characteristics of process streams

B. Haddadi, C. Gasser, C. Jordan, M. Harasek, B. Lendl, *Chem. Eng. J.* **2018**, 334, 123.

8 Enhanced mid-infrared multi-bounce ATR spectroscopy for online detection of hydrogen peroxide using a supercontinuum laser

C. Gasser, J. Kilgus, M. Harasek, B. Lendl, M. Brandstetter, *Opt. Express* **2018**, 26, 12169.

Patents

1 Distanzbasierte Offset Spektralanalyse

B. Lendl, B. Zachhuber, C. Gasser, Patent, Country: Austria, 511512; submitted: 21.05.2011, granted: 15.02.2013

2 Methods for the contactless determination of flow parameters and analytes within the flow

M. Harasek, B. Lendl, C. Gasser, B. Haddadi, C. Jordan, Patent, PCT, Nr. Wo 2018/192996; submitted: 19.04.2017, granted: 25.10.2018

Conference contributions

1 Application of tunable MEMS-based Fabry-Pérot filters and pulsable thermal infrared sources in MIR spectroscopy

C. Gasser, B. Lendl, Poster: *12th Martin and Willis student meeting*, Glasgow; 12.09.2013 - 13.09.2013

2 Stand-off SORS: Spatial Offset Raman Spectroscopy

C. Gasser, Engelene Chrysostom, B. Zachhuber, B. Lendl, Poster: *IRDG Spring Meeting Vienna*, Wien; 24.04.2014 - 25.04.2014

3 Stand-off Spatially Offset Raman spectroscopy: towards 3D stand-off imaging

C. Gasser, T. Aichinger, J. Ofner, B. Lendl, Poster: *11th Symposium Confocal Raman Imaging*, Ulm, Germany; 29.09.2014 - 01.10.2014

4 Stand-off Spatially Offset Raman spectroscopy

C. Gasser, T. Aichinger, J. Ofner, B. Lendl, Poster: *XXIV. International Conference On Raman Spectroscopy*, Jena, Germany; 10.08.2014 - 15.08.2014

5 MIR spectroscopic determination of hydrogen peroxide using tunable Fabry-Pérot MEMS filter

C. Gasser, B. Lendl, Presentation: *IR WORKshop*, Olching, Germany; 10.11.2014 - 11.11.2014

6 Contactless temperature measurement using an IR microscope and a liquid nitrogen cooled MCT-detector

W. Tomischko, C. Gasser, B. Lendl, Poster *IR WORKshop*, Olching, Germany; 10.11.2014 - 11.11.2014

7 Application of tunable Fabry-Pérot filters to MIR spectroscopy for qualitative and quantitative analysis of gas mixtures

C. Gasser, A. Genner, H. Moser, J. Ofner, B. Lendl, Poster: *ICAVS 8*, Wien; 12.07.2015 - 17.07.2015

8 Ultrasound-Enhanced In-line Raman Sensing of Solid Samples in Liquid Matrices

K. Wieland, H. Rasoulimehrabani, S. Tauber, C. Gasser, B. Lendl, Poster: *SCIX 2016*, Minneapolis, MN, USA; 18.09.2016 - 23.09.2016.

9 Stand-Off Hyperspectral Raman Imaging

C. Gasser, J. Ofner, B. Lendl, Poster: *IRDG Christmas Meeting 2016*, London; 19.12.2016.

10 Stand-off hyperspectral imaging - towards mobile, high throughput remote chemical identification and quantification using chemometrics

C. Gasser, J. Ofner, B. Lendl, Presentation: *ICAVS 9 - International Conference on Advanced Vibrational Spectroscopy*, Victoria, Canada; 11.06.2017 - 16.06.2017.

11 Towards an EC-QCL based Sensor for Monitoring Side Products of Formaldehyde Production

A. Genner, C. Gasser, H. Moser, J. Ofner, B. Lendl, Poster: *IRDG Christmas Meeting 2017*, London UK; 21.12.2017

12 Process stream characterisation by simultaneous laser doppler velocimetry and stand-off Raman spectroscopy

B. Haddadi, C. Gasser, C. Jordan, B. Lendl, M. Harasek, Presentation: *APACT 18 - Advances in Progress Analytics and Control Technology 2018 Conference*, Newcastle, UK; 25.04.2018 - 27.04.2018.

Curriculum vitae

PERSONAL INFORMATION

Christoph Gasser

📍 Gregor-Mendel-Straße 2-4/1/10, Vienna, 1180, Austria

☎ +43 650 6344649

✉ christoph.gasser@tuwien.ac.at

Sex Male | Date of birth 21/01/1988 | Nationality Italian

WORK EXPERIENCE

Jan 2018

Co-Founder of usePAT GmbH

Spin-off of the Vienna University of Technology, Start-up in the Technology Sector, Ultrasound enhanced Process Analytical Technology (<https://www.soniccatch.com/>)

- Development of add-ons for inline PAT probes to increase sensitivity, selectivity and stability.

Business or sector Industrial Technologies

Since Nov 2013

Research Assistant

Vienna University of Technology, Institute of chemical Technologies & Analytics, Research Group Environmental & Process Analytics (<http://www.cta.tuwien.ac.at/epa/pa/>)

- Development of laser based analytical equipment & handling of research projects

Business or sector Educational & Research

Aug 2012 - Nov 2013

Project Assistant

Vienna University of Technology, Institute of chemical Technologies & Analytics, Research Group Environmental & Process Analytics (<http://www.cta.tuwien.ac.at/epa/pa/>)

- Development of process analytical equipment & validation of prototypes

Business or sector Educational & Research

Aug 2011 – Sep 2011

Analytical Chemist

QuantaRed Technologies GmbH (www.quantared.com)

- Sensitive IR measurements of hydrocarbons in water and soil with quantum cascade lasers

Business or sector Chemical Industry

Aug 2008 – Sep 2008

Assistant Analytical Chemist

VOG Products (<http://www.vog-products.it/>)

- Assistant in production and process analytics department

Business or sector Food Industry

Jul 2006 – Aug 2006

Assistant in Shipping and Logistics

Fruitservice S.R.L.

- Organizing shipping and forwarding, logistics of transport

Business or sector Food Industry

Aug 2005

Internship

Winkler & Sandrini (<http://www.winkler-sandrini.it/>)

- Assistant in tax and business counselling

Business or sector Counselling

EDUCATION AND TRAINING

Since Nov 2013 **Doctoral Programme “Technical Chemistry” (ongoing)**

Vienna University of Technology, Austria

- PhD Thesis “Tunable filters in Mid-infrared and Raman Spectroscopy”

Mar 2007 – May 2013 **Master of Science
Bachelor of Science**

Vienna University of Technology, Austria

Graduated with distinction

- Master Thesis “Characterization and Application of Fabry-Pérot Tunable Detectors and Pulsed MIR Sources for Novel Sensor Elements)
- Master Programme : Technical Chemistry
- Bachelor Programme: Technical Chemistry

2002 – 2007 **Matura**

Realgymnasium Bolzano

- scientific primary and secondary education

PERSONAL SKILLS

Mother tongue(s) German

Other language(s)

| | UNDERSTANDING | | SPEAKING | | WRITING |
|---------|---------------|---------|--------------------|-------------------|---------|
| | Listening | Reading | Spoken interaction | Spoken production | |
| English | C1 | C1 | B2/C1 | B2/C1 | C1 |
| Italian | C1 | C1 | B2/C1 | B2/C1 | B2/C1 |

Levels: A1/2: Basic user - B1/2: Independent user - C1/2 Proficient user
Common European Framework of Reference for Languages

Communication skills Team and solution oriented communication skills

Computer skills Proficient user of MS Office, Latex, OriginPro, LabView, Python, Matlab

Other skills “out-of-the-box” thinking, solution oriented

Driving licence ▪ B

ADDITIONAL INFORMATION

Additional Training Laser safety officer
Publications 9 peer-reviewed publications
Conference contributions 12 conference contributions
Honours and awards Performance scholarship of South Tyrol for special performances in higher studies

Patents

TUtheTOP High potential program of the TU Wien (2014/15)
Distanzbasierte Offset Spektralanalyse, Österreich, Nr. 511512
Methods for the contactless determination of flow parameters and analytes within the flow,
PCT, Nr. Wo 2018/192996